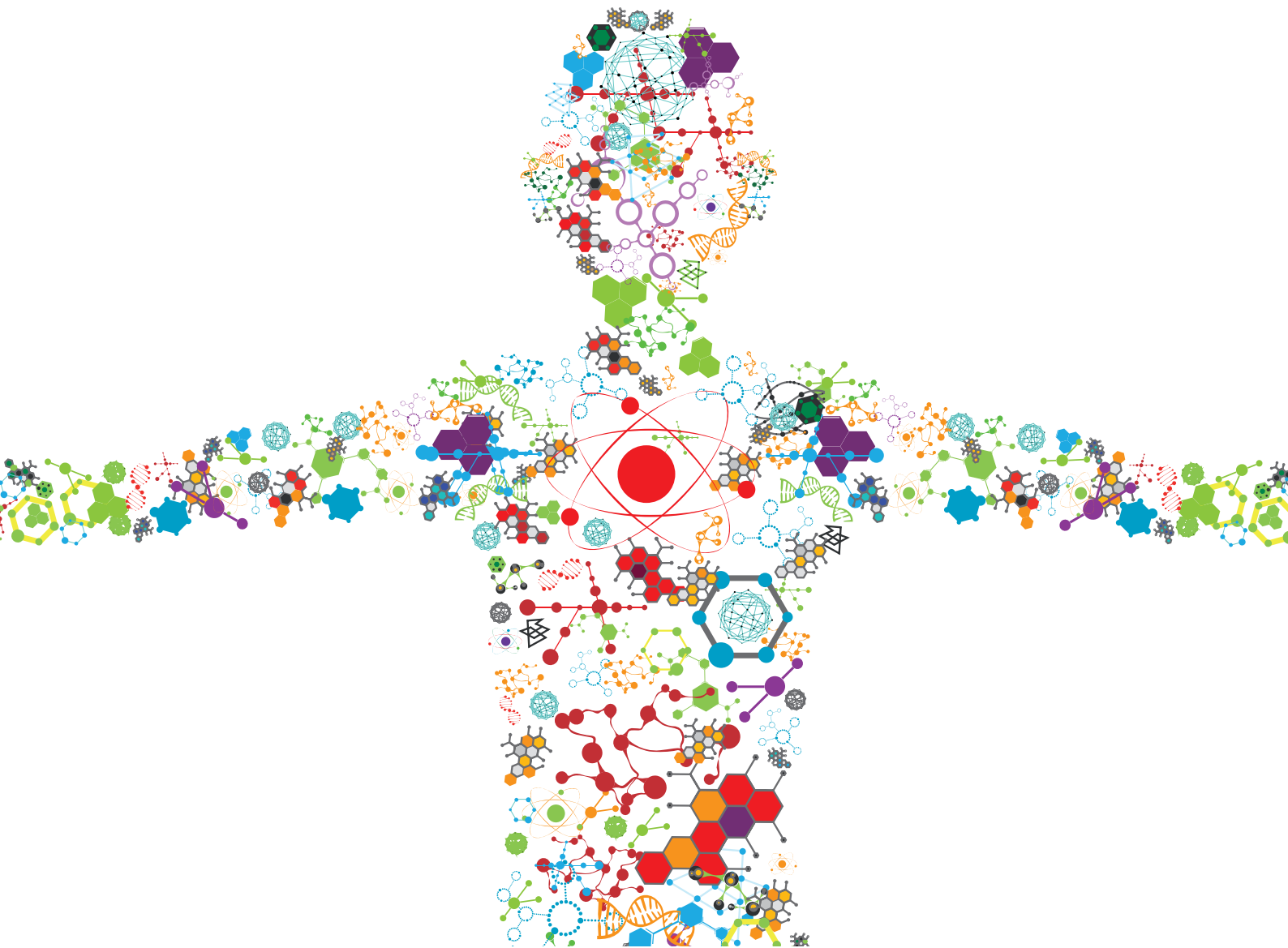


CONTINUOUS BIOMANUFACTURING IN MICROBIAL SYSTEMS

EDITED BY: Christoph Slouka, Christoph Herwig, Peter Neubauer and
Frank Delvigne

PUBLISHED IN: Frontiers in Bioengineering and Biotechnology





frontiers

Frontiers eBook Copyright Statement

The copyright in the text of individual articles in this eBook is the property of their respective authors or their respective institutions or funders. The copyright in graphics and images within each article may be subject to copyright of other parties. In both cases this is subject to a license granted to Frontiers.

The compilation of articles constituting this eBook is the property of Frontiers.

Each article within this eBook, and the eBook itself, are published under the most recent version of the Creative Commons CC-BY licence.

The version current at the date of publication of this eBook is CC-BY 4.0. If the CC-BY licence is updated, the licence granted by Frontiers is automatically updated to the new version.

When exercising any right under the CC-BY licence, Frontiers must be attributed as the original publisher of the article or eBook, as applicable.

Authors have the responsibility of ensuring that any graphics or other materials which are the property of others may be included in the CC-BY licence, but this should be checked before relying on the CC-BY licence to reproduce those materials. Any copyright notices relating to those materials must be complied with.

Copyright and source acknowledgement notices may not be removed and must be displayed in any copy, derivative work or partial copy which includes the elements in question.

All copyright, and all rights therein, are protected by national and international copyright laws. The above represents a summary only. For further information please read Frontiers' Conditions for Website Use and Copyright Statement, and the applicable CC-BY licence.

ISSN 1664-8714

ISBN 978-2-88971-120-8

DOI 10.3389/978-2-88971-120-8

About Frontiers

Frontiers is more than just an open-access publisher of scholarly articles: it is a pioneering approach to the world of academia, radically improving the way scholarly research is managed. The grand vision of Frontiers is a world where all people have an equal opportunity to seek, share and generate knowledge. Frontiers provides immediate and permanent online open access to all its publications, but this alone is not enough to realize our grand goals.

Frontiers Journal Series

The Frontiers Journal Series is a multi-tier and interdisciplinary set of open-access, online journals, promising a paradigm shift from the current review, selection and dissemination processes in academic publishing. All Frontiers journals are driven by researchers for researchers; therefore, they constitute a service to the scholarly community. At the same time, the Frontiers Journal Series operates on a revolutionary invention, the tiered publishing system, initially addressing specific communities of scholars, and gradually climbing up to broader public understanding, thus serving the interests of the lay society, too.

Dedication to Quality

Each Frontiers article is a landmark of the highest quality, thanks to genuinely collaborative interactions between authors and review editors, who include some of the world's best academicians. Research must be certified by peers before entering a stream of knowledge that may eventually reach the public - and shape society; therefore, Frontiers only applies the most rigorous and unbiased reviews.

Frontiers revolutionizes research publishing by freely delivering the most outstanding research, evaluated with no bias from both the academic and social point of view. By applying the most advanced information technologies, Frontiers is catapulting scholarly publishing into a new generation.

What are Frontiers Research Topics?

Frontiers Research Topics are very popular trademarks of the Frontiers Journals Series: they are collections of at least ten articles, all centered on a particular subject. With their unique mix of varied contributions from Original Research to Review Articles, Frontiers Research Topics unify the most influential researchers, the latest key findings and historical advances in a hot research area! Find out more on how to host your own Frontiers Research Topic or contribute to one as an author by contacting the Frontiers Editorial Office: frontiersin.org/about/contact

CONTINUOUS BIOMANUFACTURING IN MICROBIAL SYSTEMS

Topic Editors:

Christoph Slouka, Vienna University of Technology, Austria

Christoph Herwig, Vienna University of Technology, Austria

Peter Neubauer, Technical University of Berlin, Germany

Frank Delvigne, University of Liège, Belgium

Christoph Herwig is founder of Exputec GmbH.

Citation: Slouka, C., Herwig, C., Neubauer, P., Delvigne, F., eds. (2021). Continuous Biomanufacturing in Microbial Systems. Lausanne: Frontiers Media SA.
doi: 10.3389/978-2-88971-120-8

Table of Contents

04	<i>Editorial: Continuous Biomanufacturing in Microbial Systems</i> Christoph Herwig, Christoph Slouka, Peter Neubauer and Frank Delvigne
07	<i>Automation of Dead End Filtration: An Enabler for Continuous Processing of Biotherapeutics</i> Garima Thakur, Vishwanath Hebhi, Subhash Parida and Anurag S. Rathore
18	<i>The Lazarus Escherichia coli Effect: Recovery of Productivity on Glycerol/Lactose Mixed Feed in Continuous Biomanufacturing</i> Stefan Kittler, Julian Kopp, Patrick Gwen Veelenturf, Oliver Spadiut, Frank Delvigne, Christoph Herwig and Christoph Slouka
29	<i>The Impact of Glass Material on Growth and Biocatalytic Performance of Mixed-Species Biofilms in Capillary Reactors for Continuous Cyclohexanol Production</i> Ingeborg Heuschkel, Rakesh Dagini, Rohan Karande and Katja Bühler
39	<i>Integrated Continuous Bioprocess Development for ACE-Inhibitory Peptide Production by Lactobacillus helveticus Strains in Membrane Bioreactor</i> Cyril Raveschot, Barbara Deracinois, Emmeline Bertrand, Christophe Flahaut, Marc Frémont, Djamel Drider, Pascal Dhulster, Benoit Cudennec and François Coutte
52	<i>Revisiting the Growth Modulon of Corynebacterium glutamicum Under Glucose Limited Chemostat Conditions</i> Michaela Graf, Thorsten Haas, Attila Teleki, André Feith, Martin Cerff, Wolfgang Wiechert, Katharina Nöh, Tobias Busche, Jörn Kalinowski and Ralf Takors
69	<i>Intrinsically Magnetic Cells: A Review on Their Natural Occurrence and Synthetic Generation</i> Alexander Pekarsky and Oliver Spadiut
88	<i>Repetitive Fed-Batch: A Promising Process Mode for Biomanufacturing With E. coli</i> Julian Kopp, Stefan Kittler, Christoph Slouka, Christoph Herwig, Oliver Spadiut and David J. Wurm
101	<i>Single-Cell Technologies to Understand the Mechanisms of Cellular Adaptation in Chemostats</i> Naia Risager Wright, Nanna Petersen Rønnest and Nikolaus Sonnenschein
111	<i>Selective Release of Recombinant Periplasmic Protein From E. coli Using Continuous Pulsed Electric Field Treatment</i> Felix Schottroff, Jens Kastenhofer, Oliver Spadiut, Henry Jaeger and David J. Wurm



Editorial: Continuous Biomanufacturing in Microbial Systems

Christoph Herwig^{1,2*}, Christoph Slouka¹, Peter Neubauer³ and Frank Delvigne⁴

¹ Research Division Biochemical Engineering, Institute of Chemical, Environmental and Bioscience Engineering, Vienna University of Technology, Vienna, Austria, ² Competence Center CHASE GmbH, Linz, Austria, ³ Chair of Bioprocess Engineering, Department of Biotechnology, Technische Universität Berlin, Berlin, Germany, ⁴ TERRA Teaching and Research Centre, Microbial Processes and Interactions (MIPI), Gembloux Agro-Bio Tech – Université de Liège, Gembloux, Belgium

Keywords: continuous bioprocessing, microbial process, cellular mechanism, metabolic load, product location, product recovery, USP, DSP

Editorial on the Research Topic

Continuous Biomanufacturing in Microbial Systems

OPEN ACCESS

Edited by:

Saurabh Dhiman,
South Dakota School of Mines and
Technology, United States

Reviewed by:

Guodong Luan,
Qingdao Institute of Bioenergy and
Bioprocess Technology (CAS), China
Jochen Strube,
Clausthal University of
Technology, Germany

*Correspondence:

Christoph Herwig
christoph.herwig@tuwien.ac.at

Specialty section:

This article was submitted to
Bioprocess Engineering,
a section of the journal
Frontiers in Bioengineering and
Biotechnology

Received: 09 February 2021

Accepted: 12 May 2021

Published: 07 June 2021

Citation:

Herwig C, Slouka C, Neubauer P and
Delvigne F (2021) Editorial:
Continuous Biomanufacturing in
Microbial Systems.
Front. Bioeng. Biotechnol. 9:665940.
doi: 10.3389/fbioe.2021.665940

Continuous processing is without doubt the most effective and economically viable processing mode, because it optimally uses the installed assets. While most chemical industrial processes are designed and executed already in continuous operation, the biotechnology industry still relies on batchwise production, due to multiple unknown variables of complex biological systems.

Recent reports have demonstrated, specifically in the area of cell culture processes, that continuous biomanufacturing (CBM) has significant economic advantages. Continuous processes significantly influence the ecological and economic footprint, as facilities become smaller and versatile with the application of modular design approaches. Continuous cultivation approaches have the need to tightly control process variability along prolonged processing times, calling for accurate process analytics and robust control strategies.

However, establishing integrated processes for production with dedicated microbial systems is far more complicated, although of course continuous processes are standard, e.g., in the areas of biogas production, wastewater treatment and bioleaching. The complication is due to the fact that, especially in the area of the production of defined recombinant proteins, the protein often accumulates in the cell, which represents a natural physical barrier contradicting continuous operational strategies. In addition, common induction systems have a highly time dependent effect and may lead to high temporary metabolic load. Both effects lead to limitations in prolonged recombinant protein production, seen in an irreversible drop in protein productivity. Hence, the lack of basic knowledge about the regulatory mechanisms leading to population evolution during prolonged recombinant protein production prevents the industrial application of continuous biomanufacturing. But also in other microbial processes, with both engineered and non-engineered single-species microbial cell factories, continuous operation has so far rarely been realized.

So what are the current challenges and scientific enablers for advancing continuous biomanufacturing with microbial cells? Several challenges need to be answered by scientific knowledge (Figure 1, outer circle):

- How to control metabolic load for sustained recombinant product production, for example by the assessment of population stability, analyzing phenotypic, and genotypic instabilities
- How to change the product location to circumvent the internal physical limit of the cell?
- How to achieve prolonged time invariant processing providing stable productivity and product quality to the downstream process
- How to efficiently integrate upstream and downstream processing?



FIGURE 1 | Challenges (outer circle) and in the current topic addressed scientific advancements (inner circle) for enabling robust microbial continuous biomanufacturing (CBM).

The goal of this electronic article collection is to give an overview on recent scientific advances addressing above points.

The selected contributions in this Research Topic show significant scientific advancements to microbial CBM and can be classified in the following three aspects (**Figure 1** inner circle):

1. Cellular mechanisms
2. Intensified bioprocessing
3. Product recovery.

Those contributions address well the challenges mentioned above.

CELLULAR MECHANISMS

It is important to understand the population dynamics and its mechanisms of the cell being cultivated in the

bioreactor. The perspective article “Single-Cell Technologies to Understand the Mechanisms of Cellular Adaptation in Chemostats” by Risager Wright et al. addresses the importance that population heterogeneity should be taken into account for CBM design and analyzed the suitability of current analytical devices. The contribution “The Lazarus *Escherichia coli* Effect: Recovery of Productivity on Glycerol/Lactose Mixed Feed in Continuous Biomanufacturing” by Kittler et al. addresses a sudden phenomenon of productivity drop and suggests that the mixed feed of Glycerol and Lactose, but also Galactose as a light inducer, are responsible for population dynamics. Graf et al., with their contribution “Revisiting the Growth Modulon of *Corynebacterium glutamicum* Under Glucose Limited Chemostat Conditions,” analyze the control mechanisms on transcriptomic and metabolic level, with the conclusion, that glycolysis, pentose-phosphate pathway and citric acid cycle are

predominately metabolically controlled under glucose-limiting chemostat conditions and that transcriptional regulation takes control over glycolysis once glucose-rich growth conditions are installed.

PROCESSING ALTERNATIVES

How to achieve prolonged sustained productivities in the bioreactor? Challenges such as population heterogeneity, loss of the catalyst need to be overcome. In cell culture processes, perfusion techniques are the method of choice currently.

The research article “Repetitive Fed-Batch: A Promising Process Mode for Biomanufacturing With *E. coli*” by Kopp et al. found that a repetitive fed-batch for *E. coli* leads to a higher space-time yield compared to a single-cycle fed-batch and can potentially outperform continuous biomanufacturing by classical chemostats. Raveschot et al., with their contribution “Integrated Continuous Bioprocess Development for ACE-Inhibitory Peptide Production by *Lactobacillus helveticus* Strains in Membrane Bioreactor” developed an integrated continuous process for peptide production with a membrane bioreactor, which led to a 3 fold increased peptide productivity compared to batch production. In the contribution “The Impact of Glass Material on Growth and Biocatalytic Performance of Mixed-Species Biofilms in Capillary Reactors for Continuous Cyclohexanol Production,” Heuschkel et al. growth and catalytic performance of mixed-species biofilms for cyclohexanol was investigated. Four phases of the biofilm cultivation could be distinguished and the cyclohexanol production rate could be significantly improved.

PRODUCT RECOVERY

How to deliver continuous product to the downstream? In addition to the production mode, the product must be efficiently be separated from the cells in order to integrate smoothly to the subsequent downstream process.

Pekarsky and Spadiut with their review “Intrinsically Magnetic Cells: A Review on Their Natural Occurrence and Synthetic Generation” investigate the state of the art of Natural intrinsically magnetic cells which can be used to separate the cells during CBM. The research article “Selective release of recombinant periplasmic protein from *E. coli* using continuous

pulsed electric field treatment” by Schottroff et al. focusses on novel process methods to circumvent product accumulation in *E. coli* and triggering product secretion to the extracellular medium by applying pulsed electric fields. Thakur et al., with their contribution “Automation of Dead End Filtration: An Enabler for Continuous Processing of Biotherapeutics” demonstrated that Dead end filtration, which is conventionally done in batch mode, can be automated and can therefore serve as a potential tool for continuous biomanufacturing.

We believe, this topic issue made a significant contribution to advance microbial CBM to become reality. However, we are aware that many more aspects need to be addressed to complete the picture, such as PAT, modeling, and control aspects!

AUTHOR CONTRIBUTIONS

CH designed and wrote the manuscript. FD, PN, and CS revised and revised the manuscript. All authors contributed to the article and approved the submitted version.

FUNDING

Funding was kindly provided by the Competence Center CHASE GmbH, funded by the Austrian Research Promotion Agency (FFG) (No. 868615).

ACKNOWLEDGMENTS

The Editors thank all that have contributed to this special issue, and we are happy to document in this collection articles of the latest promising scientific advancement to leverage the large potential of continuous microbial cultivation and to finally assess, control, and optimize product formation in bioprocesses.

Conflict of Interest: The authors declare that the research was conducted in the absence of any commercial or financial relationships that could be construed as a potential conflict of interest.

Copyright © 2021 Herwig, Slouka, Neubauer and Delvigne. This is an open-access article distributed under the terms of the Creative Commons Attribution License (CC BY). The use, distribution or reproduction in other forums is permitted, provided the original author(s) and the copyright owner(s) are credited and that the original publication in this journal is cited, in accordance with accepted academic practice. No use, distribution or reproduction is permitted which does not comply with these terms.



Automation of Dead End Filtration: An Enabler for Continuous Processing of Biotherapeutics

Garima Thakur, Vishwanath Hebhi, Subhash Parida and Anurag S. Rathore*

Department of Chemical Engineering, Indian Institute of Technology Delhi, New Delhi, India

OPEN ACCESS

Edited by:

Christoph Herwig,
Vienna University of Technology,
Austria

Reviewed by:

Ralf Pörtner,
Hamburg University of Technology,
Germany

Ignacio Poblete-Castro,
Andres Bello University, Chile

*Correspondence:

Anurag S. Rathore
asrathore@biotechcmz.com

Specialty section:

This article was submitted to
Bioprocess Engineering,
a section of the journal
Frontiers in Bioengineering and
Biotechnology

Received: 07 April 2020

Accepted: 15 June 2020

Published: 03 July 2020

Citation:

Thakur G, Hebhi V, Parida S and
Rathore AS (2020) Automation
of Dead End Filtration: An Enabler
for Continuous Processing
of Biotherapeutics.
Front. Bioeng. Biotechnol. 8:758.
doi: 10.3389/fbioe.2020.00758

Dead end filtration is a critical unit operation that is used for primary and secondary clarification during manufacturing of both microbial and mammalian cell based biotherapeutics. Dead end filtration is conventionally done in batch mode and requires filter pre-sizing using extensive scouting studies, along with filter over-sizing before deployment to handle potential variability. However, continuous manufacturing processes require consistent use of dead-end filtration over weeks or months, with potential unpredictable variations in feed stream attributes, which is a challenge currently facing the industry. In this work, a dead-end filtration skid is designed for continuous depth filtration, incorporating multiple small-sized filters along with turbidity, and pressure sensors with immediate switching to a fresh filter whenever turbidity or pressure breakthrough above a pre-determined cut-off is detected in real time. The skid has been successfully tested for manufacturing of granulocyte colony stimulating factor from *Escherichia coli*, human serum albumin from *Pichia pastoris*, and a monoclonal antibody therapeutic from CHO cells. The proposed skid can be directly applied for any dead-end filtration application with minimal prior scouting studies or sizing calculations for scale-up. It is a useful solution for continuous processing trains where the nature of the feed, such as its turbidity or host cell proteins content, may change over long continuous campaigns, rendering previous sizing calculations inaccurate. The skid also allows significant cost savings by eliminating the sizing safety factor of 1.5–2x which is generally added before filter deployment at manufacturing scale.

Keywords: Dead end filtration, continuous bioprocessing, depth filtration, turbidity breakthrough, pressure breakthrough

INTRODUCTION

The success of biologic molecules, in particular monoclonal antibodies (mAbs), in treating various diseases has led to an increased demand and need for scale-up technologies (Ashton, 2001; Anicetti, 2009; Roger, 2010; Xu and Zhang, 2014). Increasing demand has driven significant improvements in upstream process, with current commercial titers for mAbs as high as 10 g/L (Birch and Biologics, 2005; Kelley, 2009; Pollock et al., 2013; Tran et al., 2014; Grilo et al., 2017) compared to the older processes that would have titers of <1 g/L. The titers of microbial processes have also risen up to 5–6 g/L for both *Escherichia coli* (Slouka et al., 2018; Wilson et al., 2019) and *Pichia pastoris* based platforms (Kjeldsen, 2000; Kjeldsen et al., 2002; Xie et al., 2008). High cell density is now commonly achieved in both mammalian and microbial processes, and therefore

primary recovery of cells can be a significant challenge (Wurm, 2004; Aldor et al., 2005). At manufacturing scale, mammalian, bacterial, and yeast-based harvest broths are all traditionally clarified by using depth filters. Introduction of depth filters in the downstream processing train has shown to increase the capacity of the subsequent sterilizing grade filters which are typically used to protect chromatography columns and viral filters from clogging (Kandula et al., 2009; Pegel et al., 2011). Depth filters are used not only to remove insoluble widely distributed particles in the train, but can also be exploited for removing soluble impurities such as host cell proteins (HCP), host cell DNA (HCDNA), and charged particles (Yigzaw et al., 2006; Khanal et al., 2018).

Despite the ubiquity of depth filtration, accurate sizing of the filters remains a challenge. At manufacturing scale, sizing is very important for economical utilization of filter modules, which are one of the most expensive consumables in the downstream process after chromatography resins, and can contribute up to 50% of the consumable costs for downstream clarification (Felo et al., 2013). Filter capacity and sizing studies are affected by a large number of parameters, including the type of cell line, culture conditions, aggregate levels, particle size distribution, centrifugation parameters, and lot-to-lot filter variability (Yavorsky et al., 2003; Goldrick et al., 2017). It is difficult to accurately account for potential changes in parameters such as cell viability which may lead to higher amounts of HCP and HCDNA and lead to increased turbidity of the process stream (Boerlage, 2001), thereby affecting the sizing requirements (Boerlage, 2001; Pham, 2010; Krupp et al., 2017). Over-sizing of depth filters can significantly impact the economics of the process, while under-sizing can lead to process deviations such as turbidity breakthrough, clogging of subsequent sterile filters, or fouling of chromatographic columns and ultrafiltration filters, significantly hampering product quality, and process productivity (Wakeman, 2007; Kandula et al., 2009; Lutz, 2009; Popova et al., 2016).

In industry, depth filtration sizing is currently performed by using representative samples of the process stream at small scale. Filters are usually operated under constant flow rate conditions so that volumetric flow rates remain constant over time, allowing consistent operation of subsequent downstream steps (Liu et al., 2010). For constant flow operation, the filter capacity is defined by the cumulative volume of filtrate until a maximum pressure rating or turbidity breakthrough is reached, whereas for constant pressure, the filter capacity is defined as the total volume of feed processed until the flow at that pressure becomes lower than a certain minimum cut-off. Once the process development is completed at small scale, linear scale-up is possible along with an extra safety factor of 1.5 to 2 times the linearly scaled-up filter area, as a benchmark based on manufacturing experience (Lutz, 2009; Agarwal et al., 2016). A larger safety factor increases the process resilience to deviations and reduces the risk of process material exceeding the filter capacity. However, large safety factors also significantly increase process costs due to the high cost of filters, as well as increase product loss, holdup volumes, and process preparation downtime.

Current depth filtration approaches also fall short when it comes to continuous processing trains (Jungbauer, 2013; Croughan et al., 2015; Konstantinov and Cooney, 2015). The shift from batch to continuous has been facilitated by a combination of enabling technologies such as multi-column chromatography setups, and process analytical technology (PAT) tools for real time monitoring of critical quality attributes and process parameters in accordance with the US FDA's guidance on PAT (FDA, 2004). However, adapting dead-end depth and sterile filtration for continuous operation has been neglected thus far. There have been some attempts to implement PAT approaches in dead-end filtration by incorporating in-line monitoring sensors to trigger alarms in case process limits are exceeded. For example, in-line pressure sensors have been used to monitor differential pressure across dead-end filters in real time, plot the data on monitoring charts, and trigger alarms in case of pressure build-up due to filter clogging or other issues such as kinks in tubing (Bink and Furey, 2010). Another approach utilized in-line absorbance measurements at 410 nm to measure HCP breakthrough through depth filters, as HCP complexes give detection signals at this wavelength but the target proteins do not (Rathore et al., 2010).

However, a complete solution for continuous operation of dead-end filtration has not yet been developed. The solution must incorporate enabling technology to allow process flow streams to pass through the filters without interruption over weeks or months of continuous operation (Steinebach et al., 2017). The setup should also be equipped with relevant sensors to monitor turbidity or pressure in the feed and filtrate streams and ensure that filters are replaced, either automatically or manually, when they become clogged. This should be done without affecting the filtrate quality at any point in the continuous operation, as any turbidity breakthrough or filter damage can lead to clogging of the subsequent unit operations like chromatography columns. Finally, the setup should be flexible and robust enough to handle unexpected deviations or shifts in the composition of the feed stream, such as increased turbidity or titer due to changing cell culture conditions in the upstream reactor. The filter should not rely on extensive sizing calculations, which are unlikely to be accurate in the case of months of continuous operation instead of well-characterized batches. In this paper, we propose such a filtration skid setup with three small-size filters (each with less than 10% of the required large-scale size) and integrated in-line pressure and turbidity sensors. The process flow stream is directed through one filter at constant flowrate until a pressure or turbidity breakthrough set-point is reached, at which time a valve instantly switches and directs the stream through a waiting, pre-equilibrated filter. The process can therefore run uninterrupted without any downtime or disruption in flow. Due to this continuous cycling of filters, smaller sized filters can be used and significant savings can be made in overall filter area as some filters will likely remain unused. We have demonstrated the application of the skid in various downstream steps, including harvest clarification and sterile filtration for *E. coli*, *P. pastoris*, and Chinese hamster ovary (CHO) cell expressed products.

MATERIALS AND METHODS

Materials

Electrical Components

Micrologix 5000 from Allen Bradley with analog extension modules; 24V power supply unit, extension module, multiplex, and necessary electrical components and wiring were procured from a local vendor.

Filters

B1HC, D0HC, B0HC, and X0HC were procured from Millipore Corporation; 90ZA was procured from 3M Company; HP PDD1, HP PDH4, and Sterile Acrodisc Syringe filter 4652 were procured from Pall Life Sciences.

Feed Materials

rGCSF Refolding Output

The rGCSF was produced in the form of inclusion bodies (IBs). IBs were solubilized and refolded using dilution method (Hebbi et al., 2019). After the peak point was reached (8–10 h), the refolding reaction was quenched using glacial acetic acid at pH 4. In this process, many HCP were precipitated, which are generally removed using depth filtration.

CHO Cell Culture Harvest

Monoclonal antibody cell culture harvest was obtained from a major biopharmaceutical company. Two types of cell clarification studies were conducted, first using direct cell culture harvest for filtration and the second using post-centrifugation centrate for filtration.

Pichia Broth

Pichia pastoris broth for HSA production was directly taken from bioreactor with 20.3% wet weight. Another study was conducted using centrate from the centrifugation of the broth as it was noticed that the centrate is generally unstable and becomes turbid, which demands depth filtration post-centrifugation before processing the process feed by capture chromatography.

rGCSF Drug Product

Sterile filtration was conducted for rGCSF purified drug product after inclusion body solubilization, protein refolding, and polishing chromatography steps.

mAb Drug Product

Sterile filtration was conducted for mAb drug product after centrifugation, Protein A capture chromatography, viral inactivation, and polishing chromatography steps.

Method for Pressure and Turbidity Excursion Studies

When designing a clarification scheme, the properties of the particulate matter in the process stream play a significant role in defining the outcome. Particle size, density, and nature of the process stream vary as the stream moves from upstream to the final product. For example, for clarified mammalian cell culture broth, the number of cells, cell viability, HCP levels, and HCDNA

levels are key feed attributes. For high cell density fermentations like *P. pastoris*, solid content in terms of wet weight percentage is critical. For already clarified feed streams like chromatography elutes or quenched refolding output, optical density at 600 nm or turbidity of the feed stream can provide the required input. In many cases, tools for measuring particle size distribution are used to get insight into the mechanism of clogging, which can be very useful for selecting the optimal filter for improved performance. Once a set of depth filters have been selected, screening can be started to determine the final filter choice for use in the proposed continuous skid.

Properties of the different feed streams in our study are listed in **Table 1**. In general, process streams with high cell densities are highly unstable with particle sizes in micron ranges and have to be clarified immediately after harvest. For streams after centrifugation, the particle size reduces to less than 100 nm with nephelometric turbidity units (NTU) of 200–400. The refolding output of GCSF has particle size of 50–100 nm and NTU of 1600. The GCSF drug product, on the other hand, is highly clarified as it is the final formulated product and needs to be filtered through sterile filtration before filling and packaging. Filter screening can also be performed for primary and secondary filters in series. In our trials, 90ZA, and B0HC filters were screened as secondary depth filters for harvest material after the primary depth filter 30S, which is a commonly used setup in mAb processing. An alternative approach is that to perform centrifugation followed by a single depth filtration. Depth filters X0HC, B1HC, and B0HC were used as depth filters for filtering the centrate of mAb harvest.

Process samples and their corresponding filters were selected and screened for pressure breakthrough (for secondary depth filters and sterile filters) and turbidity breakthrough (for primary depth filters). Constant-flux turbidity excursion trials were conducted to quantify the cut-off NTU value where turbidity breakthrough starts. Primary depth filters are often vulnerable to turbidity breakthrough before pressure breakthrough. Thus, their capacities are measured based on NTU cut-off rather than pressure cut-off, as high NTU in the post-filter stream can clog subsequent filters or unit operations. In our demonstrations, a cut-off of 1000 NTU was selected for turbidity breakthrough. Similarly,

TABLE 1 | Properties of different feed streams used in this study.

Feed stream	Physicochemical properties of particulate matter
<i>Pichia pastoris</i> cell broth for HSA production	NTU 3500, mean particle size 4–6 μm w/w
<i>Pichia pastoris</i> cell broth centrate	NTU 300, mean particle size < 100 nm, unstable, becomes hazy in 12–15 h
CHO cell culture harvest	NTU 1785, cell viability 85%
CHO cell culture centrate	NTU 200–400, unstable, becomes hazy in 12–15 h
Refolding output of GCSF (quenched)	NTU 1600, white precipitate due to HCP while quenching from 9.5–4 using acetic acid, 50–100 nm size
Drug product GCSF	Clear solution
Drug product mAb	Clear solution

pressure excursion studies were performed for secondary depth filters and sterile filters and a pressure cut-off of 1.5 bar was selected due to operational limitations of the filtration setup and tubing. The cut-offs can be adjusted on a case-by-case basis.

For the excursion studies, filters were washed with WFI followed by the respective buffer at 200 LMH. The washed filter was connected to the skid after the solenoid valve. The process

stream was pumped through the skid using a peristaltic pump with flow rate of 200 LMH in the case of depth filtration and 300 LMH in the case of sterile filtration. The pressure and turbidity values were recorded in real time. High performance liquid chromatography (HPLC) methods for GCSF (Hebbi et al., 2019), HSA (Chopda et al., 2017), and mAb (Kateja et al., 2016) were used for analyzing the concentrations of product in the feed and filtrate.

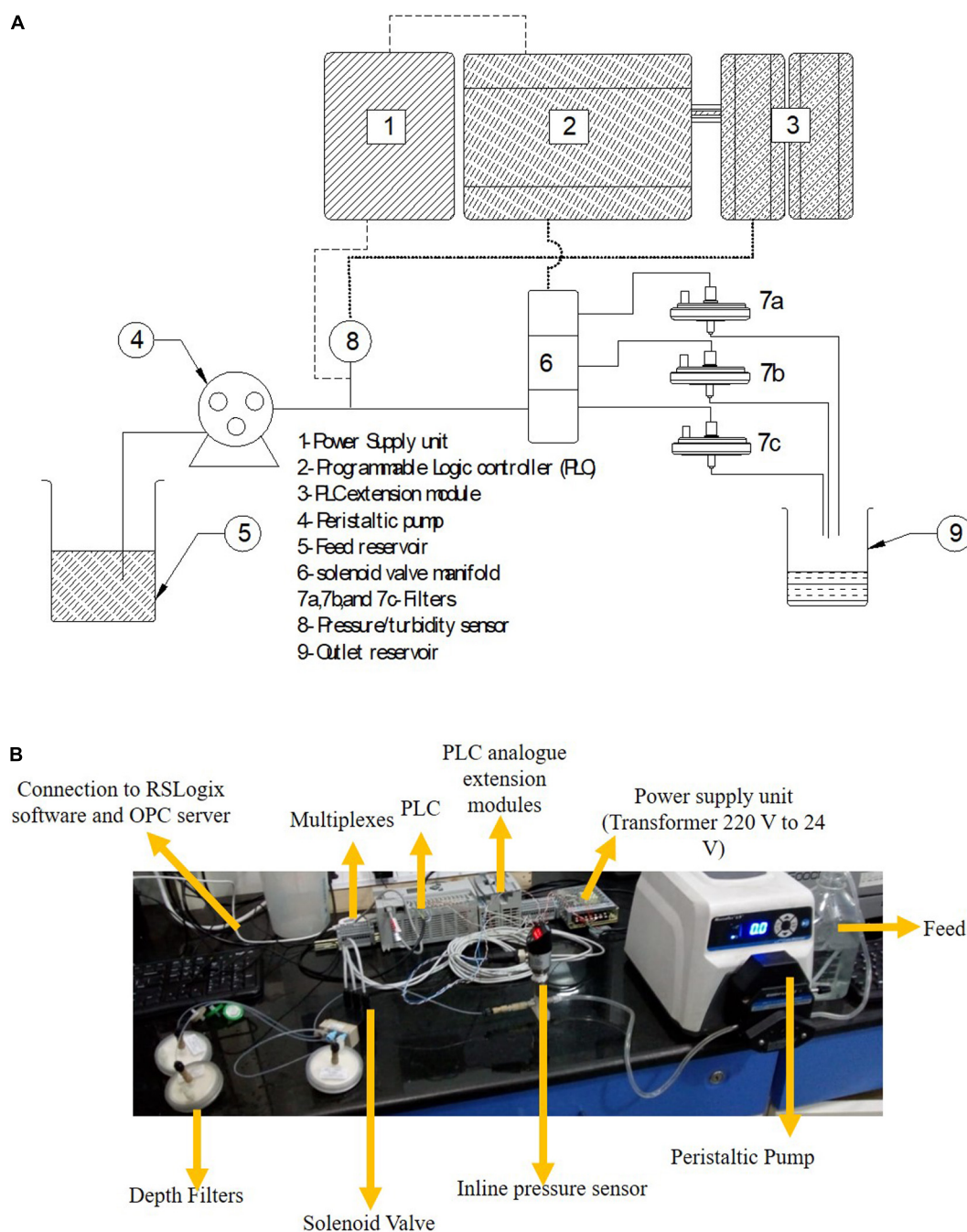


FIGURE 1 | (A) Schematic and **(B)** Image of the experimental set up.

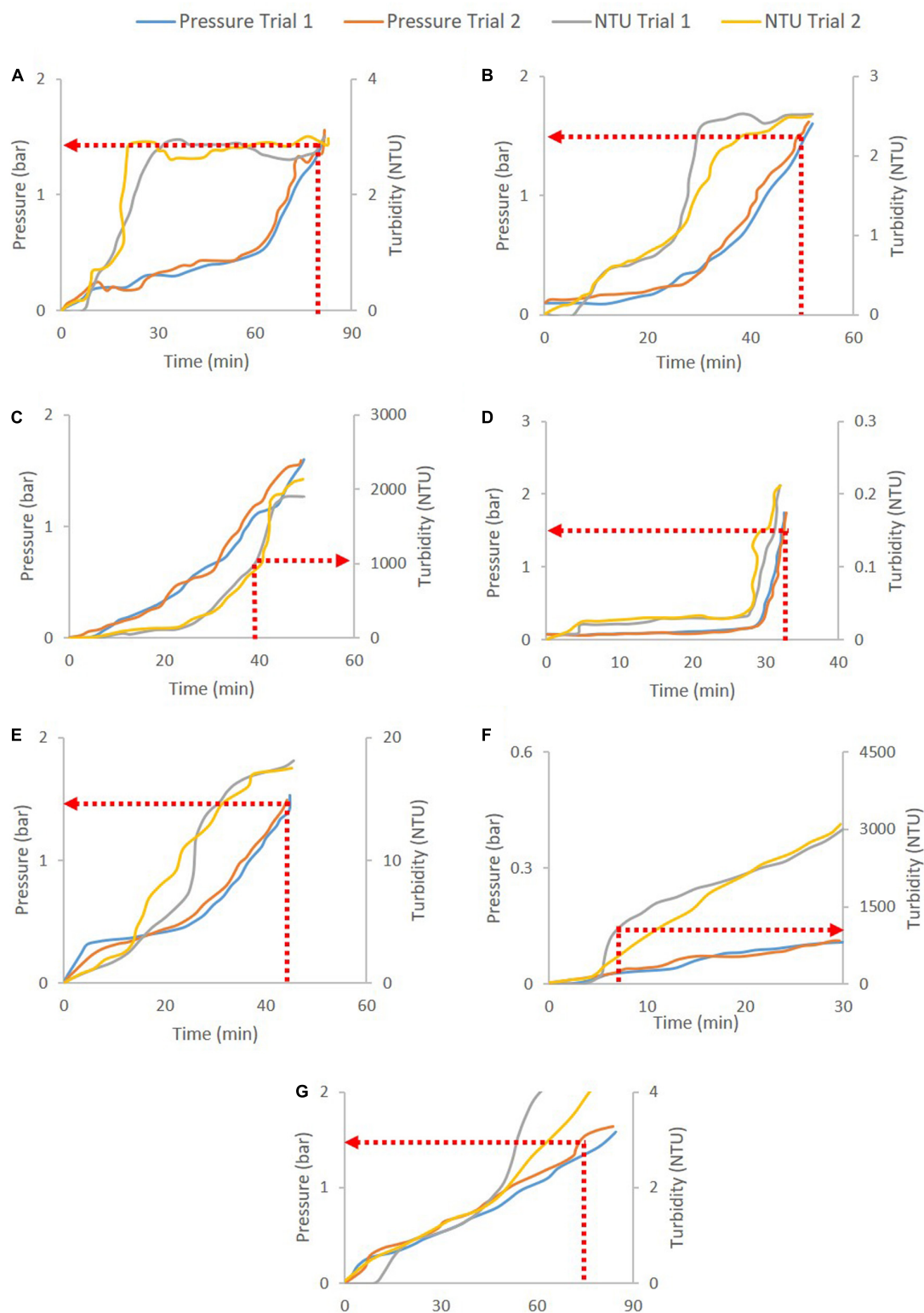
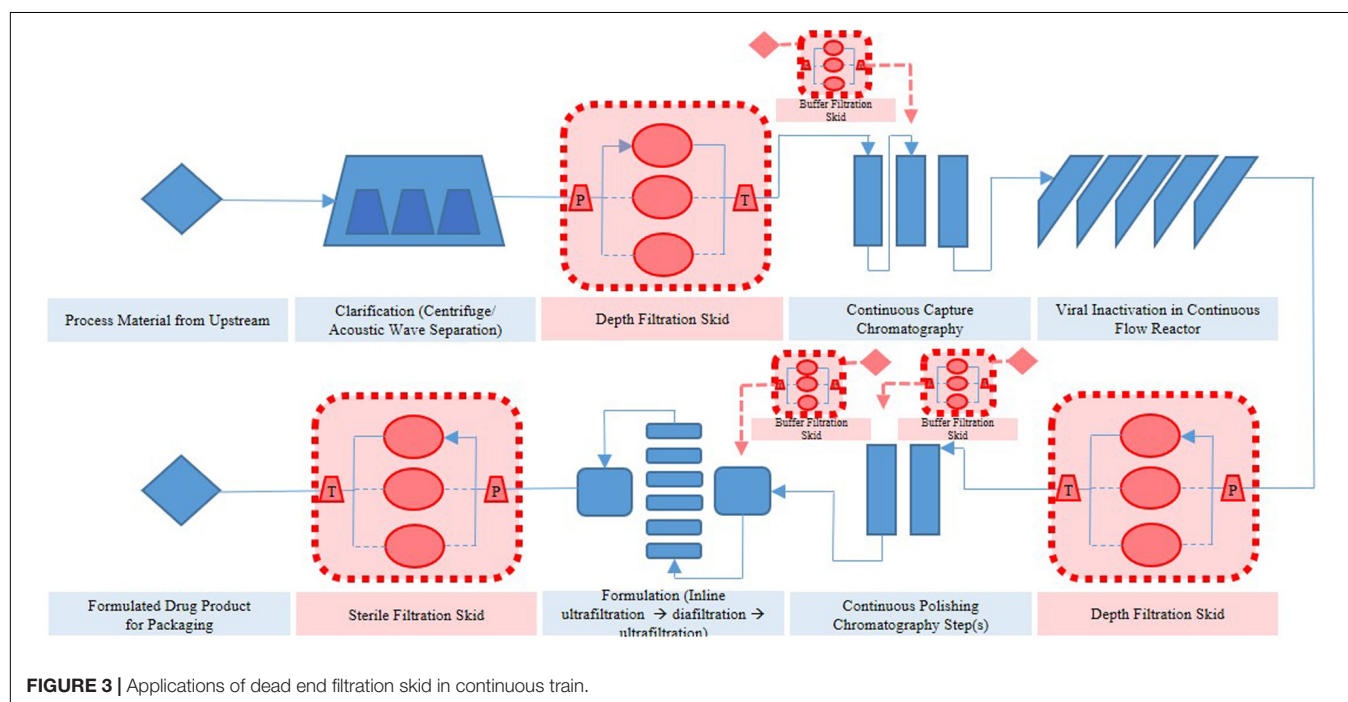


FIGURE 2 | Depth filtration pressure and turbidity profiles for different cases: **(A)** B1HC concentrate of mAb cell culture broth, **(B)** 90ZA Output of harvest filtered through 30S (harvest30S90ZA), **(C)** D0HC CHO cell culture harvest, **(D)** Acrodisc GCSF drug product, **(E)** HP PDD1 GCSF quenched refolding output, **(F)** HP PDH4 *Pichia pastoris* HSA broth with 5% solids, and **(G)** X0HC cell culture harvest concentrate. The respective cut-offs are shown in dotted red lines and arrows. Pressure cut-off of 1.5 bar is used for secondary depth and sterile filters, while turbidity cut-off of 1000 NTU is used for primary depth filters.

TABLE 2 | Pressure or turbidity breakthroughs for different filters using different feeds.

System	Filter ID	Type	Filter specification	Feed material	Selected cut-off	Filter capacity (L/m ²)	Yield (%)
mAb – CHO cell	B1HC	Secondary	0.1–0.7 μm , 23 cm ²	Centrate of mAb CHO cell culture broth	1.5 bar	266.7 \pm 6	95.23
	90ZA	Secondary	0.1–0.5 μm , 23 cm ²	mAb CHO cell culture harvest filtered through 30S (harvest→30S)	1.5 bar	166.7 \pm 9	92.45
	D0HC	Primary	0.5–10 μm , 23 cm ²	mAb CHO cell culture harvest	1000 NTU	130.1 \pm 5	91.63
	B0HC	Secondary	0.1 μm , 23 cm ²	mAb CHO cell culture harvest filtered through 30S (harvest→30S)	1.5 bar	97.2 \pm 6	90.67
	X0HC	Secondary	0.1 μm , 23 cm ²	mAb CHO cell culture centrate	1.5 bar	233.4 \pm 19	96.45
	B0HC	Secondary	0.1 μm , 23 cm ²	mAb CHO cell culture centrate	1.5 bar	114.0 \pm 7	102.38
	Acrodisc 4652	Sterile	0.2 μm , 2.8 cm ²	mAb formulated drug product	1.5 bar	68.2 \pm 4	104.67
Human serum albumin (HSA) – <i>Pichia pastoris</i>	EK1P	Primary	0.2–4 μm , 26 cm ²	HSA <i>Pichia pastoris</i> broth with 5% (wet weight basis) solids	1000 NTU	23.3 \pm 0.9	90.78
	HP PDH4	Secondary	0.4–15 μm , 26 cm ²	HSA <i>Pichia pastoris</i> broth centrate	1.5 bar	35.5 \pm 10	91.89
GCSF – <i>E. coli</i>	HP PDD1	Secondary	0.1–0.85 μm , 26 cm ²	GCSF quenched refolding output	1.5 bar	146.7 \pm 28	103.56
	HP PDH4	Secondary	0.5–15 μm , 26 cm ²	GCSF quenched refolding output	1.5 bar	360.5 \pm 32	98.49
	Acrodisc 4652	Sterile	0.2 μm , 2.8 cm ²	GCSF formulated drug product	1.5 bar	165.2 \pm 14	99.67



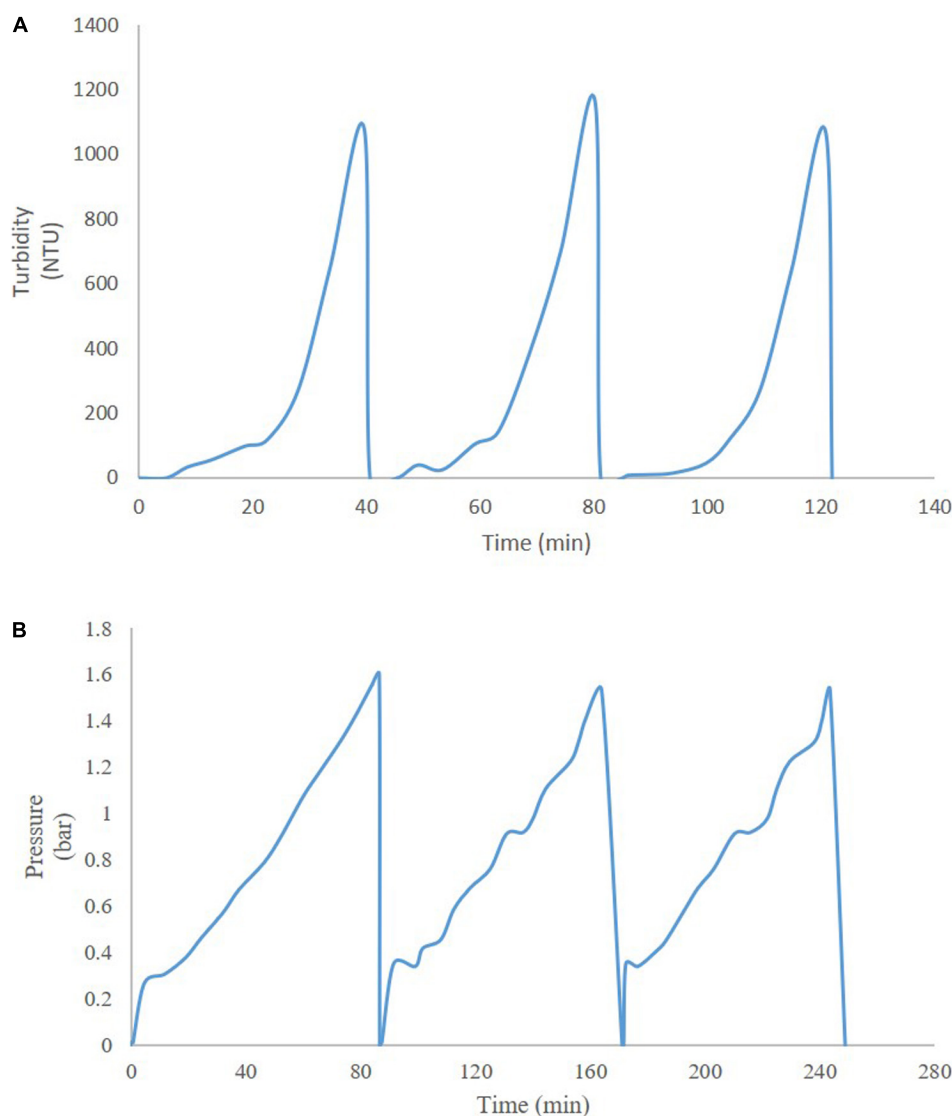


FIGURE 4 | Profiles of continuous operation with **(A)** turbidity-based switching for HP PDH4 (Sample: HSA *Pichia pastoris* broth with 5% solids on wet weight basis), and **(B)** pressure-based switching for X0HC (Sample: mAb CHO cell culture centrate).

Set-Up and Demonstration of the Continuous Skid

The schematic of the skid is shown in **Figure 1A** and the actual set up is shown in **Figure 1B**. A MicroLogix 5000 programmable logic controller (PLC) from Allen Bradley was operated by using Micrologix software. The software was layered with an OPC server (MatrikonOPC Explorer) for continuous data collection and logging. The power supply unit was connected to the PLC, pressure transmitter, and turbidity sensor. The signal from the PLC was transferred to the solenoid valve which allowed for switching of the flow stream between filters. The PLC acquired the data from the pressure transmitter and turbidity probes. The turbidity and pressure values were compared every second in real time to the cut-off value selected for the particular sample and corresponding filter. Once the current value exceeded the cut-off

value, the PLC passed a signal to the solenoid valve to trigger switching of the flow stream through a fresh filter.

RESULTS AND DISCUSSION

Turbidity and Pressure Excursion Studies

Constant-flux turbidity and pressure excursion trials were carried out for a range of feed materials for both depth and sterile filtration. Multiple process streams from CHO cell, *P. pastoris* and *E. coli* expression platforms were used to demonstrate turbidity or pressure breakthrough of depth and/or sterile filters with appropriate pore sizes. **Table 2** shows the comprehensive list of turbidity and pressure cut-offs and the corresponding filter capacities for the trials.

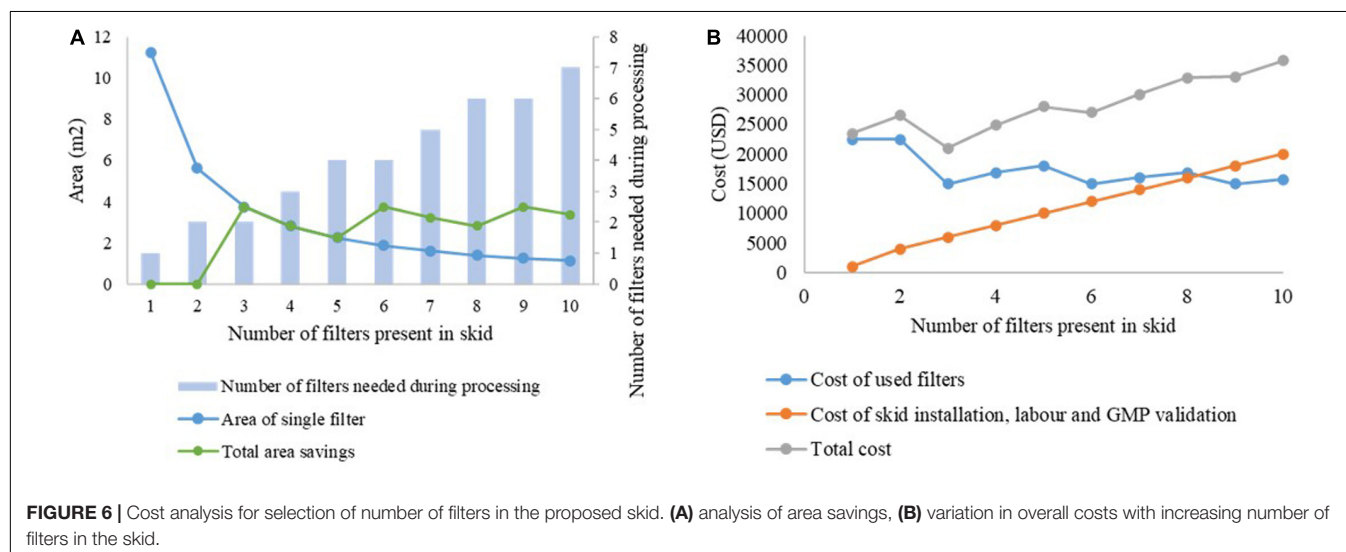
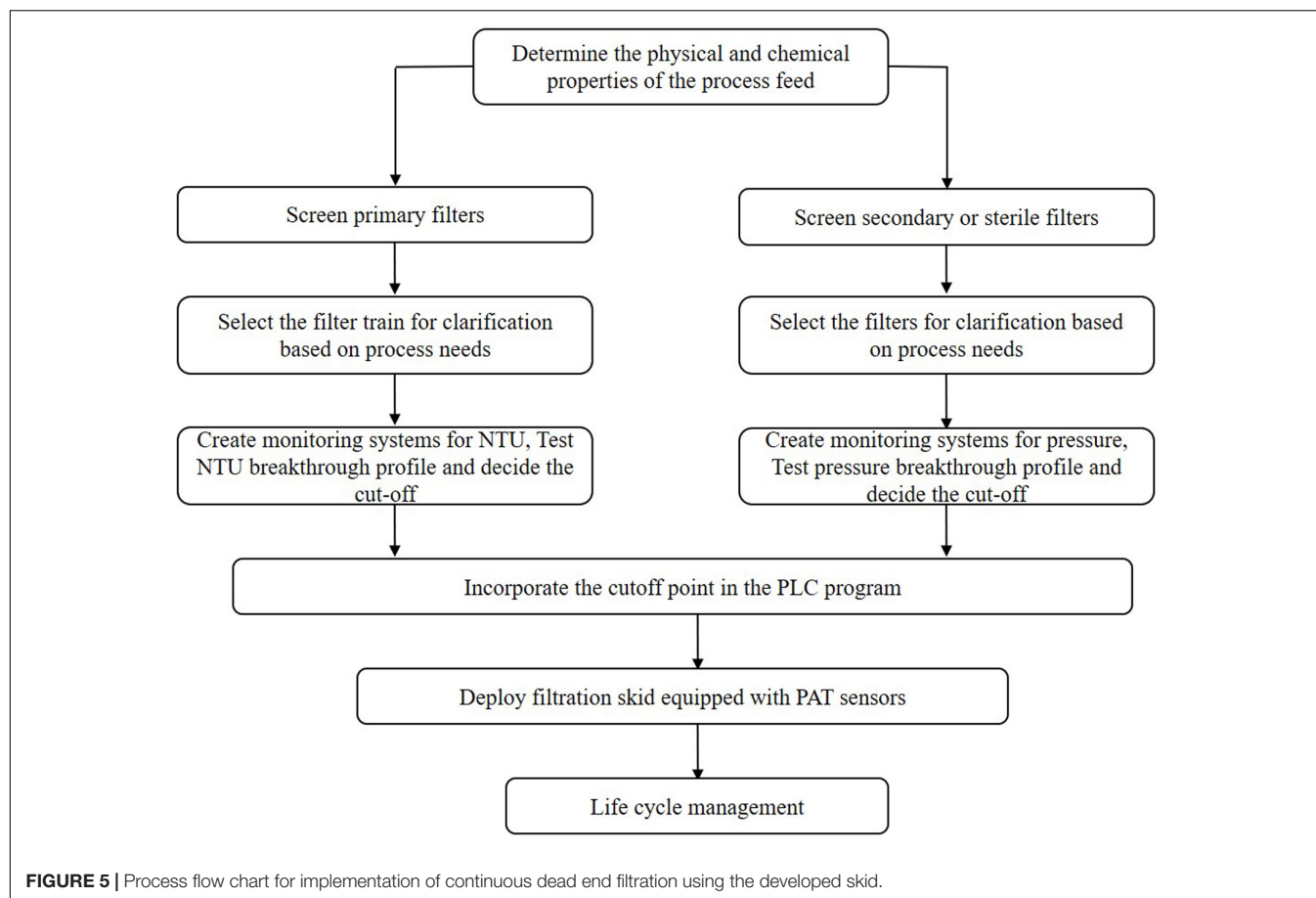


Figure 2 shows the pressure and turbidity profiles from the filter studies. Figures 2C,F show the primary depth filters used for clarifying CHO cell culture harvest (D0HC) and *P. pastoris* broth with 5% solids (HP PDH4). In both cases, turbidity breakthrough can be seen to occur prior to pressure breakthrough. In Figures 2A,B,D–F, pressure cut-off is considered for operation.

Duplicate experiments were conducted in each case. It can be seen from Figure 2 that the breakthrough profiles were similar across the duplicate pairs. The filter capacities corresponding to the cut-off points for the filters are listed in Table 2. The average and standard deviation of capacity at cut-off for the two trials was calculated in each case. The standard deviation was around 10%

of the average capacity in most trials, suggesting that utilizing turbidity of pressure cut-offs for filter switching does not affect the reliability of the capacity studies carried out in the filter screening phase. The cut-off values were program into the PLC using ladder logic to continuously monitor the readings from the pressure and turbidity sensors, and trigger the solenoid valve to switch the flow to a fresh filter when the current value exceeded the program cut-off.

Implementation of Skid in Continuous Process

Thus far, several research groups have proposed filter sizing for continuous processing on the basis of campaign duration, along with a filter area safety factor of 1.5 to 2x (Lutz, 2009). Though this sizing and safety factor method has long been in place for batch processing, it is suboptimal in continuous processing, particularly during deviations in particle size, campaign duration, bioburden levels, or flowrate, all of which have high probability of occurring downstream of continuous perfusion cultures. The proposed skid is able to overcome these issues without prior knowledge or characterization of potential deviations, as it will simply increase the rate of filter switching if fouling increases, while ensuring consistent filtrate quality in the downstream steps due to real-time monitoring of pressure and turbidity breakthrough as the trigger for filter switching. **Figure 3** shows a typical mAb continuous processing train and the multiple filtration steps where the proposed skid can be easily integrated. **Figure 4** shows continuous switching profiles for both turbidity-based and pressure-based switching implementations of our proposed skid. The flowchart in **Figure 5** illustrates the complete process for implementing the skid at any given point, starting from deciding the filter type based on physicochemical properties of the feed, followed by screening of filters, determination of the pressure or turbidity cut-off point, and program the skid.

Economics of Batch Versus Continuous Dead-End Filtration

Filters typically are the second-most expensive consumable in downstream processing of mAbs, after Protein A chromatography resins (Kelley, 2007). When doing filter sizing, a safety factor 1.5–2x is considered for deciding the final area, increasing the filter cost. By using our proposed skid for filtration, significant savings in membrane area can be made as the filter area will be split into multiple filters out of which some may remain unused during the run. The installation of the skid and valve is a one-time capital cost which is likely to be offset by the subsequent savings in consumable costs over months or years of continuous operation. Furthermore, the same skid can easily be transferred between facilities or used for different molecules by simply changing the filters plugged into the setup. However, the added complexity of the skid and the need for GMP validation of the increased components and tubing lines lead to additional costs. Therefore, selecting the size of the filter to be used in the skid is a critical decision, and should be made at the sweet spot between cost savings from area reduction and cost increase due to additional skid complexity leading to increased labor and GMP validation costs.

This is illustrated in **Figures 6A,B**. The capacity of the filter B1HC for processing mAb CHO cell harvest concentrate was found to be 266.7 L/m², as shown in **Table 2**. In traditional batch processing, a safety factor of 1.5x would be applied to determine the final area of the depth filter to be installed. Therefore, to process 2,000 L of material in a batch facility would require 11.25 m² of filter area. Using the proposed skid with filters of increasingly smaller size would lead to savings in membrane area up to the limiting value of 7.5 m², corresponding to the area required as per the calculations of filter capacity with zero safety factor, as shown in **Figure 6A**. Assuming a fixed cost of USD 2,000 per m² for the filter media, and a fixed cost of USD 1,000 for each new line in the skid (including installation, labor and GMP validation costs), the cost curve shown in **Figure 6B** is obtained. It can be seen that $n = 3$ is the optimum number of filters for this example. Similar analyses can be done on a case-by-case basis for any given application.

CONCLUSION

Dead end filtration is a critical unit operation in manufacturing of biotherapeutics, and is used in both microbial and mammalian expression systems. Dead end filtration is challenging to implement in continuous processing due to the difficulty in maintaining a constant filtrate stream across the length of a campaign with a single filter. Adding large safety factors to filter sizes results in significant increase in cost of consumables. We propose a continuous dead end filtration skid consisting of multiple small filters and in-line pressure and turbidity sensors to monitor breakthrough in real-time and use pressure or turbidity cut-off values as a trigger to direct the feed stream to a fresh filter. The proposed skid allows easy handling of cell culture broth from continuous perfusion reactors that can have variable particle sizes, and eliminates downtime during filter change, water wash and buffer wash steps. It fills the gap between unit operations in the continuous train. It also provides a significant area reduction. The skid is versatile and can be applied for depth filtration, sterile filtration, buffer filtration, and other types of dead-end filtration across the manufacturing train using either pressure or turbidity breakthrough. Finally, the system is modular and can easily be applied to scaled-up systems. The proposed skid is a significant enabler for continuous processing.

DATA AVAILABILITY STATEMENT

The raw data supporting the conclusions of this article will be made available by the authors, without undue reservation.

AUTHOR CONTRIBUTIONS

GT and VH performed the experiments. SP contributed to program of the controllers. GT wrote the first draft. AR supervised the project, got the funding and reviewed and edited the final manuscript. All authors contributed to the article and approved the submitted version.

FUNDING

We would like to acknowledge funding support from Department of Biotechnology, Ministry of Science and Technology (Number

BT/COE/34/SP15097/2015). We would also like to acknowledge Pall Life Sciences for funding and supply of consumables for this project. We would like to declare that they do not have any conflict of interest.

REFERENCES

- Agarwal, H., Rathore, A. S., Hadpe, S. R., and Alva, S. J. (2016). Artificial neural network (ANN)-based prediction of depth filter loading capacity for filter sizing. *Biotechnol. Prog.* 32, 1436–1443. doi: 10.1002/btpr.2329
- Aldor, I. S., Krawitz, D. C., Forrest, W., Chen, C., Nishihara, J. C., Joly, J. C., et al. (2005). Proteomic profiling of recombinant *Escherichia coli* in high-cell-density fermentations for improved production of an antibody fragment biopharmaceutical. *Appl. Environ. Microbiol.* 71, 1717–1728. doi: 10.1128/aem.71.4.1717-1728.2005
- Anicetti, V. (2009). Biopharmaceutical processes: a glance into the 21st century. *Bioprocess Int.* 7, S4–S11.
- Ashton, G. (2001). Growing pains for biopharmaceuticals. *Nat. Biotechnol.* 19, 307–311. doi: 10.1038/86670
- Bink, L. R., and Furey, J. (2010). Using in-line disposable pressure sensors to evaluate depth filter performance. *Bioprocess Int.* 8, 44–48.
- Birch, J., and Biologics, L. (2005). “Future Perspectives of antibody manufacturing,” in *Proceedings of the Bioproduction Conference*, Amsterdam.
- Boerlage, S. (2001). *Scaling and Particulate Fouling in Membrane Filtration Systems*. Boca Raton, FL: CRC Press.
- Chopda, V. R., Pathak, M., Batra, J., Gomes, J., and Rathore, A. S. (2017). Enabler for process analytical technology implementation in *Pichia pastoris* fermentation: Fluorescence-based soft sensors for rapid quantitation of product titer. *Eng. Life Sci.* 17, 448–457. doi: 10.1002/elsc.201600155
- Croughan, M. S., Konstantinov, K. B., and Cooney, C. (2015). The future of industrial bioprocessing: Batch or continuous? *Biotechnol. Bioeng.* 112, 648–651. doi: 10.1002/bit.25529
- FDA (2004). *Guidance for industry, PAT-A Framework for Innovative Pharmaceutical Development, Manufacturing and Quality Assurance*. Silver Spring, MD: FDA.
- Felo, M., Christensen, B., and Higgins, J. (2013). Process cost and facility considerations in the selection of primary cell culture clarification technology. *Biotechnol. Prog.* 29, 1239–1245. doi: 10.1002/btpr.1776
- Goldrick, S., Joseph, A., Mollet, M., Turner, R., Gruber, D., Farid, S. S., et al. (2017). Predicting performance of constant flow depth filtration using constant pressure filtration data. *J. Membr. Sci.* 531, 138–147. doi: 10.1016/j.memsci.2017.03.002
- Grilo, A. L., Mateus, M., Aires-Barros, M. R., and Azevedo, A. M. (2017). Monoclonal antibodies production platforms: an opportunity study of a non-protein-A chromatographic platform based on process economics. *Biotechnol. J.* 12:1700260. doi: 10.1002/biot.201700260
- Hebbi, V., Thakur, G., and Rathore, A. S. (2019). Process analytical technology implementation for protein refolding: GCSF as a case study. *Biotechnol. Bioeng.* 116, 1039–1052. doi: 10.1002/bit.26900
- Jungbauer, A. (2013). Continuous downstream processing of biopharmaceuticals. *Trends Biotechnol.* 31, 479–492. doi: 10.1016/j.tibtech.2013.05.011
- Kandula, S., Babu, S., Jin, M., and Shukla, A. A. (2009). Design of a filter train for precipitate removal in monoclonal antibody downstream processing. *Biotechnol. Appl. Biochem.* 54, 149–155. doi: 10.1042/ba20090181
- Kateja, N., Agarwal, H., Saraswat, A., Bhat, M., and Rathore, A. S. (2016). Continuous precipitation of process related impurities from clarified cell culture supernatant using a novel coiled flow inversion reactor (CFIR). *Biotechnol. J.* 11, 1320–1331. doi: 10.1002/biot.201600271
- Kelley, B. (2007). Very large scale monoclonal antibody purification: the case for conventional unit operations. *Biotechnol. Prog.* 23, 995–1008.
- Kelley, B. (2009). “Industrialization of mAb production technology: the bioprocessing industry at a crossroads,” in *MAbs*, Ed. J. M. Reichert (Milton Park: Taylor & Francis), 443–452. doi: 10.4161/mabs.1.5.9448
- Khanal, O., Singh, N., Traylor, S. J., Xu, X., Ghose, S., Li, Z. J., et al. (2018). Contributions of depth filter components to protein adsorption in bioprocessing. *Biotechnol. Bioeng.* 115, 1938–1948. doi: 10.1002/bit.26707
- Kjeldsen, T. (2000). Yeast secretory expression of insulin precursors. *Appl. Microbiol. Biotechnol.* 54, 277–286. doi: 10.1007/s002530000402
- Kjeldsen, T., Ludvigsen, S., Diers, I., Balschmidt, P., Sørensen, A. R., and Kaarsholm, N. C. (2002). Engineering-enhanced protein secretory expression in yeast with application to insulin. *J. Biol. Chem.* 277, 18245–18248. doi: 10.1074/jbc.c200137200
- Konstantinov, K. B., and Cooney, C. L. (2015). White paper on continuous bioprocessing. May 20–21, 2014 continuous manufacturing symposium. *J. Pharm. Sci.* 104, 813–820. doi: 10.1002/jps.24268
- Krupp, A., Please, C., Kumar, A., and Griffiths, I. (2017). Scaling-up of multi-capsule depth filtration systems by modeling flow and pressure distribution. *Separat. Purif. Technol.* 172, 350–356. doi: 10.1016/j.seppur.2016.07.028
- Liu, H. F., Ma, J., Winter, C., and Bayer, R. (2010). “Recovery and purification process development for monoclonal antibody production,” in *MAbs*, Ed. J. M. Reichert (Milton Park: Taylor & Francis), 480–499. doi: 10.4161/mabs.2.5.12645
- Lutz, H. (2009). Rationally defined safety factors for filter sizing. *J. Membr. Sci.* 341, 268–278. doi: 10.1016/j.memsci.2009.06.015
- Pegel, A., Reiser, S., Steurethaler, M., and Klein, S. (2011). Evaluating disposable depth filtration platforms for mAb harvest clarification. *Bioprocess Int.* 9, 52–56.
- Pham, C. Y. (2010). *Use of Depth Filtration in Series with Continuous Centrifugation to Clarify Mammalian Cell Cultures*. Google Patents No.EP1776174A1.
- Pollock, J., Bolton, G., Coffman, J., Ho, S. V., Bracewell, D. G., and Farid, S. S. (2013). Optimising the design and operation of semi-continuous affinity chromatography for clinical and commercial manufacture. *J. Chromatogr. A* 1284, 17–27. doi: 10.1016/j.chroma.2013.01.082
- Popova, D., Stonier, A., Pain, D., Titchener-Hooker, N. J., and Farid, S. S. (2016). Integrated economic and experimental framework for screening of primary recovery technologies for high cell density CHO cultures. *Biotechnol. J.* 11, 899–909. doi: 10.1002/biot.201500336
- Rathore, A., Bhambure, R., and Ghare, V. (2010). Process analytical technology (PAT) for biopharmaceutical products. *Anal. Bioanal. Chem.* 398, 137–154. doi: 10.1007/s00216-010-3781-x
- Roger, S. D. (2010). Biosimilars: current status and future directions. *Expert Opin. Biol. Ther.* 10, 1011–1018. doi: 10.1517/14712591003796553
- Slouka, C., Kopp, J., Hutwimmer, S., Strahammer, M., Strohm, D., Eitenberger, E., et al. (2018). Custom made inclusion bodies: impact of classical process parameters and physiological parameters on inclusion body quality attributes. *Microb. Cell Fact.* 17:148.
- Steinebach, F., Ulmer, N., Wolf, M., Decker, L., Schneider, V., Wälchli, R., et al. (2017). Design and operation of a continuous integrated monoclonal antibody production process. *Biotechnol. Prog.* 33, 1303–1313. doi: 10.1002/btpr.2522
- Tran, R., Lacki, K., Davidson, A., Sharma, B., and Titchener-Hooker, N. (2014). Changing manufacturing paradigms in downstream processing and the role of alternative bioseparation technologies. *J. Chem. Technol. Biotechnol.* 89, 1534–1544. doi: 10.1002/jctb.4234
- Wakeman, R. (2007). The influence of particle properties on filtration. *Separat. Purif. Technol.* 58, 234–241. doi: 10.1016/j.seppur.2007.03.018
- Wilson, D. B., Sahm, H., Stahmann, K.-P., and Koffas, M. (2019). *Industrial Microbiology*. Hoboken, NJ: John Wiley & Sons.
- Wurm, F. M. (2004). Production of recombinant protein therapeutics in cultivated mammalian cells. *Nat. Biotechnol.* 22, 1393–1398. doi: 10.1038/nbt.1026
- Xie, T., Liu, Q., Xie, F., Liu, H., and Zhang, Y. (2008). Secretory expression of insulin precursor in *Pichia pastoris* and simple procedure for producing recombinant human insulin. *Preparat. Biochem. Biotechnol.* 38, 308–317. doi: 10.1080/10826060802165147

- Xu, J., and Zhang, N. (2014). On the way to commercializing plant cell culture platform for biopharmaceuticals: present status and prospect. *Pharm. Bioprocess.* 2:499. doi: 10.4155/pbp.14.32
- Yavorsky, D., Blanck, R., Lambalot, C., and Brunkow, R. (2003). The clarification of bioreactor cell cultures for biopharmaceuticals. *Pharm. Technol.* 27, 62–77.
- Yigzaw, Y., Piper, R., Tran, M., and Shukla, A. A. (2006). Exploitation of the adsorptive properties of depth filters for host cell protein removal during monoclonal antibody purification. *Biotechnol. Prog.* 22, 288–296. doi: 10.1021/bp050274w

Conflict of Interest: The authors declare that the research was conducted in the absence of any commercial or financial relationships that could be construed as a potential conflict of interest.

Copyright © 2020 Thakur, Hebbi, Parida and Rathore. This is an open-access article distributed under the terms of the Creative Commons Attribution License (CC BY). The use, distribution or reproduction in other forums is permitted, provided the original author(s) and the copyright owner(s) are credited and that the original publication in this journal is cited, in accordance with accepted academic practice. No use, distribution or reproduction is permitted which does not comply with these terms.



The Lazarus *Escherichia coli* Effect: Recovery of Productivity on Glycerol/Lactose Mixed Feed in Continuous Biomanufacturing

Stefan Kittler^{1†}, Julian Kopp^{2†}, Patrick Gwen Veelenturf², Oliver Spadiut¹, Frank Delvigne³, Christoph Herwig^{1,2} and Christoph Slouka^{1*}

OPEN ACCESS

Edited by:

Miguel Cacho Teixeira,
University of Lisbon, Portugal

Reviewed by:

Georg A. Sprenger,
University of Stuttgart, Germany
Cecilia Calado,
Lisbon Higher Institute of Engineering
(ISEL), Portugal

*Correspondence:

Christoph Slouka
christoph.slouka@tuwien.ac.at

[†]These authors have contributed
equally to this work

Specialty section:

This article was submitted to
Bioprocess Engineering,
a section of the journal
Frontiers in Bioengineering and
Biotechnology

Received: 19 June 2020

Accepted: 29 July 2020

Published: 13 August 2020

Citation:

Kittler S, Kopp J, Veelenturf PG,
Spadiut O, Delvigne F, Herwig C and
Slouka C (2020) The Lazarus
Escherichia coli Effect: Recovery
of Productivity on Glycerol/Lactose
Mixed Feed in Continuous
Biomanufacturing.
Front. Bioeng. Biotechnol. 8:993.
doi: 10.3389/fbioe.2020.00993

¹ Research Division Biochemical Engineering, Research Group Integrated Bioprocess Development, Institute of Chemical, Environmental and Bioscience Engineering, Vienna University of Technology, Vienna, Austria, ² Christian Doppler Laboratory for Mechanistic and Physiological Methods for Improved Bioprocesses, Institute of Chemical, Environmental and Bioscience Engineering, TU Vienna, Vienna, Austria, ³ TERRA Teaching and Research Centre, Microbial Processes and Interactions (MIPI), Gembloux Agro-Bio Tech – Université de Liège, Gembloux, Belgium

Continuous cultivation with *Escherichia coli* has several benefits compared to classical fed-batch cultivation. The economic benefits would be a stable process, which leads to time independent quality of the product, and hence ease the downstream process. However, continuous biomanufacturing with *E. coli* is known to exhibit a drop of productivity after about 4–5 days of cultivation depending on dilution rate. These cultivations are generally performed on glucose, being the favorite carbon source for *E. coli* and used in combination with isopropyl β -D-1 thiogalactopyranoside (IPTG) for induction. In recent works, harsh induction with IPTG was changed to softer induction using lactose for T7-based plasmids, with the result of reducing the metabolic stress and tunability of productivity. These mixed feed systems based on glucose and lactose result in high amounts of correctly folded protein. In this study we used different mixed feed systems with glucose/lactose and glycerol/lactose to investigate productivity of *E. coli* based chemostats. We tested different strains producing three model proteins, with the final aim of a stable long-time protein expression. While glucose fed chemostats showed the well-known drop in productivity after a certain process time, glycerol fed cultivations recovered productivity after about 150 h of induction, which corresponds to around 30 generation times. We want to further highlight that the cellular response upon galactose utilization in *E. coli* BL21(DE3), might be causing fluctuating productivity, as galactose is referred to be a weak inducer. This “Lazarus” phenomenon has not been described in literature before and may enable a stabilization of continuous cultivation with *E. coli* using different carbon sources.

Keywords: *E. coli*, recombinant protein production, continuous biomanufacturing, mixed-feeding, productivity recovery

INTRODUCTION

The gram-negative bacterium *Escherichia coli* is the expression host of choice to produce 30% to 40% of recombinant enzymes [recombinant protein production (RPP)] in industry (Walsh, 2010; Gupta and Shukla, 2016). This organism has fast replication rates and can be cultivated on comparatively cheap media (DeLisa et al., 1999) and has high intracellular product titers. These benefits often outweigh the numerous purification steps (Berlec and Strukelj, 2013; Gupta and Shukla, 2016) and the missing glycosylation pattern on the recombinant product (Spadiut et al., 2014; Baeshen et al., 2015). The strain BL21(DE3) generated by Studier and Moffatt (1986) is often used in industrial scale, because of showing low acetate formation, high replication rates as an effect of the integrated T7-polymerase (Steen et al., 1986; Studier and Moffatt, 1986; Studier et al., 1990; Dubendorff and Studier, 1991; Neubauer and Hofmann, 1994; Lyakhov et al., 1998), as well as the possibility of protein secretion into the fermentation broth due to a type 2 secretion pathway (Jeong et al., 2009, 2015; Tseng et al., 2009). The *lac* operon is still one of the most favored promoters in pET-expression-systems (Dubendorff and Studier, 1991; Marbach and Bettenbrock, 2012; Wurm et al., 2016), therefore it is generally used for insertion of the gene of interest. Induction can be performed by addition of lactose or a structural analog, e.g., the well-known inducer isopropyl β -D-1 thiogalactopyranoside (IPTG) (Burstein et al., 1965; Neubauer and Hofmann, 1994; Wurm et al., 2016). IPTG is known to bind directly to the *lacI* repressor protein after uptake, whereas lactose needs to be transformed to allolactose to cause the blockage of the repressor protein (Burstein et al., 1965). Still, these “low-cost” products in *E. coli* with the pET system, are expensive in their making (Jia and Jeon, 2016), as one gram of IPTG can exceed the price of one gram of 900 gold. For economic reasons and for reduction of metabolic/product burden (Malakar and Venkatesh, 2012), lactose, generally regarded as waste product, can be used for induction (Wurm et al., 2016, 2018; Wurm et al., 2017a). Apart from induction mechanism, a replacement of the primary carbon source is also frequently discussed. The most favored carbon source in *E. coli* cultivations has always been glucose (Postma et al., 1993; Ronimus and Morgan, 2003; Deutscher et al., 2006). However, compared to other carbon sources glucose is quite expensive and causes diauxic growth upon lactose induction (Monod, 1949; Loomis and Magasanik, 1967). Glycerol has shown quite promising results in terms of biomass/substrate yield in *E. coli* cultivations (Blommel et al., 2007). In addition, mixtures of glucose, glycerol and lactose have shown good results for diverse products gained via autoinduction systems (Monod, 1949; Viitanen et al., 2003; Blommel et al., 2007). Recently, we presented that glycerol used as primary carbon source for *E. coli* cultivations performed equally well during biomass production as glucose, but even increased the specific product titer in fed batches (Kopp et al., 2017).

Most processes today rely on fed batch mode, which are state-of-the art in industry. They can be highly affected by different process parameters, like pH and T, physiological feeding (adaption of the specific substrate uptake rate) and change

in induction agent. However, the time dependence of product quality is still a major drawback using this cultivation technique. This makes determination of the correct harvest time point often challenging, as the intracellular stress often leads to very quick lysis of the cells and product degradation. This results in variations in the downstream purification process. Continuous biomanufacturing is considered to increase product quality and therefore to a facilitation of the downstream process. However, up to now, only one stable microbial industrial chemostat process was established for *Saccharomyces cerevisiae* in the 90's for production of insulin (Diers et al., 1991). A drop of productivity after a certain process time and the lower time-space yield hinder continuous upstream using microbial hosts from being applied in industry (Peebo and Neubauer, 2018; Kopp et al., 2019b).

Several efforts have been made to enable continuous processes in *E. coli* (Kopp et al., 2019a), but we are still far away from application of such systems. Long-term cultivations with *E. coli* showed enhanced cell burden using IPTG induction and clearly favored feeding of the disaccharide lactose (Dvorak et al., 2015). From an engineering point of view, higher growth rates seem to be beneficial for RPP as shown in chemostat- and fed-batch experiments (Vaiphei et al., 2009; Slouka et al., 2019). Mutations and plasmid loss are expected during long time cultivation of *E. coli* (Weikert et al., 1997; Sieben et al., 2016; Peebo and Neubauer, 2018). However, constant supply of antibiotics is believed to prevent plasmid loss in continuous cultures (Sieben et al., 2016). Change in gene regulation of the transcription upon long time cultivation are often reported. The *lac* operon resulting in multistability of induction is well known and reported in literature (Ozbudak et al., 2004). Fluctuations in plasmid number, *lac*-repressor and cAMP levels may drastically influence RPP during long time cultivation. High concentrations of metabolites, like galactose upon feeding of lactose, are known to affect β -galactosidase concentrations (Llanes and McFall, 1969; Portaccio et al., 1998). Other approaches try to integrate the gene of interest into the genome to receive stable production in combination with strong inducible promoters (Striedner et al., 2010). Reactor design is a further screw to overcome stability issues in long-term RPP with *E. coli*, as recently published by Schmideder and Weuster-Botz (2017) who implemented a cascaded system, where two stirred tank reactors are operated in parallel at different conditions.

In this contribution, we present the results of chemostat cultures using mixed feed systems first applied by Wurm et al. (2016, 2018). The goal was to accomplish a continuous process with stable productivity outperforming the frequently used fed-batch. We tested mixed feeds with glucose/lactose and glycerol/lactose in chemostat for three model proteins and compared the performance to state-of-the-art fed batches induced with IPTG. In contrast to cultivations using BL21(DE3) with glucose/lactose, glycerol/lactose-based cultivations showed a recovery of productivity at elevated induction time. Alterations regarding the choice of carbon source thus might be a key driver to possibly enable stable productivity on a long-term basis. As an already lost productivity is recovered, we annotated this resurrection of productivity with the Christian term of “Lazarus” and the corresponding “Lazarus effect.”

MATERIALS AND METHODS

Strains

Cultivations were carried out with the strain *E. coli* BL21(DE3) using three different model proteins. All three protein sequences were cloned in a pET vectors, using pET21a⁺ for green fluorescent protein (GFP), and pET28a for mCherry protein (mCherry) and Blitzenblue (BBlue). mCherry and BBlue were thankfully received from Prof. Maurer at FH Campus Wien. All cultures were kept at -80°C in 25% glycerol cryo stocks. The extracted pET21a⁺ plasmid encoding for GFP was extracted and electroporated into an HMS174(DE3) strain (Novagen, Merck, Darmstadt, Germany).

Cultivation and Process Modes

Cultivations were executed in a Minifors 2 bioreactor system (max. working volume: 1 L; Infors HT, Bottmingen, Switzerland). All cultivations were carried out using a defined minimal medium referred to DeLisa et al. (1999). Media had the same composition with different amounts of glycerol and glucose. Details on pre-culture, batch, fed batch and chemostat cultivation are given in **Table 1**. Induction was performed according to **Table 1**. The ratio of glycerol to lactose was calculated based on recent works in fed-batch regarding maximal lactose uptake versus applied $q_{s,C}$ (Wurm et al., 2016). Fed batch was always cultivated to have a standard for protein production with similar specific growth rate as applied in the chemostat. The cultivation offgas flow was analyzed online using gas sensors – IR for CO₂ and ZrO₂ based for Oxygen (BlueSens Gas analytics, Herten, Germany). Process control and feeding was established using the process control system PIMS Lucullus (Securecell, Urdorf, Switzerland).

We used glucose or glycerol as carbon source and 0.5 mM IPTG for induction. During all induction phases pH is kept constant at 6.7 and temperature at 30°C. pH was controlled with base only (12.5% NH₄OH), while acid (10% H₃PO₄) was added manually, if necessary. The pH was monitored using a pH-sensor EasyFerm Plus (Hamilton, Reno, NV, United States). Aeration

was carried out using a mixture of pressurized air and pure oxygen at about 2 vvm to keep dissolved oxygen (dO₂) always higher than 30 %. The dissolved oxygen was monitored using a fluorescence dissolved oxygen electrode Visiferm DO (Hamilton, Reno, NV, United States).

For fed batches static feed forward $q_{s,C}$ -controls were performed during induction phase. Exponential feed was established according to Eq. 1, to keep $q_{s,C}$ constant (Slouka et al., 2016; Wurm et al., 2016):

$$F(t) = \frac{q_{s,C} * X(t) * \rho_f}{C_f} \quad (1)$$

With F being the feedrate [g/h], $q_{s,C}$ the specific glycerol uptake rate [g/g/h], $X(t)$ the absolute biomass [g], ρ_f the feed density [g/L], and c_f the feed concentration [g/L], respectively. For applied control strategies adaption of the $q_{s,C}$ during the induction time was performed based on Eq. 1. Chemostat cultivations were set manually to a dilution rate of $D = 0.1 \text{ h}^{-1}$ for all performed runs.

Process Analytics

For fed batch, samples were always taken after inoculation, upon end of the batch-phase and after the non-induced-fed batch was finished. During the induction period, samples were taken in a maximum of 120 min intervals and analyzed subsequently. Details on the process analytics can be found elsewhere (Kopp et al., 2018; Slouka et al., 2018). For chemostat cultivations samples were collected after batch and afterward once or, if necessary, twice a day.

Product Analytics

Preparation

A 5 mL fermentation broth samples were centrifuged at 4800 rpm at 4°C for 10 min. The supernatant was discarded, and the pellet was resuspended to a DCW of about 4 g/L in lysis buffer (100 mM Tris, 10 mM EDTA at pH = 7.4). Afterward the sample was homogenized using a Gea PandaPlus homogenizer (Gea, AG, Germany) at 1500 bar for 10 passages. After centrifugation at 10000 rpm and 4°C for 10 min 10 ml of the supernatant were kept for analysis of the soluble protein. Soluble protein was stored in 4°C. The resulting IB pellet was washed twice with ultrapure water. Aliquotted of pellets à 2 mL broth were centrifuged again (14000 rpm, 10 min 4°C) and finally stored at -20°C .

Inclusion Body Titer

Soluble protein samples were filtered (0.2 μm mesh) and directly used in the HPLC. Inclusion Body (IB) pellet samples were prepared according to Kopp et al. (2018), and subsequently solubilized using following buffer: 7.5 M guanidine hydrochloride, 62 mM Tris at pH = 8 and 125 mM DTT was added right before use. The filtered IB samples were quantified by HPLC analysis (UltiMate 3000; Thermo Fisher, Waltham, MA, United States). The used column was manufactured by Waters (BioResolve RPmab) and was designed for monoclonal antibody measurements (Waters Corporation, Milford, MA, United States). The product was quantified with an UV detector

TABLE 1 | C source and induction for the different cultivations.

	Glucose [g/L]	Glycerol [g/L]		
Pre-culture media	8	8		
Batch media	20	20		
Feed	Glucose [g/L]	Glycerol [g/L]	Inducer	Inducer concentration
GFP chemostat mode 1		50	Lactose	25 g/L
GFP chemostat mode 2	50		Lactose	25 g/L
GFP Fed-batch mode	300		IPTG	0.5 mM
mCherry chemostat mode		50	Lactose	25 g/L
mCherry Fed-batch mode	300		IPTG	0.5 mM
BBlue chemostat mode		50	Lactose	25 g/L
BBlue Fed-batch mode	400		IPTG	0.5 mM
HMS GFP chemostat 1		50	Lactose	25 g/L
HMS GFP chemostat 2	50		Lactose	25 g/L

(Thermo Fisher, Waltham, MA, United States) at 280 nm, respectively. Mobile phase was composed of water (ultrapure) (eluent A) and acetonitrile (eluent B) both supplemented with 0.1% (v/v) trifluoroacetic acid. Details on the method are given in Kopp et al. (2020). For quantification of soluble protein, a size exclusion (=SEC) chromatography principle was applied, using a X-bridge column (Waters Corporation, Milford, MA, United States). The mobile phase was composed of 250 mM KCl and 50 mM of each KH_2PO_4 and K_2HPO_4 dissolved in Ultrapure water as described elsewhere (Goyon et al., 2018). A constant flow rate of 0.5 mL/min was applied with an isocratic elution at 25°C for 18 min. BSA standards (50, 140, 225, 320, 500, 1000, and 2000 mg/mL; Sigma Aldrich, St. Louis, MO, United States) were used for quantification.

RESULTS

Fed batch cultivations induced with IPTG are the golden standard for RPP with *E. coli*. To be able to compete with fed batches, the specific productivity in chemostat cultivations must be maximized and the duration of the productive phase prolonged, so that time space yields are significantly increased. We tested two mixed feed systems, glucose/lactose, and glycerol/lactose, to find conditions for stable protein expression in *E. coli* chemostats.

Fed-Batch and Chemostats Using BI21(DE3) Expressing GFP as Model Protein

First, we compared three different cultivation modes using GFP as model protein. As IPTG is often referred to as toxic to the cells after a certain induction time, we used lactose as mild inducer in the first run (Dvorak et al., 2015). A mixed feed consisting of glucose and lactose (Table 1) was used for the first chemostat (Figure 1). To ease the comparability between fed batch and chemostat cultivation we aimed for similar specific substrate uptake rates – $q_{s,C}$, which resulted in a dilution rate for the chemostats of 0.1 h^{-1} . Respective process parameters are presented in Table 2.

While the fed batch gave the highest product titers after 10 h of induction, the glucose/lactose chemostat system had the maximum product titer at 20 h. In the glucose chemostat, productivity dropped below the limit of quantification (LoQ) of the HPLC method after around 3 days of cultivation, including batch of 6 h, and did not recover at later induction times. This phenomenon is well known for other strains cultivated with glucose as sole carbon source in chemostat mode (Peebo and Neubauer, 2018). Based on our recent results in fed batch using glycerol as carbon source (Kopp et al., 2017), we cultivated *E. coli* producing GFP with a mixed feed of glycerol/lactose. Highest specific titer (calculated by dividing titer through biomass), was found in the beginning of the glucose/lactose chemostat (Figure 1). There are high differences in terms of productivity between the three cultivations (Table 2).

In general, inclusion bodies and soluble protein were produced simultaneously during cultivations of *E. coli* expressing GFP (Wurm et al., 2018). For easy comparison, we calculated

the total productivity as a sum of IBs and soluble protein. Productivity and titer on glycerol were far lower in the beginning in comparison to the glucose/lactose fed chemostat (compare axes in Figure 1). In contrast to the glucose/lactose chemostat a recovery in productivity appeared at about 150 h of induction time. This renewed productivity dropped again at about 250 h of induction.

Chemostat Cultivation Using *E. coli* HMS174 Expressing GFP

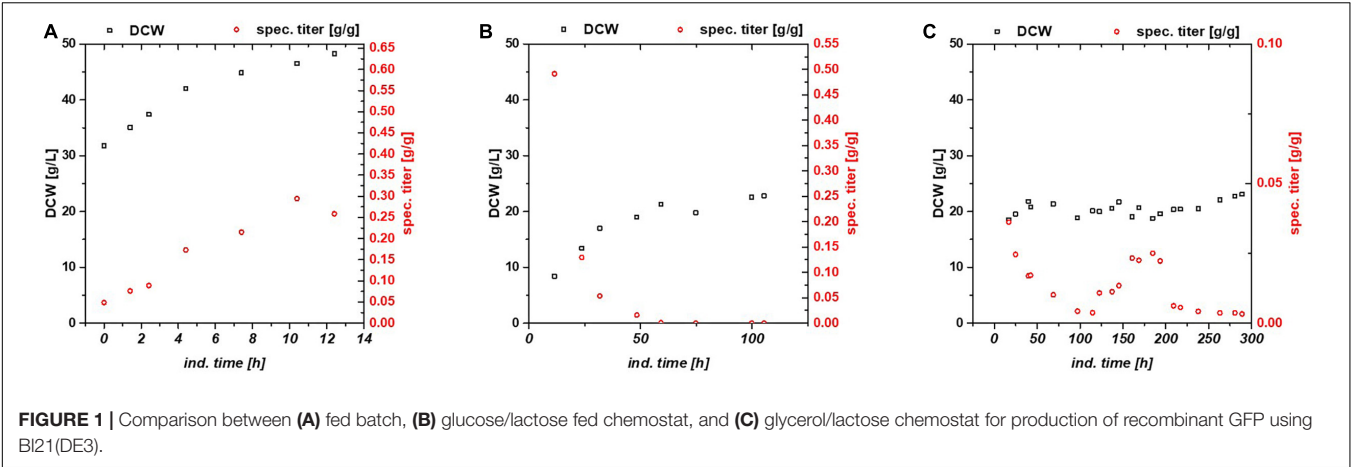
Escherichia coli BI21(DE3) lacks in a functioning Leloir pathway implementing lacking galactose uptake (Daegelen et al., 2009). To investigate effects of galactose metabolism, a recombinant *E. coli* HMS174(DE3) strain with a working galactose metabolism was examined. *E. coli* HMS174(DE3) was cultivated with glycerol and glucose as primary carbon source and lactose as inducer in chemostat cultures (Table 3). In Figure 2A, the chemostat cultivation with glucose/lactose is shown. HMS strain behaves like BI21 with initial high productivity of GFP expressed in similar specific titers. Biomass concentration was in overall higher using this strain, as galactose served as additional carbon source. The glycerol based chemostat, given in Figure 2B, showed also comparable productivity after induction to BI21, however, no recovery after 100 h of induction was observed using HMS174(DE3) strain.

Chemostat Cultivation Using BI21(DE3) Expressing mCherry and Blitzenblue as Model Proteins

To check the effects of glycerol/lactose chemostats, we produced two further fluorescent model proteins with this respective system and compared them to glucose/IPTG fed batches using the strain BI21(DE3). In Table 4 results for cultivation using *E. coli* expressing mCherry are presented. Higher productivity and specific titer were found for the fed batch cultivations. However, induction with IPTG and product titers up to 18 g/L imposed stress to cells, obvious in the low substrate to biomass yield.

A similar result was obtained for cultivation for *E. coli* recombinantly expressing BBlue (Table 4). The magnitude of specific titer and $q_{p,max}$ differed, but the trends were comparable. The substrate to biomass yield was even lower than for mCherry indicating that BBlue even imposed more stress to the host in the fed batch mode.

Chemostats for mCherry and BBlue resulted in less cellular stress compared to the fed batch cultivation. In Figure 3 DCW, specific titer and IB fraction over time are plotted for mCherry (Figure 3A) and BBlue (Figure 3B). mCherry produced a high amount of IBs in the beginning of the chemostat upon the first decrease in productivity during the cultivation. The recovery of productivity at about 200 h was exclusively soluble protein with no IB fraction anymore. BBlue showed no IB expression in fed batch nor in the chemostat and a high specific titer at the recovery at 200 h of induction time. This effect was highly different to the GFP glycerol run. While a high IB ratio was present in the GFP glycerol chemostat, the other *E. coli* expressing mCherry



and BBlue produced mainly soluble protein in the recovery phase. During intermediate time between 100 and 200 h biomass concentration was generally higher (also indicated by higher yield coefficients), so metabolism was most likely regulated toward anabolism of host cell proteins. During the recovery, DCW started to drop again because of recombinant protein expression. In contrast to GFP and BBlue, mCherry had a high overall specific titer within the entire cultivation. Elucidating this metabolic shift in regulation may be a key parameter for maintaining constant productivity in chemostat cultures.

DISCUSSION

We tested the effects on productivity using mixed feed systems with glucose/lactose and glycerol/lactose in chemostats and compared them to classical fed batches with similar specific uptake rates. In the performed chemostat cultivation, we could

distinguish between three different metabolic states (Figure 4A). Phase I is the adaption phase after the batch. This phase resembled a fed batch like behavior for *E. coli* BL21(DE3) with GFP and mCherry including high RPP. This effect was most likely linked to high IB concentrations upon protein expression during this phase, which led to increased metabolic burden for the host (Figure 4B). Rise in IB concentrations was indicated by a change of the carbon dioxide to substrate yield ($Y_{CO_2/S}$ not shown). Phase II was characterized by constant yields and carbon balance (C-balances). This phase overlapped with phase III, where recovery of productivity set in. Acetate formation measured by photometric assays (not shown) was always low for all cultivations. In contrast, BBlue chemostat did not show a phase I increase in yield coefficients of the C-balance. We believe that this was due to lack of IB expression in this strain. Surprisingly, a drop in C-balance was present upon recovery of productivity at 100–150 h (phase II and III). C-balance did not close to 1 during the entire cultivation, which indicated some other non-measured metabolites during this run. Reduction of biomass formation (decreased μ) is a common phenomenon upon RPP (Neubauer et al., 2003; Hoffmann and Rinas, 2004). Effects could be clearly seen for *E. coli* expressing GFP and mCherry in the beginning and for BBlue at the start of the recovery phase (Figures 1, 3). These effects were obviously strongly dependent on the expressed protein and could not be generalized. Comparing results of the mCherry chemostat cultivation to a chemostat cultivation for production of mCherry in literature (Schmieder and Weuster-Botz, 2017), maximum specific titer was found to be higher by a factor of 100, whereas average specific titer was higher by a factor of 10 (Table 4). As referred chemostat cultivation was induced with IPTG, we suppose that lactose induction facilitated the production of mCherry in chemostat cultivation.

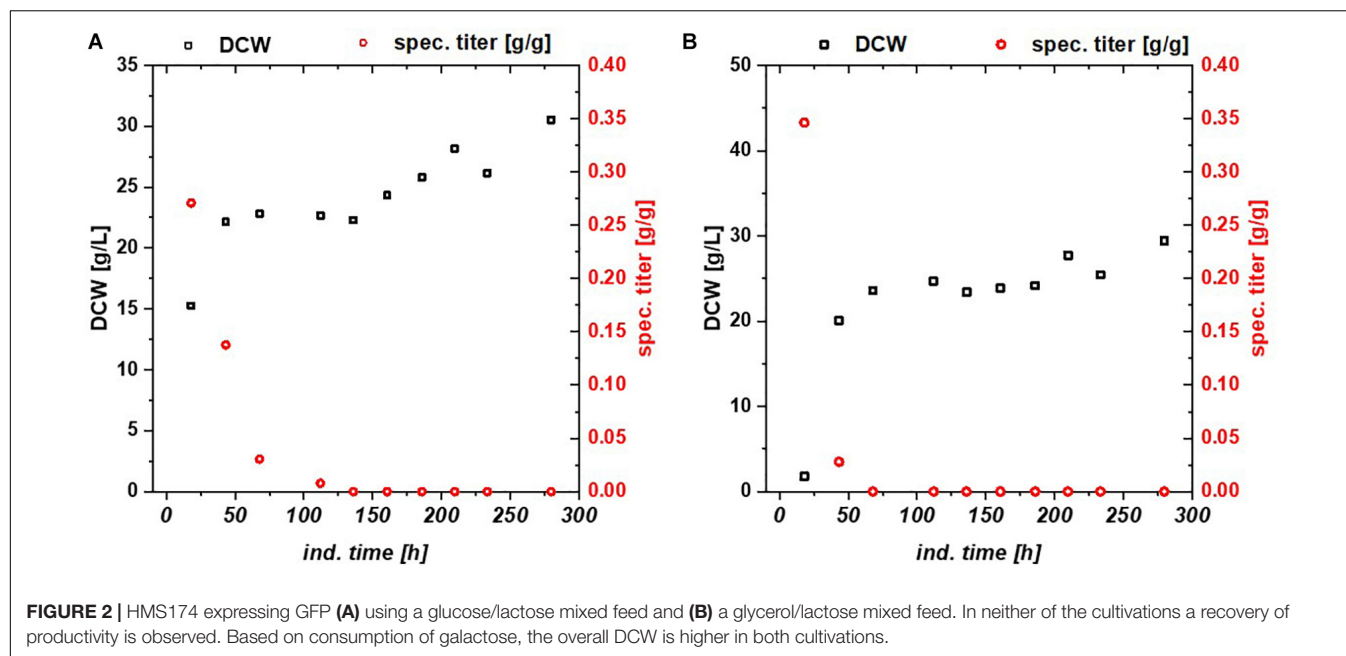
Higher dilution rates are beneficial for productivity in chemostat, as described in literature before (Seo and Bailey, 1986; Reinikainen and Virkajärvi, 1989). However, no discussion on long term stability was given, as generally steady state was assumed after three residence times (Seo and Bailey, 1986), which corresponds to $D = 0.1\text{ h}^{-1}$ at 30 h. This would only result

TABLE 2 | Process variables for three performed cultivations with BL21(DE3) expressing GFP.

Process parameters	Glucose-IPTG fed-batch	Glucose-lactose chemostat	Glycerol-lactose chemostat
spec. titer max. [g/g]	0.30	0.31	0.04
$q_{p,max}$ [g/g/h]	0.05	0.01	0.01
$q_{s,C}$ [g/g/h]	0.23 ± 0.02	0.24 ± 0.04	0.27 ± 0.04
$Y_{x/s}$ [g/g]	0.39 ± 0.09	0.49 ± 0.09	0.42 ± 0.03

TABLE 3 | Process variables for performed chemostat cultivations with HMS174(DE3) expressing GFP.

Process parameters	Glucose-lactose chemostat	Glycerol-lactose chemostat
spec. titer max. [g/g]	0.27	0.35
$q_{p,max}$ [g/g/h]	0.02	0.039
$q_{s,C}$ [g/g/h]	0.27 ± 0.05	0.27 ± 0.02
$Y_{x/s}$ [g/g]	0.37 ± 0.04	0.43 ± 0.03



in 17.3 generation times at the presented $D = 0.4 \text{ h}^{-1}$, where maximum productivity was found. The cultivations presented here, were cultivated for almost 40 generations. Stability of the long-time process is the main concern using *E. coli* as host (Peebo and Neubauer, 2018). Genetic instabilities, like plasmid loss and mutations, happen during this long term of cultivation. The recovery of the productivity in phase III was a strong indicator that only minor plasmid loss happened during cultivations and that no plasmid deficient hosts overgrew the culture.

All chemostat cultivations except for the glycerol-lactose chemostat cultivation on BL21(DE3) follow the often describe bell-shaped decrease of productivity (Peebo and Neubauer, 2018). It is not clear yet, why glucose based chemostats showed a complete loss of productivity and glycerol-based cultivations recovered after a certain time span. Diauxic growth is known to downregulate β -galactosidase activity, leading to inducer exclusion often observed in batch cultivation (Monod, 1949;

Inada et al., 1996). As feeding of carbon source and inducer was conducted using previously established feeding protocols, growth rates never exceeded μ_{\max} (Wurm et al., 2017a). Both carbon sources were taken up at all time, except for a monitored adaption phase observed for HMS174 (Supplementary Figure 1). Therefore, diauxic growth can be excluded as a possible explanation. Even though IPTG transport was found to be highly dependent on lactose permease (Fernández-Castané et al., 2012), chemostat cultivations with BL21(DE3) and IPTG induction also resulted in an irreversible drop of productivity (Kopp et al., 2019a). Only galactose accumulation was found to alter when comparing glucose and glycerol cultivations on BL21(DE3), which will be discussed in more detail. Acetate formation was present in HMS174 strains for both carbon source, while acetate concentration was always below limit of detection of our respective HPLC method for BL21(DE3) strains (Supplementary Figure 1).

Our recent work on fed batch cultivations using mixed feeds systems with glucose/lactose and glycerol/lactose showed a strong increase on productivity upon glycerol feeding (Kopp et al., 2017). Higher and better performance of cultivations using glycerol as carbon source was also found to produce different enzymes (Hansen and Eriksen, 2007; Liu et al., 2011). Difference in enzymatic regulations on glycerol consumption were reported by activation of gluconeogenesis also including “carbon stress responses” for batch culture approaches (Martínez-Gómez et al., 2012). However, in the performed chemostat cultures this glycerol carbon stress could be clearly seen for *E. coli* expressing GFP (Table 2) in yields and productivity compared to the glucose/lactose mixed feed system. Results indicate that glucose is the carbon source of choice in the beginning of a chemostat culture, as higher productivity upon glucose cultivation can be observed. As μ_{\max} is higher upon glucose cultivation compared to glycerol, energy (ATP) needed for recombinant protein

TABLE 4 | Cultivation variables for fed batch cultivation and continuous cultivation with the glycerol/lactose system for production of recombinant mCherry and recombinant Blitzenblue.

	Glucose-IPTG fed-batch	Glycerol-lactose chemostat
Process variables mCherry		
spec. titer max [g/g]	0.21	0.17
$q_{p,\max}$ [g/g/h]	0.069	0.01
$q_{s,C}$ [g/g/h]	0.28 ± 0.02	0.22 ± 0.2
$Y_{X/S}$ [g/g]	0.34 ± 0.09	0.47 ± 0.04
Process variables BBlue		
spec. titer max [g/g]	0.13	0.035
$q_{p,\max}$ [g/g/h]	0.033	0.002
$q_{s,C}$ [g/g/h]	0.29 ± 0.01	0.25 ± 0.05
$Y_{X/S}$ [g/g]	0.18 ± 0.05	0.30 ± 0.03

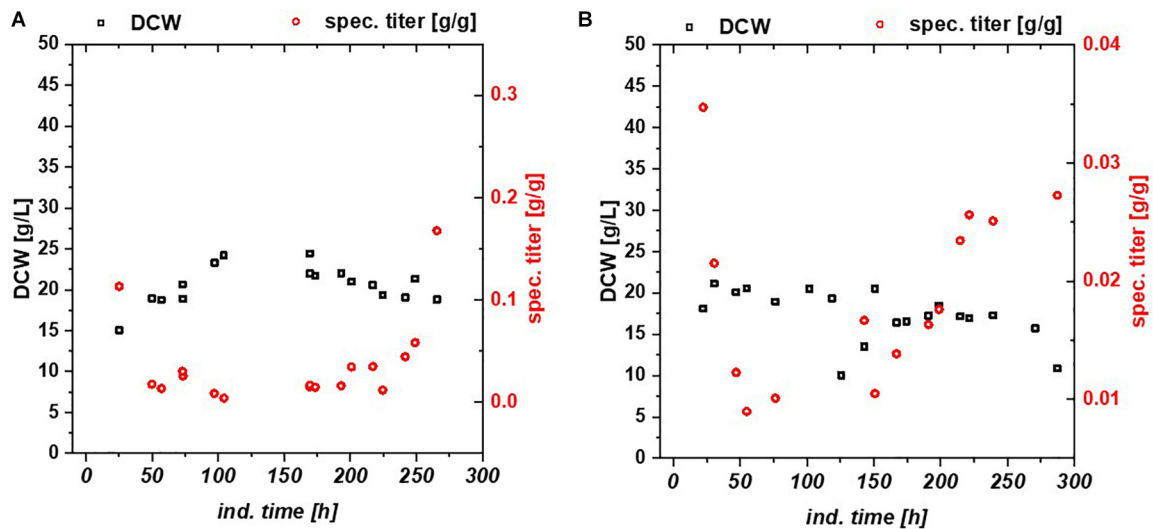


FIGURE 3 | Chemostat cultures with BI21(DE3) with glycerol/lactose mixed feed expressing (A) mCherry, (B) Blitzenblue. The recovery of the productivity is clearly visible at 200 h in both cultivations. Blitzenblue (B) exhibits only soluble protein in fed batch and continuous cultivation.

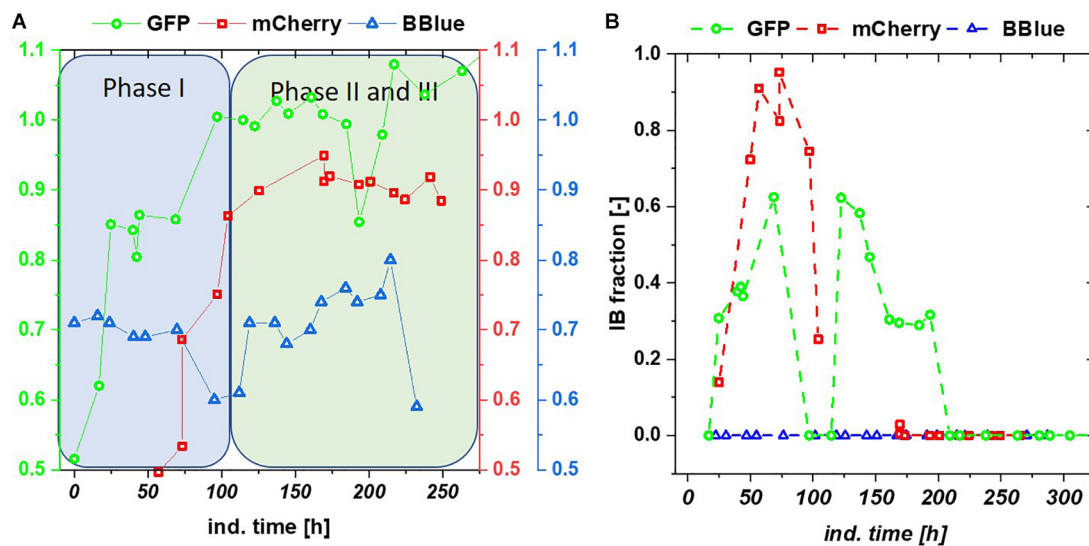


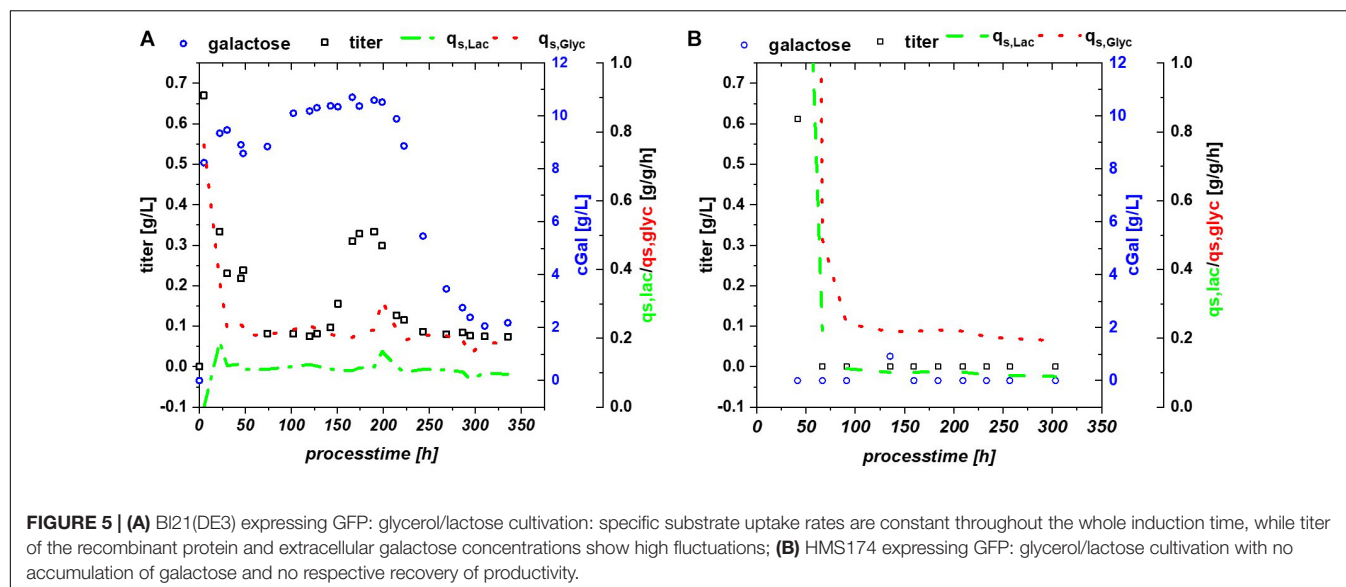
FIGURE 4 | (A) C-balances of all three chemostat cultivations with glycerol/lactose feed. Blitzenblue does not reach a balance of 1 in the entire cultivation time and does not have adaption phase I. (B) Inclusion body (IB) fractions over the timespan of glycerol-lactose chemostat cultivations: GFP IB amount increased up until 100 h and followed a subsequent drop. A recovery after 125 h of the IB fraction could be observed, mCherry showed higher IB content in the beginning of the cultivation but only recovered in productivity of the soluble fraction whereas the IB formation stopped after 100 h. Blitzenblue showed no IB-formation.

formation might be faster accessible upon start of induction (Kopp et al., 2017; Wurm et al., 2017b).

The faster metabolism on glucose cultivation, compared to glycerol consumption (Wang and Yang, 2013) could possibly explain higher productivity for glucose fed chemostats in the beginning of the cultivation. NADPH formation on glycerol is also meager, when compared to glucose cultivation, emphasizing the previous statement (Yao et al., 2016). Still, in contrast to glucose, glycerol enabled a recovery of productivity at later stage. Reasons still need to be investigated but could

possibly result from different intracellular metabolism (i.e., pyruvate dehydrogenase and TCA activity) (Murarka et al., 2008; Yao et al., 2016).

Multistability of induction was described by Ozbudak et al. (2004) showing changes in expression. In this publication, it is shown that the lac system can remain in several states, depending on the amount of LacI and cAMP molecules. With constant process parameters, changes in plasmid number during the cultivation might be a reasonable explanation for the observed effects. Based on the strong metabolic



burden in the beginning, total number of plasmids might change and lead to a bi-stability of the cultivation system. Yet, pET plasmids generally carry a LacI gene, resulting in a direct relationship between lac repressor and plasmid number and may drastically reduce those observed effects during pET-based induction. Furthermore, the study by Ozbudak et al. (2004) was performed with a strong irreversible inducer [thiomethyl galactoside (TMG)], in comparison to lactose used for our experiments. Glycerol does not provoke a cAMP response directly, but cAMP response might be present based on the metabolized glucose (from lactose) as seen in fed batch cultivations (Kopp et al., 2017), which inherited a very different regulation compared to the glucose based cultivations. A further possible alternative for this fluctuation in productivity might be intracellular galactose accumulation (**Supplementary Figure 1**). Galactose is known to affect the cellular β -galactosidase concentrations (Llanes and McFall, 1969; Portaccio et al., 1998) and has been shown to function as a weak inducer (Ukkonen et al., 2013). High intracellular galactose concentration (drop in extracellular concentration), seen in **Figure 5A**, was accompanied by a drop of productivity. However, lactose consumption was not affected by the galactose fluctuations.

HMS174 can metabolize galactose upon induction with lactose (Hausjell et al., 2018), therefore this strain was investigated using a mixed feed with glycerol/lactose. However, previously mentioned advantages, such as overflow metabolism and overall titer formation favor B strains over K strains for the RPP (Shiloach and Fass, 2005; Rosano and Ceccarelli, 2014). HMS174(DE3) expressing GFP revealed no recovery on glycerol and no pronounced accumulation of neither glycerol, nor lactose or galactose, compare to **Figure 5B**. Still constant overflow metabolism was found for HMS174(DE3) chemostat cultivations whereas no acetate accumulation could be monitored for BL21(DE3) (**Supplementary Figure 1**). As galactose was

completely metabolized in HMS174(DE3) cultivations, biomass was found to be higher compared to BL21(DE3) cultivations. Specific uptake rates were also constant, expect for deviations upon start of the induction phase. Yet, we believe that galactose variations are the most reasonable explanation for the effects seen in BL21(DE3). It is not clear why galactose is stored inside the *E. coli* cells or expelled into the supernatant as seen in shifts of galactose concentration. Previous studies indicated galactose as main player for Lazarus effect. Based on these findings we expect a non-trivial interaction of multiple factors in BL21 resulting in the observed behavior.

Furthermore, the three analyzed fluorescence proteins exhibit several differences. GFP originates from jellyfish *Aequorea Victoria* while mCherry from *Discosoma* sp. (Shaner et al., 2004) and BBlue from *Actinia equina*. BBlue and mCherry show a homology of about 60% identical amino acids. GFP was found to be highly different, as overlap in gene sequence is below 30% of amino acids. All three analyzed proteins do not have any disulfide bonding, predicted via Disulfind server (Ceroni et al., 2006). However, a high difference is reported in maturation kinetics. While GFP only exhibits one maturation step (oxidation), for mCherry a two-step mechanism is described. Therefore, far longer maturation times for mCherry, than for GFP about a factor of 10 were reported (Hebisch et al., 2013). Both maturation kinetics exhibit a pronounced growth rate

TABLE 5 | Average time-space-yield (TSY) of fed batch and glycerol/lactose chemostat including running time of chemostat to reach the performance of the fed batch for BL21(DE3).

Protein	Glucose-IPTG fed-batch average TSY [g/l/h]	Glycerol-lactose chemostat TSY [g/l/h]	Cultivation time to reach fed-batch productivity at 10 h of induction [h]
GFP	1.28	0.022	581 h
mCherry	0.87	0.052	167 h
BBlue	0.56	0.017	215 h

dependency. Knowledge about the maturation may be a key parameter in further analysis of bacterial subpopulations during chemostat cultivations (Hebisch et al., 2013).

Finally, we compared time space yields for the three glycerol/lactose-based cultivations in BL21(DE3) to fed batches in **Table 5**. No continuous glycerol/lactose cultivations could compete with fed batch cultivation. mCherry showed the highest time space yield in tested cultivations. It needed at least 167 h of cultivation with an averaged time space yield to meet the performance of a classic fed-batch (which exhibits about 7.5 g/l titer after 10 h of induction).

Long-term *E. coli* cultivations are known to cause different mutants, showing different physiology (i.e., μ , $Y_{X/S}$, etc.) compared to the original strain (Weikert et al., 1997; Binder et al., 2017; Delvigne et al., 2017; Heins et al., 2019). Long cultivation durations with wild-type strains revealed that changes in transcriptome and proteome can be already seen without recombinant protein formation (Wick et al., 2001; Peebo and Neubauer, 2018). As exact regulations in recombinant protein formation are still unknown, reasonable control strategies with further insight in the metabolic regulation are needed. We have ongoing projects identifying different productive subpopulations in *E. coli* being responsible for the change in productivity. However, new insights into the “black box” using transcriptomic analysis and measurement of plasmid and cAMP contents of the glycerol/lactose mixed feed system is mandatory and are ongoing in our group.

Summarizing, in this study we tested glycerol/lactose mixed feed systems in continuous culture using *E. coli* BL21(DE3) and HMS174 expressing different model proteins to find a system with long time stable productivity potentially outperforming fed-batches. Beside lower productivity of glycerol/lactose chemostats compared to glucose/lactose in the beginning, a recovery of productivity at times larger than 100 h (about 15 generation times) could be observed for all strains investigated. However,

further analysis like subpopulation monitoring is necessary to understand this “Lazarus” effect on a cellular level.

DATA AVAILABILITY STATEMENT

The original contributions presented in the study are included in the article/**Supplementary Material**, further inquiries can be directed to the corresponding author.

AUTHOR CONTRIBUTIONS

SK, JK, PV, and CS performed the bioreactor cultivations. SK, JK, and CS evaluated the data. CH, OS, and CS supervised the work. CH and FD gave valuable input for the manuscript. OS and CS drafted the manuscript. All authors contributed to the article and approved the submitted version.

FUNDING

The authors thank the Christian Doppler Society for funding of this project.

ACKNOWLEDGMENTS

The authors acknowledge TU Wien Bibliothek for financial support through its Open Access Funding Program.

SUPPLEMENTARY MATERIAL

The Supplementary Material for this article can be found online at: <https://www.frontiersin.org/articles/10.3389/fbioe.2020.00993/full#supplementary-material>

REFERENCES

- Baeshen, M. N., Al-Hejin, A. M., Bora, R. S., Ahmed, M. M., Ramadan, H. A., Saini, K. S., et al. (2015). Production of biopharmaceuticals in *E. coli*: current scenario and future perspectives. *J. Microbiol. Biotechnol.* 25, 953–962. doi: 10.4014/jmb.1412.12079
- Berlec, A., and Strukelj, B. (2013). Current state and recent advances in biopharmaceutical production in *Escherichia coli*, yeasts and mammalian cells. *J. Ind. Microbiol. Biotechnol.* 40, 257–274. doi: 10.1007/s10295-013-1235-1230
- Binder, D., Drepper, T., Jaeger, K.-E., Delvigne, F., Wiechert, W., Kohlheyer, D., et al. (2017). Homogenizing bacterial cell factories: analysis and engineering of phenotypic heterogeneity. *Metab. Eng.* 42, 145–156. doi: 10.1016/j.ymben.2017.06.009
- Blommel, P. G., Becker, K. J., Duvnjak, P., and Fox, B. G. (2007). Enhanced bacterial protein expression during auto-induction obtained by alteration of lac repressor dosage and medium composition. *Biotechnol. Prog.* 23, 585–598. doi: 10.1021/bp070011x
- Burstein, C., Cohn, M., Kepes, A., and Monod, J. (1965). Role du lactose et de ses produits metaboliques dans l'induction de l'operon lactose chez *Escherichia coli*. *Biochimica et Biophysica Acta (BBA)-Nucleic Acids and Protein Synthesis* 95, 634–639. doi: 10.1016/0005-2787(65)90517-90514
- Ceroni, A., Passerini, A., Vullo, A., and Frascioni, P. (2006). DISULFIND: a disulfide bonding state and cysteine connectivity prediction server. *Nucleic Acids Res.* 34(Suppl_2), W177–W181.
- Daegelen, P., Studier, F. W., Lenski, R. E., Cure, S., and Kim, J. F. (2009). Tracing ancestors and relatives of *Escherichia coli* B, and the derivation of B strains REL606 and BL21(DE3). *J. Mol. Biol.* 394, 634–643. doi: 10.1016/j.jmb.2009.09.022
- DeLisa, M. P., Li, J., Rao, G., Weigand, W. A., and Bentley, W. E. (1999). Monitoring GFP-operon fusion protein expression during high cell density cultivation of *Escherichia coli* using an on-line optical sensor. *Biotechnol. Bioeng.* 65, 54–64. doi: 10.1002/(SICI)1097-0290(19991005)65:1<54::AID-BIT7<3.0.CO;2-R
- Delvigne, F., Baert, J., Sassi, H., Fickens, P., Grünberger, A., and Dusny, C. (2017). Taking control over microbial populations: current approaches for exploiting biological noise in bioprocesses. *Biotechnol. J.* 12:1600549. doi: 10.1002/biot.201600549
- Deutscher, J., Francke, C., and Postma, P. W. (2006). How phosphotransferase system-related protein phosphorylation regulates carbohydrate metabolism in bacteria. *Microbiol. Mol. Biol. Rev.* 70, 939–1031. doi: 10.1128/MMBR.00024-26
- Diers, I., Rasmussen, E., Larsen, P., and Kjaersig, I. (1991). Yeast fermentation processes for insulin production. *Bioprocess. Technol.* 13:166.

- Dubendorff, J. W., and Studier, F. W. (1991). Controlling basal expression in an inducible T7 expression system by blocking the target T7 promoter with lac repressor. *J. Mol. Biol.* 219, 45–59. doi: 10.1016/0022-2836(91)90856-90852
- Dvorak, P., Chrast, L., Nikel, P. I., Fedr, R., Soucek, K., Sedlackova, M., et al. (2015). Exacerbation of substrate toxicity by IPTG in *Escherichia coli* BL21(DE3) carrying a synthetic metabolic pathway. *Microb Cell Fact* 14:201. doi: 10.1186/s12934-015-0393-393
- Fernández-Castané, A., Vine, C. E., Caminal, G., and López-Santín, J. (2012). Evidencing the role of lactose permease in IPTG uptake by *Escherichia coli* in fed-batch high cell density cultures. *J. Biotechnol.* 157, 391–398. doi: 10.1016/j.jbiotec.2011.12.007
- Goyon, A., Sciascera, L., Clarke, A., Guilleme, D., and Pell, R. (2018). Extending the limits of size exclusion chromatography: simultaneous separation of free payloads and related species from antibody drug conjugates and their aggregates. *J. Chromatogr. A* 1539, 19–29. doi: 10.1016/j.chroma.2018.01.039
- Gupta, S. K., and Shukla, P. (2016). Microbial platform technology for recombinant antibody fragment production: a review. *Crit. Rev. Microbiol.* 43, 31–42. doi: 10.3109/1040841X.2016.1150959
- Hansen, R., and Eriksen, N. T. (2007). Activity of recombinant GST in *Escherichia coli* grown on glucose and glycerol. *Process Biochem.* 42, 1259–1263. doi: 10.1016/j.procbio.2007.05.022
- Hausjell, J., Weissensteiner, J., Molitor, C., Halbwirth, H., and Spadiut, O. (2018). *E. coli* HMS174 (DE3) is a sustainable alternative to BL21 (DE3). *Microb Cell Fact* 17:169. doi: 10.1186/s12934-018-1016-1016
- Hebisch, E., Knebel, J., Landsberg, J., Frey, E., and Leisner, M. (2013). High variation of fluorescence protein maturation times in closely related *Escherichia coli* strains. *PLoS One* 8:e75991. doi: 10.1371/journal.pone.0075991
- Heins, A.-L., Johanson, T., Han, S., Lundin, L., Carlquist, M., Gernaey, K. V., et al. (2019). Quantitative flow cytometry to understand population heterogeneity in response to changes in substrate availability in *Escherichia coli* and *saccharomyces cerevisiae* chemostats. *Front. Bioeng. Biotech.* 7:187. doi: 10.3389/fbioe.2019.00187
- Hoffmann, F., and Rinas, U. (2004). Stress induced by recombinant protein production in *Escherichia coli*. *Adv. Biochem. Eng. Biotechnol.* 89, 73–92. doi: 10.1007/b93994
- Inada, T., Kimata, K., and Aiba, H. (1996). Mechanism responsible for glucose–lactose diauxie in *Escherichia coli*: challenge to the cAMP model. *Genes Cells* 1, 293–301. doi: 10.1046/j.1365-2443.1996.24025.x
- Jeong, H., Barbe, V., Lee, C. H., Vallenet, D., Yu, D. S., Choi, S. H., et al. (2009). Genome sequences of *Escherichia coli* B strains REL606 and BL21(DE3). *J. Mol. Biol.* 394, 644–652. doi: 10.1016/j.jmb.2009.09.052
- Jeong, H., Kim, H. J., and Lee, S. J. (2015). Complete genome sequence of *Escherichia coli* strain BL21. *Genome Announc.* 3:e00134-15. doi: 10.1128/genomeA.00134-15
- Jia, B., and Jeon, C. O. (2016). High-throughput recombinant protein expression in *Escherichia coli*: current status and future perspectives. *Open Biol.* 6:160196. doi: 10.1098/rsob.160196
- Kopp, J., Kolkman, A.-M., Veleenturf, P. G., Spadiut, O., Herwig, C., and Slouka, C. (2019a). Boosting recombinant inclusion body production—from classical fed-batch approach to continuous cultivation. *Front. Bioeng. Biotech.* 7:297. doi: 10.3389/fbioe.2019.00297
- Kopp, J., Slouka, C., Spadiut, O., and Herwig, C. (2019b). The rocky road from fed-batch to continuous processing with *E. coli*. *Front. Bioeng. Biotech.* 7:328. doi: 10.3389/fbioe.2019.00328
- Kopp, J., Slouka, C., Strohmer, D., Kager, J., Spadiut, O., and Herwig, C. (2018). Inclusion Body Bead Size in *E. coli* controlled by physiological feeding. *Microorganisms* 6:116. doi: 10.3390/microorganisms6040116
- Kopp, J., Slouka, C., Ulonska, S., Kager, J., Fricke, J., Spadiut, O., et al. (2017). Impact of glycerol as carbon source onto specific sugar and inducer uptake rates and inclusion body productivity in *E. coli* BL21 (DE3). *Bioengineering* 5:1. doi: 10.3390/bioengineering5010001
- Kopp, J., Zauner, F. B., Pell, A., Hausjell, J., Humer, D., Ebner, J., et al. (2020). Development of a generic reversed-phase liquid chromatography method for protein quantification using analytical quality-by-design principles. *J. Pharmaceut. Biomed.* 188:113412. doi: 10.1016/j.jpba.2020.113412
- Liu, J.-F., Zhang, Z.-J., Li, A.-T., Pan, J., and Xu, J.-H. (2011). Significantly enhanced production of recombinant nitrilase by optimization of culture conditions and glycerol feeding. *Appl. Microbiol. Biot.* 89, 665–672. doi: 10.1007/s00253-010-2866-y
- Llanes, B., and McFall, E. (1969). Effect of galactose on β -Galactosidase synthesis in *Escherichia coli* K-12. *J. Bacteriol.* 97, 217–222. doi: 10.1128/jb.97.1.217-222.1969
- Loomis, W. F., and Magasanik, B. (1967). Glucose-lactose diauxie in *Escherichia coli*. *J. Bacteriol.* 93, 1397–1401. doi: 10.1128/jb.93.4.1397-1401.1967
- Lyakhov, D. L., He, B., Zhang, X., Studier, F. W., Dunn, J. J., and McAllister, W. T. (1998). Pausing and termination by bacteriophage T7 RNA polymerase. *J. Mol. Biol.* 280, 201–213. doi: 10.1006/jmbi.1998.1854
- Malakar, P., and Venkatesh, K. (2012). Effect of substrate and IPTG concentrations on the burden to growth of *Escherichia coli* on glycerol due to the expression of Lac proteins. *Appl. Microbiol. Biot.* 93, 2543–2549. doi: 10.1007/s00253-011-3642-3643
- Marbach, A., and Bettenbrock, K. (2012). lac operon induction in *Escherichia coli*: systematic comparison of IPTG and TMG induction and influence of the transacetylase LacA. *J. Biotechnol.* 157, 82–88. doi: 10.1016/j.jbiotec.2011.10.009
- Martínez-Gómez, K., Flores, N., Castañeda, H. M., Martínez-Batallar, G., Hernández-Chávez, G., Ramírez, O. T., et al. (2012). New insights into *Escherichia coli* metabolism: carbon scavenging, acetate metabolism and carbon recycling responses during growth on glycerol. *Microb. Cell Fact* 11:46. doi: 10.1186/1475-2859-11-46
- Monod, J. (1949). The growth of bacterial cultures. *Annu. Rev. Microbiol.* 3, 371–394.
- Murarka, A., Dharmadi, Y., Yazdani, S. S., and Gonzalez, R. (2008). Fermentative utilization of glycerol by *Escherichia coli* and its implications for the production of fuels and chemicals. *Appl. Environ. Microbiol.* 74, 1124–1135. doi: 10.1128/AEM.02192-2197
- Neubauer, P., and Hofmann, K. (1994). Efficient use of lactose for the lac promoter-controlled overexpression of the main antigenic protein of the foot and mouth disease virus in *Escherichia coli* under fed-batch fermentation conditions. *FEMS Microbiol. Rev.* 14, 99–102. doi: 10.1111/j.1574-6976.1994.tb00080.x
- Neubauer, P., Lin, H., and Mathisizik, B. (2003). Metabolic load of recombinant protein production: inhibition of cellular capacities for glucose uptake and respiration after induction of a heterologous gene in *Escherichia coli*. *Biotechnol. Bioeng.* 83, 53–64. doi: 10.1002/bit.10645
- Ozbudak, E. M., Thattai, M., Lim, H. N., Shraiman, B. I., and Van Oudenaarden, A. (2004). Multistability in the lactose utilization network of *Escherichia coli*. *Nature* 427:737. doi: 10.1038/nature02298
- Peebo, K., and Neubauer, P. (2018). Application of continuous culture methods to recombinant protein production in microorganisms. *Microorganisms* 6:56. doi: 10.3390/microorganisms6030056
- Portaccio, M., Stellato, S., Rossi, S., Bencivenga, U., Eldin, M. M., Gaeta, F., et al. (1998). Galactose competitive inhibition of β -galactosidase (*Aspergillus oryzae*) immobilized on chitosan and nylon supports. *Enzyme Microb. Tech.* 23, 101–106. doi: 10.1016/S0141-0229(98)00018-10
- Postma, P. W., Lengeler, J. W., and Jacobson, G. R. (1993). Phosphoenolpyruvate:carbohydrate phosphotransferase systems of bacteria. *Microbiol. Rev.* 57, 543–594.
- Reinikainen, P., and Virkajärvi, I. (1989). *Escherichia coli* growth and plasmid copy numbers in continuous cultivations. *Biotechnol. Lett.* 11, 225–230. doi: 10.1007/BF01031568
- Ronimus, R. S., and Morgan, H. W. (2003). Distribution and phylogenies of enzymes of the Embden-Meyerhof-Parnas pathway from archaea and hyperthermophilic bacteria support a gluconeogenic origin of metabolism. *Archaea* 1, 199–221. doi: 10.1155/2003/162593
- Rosano, G. L., and Ceccarelli, E. A. (2014). Recombinant protein expression in *Escherichia coli*: advances and challenges. *Front. Microbiol.* 5:172. doi: 10.3389/fmicb.2014.00172
- Schmideder, A., and Weuster-Botz, D. (2017). High-performance recombinant protein production with *Escherichia coli* in continuously operated cascades of stirred-tank reactors. *J. Ind. Microbiol. Biotechnol.* 44, 1021–1029. doi: 10.1007/s10295-017-1927-y
- Seo, J. H., and Bailey, J. E. (1986). Continuous cultivation of recombinant *Escherichia coli*: existence of an optimum dilution rate for maximum plasmid and gene product concentration. *Biotechnol. Bioeng.* 28, 1590–1594. doi: 10.1002/bit.260281018

- Shaner, N. C., Campbell, R. E., Steinbach, P. A., Giepmans, B. N., Palmer, A. E., and Tsien, R. Y. (2004). Improved monomeric red, orange and yellow fluorescent proteins derived from *Discosoma sp. red fluorescent protein*. *Nat. Biotechnol.* 22, 1567–1572. doi: 10.1038/nbt1037
- Shiloach, J., and Fass, R. (2005). Growing *E. coli* to high cell density—a historical perspective on method development. *Biotechnol. Adv.* 23, 345–357. doi: 10.1016/j.biotechadv.2005.04.004
- Sieben, M., Steinhorn, G., Müller, C., Fuchs, S., Chin, L. A., Regestein, L., et al. (2016). Testing plasmid stability of *Escherichia coli* using the continuously operated shaken BIOreactor system. *Biotechnol. Prog.* 32, 1418–1425. doi: 10.1002/btpr.2341
- Slouka, C., Kopp, J., Hutwimmer, S., Strahammer, M., Strohmmer, D., Eitenberger, E., et al. (2018). Custom made inclusion bodies: impact of classical process parameters and physiological parameters on inclusion body quality attributes. *Microb Cell Fact* 17:148. doi: 10.1186/s12934-018-0997-995
- Slouka, C., Kopp, J., Strohmmer, D., Kager, J., Spadiut, O., and Herwig, C. (2019). Monitoring and control strategies for inclusion body production in *E. coli* based on glycerol consumption. *J. Biotechnol.* 296, 75–82. doi: 10.1016/j.jbiotec.2019.03.014
- Slouka, C., Wurm, D. J., Brunauer, G., Welzl-Wachter, A., Spadiut, O., Fleig, J., et al. (2016). A novel application for low frequency electrochemical impedance spectroscopy as an online process monitoring tool for viable cell concentrations. *Sensors (Basel)* 16:1900. doi: 10.3390/s16111900
- Spadiut, O., Capone, S., Krainer, F., Glieder, A., and Herwig, C. (2014). Microbials for the production of monoclonal antibodies and antibody fragments. *Trends Biotechnol.* 32, 54–60. doi: 10.1016/j.tibtech.2013.10.002
- Steen, R., Dahlberg, A. E., Lade, B. N., Studier, F. W., and Dunn, J. J. (1986). T7 RNA polymerase directed expression of the *Escherichia coli* rrnB operon. *EMBO J.* 5, 1099–1103. doi: 10.1002/j.1460-2075.1986.tb04328.x
- Striedner, G., Pfaffenzeller, I., Markus, L., Nemecek, S., Grabherr, R., and Bayer, K. (2010). Plasmid-free T7-based *Escherichia coli* expression systems. *Biotechnol. Bioeng.* 105, 786–794. doi: 10.1002/bit.22598
- Studier, F. W., and Moffatt, B. A. (1986). Use of bacteriophage T7 RNA polymerase to direct selective high-level expression of cloned genes. *J. Mol. Biol.* 189, 113–130. doi: 10.1016/0022-2836(86)90385-2
- Studier, F. W., Rosenberg, A. H., Dunn, J. J., and Dubendorff, J. W. (1990). Use of T7 RNA polymerase to direct expression of cloned genes. *Methods Enzymol.* 185, 60–89. doi: 10.1016/0076-6879(90)85008-c
- Tseng, T. T., Tyler, B. M., and Setubal, J. C. (2009). Protein secretion systems in bacterial-host associations, and their description in the gene ontology. *BMC Microbiol.* 9(Suppl. 1):S2. doi: 10.1186/1471-2180-9-S1-S2
- Ukkonen, K., Mayer, S., Vasala, A., and Neubauer, P. (2013). Use of slow glucose feeding as supporting carbon source in lactose autoinduction medium improves the robustness of protein expression at different aeration conditions. *Protein Expr. Purif.* 91, 147–154. doi: 10.1016/j.pep.2013.07.016
- Vaiphei, S. T., Pandey, G., and Mukherjee, K. J. (2009). Kinetic studies of recombinant human interferon-gamma expression in continuous cultures of *E. coli*. *J. Ind. Microbiol. Biotechnol.* 36:1453. doi: 10.1007/s10295-009-0632-x
- Viitanen, M. I., Vasala, A., Neubauer, P., and Alatossava, T. (2003). Cheese whey-induced high-cell-density production of recombinant proteins in *Escherichia coli*. *Microb Cell Fact* 2:2. doi: 10.1186/1475-2859-2-2
- Walsh, G. (2010). Biopharmaceutical benchmarks 2010. *Nat. Biotechnol.* 28, 917–924. doi: 10.1038/nbt0910-917
- Wang, Z., and Yang, S.-T. (2013). Propionic acid production in glycerol/glucose co-fermentation by *Propionibacterium freudenreichii* subsp. *shermanii*. *Bioresour. Technol.* 137, 116–123. doi: 10.1016/j.biortech.2013.03.012
- Weikert, C., Sauer, U., and Bailey, J. E. (1997). Use of a glycerol-limited, long-term chemostat for isolation of *Escherichia coli* mutants with improved physiological properties. *Microbiology* 143, 1567–1574. doi: 10.1099/00221287-143-5-1567
- Wick, L. M., Quadroni, M., and Egli, T. (2001). Short- and long-term changes in proteome composition and kinetic properties in a culture of *Escherichia coli* during transition from glucose-excess to glucose-limited growth conditions in continuous culture and vice versa. *Environ. Microbiol.* 3, 588–599. doi: 10.1046/j.1462-2920.2001.00231.x
- Wurm, D. J., Hausjell, J., Ulonska, S., Herwig, C., and Spadiut, O. (2017a). Mechanistic platform knowledge of concomitant sugar uptake in *Escherichia coli* BL21 (DE3) strains. *Sci. Rep.* 7:45072. doi: 10.1038/srep45072
- Wurm, D. J., Herwig, C., and Spadiut, O. (2017b). How to determine interdependencies of glucose and lactose uptake rates for heterologous protein production with *E. coli*. *Methods Mol. Biol.* 1586, 397–408. doi: 10.1007/978-1-4939-6887-9_26
- Wurm, D. J., Quehenberger, J., Mildner, J., Eggenreich, B., Slouka, C., Schwaighofer, A., et al. (2018). Teaching an old pET new tricks: tuning of inclusion body formation and properties by a mixed feed system in *E. coli*. *Appl. Microbiol. Biot.* 102, 667–676. doi: 10.1007/s00253-017-8641-8646
- Wurm, D. J., Veiter, L., Ulonska, S., Eggenreich, B., Herwig, C., and Spadiut, O. (2016). The *E. coli* pET expression system revisited—mechanistic correlation between glucose and lactose uptake. *Appl. Microbiol. Biotechnol.* 100, 8721–8729. doi: 10.1007/s00253-016-7620-7627
- Yao, R., Xiong, D., Hu, H., Wakayama, M., Yu, W., Zhang, X., et al. (2016). Elucidation of the co-metabolism of glycerol and glucose in *Escherichia coli* by genetic engineering, transcription profiling, and ¹³C metabolic flux analysis. *Biotechnol. Biofuels* 9:175. doi: 10.1186/s13068-016-0591-591

Conflict of Interest: The authors declare that the research was conducted in the absence of any commercial or financial relationships that could be construed as a potential conflict of interest.

Copyright © 2020 Kittler, Kopp, Veelenturf, Spadiut, Delvigne, Herwig and Slouka. This is an open-access article distributed under the terms of the Creative Commons Attribution License (CC BY). The use, distribution or reproduction in other forums is permitted, provided the original author(s) and the copyright owner(s) are credited and that the original publication in this journal is cited, in accordance with accepted academic practice. No use, distribution or reproduction is permitted which does not comply with these terms.



The Impact of Glass Material on Growth and Biocatalytic Performance of Mixed-Species Biofilms in Capillary Reactors for Continuous Cyclohexanol Production

Ingeborg Heuschkel, Rakesh Dagini, Rohan Karande* and Katja Bühler

Department of Solar Materials, Helmholtz-Centre for Environmental Research, Leipzig, Germany

OPEN ACCESS

Edited by:

Christoph Slouka,
Vienna University of Technology,
Austria

Reviewed by:

Harald Horn,
Karlsruhe Institute of Technology
(KIT), Germany
Cormac Murphy,
University College Dublin, Ireland

*Correspondence:

Rohan Karande
rohan.karande@ufz.de

Specialty section:

This article was submitted to
Bioprocess Engineering,
a section of the journal
Frontiers in Bioengineering and
Biotechnology

Received: 29 July 2020

Accepted: 25 August 2020

Published: 15 September 2020

Citation:

Heuschkel I, Dagini R, Karande R
and Bühler K (2020) The Impact
of Glass Material on Growth
and Biocatalytic Performance
of Mixed-Species Biofilms in Capillary
Reactors for Continuous
Cyclohexanol Production.
Front. Bioeng. Biotechnol. 8:588729.
doi: 10.3389/fbioe.2020.588729

In this study, the growth and catalytic performance of mixed-species biofilms consisting of photoautotrophic *Synechocystis* sp. PCC 6803 and chemoheterotrophic *Pseudomonas* sp. VLB120 was investigated. Both strains contained a cytochrome P450 monooxygenase enzyme system catalyzing the oxyfunctionalization of cyclohexane to cyclohexanol. Biofilm cultivation was performed in capillary glass reactors made of either, borosilicate glass (Duran) or quartz glass, in different flow regimes. Consequently, four phases could be distinguished for mixed-species biofilm growth and development in the glass-capillaries. The first phase represents the limited growth of mixed-species biofilm in the single-phase flow condition. The second phase includes a rapid increase in biofilm spatial coverage after the start of air-segments. The third phase starts with the sloughing of large biofilm patches from well-grown biofilms, and the final stage consists of biofilm regrowth and the expansion of the spatial coverage. The catalytic performance of the mixed-species biofilm after the detachment process was compared to a well-grown biofilm. With an increase in the biofilm surface coverage, the cyclohexanol production rate improved from 1.75 to 6.4 g m⁻² d⁻¹, resulting in comparable production rates to the well-grown biofilms. In summary, high productivities can be reached for biofilms cultivated in glass capillaries, but stable product formation was disturbed by sloughing events.

Keywords: cytochrome P450 monooxygenase, pseudomonas, synechocystis, biotransformation, cyclohexane oxidation, phototrophic biofilm, continuous photobioreactor

INTRODUCTION

The ability of the microbial photosynthetic machinery to convert solar radiation into chemical energy for fixing carbon dioxide into value-added chemicals has attracted academic and industrial attention for several decades (Böhmer et al., 2017; Mellor et al., 2017). Such photo-bioprocesses are currently confined to the production of niche market products, including astaxanthin and β -carotene, with product prices within the range of 100–1,000 €/kg (Pulz and Gross, 2004; Spolaore et al., 2006; Posten, 2009; Fernandes et al., 2015; Fernández et al., 2019). The rapid progress in metabolic engineering and synthetic biology tools have broadened the available product spectrum

to exploit cyanobacteria as cell factories (Angermayr et al., 2015; Hays and Ducat, 2015; Erb and Zarzycki, 2016; Gao et al., 2016; Noreña-Caro and Benton, 2018; Sun et al., 2018; Santos-Merino et al., 2019; Mukherjee et al., 2020). However, product titers and volumetric productivities obtained in these proof of concept studies have been very low compared to processes based on heterotrophic hosts such as *E. coli* or *Pseudomonas* (Liang et al., 2018; Santos-Merino et al., 2019).

Some of these challenges could be circumvented by the cultivation of phototrophic organisms in a biofilm format, where cells are naturally immobilized in a self-produced extracellular polymeric matrix. Biofilms, in comparison to suspended cells, allow long retention times for slow-growing phototrophic organisms (Elenter et al., 2007), high tolerance toward toxic chemicals (Rosche et al., 2009; Halan et al., 2016), and generate high cell density (Chang et al., 2014; Hoschek et al., 2019a), resulting in a compact reactor design and continuous operation with high volumetric productivities. In this context, a mixed-species biofilm concept, constituting phototrophic *Synechocystis* sp. PCC 6803 and heterotrophic *Pseudomonas* sp. VLB120 was established in a capillary reactor made from polystyrene (Karande et al., 2018; Hoschek et al., 2019a). This phototrophic biofilm reactor concept reported high cell densities up to 51.8 g_{BDW} L⁻¹. It was successfully used for converting cyclohexane to the corresponding alcohol and resulted in 98% substrate conversion and a stable product flux of 3.76 g m⁻² d⁻¹ for one month.

For the continuous production of chemicals on a technical scale by using phototrophic biofilms, crucial factors are to obtain high and stable volumetric productivities. Additionally, the scale-up of the phototrophic capillary biofilm reactor system based on the numbering-up concept or by using glass monoliths needs to be validated (Ebrahimi et al., 2005; Kreutzer et al., 2005a,b, 2006). One major issue in this respect is the material used for the capillary biofilm reactor. In the above mentioned capillary reactor, polystyrene was used as a cheap and easy to handle material. However, it is subjected to rapid yellowing and embrittlement under UV light, limiting long-term outdoor applications (Yousif and Haddad, 2013). Additionally, this material is susceptible to deformation in the presence of organic solvents (Whelan and Whelan, 1994). Commercial photobioreactors mostly consist of glass due to its high chemical stability, non-solarizing effects during UV-light exposure, resistance to temperature variations, and exceptionally long service life up to 20 years (Burgess et al., 2007). In this work, we aim to evaluate glass as a possible material for capillary reactors and study its impact on mixed-species biofilm development and catalytic performance.

For continuous operation and stable volumetric productivities, biofilm growth and detachment need to be balanced to acquire a defined amount of active biomass within the reactors (Elenter et al., 2007; Rumbaugh and Sauer, 2020). Conversely, significant biofilm detachment events, termed as sloughing, could severely affect biofilm catalytic performance (Morgenroth and Wilderer, 2000; Telgmann et al., 2004). What fraction of mixed-species biofilm detaches in capillary reactors and how these affect the overall performance of a continuous system is not well understood. The objectives of the current

work were (i) to evaluate mixed-species biofilm growth in glass capillaries under single-phase flow and segmented flow conditions (ii) to assess mixed-species biofilm stability based on the detachment process and (iii) to investigate the influence of detachment on the catalytic performance. Two glass materials, quartz and borosilicate glass were selected to study mixed-species biofilm development. The biofilm consisted of a phototrophic *Synechocystis* sp. PCC 6803 and a heterotrophic *Pseudomonas* sp. VLB120, both organisms are harboring a cytochrome P450 monooxygenase for cyclohexanol production from cyclohexane. The average cyclohexanol (CHOL) production rates of 4.72 g_{CHOL} m⁻² d⁻¹ and 4.08 g_{CHOL} m⁻² d⁻¹ could be reached for biofilms grown in quartz and borosilicate capillaries. Nevertheless, the overall biocatalytic performance for mixed-species biofilms in both glass capillaries was influenced by detachment events.

MATERIALS AND METHODS

Chemicals

All Chemicals used for medium preparation were purchased from Carl-Roth GmbH (Karlsruhe, Germany), Merck (Darmstadt, Germany) in the highest purity available. Cyclohexane ($\geq 99.8\%$ purity) was obtained from Merck (Darmstadt, Germany), and cyclohexanone and cyclohexanol, $\geq 99.5\%$ purity, were purchased from Sigma-Aldrich (Steinheim, Germany).

Bacterial Strains and Plasmids

Bacterial strains and plasmids used in this study are listed in Table 1.

Cultivation of *Synechocystis* sp. PCC6803

Cells were grown in YBG11 medium (10 and 50 mM HEPES depending on the application) without citrate and supplemented with 50 mM NaHCO₃, composition: 1.49 g L⁻¹ NaNO₃, 0.074 g L⁻¹ MgSO₄ 7 H₂O, 0.0305 g L⁻¹ K₂HPO₄, 10 mL L⁻¹ YBG11 trace elements (100x), 0.019 g L⁻¹ Na₂CO₃, 10 or 50 mM HEPES (pH 7.2); YBG11 trace elements (100x): 3.6 g L⁻¹ CaCl₂ 2 H₂O, 0.28 g L⁻¹ boric acid, 0.11 g L⁻¹ MnCl₂ 4 H₂O, 0.02 g L⁻¹ ZnSO₄ 7 H₂O, 0.039 g L⁻¹ Na₂MoO₄ 2 H₂O, 0.007 g L⁻¹ CuSO₄ 5 H₂O,

TABLE 1 | Strains and plasmid used in this study.

Strain	Description	References
<i>Synechocystis</i> sp. PCC 6803	Geographical origin: California, United States; Received from Pasteur Culture Collection of Cyanobacteria (PCC, Paris, France)	Stanier et al., 1971
<i>Pseudomonas</i> sp. VLB120	Wild-type <i>Pseudomonas</i>	Panke et al., 1998
Plasmid		
pCyp	Based on pAH032; CYP, FdR, and FR genes under the control of P _{trc} 10 promoter system, RBS* optimized for <i>Synechocystis</i> sp. PCC 6803 in front of CYP gene	Hoschek et al., 2019b

0.005 g L⁻¹ Co(NO₃)₂ 6 H₂O, 0.162 g L⁻¹ FeCl₃ 6 H₂O, 0.6 g L⁻¹ Na₂EDTA 2 H₂O, 4.2 g L⁻¹ NaHCO₃ (Shcolnick et al., 2007).

Pre-cultures were inoculated using 200 µL of a *Synechocystis* sp. PCC 6803 cryo-stock in 20 mL YBG11 medium (50 mM HEPES) and cultivated in a 100 mL baffled shake flask at 30°C, 50 µE m⁻² s⁻¹ (LED), ambient CO₂ (0.04%), 150 rpm (2.5 cm amplitude), and 75% humidity in an orbital shaker (Multitron Pro shaker, Infors, Bottmingen, Switzerland) for 4 days. This culture was used to inoculate a 20 mL YBG11 main culture to a starting OD₇₅₀ of 0.08 and furthermore incubated for 4 days under the same conditions.

Cultivation of *Pseudomonas* sp. VLB120

Overnight cultures were inoculated directly from a 10% glycerol stock and used for inoculation of 5 mL lysogeny broth medium (Bertani, 1951) grown at 30°C and 200 rpm (2.5 cm amplitude) in a Multitron Pro shaker (Infors). 20 mL of M9* medium (Sambrook et al., 2001) pre-cultures were inoculated (1% v/v) from this overnight culture and incubated for 24 h in 100 mL baffled shake flasks. Minimal medium main cultures were subsequently inoculated to an OD₄₅₀ of 0.2 and grown under the same conditions for 8 h in 20 mL M9* medium.

Pre-mixing of Bacterial Strains

The optical density of each prepared main culture (*Synechocystis* sp. PCC 6803 and *Pseudomonas* sp. VLB120) was measured and the culture completely utilized for the pre-mixing, concentrated by centrifugation (5000 × g, 4°C, 7 min), and resuspended in 2 mL YBG11 medium (w/o citrate, 50 mM HEPES, 50 mM NaHCO₃, Kanamycin 50 µg mL⁻¹). The mixed culture was inoculated in 20 mL YBG11 medium (w/o citrate, 50 mM HEPES, 50 mM NaHCO₃) from the resulting cell suspensions to an OD₇₅₀ and OD₄₅₀ value of 1, cultivated in a 100 mL baffled shake flask and incubated at 30°C, 50 µmol m⁻² s⁻¹ (LED), ambient CO₂ (0.04%), 150 rpm (2.5 cm amplitude), and 75% humidity in a Multitron Pro shaker (Infors) for 24 h.

Capillary Reactor System Setup

Biofilms were cultivated in the capillary reactor system (Supplementary Figure S1A), as previously described (Heuschkel et al., 2019). Quartz (wall thickness (w.th.) 1 mm, inner diameter (i.d.) 3 mm) and borosilicate glass tubes (w.th. 1 mm, i.d. 3.5 mm) were cut to a length of 20 cm to serve as capillary reactors. YBG11 medium (10 mM HEPES, 50 mM NaHCO₃) was supplied via Tygon tubing (LMT-55, 2.06 mm i.d., 0.88 mm w.th., Ismatec, Wertheim, Germany) using a peristaltic pump (ISM945D, Ismatec, Wertheim, Germany). The reactor system was inoculated by syringes through injection ports (ibidi GmbH, Martinsried, Germany) established in front of the capillary. Gas exchange for medium inlet as well as outlet and air segment generation was enabled through sterile filters (0.2 µm, Whatman, Maidstone, United Kingdom). Cultivation was performed at room temperature (RT, 24°C), and fluorescent light tubes were used as a light source (50 µmol m⁻² s⁻¹). When applied for the experiment, the air was introduced into the system via Tygon tubing connected by a T-connector in the form of air segments after 7 days of cultivation.

Inoculation of the Capillary Reactor System

The capillary reactors were inoculated with mixed-species cell suspensions (as described in section “Pre-mixing of Bacterial Strains”) by purging 2 mL of each culture through the injection port. The medium flow was started 15 h after inoculation at a rate of ca. 52 µL min⁻¹ (flow velocity of 0.09–0.12 mm s⁻¹). When appropriate, air segments were started 7 days after inoculation at a rate of ca. 52 µL min⁻¹ (flow velocity of 0.09–0.12 mm s⁻¹), resulting in an increased overall flow rate of ca. 104 µL min⁻¹ in the capillaries.

Cyclohexane Oxyfunctionalization in Capillary Biofilm Reactors

Cyclohexane was supplied via the gas feed. Therefore, the T connector combining air feed with the medium supply was connected to a cyclohexane saturation bottle. A silicone tube was used for cyclohexane diffusion into the feed stream and was submerged in 80 mL cyclohexane in a closed 100 mL Schott glass bottle (Supplementary Figure S1B). Heterologous gene expression in *Pseudomonas* sp. VLB120_pCyp (Ps_CYP) and *Synechocystis* sp. PCC 6803_pCyp (Syn_CYP) of the cytochrome P450 monooxygenase was induced after 39–41 days of cultivation by the addition of 1 mM IPTG to the medium and the cyclohexane feed was connected after one day to the capillary inlet using PTFE tubes. Liquid phase samples (1.2 mL) were collected from the reactor inlet and outlet. One mL sample was directly extracted by vigorous mixing for 2 min with 500 µL of ice-cold diethyl ether (0.2 mM decane as internal standard) followed by centrifugation (17,000 × g, 2 min, RT). The ether phase on top of the aqueous phase was removed, dried using anhydrous Na₂SO₄, and applied for quantification by gas chromatography.

Gas Chromatography (GC) for Cyclohexane, Cyclohexanol and Cyclohexanone Quantification

Ether samples (1 µL) were injected by a PTV injector, programmed with a temperature gradient of 10°C s⁻¹ from 90–300°C into a GC Trace 1310 (Thermo Fisher Scientific) equipped with a TG-5MS capillary column (5% diphenyl/95% dimethyl polysiloxane, 30 m, i.d. 0.25 mm, film thickness: 0.25 µm, Thermo Fisher Scientific). A split ratio of 11 was applied, and the oven temperature profile was set to 40°C for 1 min, 40–80°C at 10°C min⁻¹, 80–320°C at 100°C min⁻¹, and 320°C for 10 min, N₂ was applied as carrier gas (flow rate: 1.5 mL min⁻¹). The flame ionization detector was operated at 320°C, 350 mL min⁻¹ air, 30 mL min⁻¹ makeup gas, and 35 mL min⁻¹ hydrogen gas flow.

O₂ Quantification in Gas and Liquid Phases

Dissolved O₂ in the reactor outlet was quantified by a Clark-type flow-through sensor (OX-500 Oxygen Microsensor, Unisense, Aarhus, Denmark) connected to a microsensor amplifier (Microsensor multimeter, Unisense). When air segments were

used, bubble traps (sealed with a PTFE coated silicone septum, Duran, Mainz, Germany) were attached to the capillary outlet and equilibrated for 24 h. Gas-phase (100 μL) samples were obtained from the bubble traps using gas-tight syringes (Hamilton, Reno, United States) and quantified using a Trace 1310 gas chromatograph (Thermo Fisher Scientific, Waltham, United States). The gas chromatograph was equipped with a TG-BOND Msieve 5A capillary column (30 m, ID: 0.32 mm, film thickness: 30 μm , Thermo Fisher Scientific) and a thermal conductivity detector operating at 100°C with a filament temperature of 300°C and a reference gas flow rate of 4 mL min^{-1} . Argon gas was applied as carrier gas at a constant flow rate of 2 mL min^{-1} . The sample injection temperature was set to 50°C with a split ratio of 2, and the oven temperature was kept constant at 35°C for 3 min.

Determination of Biofilm Dry Weight

For biomass quantifications, the capillary reactor setup was disassembled, and the biomass removed from the tubes. The collected biomass was concentrated by centrifugation (5000 $\times g$, 20°C, 7 min) in pre-dried and weight Pyrex tubes, dried again for 1 week at 80°C in an oven (Model 56, Binder GmbH, Tuttlingen, Germany) and was subsequently weighted.

RESULTS

High Oxygen Amount Impedes Biofilm Development in the Single-Phase Medium Flow Conditions

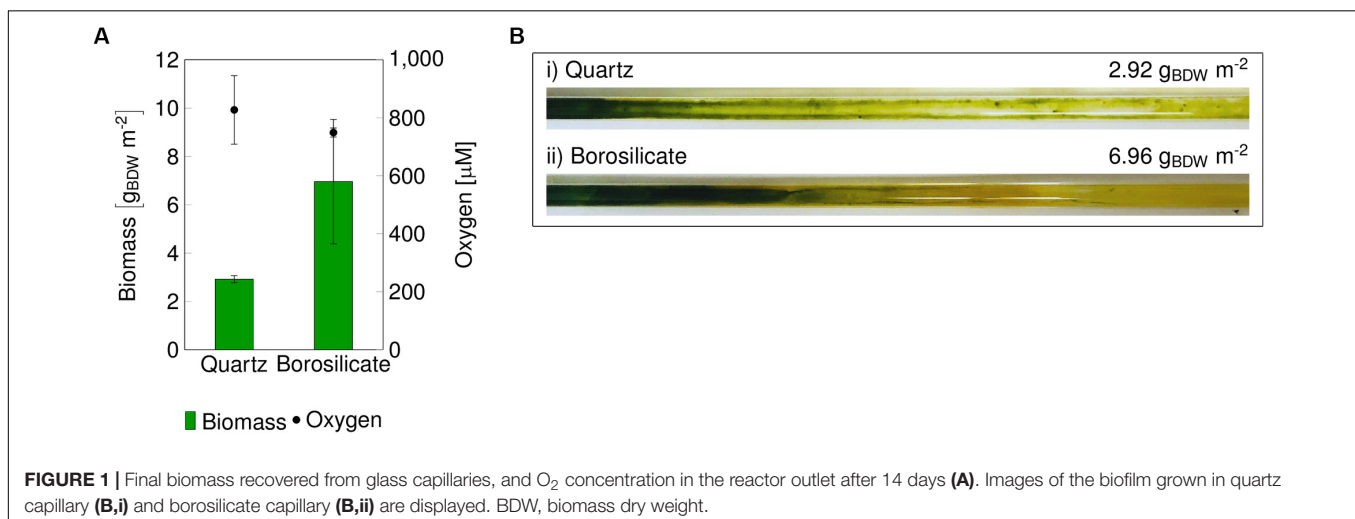
The impact of the capillary material on the mixed-species biofilm development was evaluated by inoculating quartz and borosilicate glass capillaries with a mixed culture (ratio 1:1) of *Synechocystis* sp. PCC 6803 (pCyp) and *Pseudomonas* sp. VLB120 (pCyp). Two biological replicates for each capillary material were analyzed. The system was operated with a continuous feed of aqueous medium supplied at a flow velocity of 0.09–0.12 mm

s^{-1} for 14 days (Supplementary Figure S2). Oxygen evolution and total biomass formation were determined at the end of the experiment (Figure 1A).

In both materials, biofilm formation followed a gradient from sufficient growth in the beginning to weak growth toward the end of the capillary. The color of the biofilm changed accordingly from dark green to yellow and reflected the viability of *Synechocystis*, which tends to “bleach” when the organism is stressed or starved. Oxygen accumulated over the capillary length and a maximum oxygen amount of $748 \pm 16 \mu\text{mol L}^{-1}$ was measured in the medium phase at the end of the borosilicate capillaries. Only 6.96 g biomass dry weight (BDW) m^{-2} developed under these conditions. The saturation concentration of O_2 in water at 25°C corresponds to 276 $\mu\text{mol L}^{-1}$ indicating a pronounced oxygen oversaturation within such capillary reactors. With the highest O_2 concentration of $827 \pm 118 \mu\text{mol L}^{-1}$ in the quartz capillary, the biofilm turned to a bright yellow color with the lowest biomass content 2.92 g_{BDW} m^{-2} compared to the borosilicate capillary reactor (Figure 1B). A similar effect of high O_2 concentrations causing a weak development of the mixed-species biofilm in polystyrene capillaries was described in the previous study (Hoschek et al., 2019a). The transition of biofilm color from light green to yellow indicates impairment of photosystem II and associated photo-pigments (Latifi et al., 2009; Hoschek et al., 2019a) due to oxygen oversaturation. Strategies to overcome oxygen stress are necessary to develop high cell density (HCD) phototrophic biofilms.

Air Segments Relieve High Oxygen Stress but Facilitate Biofilm Flush Outs in Glass Capillaries

In both glass capillary materials, the mixed-species biofilm grown in single-phase medium flow produced high amounts of O_2 , subsequently restricting biofilm growth. In order to relieve the oxidative stress imposed by O_2 , air segments were introduced into the medium flow. Within 24 h, the biofilm started to turn



from yellow to green (**Supplementary Figure S3**), indicating that the high O_2 concentration was being relieved, and the impairment of the photosystem II and associated photo-pigments was reversible. The segmented flow resulted in the complete surface coverage by the dark green biofilm within 7 days (**Figure 2**). After the biofilm was well grown, large biofilm parts were detached in both capillaries (**Figure 2**). The detachment of large biofilm chunks was frequently identified at the rear part of the capillary, and the amount of detached biofilm varied profoundly (**Figure 2**). In these experiments sloughing events were observed after a total of 14 days of biofilm cultivation. After the detachment, the biofilm regenerated itself, which under these conditions took one to two weeks after the sloughing events to achieve maximum surface coverage.

Overall, four phases of mixed-species biofilm growth and development could be distinguished in glass capillaries. Phase 1 includes mixed-species biofilm growth under single-phase flow for 6–7 days. In this phase, the biofilm growth and development are limited due to oversaturated oxygen in the aqueous phase. In phase 2, the start of air-segments relieved oxygen stress and resulted in a rapid increase of biofilm spatial coverage. Phase 3 begins with the sloughing of large biofilm patches from well-grown biofilms. Whereas, phase 4 consists of biofilm regrowth and the expansion of the spatial coverage. When cultivated further, phases 3 and 4 were observed to be recurring.

Stable Biocatalytic Performance of Mixed-Species Biofilms in Both Glass Materials Are Affected by Sloughing Events

The catalytic performance of biofilms is strongly associated with its development phases (Elenter et al., 2007). Therefore, we evaluated mixed-species catalytic performance at different biofilm developmental phases. The mixed-species biofilm was grown as described above, and the biotransformation was initiated for mixed-species biofilms at a matured state (phase 2). The product formation was measured for 13 days (**Figures 3B,C**).

In comparison to the previous experiments (**Figure 2**), phase 2 was prolonged up to day 50–54 for both glass capillaries (**Figure 3**). The reason for this difference in the time interval is not clear.

In both capillaries, the production rate was at a maximum at the start and dropped to $1.0\text{--}1.2\text{ g m}^{-2}\text{ d}^{-1}$ within the next 8 to 10 days. No detachments were recorded directly after starting the cyclohexane (CHX) feed. The average cyclohexanol (CHOL) production rate was $4.72\text{ gCHOL m}^{-2}\text{ d}^{-1}$ for 10 days of biotransformation in the quartz capillary and $4.08\text{ gCHOL m}^{-2}\text{ d}^{-1}$ for the first 8 days in the borosilicate capillary. The overoxidation of CHOL to cyclohexanone (CHON) was observed in both glass capillaries to be around 13%. In the quartz capillary, minor biofilm detachments were observed on day 52, leading to a drop in total product amount from 1.25 to 1.01 mM. On day 54, most parts of the biofilm were flushed out (**Figure 3A**), and the total production rate dropped to $0.93\text{ g m}^{-2}\text{ d}^{-1}$.

In the borosilicate glass tube, two-third of the biofilm was detached at day 51, leading to a drop in the cyclohexanol production rate from $3.70\text{ gCHOL m}^{-2}\text{ d}^{-1}$ to $1.94\text{ gCHOL m}^{-2}\text{ d}^{-1}$. Further decrease in the production rate to $1.27\text{ gCHOL m}^{-2}\text{ d}^{-1}$ was identified on day 54. Overall, the total product formation in quartz glass was slightly higher (17%) than the borosilicate glass. Nevertheless, sloughing events were observed in both glass capillaries, resulting in a severe loss of biomass and subsequently production rates.

Biofilm Regrowth in Borosilicate Capillaries in the Presence of Cyclohexane Leads to High Productivities

In these experiments, we investigated mixed-species biofilm growth and biocatalytic performance after biofilm sloughing events (phase 3). As no major difference was observed for biofilm growth and development in both glass materials, borosilicate was chosen for further experiments. A significant portion of biofilm detached after 36–39 days (**Figure 4A**) due to sloughing.


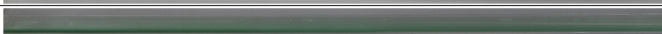



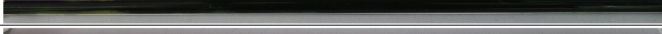



Description	Day	Image	→ flow
Inoculation	0		
	1		
Phase 1	6		
	7		
Phase 2	13		
	14		
Phase 3	18		
	19		
Phase 4	24		

FIGURE 2 | Four stages of biofilm development in a quartz glass capillary. The biofilm was grown without air segments for 7 days (phase 1) with a medium flow velocity of $0.09\text{--}0.12\text{ mm s}^{-1}$, and air segments were started subsequently at the same flow rate (phase 2), which led to a fast surface coverage of the entire capillary (phase 2, 13 days total cultivation). After that, sloughing events (phase 3) and biofilm regrowth were observed (phase 4).

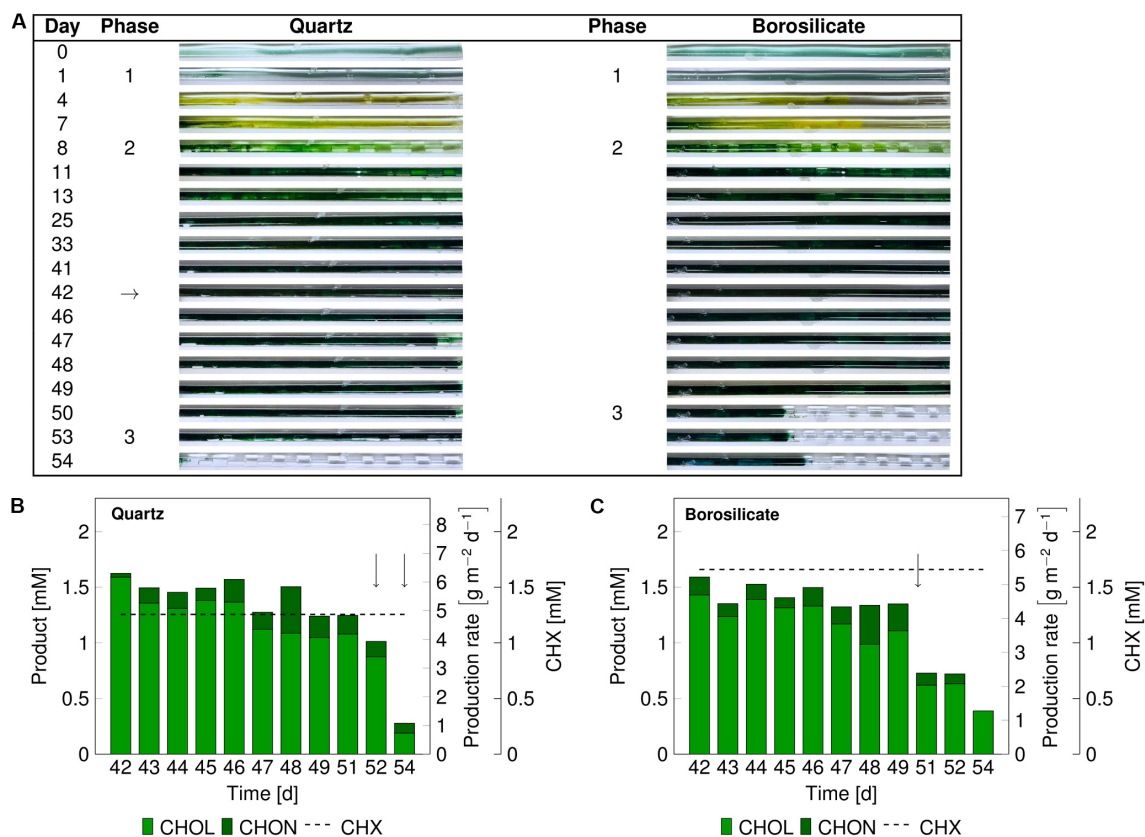


FIGURE 3 | Images of the mixed-species biofilm cultivated in quartz and borosilicate glass capillaries. Flush outs were observed after 50 days of biofilm cultivation in both capillaries (**A**). Medium and air segments (from day 8 on) were fed at a flow velocity of 0.09–0.12 mm s⁻¹. The biotransformation was introduced after 42 days (arrow panel **A**), and the product formation recorded (panels **B,C**). The cyclohexane feed is represented as a dashed line for the quartz capillary at 1.35 ± 0.42 mM and the borosilicate capillary at 1.63 ± 0.45 mM. The arrows in panels (**B,C**) indicate sloughing effects. CHX-cyclohexane.

The biotransformation was initiated on day 41. Under the biotransformation conditions, the biofilms were able to recover completely in the following 7 days.

In the borosilicate capillary 1, the cyclohexanol production rate increased from 1.75 g_{CHOL} m⁻² d⁻¹ to 6.4 g_{CHOL} m⁻² d⁻¹, and it reached a steady-state after day 45 (**Figure 4B**). In this case, the system seemed to be CHX limited, as 98% of the supplied substrate was converted. In the borosilicate capillary 2, the cyclohexanol production rate increased from 1.8 g_{CHOL} m⁻² d⁻¹ to 4.89 g_{CHOL} m⁻² d⁻¹ from day 41 to 48, respectively (**Figure 4C**). Here, the system was not CHX limited, as only 76% of the CHX feed was converted. In both cases, minor amounts (3–4%) of the overoxidation product CHON were detected.

At day 49 and 55, the light was turned off to investigate the impact of photosynthesis on the heterologous reaction. During the first dark period, the O₂ concentration in the air phase dropped by 5.0% and 3.7% in capillary 1 and 2, respectively (**Supplementary Figure S4**). Additionally, the product amount in the outflow was significantly reduced below 0.15 mM in both capillaries. Similar effects of the drop in O₂ and CHOL production were seen during the second dark period on day 55. These results led to the conclusion that electrons provided by photosynthetic water splitting fueled the biotransformation

reaction. After the regrowth of the biofilms in both capillaries under biotransformation conditions, sloughing effects were detected again. This detachment resulted in a significant drop in the product concentration on day 57 and 53 in the capillary 1 and 2, respectively. Overall, we could conclude that the catalytic performance of mixed-species biofilm is dependent on the amount of available biomass with the capillary system.

DISCUSSION

Cyanobacteria are considered to be promising microorganisms for converting CO₂, water, and solar radiation into value-added chemicals (Wijffels et al., 2013; Fernandes et al., 2015; Fernández et al., 2019). The capability of cyanobacteria to assimilate CO₂ depends primarily on the catalytic properties of the ribulose-1,5-bisphosphate carboxylase/oxygenase (Rubisco) (Tcherkez, 2016). However, Rubisco's inability to discriminate between O₂ and CO₂ results in carboxylation and oxygenase activity, depending on their concentrations and the kinetic parameters (Liang et al., 2018; Flamholz et al., 2019). As oxygen is continuously generated in the oxygenic photosynthesis during the light reaction, its amount within the photosynthetic cell is considered to be

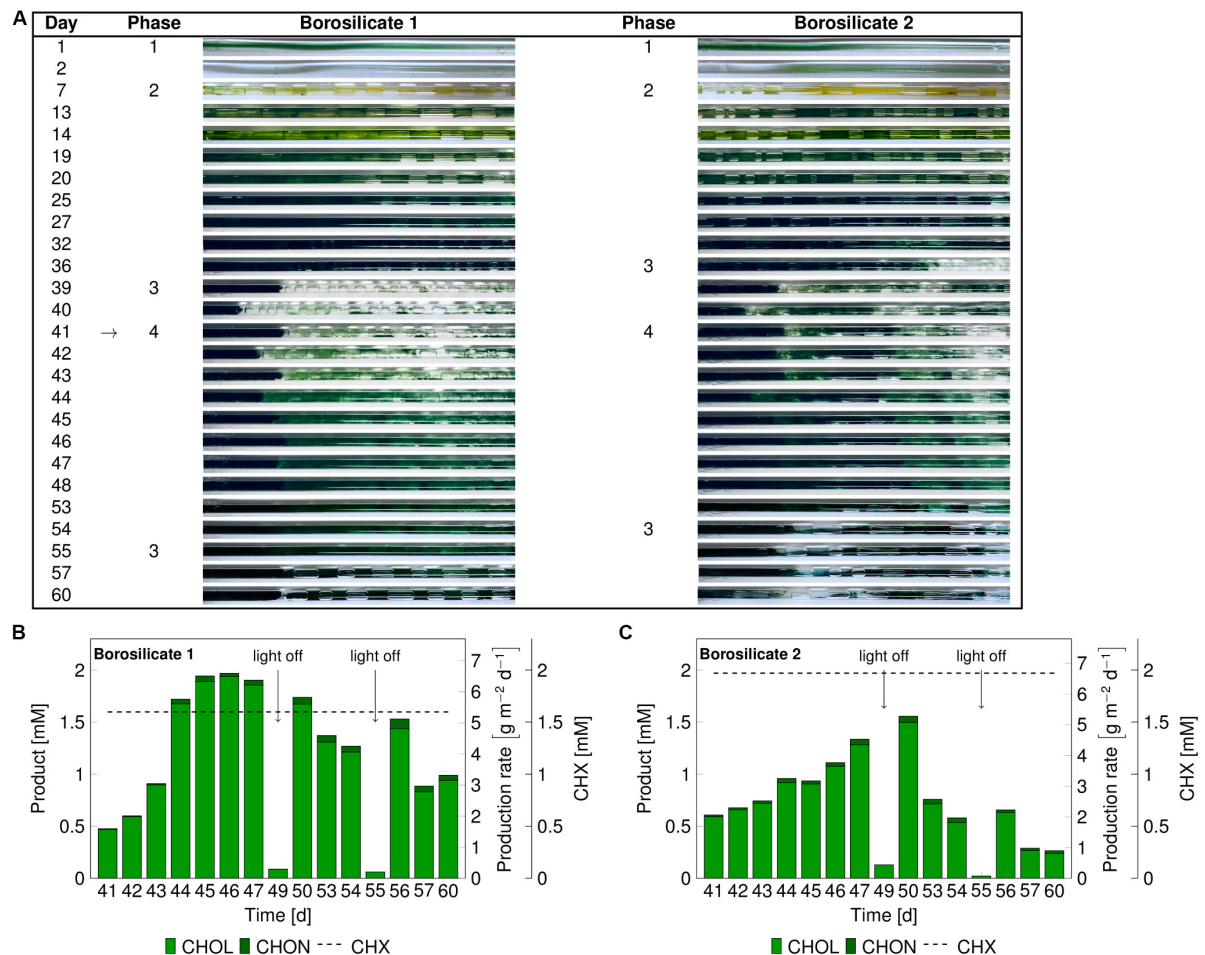


FIGURE 4 | Images of the mixed-species biofilm cultivated in borosilicate capillaries (A). Flush outs were found after 36 days, the biotransformation was initiated after 41 days (arrow panel A) and product formation recorded (panels B,C). Medium and air segments (from day 7 on) were fed at a flow velocity of 0.09–0.12 mm s⁻¹. The cyclohexane feed was visualized as a dashed line for capillary 1 at 1.60 ± 0.3 mM and for capillary 2 at 1.97 ± 0.70 mM. The arrows in panel (B,C) indicate light-off conditions. Abbreviation: CHX-cyclohexane.

higher than the ambient oxygen level (Kihara et al., 2014). Excess oxygen concentration in the functional photosynthetic cells not only affects the net carboxylation rate but can form reactive oxygen species (ROS), leading to oxidative damage of DNA, lipids, and proteins. In contrast to the suspended format, cyanobacterial cells growing in biofilms or microbial mats could reach oxygen concentrations several times higher (ca. 1000 μM) than the air-saturated water resulting in oxygen bubble formation (Jorgensen et al., 1983; Revsbech et al., 1983; Bosak et al., 2010). Correspondingly, we observed high oxygen amount of 748 to 827 μM in the reactor outflow (Figure 1). Under such high oxygen content, the development of the mixed-species cyanobacterial (Syn. sp. PCC6803) biofilms were severely affected, leading to low biomass concentration in the glass capillaries.

In the previous work, high oxidative stress was overcome by introducing air segments, utilizing citrate catabolism in *Pseudomonas* species, and an oxygen-dependent biotransformation reaction to enable HCD mixed-species

phototrophic biofilms in polystyrene capillary reactor (Hoschek et al., 2019a). In this work, air segments were introduced into the medium flow to extract excess O₂ from the biofilm and thereby to relieve oxidative stress imposed onto the cells. Overcoming the stress resulted in thick and dense biofilm growth (Figure 2). However, the mixed-species phototrophic biofilm growth and development in the glass capillaries showed four distinct phases based on the investigated time frame as compared to only two phases in polystyrene capillary reactors (Hoschek et al., 2019a).

Biofilm Sloughing: A Critical Issue in the Development of Stable Mixed-Species Biofilm

Biofilm development is characterized by constant removal of cells from the biofilm either when small portions of the biofilm are lost by frictional forces (erosion) or when large fractions are lost based on sloughing events (Rumbaugh and Sauer, 2020).

TABLE 2 | Comparison of literature data for cyclohexanol production from cyclohexane.

Biofilm	Capillary material	Average space-time yield [$\text{g}_{\text{CHOL}} \text{m}_{\text{tube}}^{-2} \text{d}^{-1}$] ($[\text{g}_{\text{CHOL}} \text{L}_{\text{tube}}^{-1} \text{h}^{-1}]$)	Stability [d]	Electron donor	Remark	References
<i>Pseudomonas</i> sp. VLB 120	Silicone tube	4.8 (0.4)	18	Yeast extract	Organic carbon	Karande et al., 2016
Mixed species ^a	Polystyrene	3.8 (0.2)	31	Water	Minimal medium, no organic carbon	Hoschek et al., 2019a
Mixed species ^a	Quartz glass	4.72 (0.3)	10	Water	Minimal medium, no organic carbon	This study
Mixed species ^a	Borosilicate glass	4.08 (0.2)	8	Water	Minimal medium, no organic carbon	This study

^aMixed species biofilm *Synechocystis* sp. PCC6803 and *Pseudomonas* sp. VLB120.

Sloughing is considered to be an integral part of biofilm development (Telgmann et al., 2004), which could lead to a loss of more than 90% biomass within one day (Figure 2). A similar event was described by Telgmann et al. (2004), where 80% of biomass was lost due to the detachment of large biofilm portions. Reasons for sloughing are widespread. These include shear stresses, nutrient to oxygen gradients as well as a change in c-di-GMP levels inside the biofilm, e.g., by c-di-GMP-degradation (Hunt et al., 2004; Thormann et al., 2006; Stewart and Franklin, 2008; Rumbaugh and Sauer, 2020). In the mixed-species biofilm, the change in biomass and thickness with the biofilm growth (phase 2) in glass capillaries could increase (aqueous-air) segmented flow velocity and subsequently intensify shear stresses and aqueous-air interfacial forces. These external fluidic forces might become more substantial than the biofilm adhesive forces leading to the sloughing or detachment (Stoodley et al., 2002; Horn et al., 2003; Sharma et al., 2005; Paul et al., 2012). However, such events were not frequently observed in polystyrene capillaries (Hoschek et al., 2019a). This outcome points out that mixed-species biofilms have weakly adhered to glass capillaries as compared to the polystyrene capillary. There is also a possibility that biofilm adhesion to the glass surfaces becomes weaker with growth due to nutrient starvation or a different stress response of the biofilm. In the mixed-species biofilm, we observed yellow locations at the bottom of biofilm (Figure 2). These color changes (green to yellow) might indicate nutrient starvation or oxidative stress because of high local O_2 concentrations. Such stresses might weaken the cell attachment and overall biofilm structure, leading to biofilm dispersion and subsequent detachment (Ohashi and Harada, 1995; Bazin and Prosser, 2018). Overall, the increase of external fluidic forces with biofilm growth and the decrease of internal biofilm strength caused by the hydrolysis of the polymeric biofilm matrix or due to oxidative stresses could be possible reasons for biofilm sloughing.

Biofilm Sloughing Severely Affects Mixed-Species Catalytic Performance

Sloughing may have two different effects on the product formation rate: (I) No impact on reactor performance, when only inactive biomass is lost, (II) severe impact on reactor performance due to the removal of active biomass (Elenter et al., 2007). In our experiments, sloughing was observed after the mixed-species biofilm reached a well-grown or matured stage, and this detachment was accompanied by a severe drop in the catalytic

activity (Figures 3, 4). These results conclude that the lost biofilm consisted mainly of active biomass. An average production rate of $4.72 \text{ g}_{\text{CHOL}} \text{m}^{-2} \text{d}^{-1}$ ($7.18 \text{ g L}^{-1} \text{d}^{-1}$) could be reached for a maximum of 10 days for the biofilm grown in the quartz glass capillary (Table 2).

Still, for a continuous biofilm-based process, 10 days of stable biocatalytic performance is considerably short. Our previous study reported a stable production rate of $3.8 \text{ g}_{\text{CHOL}} \text{m}^{-2} \text{d}^{-1}$ for 31 days in a capillary reactor made from polystyrene (Karande et al., 2018; Hoschek et al., 2019a). In comparison to polystyrene capillaries, the glass surface has little texture, with an average roughness of 100 nm (for borosilicate glass) (Preedy et al., 2014). Here, a rougher surface might promote biofilm attachment and resistance against hydrodynamic forces to minimize sloughing events (Picioreanu et al., 2000). Furthermore, the light focusing effect of the glass-capillaries (Posten, 2009) might lead to increased light input resulting in high photosynthetic activity and enhanced O_2 accumulation. Such high oxygen content could trigger sloughing events and, therefore, biofilm growth and development at different light intensities (low $25 \mu\text{E m}^{-2} \text{s}^{-1}$, high $100 \mu\text{E m}^{-2} \text{s}^{-1}$) or with light-dark cycles need to be investigated to minimize sloughing events and retain constant production rates in glass capillaries.

CONCLUSION

We observed four-phases for mixed-species biofilm growth in the glass-capillaries. It comprises biofilm growth, detachment, and regrowth. The change in flow condition from single to aqueous-air segmented flow resulted in faster growth, improved surface coverage, and enhanced biomass formation. For mature biofilms, biofilm detachment via sloughing and regrowth was frequently observed in glass capillaries. The biocatalytic performance of mixed-species was evaluated at different developmental phases. For mature biofilms, an average production rate of $4.72 \text{ g}_{\text{CHOL}} \text{m}^{-2} \text{d}^{-1}$ for 10 days and $4.08 \text{ g}_{\text{CHOL}} \text{m}^{-2} \text{d}^{-1}$ for 8 days were obtained for quartz and borosilicate glass, respectively. Product formation was associated with biofilm biomass and increased with the re-growing biofilm. Maximum product formation of $6.5 \text{ g m}^{-2} \text{d}^{-1}$ was observed in the borosilicate capillary, although both glass types showed comparable results. The presence of the toxic substrate cyclohexane did not hamper biofilm growth and spatial coverage. The utilization of glasses as capillary reactor materials offers several benefits, such as the light focusing

effect and excellent stability against solvents or UV radiation. Nevertheless, sloughing events were observed to be higher compared to other capillary materials, e.g., polystyrene (Hoschek et al., 2019a). Therefore, future research efforts on understanding sloughing mechanisms in the mixed-species biofilms and finding solutions to minimize them in glass capillaries are necessary.

DATA AVAILABILITY STATEMENT

The raw data supporting the conclusions of this article will be made available by the authors, without undue reservation.

AUTHOR CONTRIBUTIONS

RD and IH planned and conducted the experimental work and analyzed data. IH wrote the manuscript. RK and KB participated in designing experiments, data analysis, and correcting the manuscript. All authors contributed to the article and approved the submitted version.

REFERENCES

- Angermayr, S. A., Rovira, A. G., and Hellingwerf, K. J. (2015). Metabolic engineering of cyanobacteria for the synthesis of commodity products. *Trends Biotechnol.* 33, 352–361. doi: 10.1016/j.tibtech.2015.03.009
- Bazin, M. J., and Prosser, J. I. (2018). *Physiological Models in Microbiology*, Vol. 2. Boca Raton, FL: CRC revivals.
- Bertani, G. (1951). Studies on lysogeny. I. The mode of phage liberation by lysogenic *Escherichia coli*. *J. Bacteriol.* 62, 293–300. doi: 10.1128/JB.62.3.293-300.1951
- Böhmer, S., Köninger, K., Gómez-Baraibar, Á., Bojarrá, S., Mügge, C., Schmidt, S., et al. (2017). Enzymatic oxyfunctionalization driven by photosynthetic water-splitting in the cyanobacterium *Synechocystis* sp. PCC6803. *Catalysts* 7:240. doi: 10.3390/catal7080240
- Bosak, T., Bush, J. W. M., Flynn, M. R., Liang, B., Ono, S., Petroff, A. P., et al. (2010). Formation and stability of oxygen-rich bubbles that shape photosynthetic mats. *Geobiology* 8, 45–55. doi: 10.1111/j.1472-4669.2009.00227.x
- Burgess, G., Fernández-Velasco, J. G., and Lovegrove, K. (2007). Materials, geometry, and net energy ratio of tubular photobioreactors for microalgal hydrogen production. *Int. J. Hydrog. Energy* 32, 1225–1234. doi: 10.1016/j.ijhydene.2006.10.055
- Chang, H. N., Jung, K., Choi, J., Lee, J. C., and Woo, H. C. (2014). Multi-stage continuous high cell density culture systems: a review. *Biotechnol. Adv.* 32, 514–525. doi: 10.1016/j.biotechadv.2014.01.004
- Ebrahimi, S., Picioreanu, C., Xavier, J. B., Kleerebezem, R., Kreutzer, M., Kapteijn, F., et al. (2005). Biofilm growth pattern in honeycomb monolith packings: effect of shear rate and substrate transport limitations. *Catal. Today* 105, 448–454. doi: 10.1016/j.cattod.2005.06.051
- Elenter, D., Milferstedt, K., Zhang, W., Hausner, M., and Morgenroth, E. (2007). Influence of detachment on substrate removal and microbial ecology in a heterotrophic/autotrophic biofilm. *Water Res.* 41, 4657–4671. doi: 10.1016/j.watres.2007.06.050
- Erb, T. J., and Zarzycki, J. (2016). Biochemical and synthetic biology approaches to improve photosynthetic CO₂ fixation. *Curr. Opin. Chem. Biol.* 34, 72–79. doi: 10.1016/j.cbpa.2016.06.026
- Fernandes, B. D., Mota, A., Teixeira, J. A., and Vicente, A. A. (2015). Continuous cultivation of photosynthetic microorganisms: approaches, applications and future trends. *Biotechnol. Adv.* 33, 1228–1245. doi: 10.1016/j.biotechadv.2015.03.004
- Fernández, F. G. A., Fernández Sevilla, J. M., and Molina Grima, E. (2019). “Costs analysis of microalgae production,” in *Biofuels From Algae*, eds A. Pandey,

FUNDING

IH was funded by the ERA-IB Project PolyBugs ID:16-006 and the Sächsisches Ministerium für Wissenschaft und Kunst (SMWK) Project ID: 100318259.

ACKNOWLEDGMENTS

We acknowledge the use of the facilities of the Centre for Biocatalysis (MiKat) at the Helmholtz Centre for Environmental Research. The Helmholtz Centre for Environmental Research is supported by the European Regional Development Funds (EFRE, Europe funds Saxony) and the Helmholtz Association.

SUPPLEMENTARY MATERIAL

The Supplementary Material for this article can be found online at: <https://www.frontiersin.org/articles/10.3389/fbioe.2020.588729/full#supplementary-material>

- D.-J. Lee, Y. Chisti, and C. R. Soccol (Amsterdam: Elsevier), 551–566. doi: 10.1016/b978-0-444-64192-2.00021-4
- Flamholz, A. I., Prywes, N., Moran, U., Davidi, D., Bar-On, Y. M., Oltrogge, L. M., et al. (2019). Revisiting trade-offs between rubisco kinetic parameters. *Biochemistry* 58, 3365–3376. doi: 10.1021/acs.biochem.9b00237
- Gao, X., Sun, T., Pei, G., and Chen, L. (2016). Cyanobacterial chassis engineering for enhancing production of biofuels and chemicals. *Appl. Microbiol. Biotechnol.* 100, 3401–3413. doi: 10.1007/s00253-016-7374-2
- Halan, B., Karande, R., Buehler, K., and Schmid, A. (2016). Catalytic *Pseudomonas taiwanensis* VLB120ΔC biofilms thrive in a continuous pure styrene generated by multiphasic segmented flow in a capillary microreactor. *J. Flow Chem.* 6, 39–42. doi: 10.1556/1846.2015.00037
- Hays, S. G., and Ducat, D. C. (2015). Engineering cyanobacteria as photosynthetic feedstock factories. *Photosynth. Res.* 123, 285–295. doi: 10.1007/s11120-014-9980-0
- Heuschkel, I., Hoschek, A., Schmid, A., Bühler, B., Karande, R., and Bühler, K. (2019). Mixed-trophies biofilm cultivation in capillary reactors. *MethodsX* 6, 1822–1831. doi: 10.1016/j.mex.2019.07.021
- Horn, H., Reiff, H., and Morgenroth, E. (2003). Simulation of growth and detachment in biofilm systems under defined hydrodynamic conditions. *Biotechnol. Bioeng.* 81, 607–617. doi: 10.1002/bit.10503
- Hoschek, A., Heuschkel, I., Schmid, A., Bühler, B., Karande, R., Bühler, K., et al. (2019a). Mixed-species biofilms for high-cell-density application of *Synechocystis* sp. PCC 6803 in capillary reactors for continuous cyclohexane oxidation to cyclohexanol. *Bioresour. Technol.* 282, 171–178. doi: 10.1016/j.biortech.2019.02.093
- Hoschek, A., Toepel, J., Hochkeppel, A., Karande, R., Bühler, B., Schmid, A., et al. (2019b). Light-dependent and aeration-independent gram-scale hydroxylation of cyclohexane to cyclohexanol by CYP450 harboring *Synechocystis* sp. PCC 6803. *Biotechnol. J.* 14, 1–10. doi: 10.1002/biot.201800724
- Hunt, S. M., Werner, E. M., Huang, B., Hamilton, M. A., and Stewart, P. S. (2004). Hypothesis for the role of nutrient starvation in biofilm detachment. *Appl. Environ. Microbiol.* 70, 7418–7425. doi: 10.1128/AEM.70.12.7418
- Jorgensen, B. B., Revsbech, N. P., and Cohen, Y. (1983). Photosynthesis and structure of benthic microbial mats: microelectrode and SEM studies of four cyanobacterial communities. *Limnol. Oceanogr.* 28, 1075–1093. doi: 10.4319/lo.1983.28.6.1075
- Karande, R., Debor, L., Salamanca, D., Bogdahn, F., Engesser, K. H., Buehler, K., et al. (2016). Continuous cyclohexane oxidation to cyclohexanol using a novel cytochrome P450 monooxygenase from *Acidovorax* sp. CHX100 in

- recombinant *P. taiwanensis* VLB120 biofilms. *Biotechnol. Bioeng.* 113, 52–61. doi: 10.1002/bit.25696
- Karande, R., Hoschek, A., Heuschkel, I., Bühler, K., and Schmid, A. (2018). A composition of photoautotrophic microorganisms and chemoheterotrophic microorganisms in a biofilm. *Biotechnol. Bioeng.* 113, 52–61.
- Kihara, S., Hartzler, D. A., and Savikhin, S. (2014). Oxygen concentration inside a functioning photosynthetic cell. *Biophys. J.* 106, 1882–1889. doi: 10.1016/j.bpj.2014.03.031
- Kreutzer, M. T., Bakker, J. J. W., Kapteijn, F., Moulijn, J. A., and Verheijen, P. J. T. (2005a). Scaling-up multiphase monolith reactors: linking residence time distribution and feed maldistribution. *Ind. Eng. Chem. Res.* 44, 4898–4913. doi: 10.1021/ie0492350
- Kreutzer, M. T., Kapteijn, F., Moulijn, J. A., and Heiszwolf, J. J. (2005b). Multiphase monolith reactors: chemical reaction engineering of segmented flow in microchannels. *Chem. Eng. Sci.* 60, 5895–5916. doi: 10.1016/j.ces.2005.03.022
- Kreutzer, M. T., Kapteijn, F., and Moulijn, J. A. (2006). Shouldn't catalysts shape up? Structured reactors in general and gas-liquid monolith reactors in particular. *Catal. Today* 111, 111–118. doi: 10.1016/j.cattod.2005.10.014
- Latifi, A., Ruiz, M., and Zhang, C. (2009). Oxidative stress in cyanobacteria. *FEMS Microbiol. Rev.* 33, 258–278. doi: 10.1111/j.1574-6976.2008.00134.x
- Liang, F., Englund, E., Lindberg, P., and Lindblad, P. (2018). Engineered cyanobacteria with enhanced growth show increased ethanol production and higher biofuel to biomass ratio. *Metab. Eng.* 46, 51–59. doi: 10.1016/j.ymben.2018.02.006
- Mellor, S. B., Vavitsas, K., Nielsen, A. Z., and Jensen, P. E. (2017). Photosynthetic fuel for heterologous enzymes: the role of electron carrier proteins. *Photosynth. Res.* 134, 329–342. doi: 10.1007/s11120-017-0364-0
- Morgenroth, E., and Wilderer, P. A. (2000). Influence of detachment mechanism on competition in biofilms. *Water Resour.* 34, 417–426. doi: 10.1016/s0043-1354(99)00157-8
- Mukherjee, B., Madhu, S., and Wangikar, P. P. (2020). The role of systems biology in developing non-model cyanobacteria as hosts for chemical production. *Curr. Opin. Biotechnol.* 64, 62–69. doi: 10.1016/j.copbio.2019.10.003
- Noreña-Caro, D., and Benton, M. G. (2018). Cyanobacteria as photoautotrophic biofactories of high-value chemicals. *J. CO₂ Util.* 28, 335–366. doi: 10.1016/j.jcou.2018.10.008
- Ohashi, A., and Harada, H. (1995). Characterization of detachment mode of biofilm developed in an attached-growth reactor. *Water Sci. Technol.* 30, 35–45. doi: 10.2166/wst.1994.0544
- Panke, S., Witholt, B., Schmid, A., and Wubbolts, M. G. (1998). Towards a biocatalyst for (S)-styrene oxide production: characterization of the styrene degradation pathway of *Pseudomonas* sp. strain VLB120. *Appl. Environ. Microbiol.* 64, 2032–2043. doi: 10.1128/aem.64.6.2032-2043.1998
- Paul, E., Ochoa, J. C., Pechaud, Y., Liu, Y., and Line, A. (2012). Effect of shear stress and growth conditions on detachment and physical properties of biofilms. *Water Res.* 46, 5499–5508. doi: 10.1016/j.watres.2012.07.029
- Picioreanu, C., Van Loosdrecht, M. C. M., and Heijnen, J. J. (2000). Two-dimensional model of biofilm detachment caused by internal stress from liquid flow. *Biotechnol. Bioeng.* 72, 205–218. doi: 10.1002/1097-0290(2000120)72:2<205::aid-bit9>3.0.co;2-l
- Posten, C. (2009). Design principles of photo-bioreactors for cultivation of microalgae. *Eng. Life Sci.* 9, 165–177. doi: 10.1002/elsc.200900003
- Preedy, E., Perni, S., Nipic, D., Bohinc, K., and Prokopovich, P. (2014). Surface roughness mediated adhesion forces between borosilicate glass and gram-positive bacteria. *Langmuir* 30, 9466–9476. doi: 10.1021/la501711t
- Pulz, O., and Gross, W. (2004). Valuable products from biotechnology of microalgae. *Appl. Microbiol. Biotechnol.* 65, 635–648. doi: 10.1007/s00253-004-1647-x
- Revsbech, N. P., Jørgensen, B. B., Blackburn, T. H., and Cohen, Y. (1983). Microelectrode studies of the photosynthesis and O₂, H₂S, and pH profiles of a microbial mat. *Limnol. Oceanogr.* 28, 1062–1074. doi: 10.4319/lo.1983.28.6.1062
- Rosche, B., Li, X. Z., Hauer, B., Schmid, A., and Buehler, K. (2009). Microbial biofilms: a concept for industrial catalysis? *Trends Biotechnol.* 27, 636–643. doi: 10.1016/j.tibtech.2009.08.001
- Rumbaugh, K. P., and Sauer, K. (2020). Biofilm dispersion. *Nat. Rev. Microbiol.* doi: 10.1038/s41579-020-0385-0
- Sambrook, J., Russell, D. W., and Maniatis, T. (2001). *Molecular Cloning: A Laboratory Manual*, 3rd Edn. Cold Spring Harbor, NY: Cold Spring Harbor Laboratory Press.
- Santos-Merino, M., Singh, A. K., and Ducat, D. C. (2019). New applications of synthetic biology tools for cyanobacterial metabolic engineering. *Front. Bioeng. Biotechnol.* 7:33. doi: 10.3389/fbioe.2019.00033
- Sharma, P. K., Gibcus, M. J., Van Der Mei, H. C., and Busscher, H. J. (2005). Influence of fluid shear and microbubbles on bacterial detachment from a surface. *Appl. Environ. Microbiol.* 71, 3668–3673. doi: 10.1128/AEM.71.7.3668-3673.2005
- Shcolnick, S., Shaked, Y., and Kelenn, N. (2007). A role for mrgA, a DPS family protein, in the internal transport of Fe in the cyanobacterium *Synechocystis* sp. PCC6803. *Biochim. Biophys. Acta Bioenerget.* 1767, 814–819. doi: 10.1016/j.bbabo.2006.11.015
- Spolaore, P., Joannis-Cassan, C., Duran, E., and Isambert, A. (2006). Commercial applications of microalgae. *J. Biosci. Bioeng.* 101, 87–96. doi: 10.1263/jbb.101.87
- Stanier, R. Y., Kunisawa, R., Mandel, M., and Cohen-Bazire, G. (1971). Purification and properties of unicellular blue-green algae (Order Chroococcales). *Bacteriol. Rev.* 35, 171–205. doi: 10.1016/j.jbictoc.2013.07.020
- Stewart, P. S., and Franklin, M. J. (2008). Physiological heterogeneity in biofilms. *Nat. Rev. Microbiol.* 6, 199–210. doi: 10.1038/nrmicro1838
- Stoodley, P., Cargo, R., Rupp, C. J., Wilson, S., and Klapper, I. (2002). Biofilm material properties as related to shear-induced deformation and detachment phenomena. *J. Ind. Microbiol. Biotechnol.* 29, 361–367. doi: 10.1038/sj.jim.7000282
- Sun, T., Li, S., Song, X., Diao, J., Chen, L., and Zhang, W. (2018). Toolboxes for cyanobacteria: recent advances and future direction. *Biotechnol. Adv.* 36, 1293–1307. doi: 10.1016/j.biotechadv.2018.04.007
- Tcherkez, G. (2016). The mechanism of Rubisco-catalysed oxygenation. *Plant Cell Environ.* 39, 983–997. doi: 10.1111/pce.12629
- Telgmann, U., Horn, H., and Morgenroth, E. (2004). Influence of growth history on sloughing and erosion from biofilms. *Water* 38, 3671–3684. doi: 10.1016/j.watres.2004.05.020
- Thormann, K. M., Duttler, S., Saville, R. M., Hyodo, M., Shukla, S., Hayakawa, Y., et al. (2006). Control of formation and cellular detachment from *Shewanella oneidensis* MR-1 biofilms by cyclic di-GMP. *J. Bacteriol.* 188, 2681–2691. doi: 10.1128/JB.188.7.2681
- Whelan, A., and Whelan, T. (1994). *Polymer Technology Dictionary*. Berlin: Springer Science & Business Media.
- Wijffels, R. H., Kruse, O., and Hellingwerf, K. J. (2013). Potential of industrial biotechnology with cyanobacteria and eukaryotic microalgae. *Curr. Opin. Biotechnol.* 24, 405–413. doi: 10.1016/j.copbio.2013.04.004
- Yousif, E., and Haddad, R. (2013). Photodegradation and photostabilization of polymers, especially polystyrene: review. *SpringerPlus* 2:398. doi: 10.1186/2193-1801-2-398

Conflict of Interest: The authors declare that the research was conducted in the absence of any commercial or financial relationships that could be construed as a potential conflict of interest.

Copyright © 2020 Heuschkel, Dagini, Karande and Bühler. This is an open-access article distributed under the terms of the Creative Commons Attribution License (CC BY). The use, distribution or reproduction in other forums is permitted, provided the original author(s) and the copyright owner(s) are credited and that the original publication in this journal is cited, in accordance with accepted academic practice. No use, distribution or reproduction is permitted which does not comply with these terms.



Integrated Continuous Bioprocess Development for ACE-Inhibitory Peptide Production by *Lactobacillus helveticus* Strains in Membrane Bioreactor

Cyril Raveschot^{1,2}, Barbara Deracinois¹, Emmeline Bertrand¹, Christophe Flahaut¹, Marc Frémont², Djamel Drider¹, Pascal Dhulster¹, Benoit Cudennec¹ and François Coutte^{1*}

¹ UMR Transfrontalière BioEcoAgro N° 1158, Université de Lille, INRAE, Université de Liège, UPJV, YNCREA, Université d'Artois, Université du Littoral Côte d'Opale, ICV – Institut Charles Viollette, Lille, France, ² VF Bioscience, Loos-lez-Lille, France

OPEN ACCESS

Edited by:

Christoph Slouka,
Vienna University of Technology,
Austria

Reviewed by:

Surajit Mandal,
West Bengal University of Animal
and Fishery Sciences, India
Amar Ashok Sakure,
Anand Agricultural University, India

*Correspondence:

François Coutte
francois.coutte@univ-lille.fr;
francois.coutte@polytech-lille.fr

Specialty section:

This article was submitted to
Bioprocess Engineering,
a section of the journal
Frontiers in Bioengineering and
Biotechnology

Received: 21 July 2020

Accepted: 31 August 2020

Published: 25 September 2020

Citation:

Raveschot C, Deracinois B,
Bertrand E, Flahaut C, Frémont M,
Drider D, Dhulster P, Cudennec B and
Coutte F (2020) Integrated
Continuous Bioprocess Development
for ACE-Inhibitory Peptide Production
by *Lactobacillus helveticus* Strains
in Membrane Bioreactor.
Front. Bioeng. Biotechnol. 8:585815.
doi: 10.3389/fbioe.2020.585815

Production of bioactive peptides (BAPs) by *Lactobacillus* species is a cost-effective approach compared to the use of purified enzymes. In this study, proteolytic *Lactobacillus helveticus* strains were used for milk fermentation to produce BAPs capable of inhibiting angiotensin converting enzyme (ACE). Fermented milks were produced in bioreactors using batch mode, and the resulting products showed significant ACE-inhibitory activities. However, the benefits of fermentation in terms of peptide composition and ACE-inhibitory activity were noticeably reduced when the samples (fermented milks and non-fermented controls) were subject to simulated gastrointestinal digestion (GID). Introducing an ultrafiltration step after fermentation allowed to prevent this effect of GID and restored the effect of fermentation. Furthermore, an integrated continuous process for peptide production was developed which led to a 3 fold increased peptide productivity compared to batch production. Using a membrane bioreactor allowed to generate and purify in a single step, an active ingredient for ACE inhibition.

Keywords: ACE-inhibitory peptides, fermented milk, gastrointestinal digestion, *Lactobacillus*, membrane bioreactor

INTRODUCTION

Milk proteins are source of numerous bioactive peptides (BAPs). Proteins such as caseins and whey proteins have been used for the production of BAPs because inexpensive and safe sources are readily available (Wakai and Yanamoto, 2012). These peptides can be liberated from proteins upon gastrointestinal digestion (GID), enzymatic hydrolysis or microbial fermentation (Korhonen, 2009). Multiple biological activities, such as antihypertensive, antioxidant, opioid, immunostimulating or calcium binding activities have been associated with BAPs (Nongonierma and FitzGerald, 2015; Nielsen et al., 2017). The most extensively studied BAPs are those capable of inhibiting angiotensin converting enzyme (ACE). ACE catalyzes the conversion of angiotensin

I into angiotensin II which acts as a vasoconstrictor leading to an elevated blood pressure; ACE inhibition therefore constitutes a major strategy to prevent hypertension (Guang et al., 2012; Wu et al., 2017).

The production of BAPs through fermentation is commonly conducted using lactic acid bacteria (LAB). Within this group, *Lactobacillus helveticus* (*L. helveticus*) is considered as a highly proteolytic species which could be used to generate specific peptide sequences by fermentation (Griffiths and Tellez, 2013; Raveschot et al., 2018). In particular, *L. helveticus* species are recognized for their capability to produce ACE-inhibitory peptides during fermentation (Wakai and Yanamoto, 2012; Elfahri et al., 2014; Ahtesh et al., 2018). The well-known ACE-inhibitory peptides Ile-Pro-Pro (IPP) and Val-Pro-Pro (VPP) are commonly found in milk fermented by various *L. helveticus* strains (Wakai and Yanamoto, 2012; Bakr Shori and Salihin Baba, 2015). Moreover, the peptide Ala-Ile-Pro-Pro-Lys-Lys-Asn-Gln-Asp (AIPPKKNQD) was also identified in milk fermented by the *L. helveticus* 130B4 strain (Shuang et al., 2008). These examples show that *L. helveticus* strains can be used to functionalize milk products, conferring health-beneficial properties to fermented milk thanks to the presence of BAPs (Marco et al., 2017).

Microbial fermentation is a cost effective method for BAPs production in comparison to the use of purified enzymes (Daliri et al., 2017). However, the industrial BAP production is still suffering from a lack of suitable large scale technologies (Wu et al., 2013; Agyei et al., 2016). Usually, fermented milks are prepared from batch fermentations without pH control generally resulting in yogurt-like, coagulated products (Li et al., 2017). In this case, optimization of BAPs production is difficult because of the absence of controlled conditions during the fermentation process. Furthermore, it was estimated that only 1–2% of milk proteins undergo proteolysis during fermentation by *Lactobacillus* species, resulting in low peptide productivity (Griffiths and Tellez, 2013). The use of bioreactors with controlled conditions during fermentation could improve peptide yields (Matar et al., 1996; Ahtesh et al., 2018). Among the different types of bioreactors, membrane bioreactors (MBR) operating in a continuous mode with total cell recycling using microfiltration, represents a suitable process to produce different biomolecules by fermentation (Coutte et al., 2017). Indeed, due to membrane retention, bacterial cells and non-hydrolyzed proteins can be concentrated in the bioreactor to undergo an advanced proteolysis during the process. Several studies used *Lactobacillus* strains in MBR for lactic acid production (Choudhury and Swaminathan, 2006; Xu et al., 2006; Probst et al., 2013; Taleghani et al., 2017; Tang et al., 2017) but to date, no report presented the use of MBR for BAPs production by *Lactobacilli*.

Another issue regarding the development of functional foods such as fermented milk is the impact of GID on the product. Indeed, proteolytic enzymes (pepsin, pancreatic enzymes, and intestinal brush barrier peptidases) present in the digestive tract will modify the peptide profile of fermented products following oral consumption. Consequently, the impact of GID on a given fermented product must be assessed to get a better prediction of the *in vivo* activities. GID increases the release of BAPs from fermented products, as they still contain proteins and large

peptides that will be hydrolyzed during GID, generating small ACE-inhibitory peptides (Matar et al., 1996; Hernández-Ledesma et al., 2004; Jin et al., 2016).

The ultimate goal of this study was to develop a ready-to-use, BAPs-containing ingredient that would still present beneficial activity after GID. The targeted biological activity was ACE inhibition, which was assessed either through biochemical activity assay, or through peptide identification (mass spectrometry) followed by activity prediction using quantitative structure activity relationship (QSAR) modeling. To show the beneficial effect conferred by fermentation and to be closer to the real *in vivo* activities, the impact of a simulated GID was studied on the produced fermented milk. Finally, this work demonstrated the technical feasibility of an MBR-based continuous process for BAP production by *L. helveticus* strains.

MATERIALS AND METHODS

Materials

Three *Lactobacillus* strains were used in this study: *L. helveticus* 45a, *L. helveticus* 49d, and *L. helveticus* 60b. These strains were previously isolated from different Mongolian dairy products based on their proteolytic abilities (Raveschot et al., 2020).

Maltodextrin (Glucidex IT 12) was obtained from Roquette (Lestrem, France). The fluorescent substrate for ACE (Abz-Gly-Phe(NO₂)-Pro) was purchased from Bachem (Bubendorf, Switzerland). Finally, skim milk powder and all other reagents were purchased from Sigma-Aldrich (St. Louis, MO, United States).

Batch Fermentation

Production of Fermented Milk

Each strain was taken from a frozen vial and transferred into De Man, Rogosa and Sharpe (MRS) medium (De Man et al., 1960) for 48 h growth at 37°C in anaerobic conditions. The resulting culture was used to inoculate a second preculture in a medium composed of skim milk (10%, w/v) and yeast extract (0.1%, w/v) (sterilized at 110°C for 30 min) for 24 h growth at 37°C in anaerobic conditions. This last step was repeated to obtain the final preculture used for batch fermentation.

Batch fermentation was conducted in a MiniBio 500 (Applikon Biotechnology, Delft, Netherlands) filled up with 300 mL of a skim milk medium supplemented with yeast extract as described above. The preculture was used to inoculate (10%, v/v) the medium with a starting optical density (OD_{600nm}) of 0.3. Fermentation was conducted for 72 h at a constant temperature of 40°C with an agitation rate of 300 rpm in a final working volume of 330 mL. Dinitrogen was sparged continuously (20 mL.min⁻¹) to maintain anaerobic conditions. The pH was set to 6 with H₃PO₄ (1 M) and NaOH (3 M) solutions. The skim milk fermentate was periodically sampled for determination of growth and peptide concentration. Experiments were performed in duplicate and mean values are presented. At the end of fermentation, the complete broth was centrifuged at 13,000 × g for 10 min and the supernatant was stored at -20°C for further analysis. In parallel, a control product (FCtl) was prepared,

consisting of a non-inoculated medium but similarly incubated and centrifuged.

Bacterial Growth and Peptide Analysis

Samples taken from batch fermentation were analyzed for bacterial growth and peptide production using protocols previously described (Raveschot et al., 2020). Briefly, bacterial growth was determined by OD_{600nm} measurement after broth dilution in 2% ethylenediaminetetraacetic acid (EDTA), pH 12 solution. After centrifugation (13,000 × *g* for 10 min), the cell pellet was used for bacterial growth determination, and the supernatant was analyzed for protein and peptide contents using size exclusion chromatography (SEC) based on a fast protein liquid chromatography (FPLC) with a Superdex Peptide 10/300 GL column (10 × 300–310 mm, 13 μm, GE Healthcare, Little Chalfont, United Kingdom) coupled to an AKTA Protein Purification System (GE Healthcare, Little Chalfont, United Kingdom). Twenty-five microliters of sample were loaded, eluted in isocratic conditions with 30% acetonitrile (ACN), 0.1% trifluoroacetic acid (TFA) solution at a flow rate of 0.5 mL.min⁻¹ for 60 min and monitored at 214 nm. The column was calibrated using compounds of known molecular weight (Glutathione 307.3 Da, Vitamin B12, 1,355 Da, Aprotinin, 6,500 Da, Cytochrome C, 12,400 Da and Albumin, 60 kDa for the dead volume). Protein and peptide contents, and peptide molecular weight distribution in each sample were estimated through chromatogram integration. Two molecular weight ranges were defined, the first corresponding to the high molecular weight proteins/peptides (HMWPs) with an apparent molecular weight higher than 1,700 Da, and the second, to the low molecular weight peptides (LMWPs) with an apparent molecular weight lower than 1,700 Da. The content estimation for each range was expressed as percentage of the area under the curve (%HMWPs and %LMWPs). Finally, peptide concentration in each sample was assessed after protein precipitation with trichloroacetic acid (TCA, 1% final concentration) using the Folin-Ciocalteu reagent (Lowry et al., 1951; McSweeney and Fox, 1997). A peptide digest standard (Peptide digest assay standard, Thermo Fisher Scientific, Waltham, MA, United States) was used for peptide quantification.

Peptide Separation by Ultrafiltration

After batch fermentation, the centrifuged broth was either kept intact (F Raw) or submitted to an ultrafiltration step for peptide separation. The membrane used was a Hydrosart cartridge (Sartorius, Göttingen, Germany) of 0.1 m² with a 10 kDa molecular weight cut off. The resulting permeate from ultrafiltration (F UFP) containing molecules lower than 10 kDa was dried by centrifugal evaporation (miVac Centrifugal Vacuum Concentrators, Gene Vac, Ipswich, United Kingdom) at 40°C to 10% of the initial volume.

Simulated Gastrointestinal Digestion

The products obtained from batch fermentation (F Raw and F UFP) were subjected to an *in vitro* static simulated gastrointestinal digestion (SGID). Gastric and intestinal steps of the GID process were successively simulated by adding different

fluids to the fermented product. The protocol used and fluids composition were described by Caron et al. (2015). Briefly, 20 mL of fermented product containing 100 g.L⁻¹ of dry matter were mixed with 24 mL of gastric fluid containing 37.5 mg of porcine pepsin (E:S ratio = 1/40). The reaction was conducted for 2 h at 37°C with a constant pH of 2.5–3. After the gastric phase, the intestinal step was simulated by the addition of 12 mL of bile solution, 24 mL of intestinal fluid containing 16.65 mg of porcine pancreatic enzyme (E:S ratio = 1/50), and 4 mL of NaHCO₃ (1 M). The reaction was conducted for 2 h at 37°C with a constant pH of 7–7.5. Samples were taken at the end of the gastric and intestinal steps (called G2 and I2, respectively), inactivated by heat treatment and analyzed for peptide content by Folin-Ciocalteu reagent and SEC as described above. For each fermented product (F Raw and F UFP), experiments were performed in triplicate.

ACE Inhibition Analysis

Biochemical Test

The biochemical test used to evaluate the ACE-inhibitory activity of fermented products was described by Sentandreu and Toldrà (2006). Briefly, samples, ACE and its substrate were prepared in a 150 mM Tris-HCl, pH 8.3 buffer. The inhibition reaction was performed in a final volume of 300 μL containing 50 μL of samples (or buffer for negative control), 50 μL of ACE solution (0.05 U.mL⁻¹) and 200 μL of ACE substrate (Abz-Gly-Phe(NO₂)-Pro) (0.45 mM). A control without ACE was also used where the enzyme was replaced by buffer solution. The fluorescence of the enzymatic reaction product substrate was monitored every 2 min for 1 h at 37°C in a spectrofluorometer (Xenius XC, Safas Monaco, Monaco, France) with excitation and emission wavelengths of 365 and 415 nm, respectively. The inhibition percentage toward ACE was defined as the percentage of ACE activity inhibited by a given concentration of the fermented products compared to the negative control. For each product, the concentration required to cause 50% of inhibition of ACE activity (IC₅₀) was determined by plotting the inhibition percentage as a function of sample final concentration natural logarithmic. IC₅₀ were expressed in mg.mL⁻¹ of dry matter. Experiments were performed in triplicate.

Prediction of ACE-Inhibitory Activity

Peptides contained in the raw fermented products before and after SGID (F Raw and F Raw I2, respectively) were purified and identified by mass spectrometry (UPLC-ESI-qTOF-MS/MS) as described previously (Raveschot et al., 2020). Peptides were purified on Bond Elut C₁₈ microcolumns (Agilent Technologies, Santa Clara, CA, United States) and dried by centrifugal evaporation (miVac Centrifugal Vacuum Concentrators, Gene Vac, Ipswich, United Kingdom) for 2 h at 40°C. Dried peptides were redissolved in 100 μL H₂O, 0.1% TFA. Ten microliters were chromatographed on an ACQUITY UPLC system (Waters, Manchester, United Kingdom) using a C₁₈-Kinetex column (150 × 4.6 mm, 2.6 μm 100 Å, Phenomenex, Torrance, CA, United States), a linear gradient of ACN containing 0.1% FA and a flow rate of 500 μL.min⁻¹. The HPLC eluent was directly electrosprayed from the column end at an applied

voltage of 3 kV, using a desolvation gas (dinitrogen) flow of 600 L.h⁻¹, a nebulizer gas flow of 2.5 bar and desolvation temperature of 300°C, respectively. The chromatography device was coupled to SYNAPT-G2-Si mass spectrometer (Waters, Manchester, United Kingdom). MS analysis was performed in sensitivity, positive ions and data dependent analysis (DDA) modes and MS data were collected in the 100–2,000 m/z range with a scan time of 0.2 s. A maximum of 15 precursor ions with an intensity threshold of 10,000 counts were selected for ion trap collision-induced dissociation (CID) fragmentation and subjected to a collision energy ramping from 8 to 9 V for low mass and 40 to 90 V for high mass. The MS/MS spectra were recorded on the 100–2,000 m/z range with a scan time of 0.1 s. Peaks were analyzed using Mass Lynx software (4.1. version, Waters, Manchester, United Kingdom).

The 3D-maps of LC-MS/MS signals were analyzed using Progenesis QI for proteomics software (4.0. version, Nonlinear Dynamics, Manchester, United Kingdom) by principal component analysis (PCA). Database searches via PEAKS Studio 7.0 (Bioinformatics Solutions Inc., Waterloo, ON, Canada) were performed using the UniProt databases (May 15, 2017) restricted to *Bos taurus* organism. A mass tolerance of 35 ppm and three missing cleavage sites, no specific enzyme, variable methionine oxidation and an MS/MS tolerance of 0.2 Da were allowed. No fixed modification was used for the peptide identifications. The relevance of protein and peptide identities was judged according to their identification generated by PEAKS Studio 7.0 ($p < 0.05$) and a false discovery rate <to 1%. Experiments were performed in triplicate.

For each fermented product, the prediction of ACE-inhibitory activity was only performed on peptides identified in all three technical repetitions of the LC-MS/MS analysis. Prediction of ACE-inhibitory activity was performed using a QSAR model developed by Pripp et al. (2004). This model predicts IC₅₀ for each peptide based on the last two amino acids found at the C-terminal position. QSAR modeling was performed using Microsoft Excel software (2013 version). Predicted IC₅₀ were then categorized and frequencies for each range of IC₅₀ were calculated. Results were expressed as the percentage of the total number of peptides in a given fermented product.

Continuous Process for Peptide Production

Continuous culture was performed without total cell recycling in a classical bioreactor. Fermentations were performed in a MiniBio 500 filled with 300 mL of medium. Firstly, strain was cultivated in a classical batch mode for 24 h in anaerobic conditions (dinitrogen sparged) at 40°C with a pH maintained at 6 and agitation rate of 300 rpm. After 24 h, the fermenter was continuously fed at a dilution rate of 0.1 h⁻¹ (30 mL.h⁻¹) and broth was withdrawn from the fermenter at the same flow rate.

For each experiment, the broth was periodically sampled for determination of growth, peptide and carbohydrate (lactose and lactic acid) concentrations. Experiments were performed in duplicate and mean values were presented.

Continuous Process for Peptide Production in Membrane Bioreactor

Continuous fermentation was also performed in a membrane bioreactor (MBR) (Applikon Biotechnology, Delft, Netherlands) containing 3 L of the previously described skim milk medium. The bioreactor was coupled with a 3,600 cm² hollow fiber membrane with 0.2 µm of pore size (GE Healthcare, Little Chalfont, United Kingdom). Batch phase of culture was performed as described above. Hereafter, during the continuous phase, a peristaltic pump was used for broth circulation from the bioreactor to the filtration membrane at a flow rate of 1.1 L.min⁻¹. The fermenter was continuously fed at the same dilution rate of 0.1 h⁻¹ (0.3 L.h⁻¹) with fresh medium. In order to keep the fermenter volume constant, permeate of the microfiltration was withdrawn at a same flow rate as the feeding. The fermented product containing the produced peptides was collected in a tank and stored at -20°C for further analysis. For each experiment, the broth was periodically sampled for determination of growth, peptide and carbohydrate (lactose and lactic acid) concentrations. Experiments were performed in duplicate and mean values are presented.

Analytical Methods for Fermentation Monitoring

Strain growth and peptide quantification by the Folin-Ciocalteu reagent were performed on samples as described in the “Bacterial Growth and Peptide Analysis” section. Carbohydrates analysis were performed by high performance liquid chromatography (HPLC) using a Fast Fruit Juice (50 Å, 7 µm, 7.8 × 50 mm, Waters, Manchester, United Kingdom) column coupled to a Spectra SYSTEM (Thermo Electron Corporation, San Jose, CA, United States). Briefly, 20 µL of samples were chromatographed in isocratic condition with a 0.05 M H₃PO₄ solution at a flow rate of 0.8 mL.min⁻¹ for 10 min. Eluted molecules were detected by a refractometer (Spectra SYSTEM RI-150, Thermo Electron Corporation, San Jose, CA, United States).

Spray Drying of the Fermented Product and Biological Activity of the Resulting Ingredient

Atomization of the fermented product (which corresponds to the total permeate of the microfiltration) obtained from the MBR was performed with a Mini atomizer B-290 (Buchi, Rungis, France). A maltodextrin powder (Glucidex IT 12) was used as a charge agent at 0, 5, 10 or 20% (w/v). For each experiment, 200 mL of fermented product at room temperature (22°C) were pulverized at a flow rate of 8 mL.min⁻¹ and dried by air set at 130°C. Characteristics of the inlet air were analyzed using a psychrometer and were 22°C with 64% of humidity (dew temperature of 15.5°C and wet bulb temperature of 17.9°C). The outlet temperature of the final dried product was about 68°C. Atomization yields were calculated according to the dry matter collected after spray drying process on the theoretical dry matter before atomization. Experiments were performed in triplicate.

Finally, the ACE-inhibitory activity of the fermented product before and after atomization was evaluated by a biochemical test as described in the “Biochemical Test” section.

Statistical Analysis

All statistical analysis were performed using one-way ANOVA and Tukey's *post-hoc* test for pairwise comparison. Differences between means were considered significant when p value < 0.05. Statistical analyses were performed on R software (R core team, 2016, Vienna, Austria).

RESULTS AND DISCUSSION

Strain Growth and Peptide Production During Batch Fermentation

Batch fermentations were conducted in order to produce fermented milk products from three strains of *L. helveticus*. Strains were inoculated at an initial OD_{600nm} of 0.3 (Figure 1A). During the exponential phase, the specific growth rate (μ) was about 0.09 h⁻¹ for *L. helveticus* 45a, 0.07 h⁻¹ for *L. helveticus* 49d, and 0.08 h⁻¹ for *L. helveticus* 60b. After 31 h of culture, cell concentrations remained constant for the rest of the fermentation process. The highest biomass concentration was observed for *L. helveticus* 45a strain, reaching an OD_{600nm} of about 5. The two other strains reached an OD_{600nm} of 3–4. The initial peptide concentration in the skim milk medium was 3.12 g.L⁻¹ right after inoculation (Figure 1B), these peptides originating most probably from the inoculum. Peptide concentration increased with time proportionally to the strain growth, with a particularly important production during the first 31 h of culture with the strain *L. helveticus* 45a. Thereafter, until the end of the fermentation, peptide concentrations increased slowly or remained constant depending on the strain considered. The highest concentration was observed with the *L. helveticus* 45a strain, reaching 19.33 g.L⁻¹ after 72 h of culture. For strains *L. helveticus* 49d and 60b, peptide concentrations reached values of 6.87 and 8.91 g.L⁻¹, respectively. In order to follow protein hydrolysis during fermentation, samples from the bioreactor were analyzed by SEC (Figure 1C). Molecular weight repartitions at the beginning of the culture were 85–86% for HMWPs and 15–20% for LMWPs. As a result of protein hydrolysis by *Lactobacillus* strains, the proportion of LMWPs increased over time during fermentation. The homofermentative profile of *L. helveticus* leads to an important production of lactic acid from lactose and consequently a high acidification capacity (Hebert et al., 2000). In this study, a pH value of 6 was chosen to prevent protein precipitation in the medium, while being close to the optimal pH for *Lactobacillus* proteinase activity (Fira et al., 2001). This approach has been used by Matar et al. (1996) for *L. helveticus* L89 strain. Indeed, the bacterial growth was not affected by a pH-controlled vs. a non-controlled one, but the peptide production was significantly improved in a pH-controlled medium.

After fermentation, products were centrifuged for bacterial cell elimination. The supernatants were either used directly (F Raw) or subjected to an ultrafiltration step in order to obtain

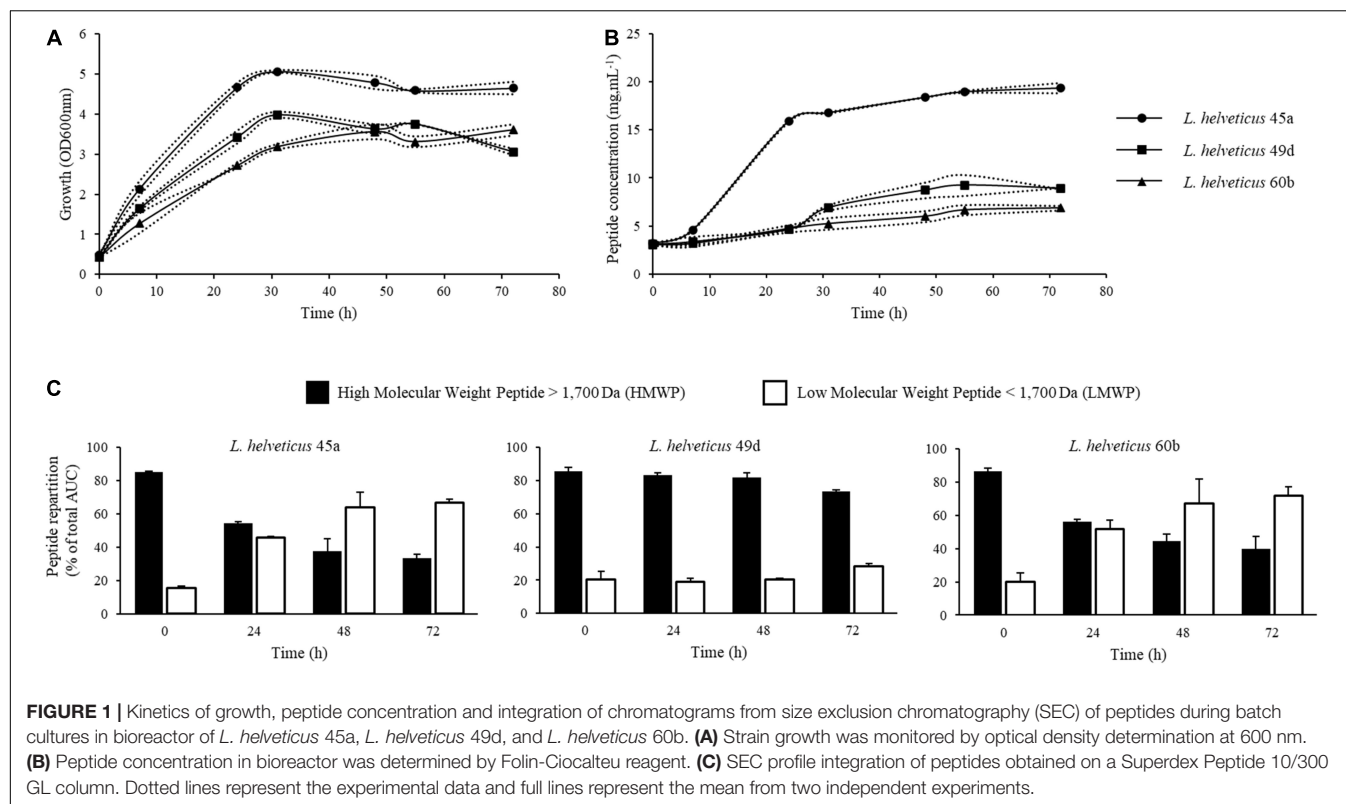
permeates without proteins (F UFP). Moreover, a control product consisting in a non-fermented milk was included in the study.

Changes in the Peptide Content of Fermented Products During SGID

A SGID was performed on fermented products to study the impact of gastrointestinal proteolysis on peptide content and ACE-inhibitory activity. Indeed, GI enzymes can further degrade partially hydrolyzed proteins in fermented products, generating new, smaller peptides which are potentially bioactive (Caron et al., 2016; Daliri et al., 2017; Lamothe et al., 2017; Sanchón et al., 2018). Peptide quantification was performed before and after SGID; molecular weight repartition was analyzed by SEC (Figure 2 and Table 1). Notably, raw fermented products showed an important increase of their peptide content after SGID (Figure 2A), with concentrations increasing from 2 to 12 fold. These observations were confirmed by SEC analyses: the control product (FCtl Raw) showed a significant modification of its apparent peptide molecular weight distribution, with a complete hydrolysis of high molecular weight proteins after the intestinal phase (Figure 2B and Table 1). A similar observation was made for the F45a Raw product (Figure 2C and Table 1) although in this case, because of bacterial fermentation, the proportion of HMWPs before GID was lower than in the control sample. These results are consistent with previous studies showing that milk proteins are very efficiently digested upon SGID or passage through human jejunum (Sanchón et al., 2018). For UFP products, modifications in peptide content before and after SGID were much smaller (Figure 2D and Table 1), except in the control product (FCtl UFP I2) where a notable increase was observed, probably resulting from the auto-hydrolysis of GI enzymes. Regarding molecular weight distribution, SGID of F UFP products did not lead to major changes. SEC analysis showed the efficacy of the ultrafiltration step with an absence of molecules higher than 10 kDa (Figures 2E,F and Table 1). Altogether, these results suggest that ultrafiltered products are much less sensitive to alterations by GI enzymes, and therefore that biological activities of these products may be maintained even in an *in vivo* setting. It has already been reported the tripeptides Ile-Pro-Pro and Val-Pro-Pro produced by some *L. helveticus* strains, are not affected by SGID (Ohsawa et al., 2008).

ACE Inhibition Activities of the Produced Hydrolysates

Angiotensin converting enzyme-inhibitory activity in *Lactobacillus* fermented products was already reported (Fernandez et al., 2017; Georgalaki et al., 2017; Kliche et al., 2017; Solanki et al., 2017; Alhaj et al., 2018), and numerous ACE-inhibitory peptides have been identified (Pihlanto, 2013; Li et al., 2017). In this study, ACE-inhibitory activity was assessed by a biochemical test performed on samples, and predicted using a QSAR model on peptides identified by LC-MS/MS. 85–317 peptide sequences were identified in the fermented samples (F Raw), and 283–511 sequences in the products which had undergone simulated GI digestion (F Raw I2). Database searches showed that none of these sequences came from yeasts



or *L. helveticus* proteomes. Peptides were considered to display a relevant ACE-inhibitory activity when the predicted IC_{50} was lower than 200 μ M. As an example, our QSAR model predicted an IC_{50} of 26.85 μ M for the well-known ACE inhibitors IPP and VPP. Predicted IC_{50} varied widely in the fermented products, with values ranging from 5.8 to 2000 μ M (Figure 3A). 19% of the peptides in non-fermented milk (Fctl Raw) had a predicted IC_{50} lower than 50 μ M, 32% between 50 and 100 μ M and 0% between 100 and 200 μ M. This repartition profile corresponds to a basal level of inhibitory peptides found in raw, untreated milk. By comparison, the fermented products showed higher proportions (23–34%) of peptides with a predicted IC_{50} lower than 50 μ M. Fermentation therefore led to an enrichment of the samples in peptides with high ACE-inhibitory activity. However, applying a simulated GID after fermentation led to a complete loss fermentation's benefits : the proportion of peptides with a predicted IC_{50} lower than 50 μ M became virtually similar (between 27 and 27.89%) in the non-fermented control, and in the three fermented products (Figure 3B). To confirm these observations, peptide heterogeneity between samples was evaluated by conducting a PCA on 3D-maps of LC-MS/MS signals (Figure 3C). The principal components, named Dim1 and Dim2, explained 20.08 and 15.02% of the total variance, respectively. F Raw samples were scattered along the positive side of Dim1 whereas the digested products (F Raw I2) were grouped on the negative side. Samples treated by SGID (including the non-fermented control) were grouped together as a small, homogeneous cluster whereas for raw, undigested samples, the non-fermented control was clearly separated from

the fermented products. SGID therefore appears to erase the differences between non-fermented control and fermented samples, in terms of both peptide composition and predicted ACE-inhibitory activity.

Angiotensin converting enzyme-inhibitory activity was also evaluated *in vitro* using a biochemical assay. Table 2 shows the IC_{50} determined for the fermented products and after their treatment by ultrafiltration, SGID or both. All raw fermented products presented lower IC_{50} than the non-fermented milk : IC_{50} for non-fermented milk was 12.76 mg.mL⁻¹, whereas the IC_{50} for the two most potent products, F45a and F49d, were 0.57 and 0.76 mg.mL⁻¹, respectively. After SGID (F Raw I2), a decrease of IC_{50} was observed in all products (IC_{50} values ranging from 0.25 to 0.42 mg.mL⁻¹) but there were no more statistically significant differences between the samples. These results are in accordance with the bioactivities predicted using the QSAR model, and with the PCA analysis of peptide homogeneity; in particular, the correlation between the proportion of peptides with predicted high inhibitory capacity and the results of the biochemical test demonstrate the relevance of our QSAR model. An important observation, though, is that performing SGID on samples totally erases the differences which existed initially between the fermented samples and the non-fermented control, thereby causing a loss of the fermentation's benefit. According to these observations, the consumption of fermented milk is no more beneficial than the consumption of non-fermented milk.

To prevent the impact of SGID on the biological activity, an ultrafiltration step was conducted on the fermented products to remove the proteins that had not been hydrolyzed during

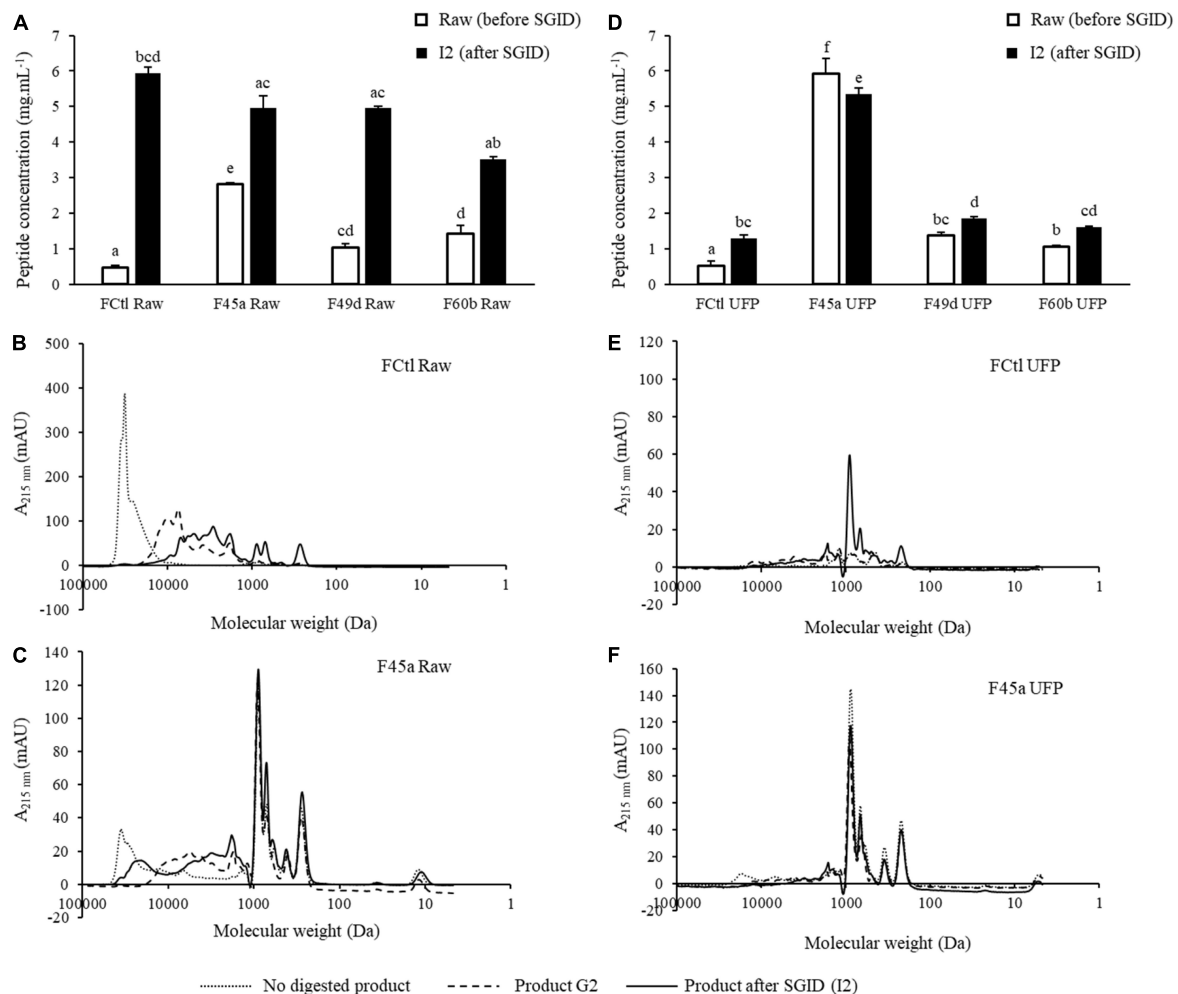


FIGURE 2 | Evolution of peptide concentrations and size exclusion chromatography (SEC) profiling during *in vitro* simulated gastrointestinal digestion (SGID) of fermented and control products. Products were submitted either in their raw (Raw) or in their ultrafiltrated forms (UFP). **(A,D)** Evolution of peptide concentrations determined by the Folin-Ciocalteu reagent before and after SGID of the raw and the UFP products. Data were represented as mean \pm SD of three independent experiments. Statistical analysis using one way ANOVA and Tukey's *post-hoc* test. Mean values in the same graph without a common letter differ significantly (p value < 0.05). **(B,C,E,F)** SEC profiles of peptides from the Fctl Raw, the F45a Raw, the Fctl UFP, and the F45a UFP products before (not digested), at the end of the gastric step (G2) and at the end of SGID (I2). SEC profiles were obtained on a Superdex 10/300 GL column.

the fermentation process. The distribution of IC_{50} from these ultrafiltrated products (F UFP) showed the same tendency as the one observed for raw products (Table 2). An IC_{50} of 8.38 mg.mL^{-1} was reported for the control (Fctl UFP), compared to 2.11 to 0.47 mg.mL^{-1} for the fermented products, with the F45a UFP being the most potent product. After SGID, the IC_{50} of the non-fermented control (Fctl UFP I2) decreased to 2.13 mg.mL^{-1} . The F49d and F60b UFP I2 presented similar IC_{50} of 1.97 and 3.3 mg.mL^{-1} , respectively. Finally, the IC_{50} value for the F45a UFP I2 was four times lower than the control one, at 0.56 mg.mL^{-1} (statistically significant difference). Therefore, the impact of fermentation was maintained even after SGID in milk fermented with the *L. helveticus* 45a strain.

Altogether, these results demonstrate the ability of the strain *L. helveticus* 45a to produce ACE-inhibitory peptides by milk fermentation. Nevertheless, a peptide separation step

was required to obtain a significant improvement of the biological activity in comparison to a non-fermented milk. A fragmentation strategy could now be used to identify peptides generated by *L. helveticus* 45a, and involved in ACE inhibition (Sharma et al., 2011).

Continuous Fermentation in Membrane Bioreactor

The above results allow two important conclusions : (i) fermentations conducted in batch mode are only partial and leave large amounts of undigested proteins, which during GID can be further hydrolyzed to bring peptides of interest; (ii) an ultrafiltration step on the culture broth allows to standardize the end-product with respect to the GID by keeping only the most active small peptides produced by *Lactobacillus* strains. Based

on these results, an integrated continuous process for peptide production was developed using the *L. helveticus* 45a strain. One of the limitations of the use of Lactobacilli for peptide production is the lack of efficient industrial processes (Aggei et al., 2016). Experiments were performed either in a classical bioreactor (CBR) or in a membrane cell-recycle bioreactor (MBR) consisting in a bioreactor coupled to a microfiltration membrane (0.2 μm). The use of an MBR presents the advantage to simultaneously, in a single step, produce and purify an active ingredient. Additionally, high peptide yield can be obtained because of the concentration of proteins and bacterial cells in the bioreactor.

Bacterial strains were cultured in the same conditions as for batch fermentation. The initial $\text{OD}_{600\text{nm}}$ at the beginning of the culture was 0.3 (Figure 4A). During the first 24 h, fermentations were conducted in batch mode, and bacterial concentration reached an $\text{OD}_{600\text{nm}}$ mean of 4.5. After switching to the continuous mode, the bacterial concentration in CBR decreased to reach an $\text{OD}_{600\text{nm}}$ of 2.7 after 32 h of culture, before stabilizing for the rest of the culture at an $\text{OD}_{600\text{nm}}$ of about 3. Conversely to CBR, the bacterial concentration in MBR showed a strong increase after 24 h of continuous mode, reaching an $\text{OD}_{600\text{nm}}$ of 12.7, as a result of bacterial retention by the membrane. Bacterial growth then stabilized, the $\text{OD}_{600\text{nm}}$ finally reaching a value of 14.4 at the end of the culture. Substrate availability during fermentation was evaluated by quantification of lactose and lactic acid. The initial lactose concentration was about 52 g.L^{-1} at the beginning of the culture (Figure 4B). During the batch phase,

an important decrease of lactose concentration was observed with only 0.1 g.L^{-1} of lactose left after 24 h. Consistently, lactic acid concentrations increased from 0.8 to 34 g.L^{-1} . During the continuous phase, lactose concentration increased in the CBR, reaching 11 g.L^{-1} after 52 h of culture and then remained stable until the end of fermentation. Lactic acid concentration decreased at the beginning of the continuous phase to reach a concentration of 12 g.L^{-1} after 32 h of culture. A continuous increase of lactic acid concentration was then observed for the rest of the culture (22 g.L^{-1} at the end of the fermentation). In the MBR, lactose concentration remained constant during the continuous phase, reaching 1.6 g.L^{-1} at 48 h of culture suggesting that lactose supplied during this phase was instantly consumed by the bacterial population. Lactic acid concentration increased at the beginning of the continuous phase, following the bacterial growth and reached 43 g.L^{-1} after 48 h of culture. A stabilization of lactic acid concentration was then observed for the rest of the fermentation. Lactic acid can inhibit the growth of *Lactobacillus* strains (Aguirre-Ezkauriatza et al., 2010), the important concentration of lactic acid found after 48 h of culture could therefore explain the growth limitation observed in MBR. Moreover, the dilution rate applied during the continuous phase (0.1 h^{-1} , flow rate of 5 mL.min^{-1}) represented also a limitation for bacterial growth probably due to a lack of lactose supply in the bioreactor. Indeed, during the initial 24 h batch phase, bacterial cells consumed a large part of the lactose initially found in milk; lactose supply during the continuous phase was then insufficient, resulting in growth limitation after 48 h of culture.

TABLE 1 | SEC profile integration of peptides from each fermented and control product before (no digested product), during (product G2), and after GID (product after GID, I2).

F Ctl Raw					F Ctl UFP				
	%HMWP	SD	%LMWP	SD		%HMWP	SD	%LMWP	SD
No digested product	97.9	0.4	2.1	0.4	No digested product	10.2	0.7	89.8	0.7
Product G2	76.2	1.6	23.8	1.6	Product G2	33.2	2.2	66.8	2.2
Product after GID (I2)	43.3	1.4	56.7	1.4	Product after GID (I2)	4.1	3.6	95.9	3.6
F 45a Raw					F 45a UFP				
No digested product	92.0	0.7	8.0	0.7	No digested product	10.7	0.5	89.3	0.5
Product G2	38.5	1.6	61.5	1.6	Product G2	4.6	3.6	95.4	3.6
Product after GID (I2)	19.4	3.2	80.6	3.2	Product after GID (I2)	1.0	0.5	99.0	0.5
F 49d Raw					F 49d UFP				
No digested product	86.1	1.7	13.9	1.7	No digested product	3.3	2.9	96.7	2.9
Product G2	67.5	3.3	32.5	3.3	Product G2	10.8	9.5	89.2	9.5
Product after GID (I2)	34.7	0.9	65.3	0.9	Product after GID (I2)	0.2	0.2	99.8	0.2
F 60b Raw					F 60b UFP				
No digested product	80.7	4.7	19.3	4.7	No digested product	2.5	1.3	97.5	1.3
Product G2	58.5	4.5	41.5	4.5	Product G2	8.6	8.5	91.4	8.5
Product after GID (I2)	30.7	1.8	69.3	1.8	Product after GID (I2)	1.1	0.9	98.9	0.9

Products were tested either in a raw form (F Raw) or either after an ultrafiltration step (F UFP). SEC profiles were obtained on a Superdex 10/300 GL column. Two molecular weight ranges were defined, the first corresponding to the high molecular weight proteins/peptides (HMWP) with an apparent molecular weight higher than 1,700 Da, and the second, to the low molecular weight peptides (LMWP) with an apparent molecular weight lower than 1,700 Da. The content estimation for each range was expressed as percentage of the area under the curve (%HMWP and %LMWP).

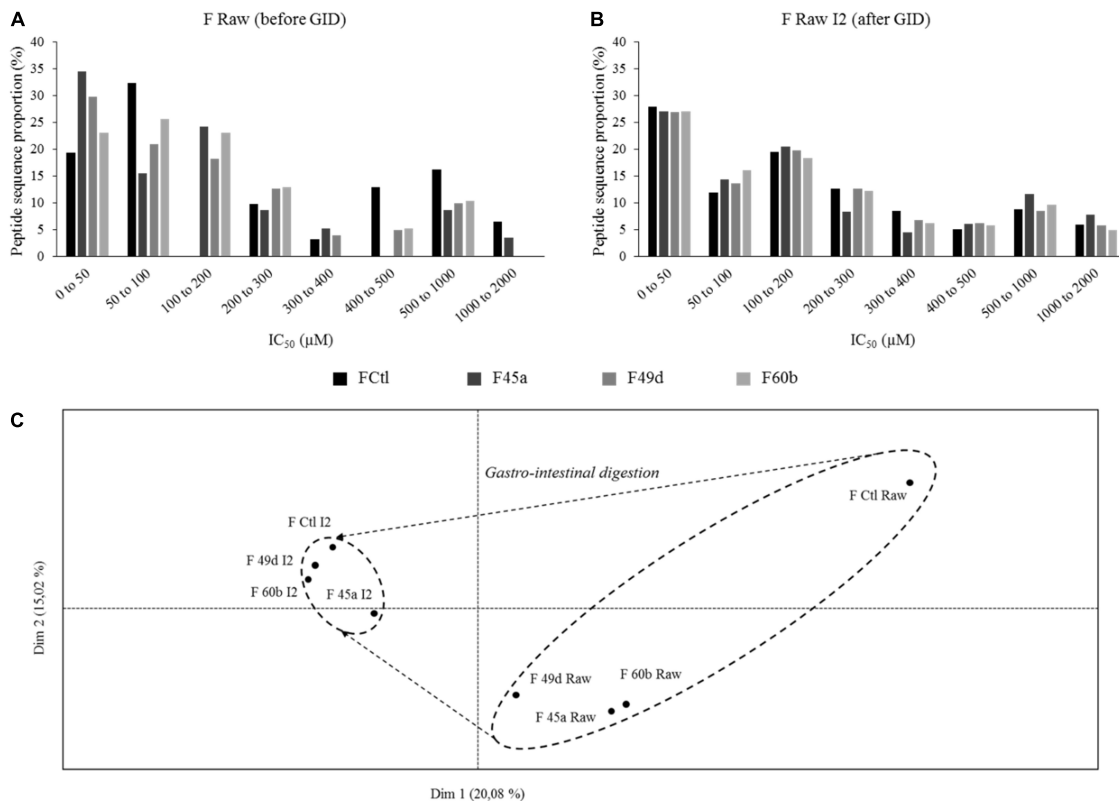


FIGURE 3 | Predicted IC₅₀ toward angiotensin converting enzyme (ACE) inhibition repartition of identified peptides and principal component analysis (PCA) of the 3D-maps obtained from mass spectrometry (LC-MS/MS) analysis of peptides extracted from the fermented and control products. IC₅₀ were predicted using a quantitative structure activity relationship (QSAR) model and peptide proportions in different ranges of IC₅₀ were calculated for (from dark to light) the control product (FCtl) and the products obtained by fermentation with *L. helveticus* 45a (F45a), *L. helveticus* 49d (F49d), and *L. helveticus* 60b (F60b) strains. **(A)** Predicted IC₅₀ repartition from raw products. **(B)** Predicted IC₅₀ repartition from products submitted to a simulated gastro-intestinal digestion (SGID). **(C)** PCA of 3D-maps obtained from LC-MS/MS analysis of peptides extracted from the raw products before (Raw) and at the end of the SGID (I2).

TABLE 2 | IC₅₀ toward ACE inhibition determined *in vitro* from each fermented and control product.

F Raw			F UFP		
	IC ₅₀ (mg.mL ⁻¹)	SD		IC ₅₀ (mg.mL ⁻¹)	SD
FCtl	12.76 ^c	0.07	FCtl	8.38 ^b	1.78
F45a	0.57 ^a	0.03	F45a	0.47 ^a	0.03
F49d	0.76 ^a	0.03	F49d	1.76 ^a	0.1
F60b	4.22 ^b	0.09	F60b	2.11 ^a	0.46
F Raw after GID (F Raw I2)			F UFP after GID (F UFP I2)		
FCtl	0.32 ^a	0.15	FCtl	2.13 ^b	0.4
F45a	0.38 ^a	0.08	F45a	0.56 ^a	0.05
F49d	0.25 ^a	0.04	F49d	1.97 ^b	0.64
F60b	0.42 ^a	0.14	F60b	3.3 ^b	0.44

Products were tested either in a raw form (F Raw) or either after an ultrafiltration step (F UFP). These products were also tested after a SGID (I2). The statistical analysis were performed using one-way ANOVA and Tukey's post-hoc test. Mean values in the same part without a common letter differ significantly (*p* value < 0.05).

Regarding peptide production, the initial peptide concentration was equal to 3 g.L⁻¹, this concentration increased to 14 g.L⁻¹ at the end of the batch phase (Figure 4C). In CBR, peptide

concentration decreased after 52 h of culture to reach 7 g.L⁻¹ and then remained constant until the end of the fermentation process. Regarding the MBR, peptide concentration increased slightly during the continuous phase in comparison to the batch mode, reaching 19 g.L⁻¹ after 72 h of culture. In this bioreactor, peptides were separated from the medium by the microfiltration membrane. However, an important part of the peptides remained in the bioreactor. After 72 h of culture, peptide quantities in the bioreactor and in the product tank were equal to 57.9 and 155.2 g, respectively. This clearly indicates a phenomenon of peptide retention by the microfiltration membrane during the process. Retention of non-casein nitrogen during milk microfiltration was observed previously (Boiani et al., 2017; Renhe and Corredig, 2018) probably due to interactions with caseins and calcium-phosphate clusters (Cross et al., 2005).

Peptide productivities of the different processes (batch, continuous in CBR and in MBR) used in this study were compared (Table 3). The productivity at the stationary phase (72 h of culture) was higher in the MBR. Similarly, the mean productivity in MBR was equal to 0.27 g.L⁻¹.h⁻¹, vs. 0.1 g.L⁻¹.h⁻¹ in the CBR, showing the interest of MBR approach for peptide production. Moreover, fermentation conducted in batch mode showed an equivalent productivity (0.33 g.L⁻¹.h⁻¹)

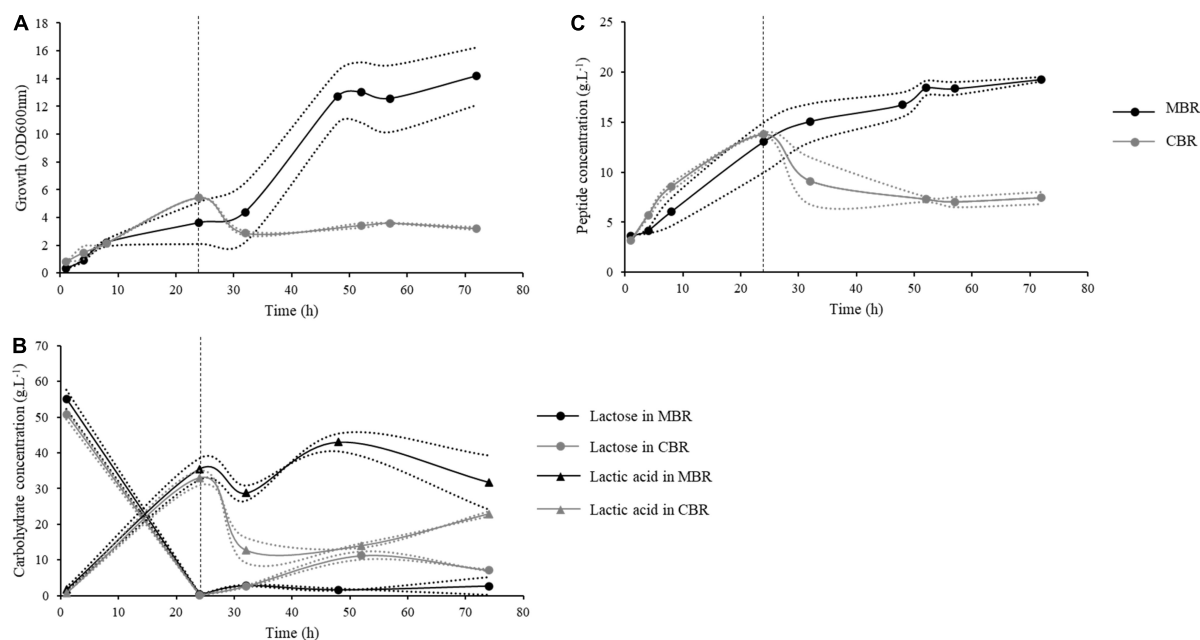


FIGURE 4 | Kinetics of growth, peptide concentrations and carbohydrate concentrations during continuous processes conducted in a classical (CBR, gray) or a membrane bioreactor (MBR, black) with the *L. helveticus* 45a strain. The first 24 h of culture were conducted in batch mode, then bioreactors were fed continuously at a dilution factor of 0.1 h^{-1} . **(A)** Strain growth was monitored by optical density determination at 600 nm. **(B)** Peptide concentration in bioreactor were determined by Folin-Ciocalteu reagent. **(C)** Lactose (circle) and lactic acid (triangle) concentrations were determined by high performance liquid chromatography (HPLC) using a Fast Fruit Juice column. Dotted lines represent the experimental data and full lines represent the mean from two independent experiments.

TABLE 3 | Mean peptide concentration and peptide productivities from the different processes used in this study.

	Batch (48 h)	Continuous (CBR, 72 h)	Continuous (MBR, 72 h)
Mean peptide concentration (g.L^{-1})	15.9 (± 0.1)	7.43 (± 0.8)	19.3 (± 0.3)
Mean productivity ($\text{g.L}^{-1}.\text{h}^{-1}$)	0.33 (± 0.01)	0.103 (± 0.02)	0.27 (± 0.01)
Instantaneous productivity ($\text{g.L}^{-1}.\text{h}^{-1}$)	0.67 (± 0.01)*	0.74 (± 0.11)	1.93 (± 0.04)
Specific productivity (g.g^{-1})	9.99 (± 0.28)	7.13 (± 0.65)	15.8 (± 0.45)

*In batch mode, the maximum instantaneous productivity of peptides was calculated from 7 to 24 h of culture.

in comparison to fermentation in MBR. Peptide productivities were also calculated as a function of the bacterial biomass, leading to the determination of specific productivities. The continuous process in CBR showed a specific productivity of 7.13 g.g^{-1} which is close to that obtained in batch mode (9.99 g.g^{-1}); continuous process in MBR, however, presented a much higher productivity (15.8 g.g^{-1}). The instantaneous productivity in CBR was equal to $0.74 \text{ g.L}^{-1}.\text{h}^{-1}$, compared to $1.93 \text{ g.L}^{-1}.\text{h}^{-1}$ in the MBR, showing the interest for using this type of bioreactor in a continuous process. Concomitantly, the instantaneous productivity in batch mode was calculated at the maximum peptide production time (between 7 and 24 h of culture) and was equal to $0.67 \text{ g.L}^{-1}.\text{h}^{-1}$. Finally, the use of a continuous process in MBR increased by almost 3-fold the instantaneous peptide

productivity in comparison to the batch process. Moreover, it was calculated that 5.3 batch fermentations (whose preparation is time consuming) would be required to obtain the same peptide quantity than the one produced with only one continuous process in MBR. An important lactic acid production was observed during this process; actually, *Lactobacillus* cultures were generally conducted in MBR to study lactic acid production from various nutrient sources (Choudhury and Swaminathan, 2006; Xu et al., 2006; Probst et al., 2013; Taleghani et al., 2017; Tang et al., 2017). Further optimizations, particularly on the dilution rate applied during the continuous phase, could lead to a further improvement of peptide productivities by this process.

Spray Drying Optimization and Analysis of the Resulting Ingredient

The continuous process in MBR allowed to produce by fermentation, a semi-purified product containing, among others, peptides of interest and lactic acid with respective concentrations of 10.51 g.L^{-1} and 29.73 g.L^{-1} . The pH was equal to 5.95 and dry matter content was 7.86%. Spray drying optimization of the product was conducted based on the maltodextrin concentration required to improve the atomization yield. Maltodextrin concentrations were tested from 0 to 20% (w/v) and the dry matter yields were calculated after spray drying process. Atomization without maltodextrin led to a yield of 0% due to the stickiness of the resulting product which was impossible to collect after drying. A yield of 38% ($\pm 7\%$) of dry matter was obtained for a 5% maltodextrin concentration. Concentrations of

10 and 20% of maltodextrin led to dry matter yields of 66% ($\pm 6\%$) and 72% ($\pm 2\%$), respectively, with no statistical differences reported between these values. Subsequently, a maltodextrin concentration of 10% was selected for the spray drying process of the fermented product.

The fermented product was then tested for its ACE-inhibitory activity before and after atomization. The non-atomized product (P 45a) showed an IC_{50} of 1.87 mg.mL^{-1} (**Supplementary Figure S1**). A 10% maltodextrin solution was also tested and showed no ACE-inhibitory activity (data not shown). The IC_{50} of the atomized product P 45a A was equal to 1.23 mg.mL^{-1} (corrected to take into account the maltodextrin weight), which was not statistically different from the non-atomized product, suggesting that spray drying did not alter the ACE-inhibitory capacity of the fermented product. Finally, the IC_{50} of the fermented product obtained by continuous fermentation in MBR was compared with previously obtained fermented products (from batch processes followed by an ultrafiltration step). As reported above, IC_{50} of the F45a UFP was equal to 0.47 mg.mL^{-1} and to 8.37 mg.mL^{-1} for the control condition (Fctl UFP). Interestingly, no statistical differences were observed between the previously obtained F45a UFP and the product resulting from continuous fermentation (P 45a A). These results show the robustness and repeatability of biologically active peptide production during fermentation with the *L. helveticus* 45a strain. Moreover, they demonstrate the feasibility of an MBR-based continuous process for the production of a bioactive ingredient aimed at ACE inhibition.

CONCLUSION

Batch fermentation leads to the production of fermented milks containing ACE-inhibitory peptides. However, the benefits of fermentation (higher concentration of potentially active peptides compared to the control, increased activity in biochemical assay) are lost when samples are subsequently subjected to SGID. Adding a step of ultrafiltration following fermentation allows to maintain the statistical differences between the fermented products and the non-fermented control, even after SGID. Finally, the feasibility of an MBR-based continuous production process of an active ingredient was demonstrated with an increase in productivity. Further developments are needed to improve the productivity of this process, such as optimization of the dilution rate.

REFERENCES

- Aguirre-Ezkauriatza, E. J., Aguilar-Yáñez, J. M., Ramírez-Medrano, A., and Alvarez, M. M. (2010). Production of probiotic biomass (*Lactobacillus casei*) in goat milk whey: comparison of batch, continuous and fed-batch cultures. *Bioresour. Technol.* 101, 2837–2844. doi: 10.1016/j.biortech.2009.10.047
- Agyei, D., Ongkudon, C. M., Wei, C. Y., Chan, A. S., and Danquah, M. K. (2016). Bioprocess challenges to the isolation and purification of bioactive peptides. *Food Bioprod. Process.* 98, 244–256. doi: 10.1016/j.fbp.2016.02.003

DATA AVAILABILITY STATEMENT

The raw data supporting the conclusions of this article will be made available by the authors, without undue reservation.

AUTHOR CONTRIBUTIONS

CR, BC, and FC conceptualized the experiments. CR, BD, and EB took part in the investigation, methodology, and analysis. CR and FC wrote the manuscript. FC, BC, MF, DD, PD, and CF supervised and helped in the critical review and the editing of the manuscript and participated in the funding acquisition. All authors contributed to the article and approved the submitted version.

FUNDING

This research was supported by a grant from the Bpifrance/Métropole Européenne de Lille/Région Hauts de France (DOS0020745) and by a grant from Association Nationale Recherche Technologie (ANRT). This work was supported by the Hauts-de-France region funding through the ALIBIOTECH research program. The batch fermentation experiments and the LC-MS/MS analysis were performed on the REALCAT platform funded by a French governmental subsidy managed by the French National Research Agency (ANR) within the frame of the “Future Investments” program (ANR-11-EQPX-0037). The Hauts-de-France region and the FEDER, the Ecole Centrale de Lille, and the Centrale Initiatives Foundation are also warmly acknowledged for their financial contributions to the acquisition of REALCAT platform equipment.

ACKNOWLEDGMENTS

The authors would like to thank Robert Marmulla from Roquette for his donation of maltodextrins.

SUPPLEMENTARY MATERIAL

The Supplementary Material for this article can be found online at: <https://www.frontiersin.org/articles/10.3389/fbioe.2020.585815/full#supplementary-material>

- Ahtesh, F. B., Stojanovska, L., and Apostolopoulos, V. (2018). Anti-hypertensive peptides released from milk proteins by probiotics. *Maturitas* 115, 103–109. doi: 10.1016/j.maturitas.2018.06.016
- Alhaj, O. A., Metwalli, A. A., Ismail, E. A., Ali, H. S., Al-Khalifa, A. S., and Kanekanian, A. D. (2018). Angiotensin converting enzyme-inhibitory activity and antimicrobial effect of fermented camel milk (*Camelus dromedarius*). *Int. J. Dairy Technol.* 71, 27–35. doi: 10.1111/1471-0307.12383
- Bakr Shori, A., and Salihin Baba, A. (2015). Fermented milk derives bioactive peptides with antihypertensive effects. *Integr. Food Nutr. Metab.* 2, 180–183. doi: 10.15761/IFNM.1000126

- Boiani, M., McLoughlin, P., Auty, M. A. E., FitzGerald, R. J., and Kelly, P. M. (2017). Effects of depleting ionic strength on 31 P nuclear magnetic resonance spectra of micellar casein during membrane separation and diafiltration of skim milk. *J. Dairy Sci.* 100, 6949–6961. doi: 10.3168/jds.2016-12351
- Caron, J., Cudennec, B., Domenger, D., Belguesmia, Y., Flahaut, C., Kouach, M., et al. (2016). Simulated GI digestion of dietary protein: release of new bioactive peptides involved in gut hormone secretion. *Food Res. Int.* 89, 382–390. doi: 10.1016/j.foodres.2016.08.033
- Caron, J., Domenger, D., Belguesmia, Y., Kouach, M., Lesage, J., Goossens, J.-F., et al. (2015). Protein digestion and energy homeostasis: how generated peptides may impact intestinal hormones? *Food Res. Int.* 88, 310–318. doi: 10.1016/j.foodres.2015.12.018
- Choudhury, B., and Swaminathan, T. (2006). Lactic acid fermentation in cell-recycle membrane bioreactor. *Appl. Biochem. Biotechnol.* 128, 171–183. doi: 10.1385/abab:128:2:171
- Coutte, F., Lecouturier, D., Firdaous, L., Kapel, R., Bazinet, L., Cabassud, C., et al. (2017). “Recent trends in membrane bioreactors,” in *Current Developments in Biotechnology and Bioengineering*, eds C. Larroche, M. Á. Sanromán, G. Du, and A. Pandey (Amsterdam: Elsevier), 279–311. doi: 10.1016/b978-0-444-63663-8.00010-0
- Cross, K. J., Huq, N. L., Palamara, J. E., Perich, J. W., and Reynolds, E. C. (2005). Physicochemical characterisation of casein phosphopeptide-amorphous calcium phosphate nanocomplexes. *J. Biol. Chem.* 280, 15362–15369. doi: 10.1074/jbc.M413504200
- Daliri, E., Oh, D., and Lee, B. (2017). Bioactive peptides. *Foods* 6:32. doi: 10.3390/foods6050032
- De Man, J. C., Rogosa, M., and Sharpe, M. E. (1960). A medium used for the cultivation of *Lactobacilli*. *J. Appl. Bacteriol.* 23, 130–135. doi: 10.1111/j.1365-2672.1960.tb00188.x
- Elfahri, K. R., Donkor, O. N., and Vasiljevic, T. (2014). Potential of novel *Lactobacillus helveticus* strains and their cell wall bound proteases to release physiologically active peptides from milk proteins. *Int. Dairy J.* 38, 37–46. doi: 10.1016/j.idairyj.2014.03.010
- Fernandez, M. A., Panahi, S., Daniel, N., Tremblay, A., and Marette, A. (2017). Yogurt and cardiometabolic diseases: a critical review of potential mechanisms. *Adv. Nutr.* 8, 812–829. doi: 10.3945/an.116.013946
- Fira, D., Kojic, M., Banina, A., Spasojevic, I., Strahinic, I., and Topisirovic, L. (2001). Characterization of cell envelope-associated proteinases of thermophilic lactobacilli. *J. Appl. Microbiol.* 90, 123–130. doi: 10.1046/j.1365-2672.2001.01226.x
- Georgalaki, M., Zoumpopoulou, G., Mavrogonatou, E., Van Driessche, G., Alexandraki, V., Anastasiou, R., et al. (2017). Evaluation of the antihypertensive angiotensin-converting enzyme inhibitory (ACE-I) activity and other probiotic properties of lactic acid bacteria isolated from traditional Greek dairy products. *Int. Dairy J.* 75, 10–21. doi: 10.1016/j.idairyj.2017.07.003
- Griffiths, M. W., and Tellez, A. M. (2013). *Lactobacillus helveticus*: the proteolytic system. *Front. Microbiol.* 4:30. doi: 10.3389/fmicb.2013.00030
- Guang, C., Phillips, R. D., Jiang, B., and Milani, F. (2012). Three key proteases - Angiotensin-I-converting enzyme (ACE), ACE2 and renin - within and beyond the renin-angiotensin system. *Arch. Cardiovasc. Dis.* 105, 373–385. doi: 10.1016/j.acvd.2012.02.010
- Hebert, E. M., Raya, R. R., and De Giori, G. S. (2000). Nutritional requirements and nitrogen-dependent regulation of proteinase activity of *Lactobacillus helveticus* CRL 1062. *Appl. Environ. Microbiol.* 66, 5316–5321. doi: 10.1128/AEM.66.12.5316-5321.2000
- Hernández-Ledesma, B., Amigo, L., Ramos, M., and Recio, I. (2004). Application of high-performance liquid chromatography-tandem mass spectrometry to the identification of biologically active peptides produced by milk fermentation and simulated gastrointestinal digestion. *J. Chromatogr. A* 1049, 107–114. doi: 10.1016/j.chroma.2004.07.025
- Jin, Y., Yu, Y., Qi, Y., Wang, F., Yan, J., and Zou, H. (2016). Peptide profiling and the bioactivity character of yogurt in the simulated gastrointestinal digestion. *J. Proteomics* 141, 24–46. doi: 10.1016/j.jprot.2016.04.010
- Kliche, T., Li, B., Bockelmann, W., Habermann, D., Klempt, M., de Vrese, M., et al. (2017). Screening for proteolytically active lactic acid bacteria and bioactivity of peptide hydrolysates obtained with selected strains. *Appl. Microbiol. Biotechnol.* 101, 7621–7633. doi: 10.1007/s00253-017-8369-3
- Korhonen, H. (2009). Milk-derived bioactive peptides: from science to applications. *J. Funct. Foods* 1, 177–187. doi: 10.1016/j.jff.2009.01.007
- Lamothe, S., Rémillard, N., Tremblay, J., and Britten, M. (2017). Influence of dairy matrices on nutrient release in a simulated gastrointestinal environment. *Food Res. Int.* 92, 138–146. doi: 10.1016/j.foodres.2016.12.026
- Li, C., Kwok, L.-Y., Mi, Z., Bala, J., Xue, J., Yang, J., et al. (2017). Characterization of the angiotensin-converting enzyme inhibitory activity of fermented milks produced with *Lactobacillus casei*. *J. Dairy Sci.* 100, 9495–9507. doi: 10.3168/jds.2017-12970
- Lowry, O. H., Rosebrough, N. J., Farr, L. A., and Randall, R. J. (1951). Protein measurement with the folin phenol reagent. *J. Biol. Chem.* 193, 265–275. doi: 10.1016/0304-3894(92)87011-4
- Marco, M. L., Heeney, D., Binda, S., Cifelli, C. J., Cotter, P. D., Foligné, B., et al. (2017). Health benefits of fermented foods: microbiota and beyond. *Curr. Opin. Biotechnol.* 44, 94–102. doi: 10.1016/j.copbio.2016.11.010
- Matar, C., Amiot, J., Savoie, L., and Goulet, J. (1996). The effect of milk fermentation by *Lactobacillus helveticus* on the release of peptides during in vitro digestion. *J. Dairy Sci.* 79, 971–979. doi: 10.3168/jds.S0022-0302(96)76448-2
- McSweeney, P. L. H., and Fox, P. F. (1997). Chemical methods for the characterization of proteolysis in cheese during ripening. *Lait* 77, 41–76. doi: 10.1051/laite:199713
- Nielsen, S. D., Beverly, R. L., Qu, Y., and Dallas, D. C. (2017). Milk bioactive peptide database: a comprehensive database of milk protein-derived bioactive peptides and novel visualization. *Food Chem.* 232, 673–682. doi: 10.1016/j.foodchem.2017.04.056
- Nongonierma, A. B., and FitzGerald, R. J. (2015). The scientific evidence for the role of milk protein-derived bioactive peptides in humans: a review. *J. Funct. Foods* 17, 640–656. doi: 10.1016/j.jff.2015.06.021
- Ohsawa, K., Satsu, H., Ohki, K., Enjoh, M., Takano, T., and Shimizu, M. (2008). Producibility and digestibility of antihypertensive?-casein tripeptides, Val-pro-pro and ile-pro-pro, in the gastrointestinal tract: analyses using an in vitro model of mammalian gastrointestinal digestion. *J. Agric. Food Chem.* 56, 854–858. doi: 10.1021/jf072671n
- Pihlanto, A. (2013). “Lactic fermentation and bioactive peptides,” in *Lactic Acid Bacteria – R & D for Food, Health and Livestock Purposes*, ed. J. Marcelino Kongo (London: IntechOpen), 310–331.
- Pripp, A. H., Isaksson, T., Stepaniak, L., and Sørhaug, T. (2004). Quantitative structure-activity relationship modelling of ACE-inhibitory peptides derived from milk proteins. *Eur. Food Res. Technol.* 219, 579–583. doi: 10.1007/s00217-004-1004-4
- Probst, M., Fritsch, A., Wagner, A., and Insam, H. (2013). Biowaste: a *Lactobacillus* habitat and lactic acid fermentation substrate. *Bioresour. Technol.* 143, 647–652. doi: 10.1016/j.biortech.2013.06.022
- Raveschot, C., Cudennec, B., Coutte, F., Flahaut, C., Fremont, M., Drider, D., et al. (2018). Production of bioactive peptides by *Lactobacillus* species: from gene to application. *Front. Microbiol.* 9:2354. doi: 10.3389/fmicb.2018.02354
- Raveschot, C., Cudennec, B., Deracinois, B., Frémont, M., Vaeremans, M., Dugersuren, J., et al. (2020). Proteolytic activity of *Lactobacillus* strains isolated from Mongolian traditional dairy products: a multiparametric analysis. *Food Chem.* 304, 125415. doi: 10.1016/j.foodchem.2019.125415
- Renhe, I. R. T., and Corredig, M. (2018). Effect of partial whey protein depletion during membrane filtration on thermal stability of milk concentrates. *J. Dairy Sci.* 101, 1–10. doi: 10.3168/JDS.2018-14407
- R core team (2016). *R: A Language and Environment for Statistical Computing*. Vienna: R Foundation for Statistical Computing.
- Sanchón, J., Fernández-Tomé, S., Miralles, B., Hernández-Ledesma, B., Tomé, D., Gaudichon, C., et al. (2018). Protein degradation and peptide release from milk proteins in human jejunum. Comparison with in vitro gastrointestinal simulation. *Food Chem.* 239, 486–494. doi: 10.1016/j.foodchem.2017.06.134
- Sentandreu, M. A., and Toldrá, F. (2006). A fluorescence-based protocol for quantifying angiotensin-converting enzyme activity. *Nat. Protoc.* 1, 2423–2427. doi: 10.1038/nprot.2006.349
- Sharma, S., Singh, R., and Rana, S. (2011). Bioactive peptides: a review. *Int. J. Bioautomat.* 15, 223–250.
- Shuang, Q., Tsuda, H., and Miyamoto, T. (2008). Angiotensin I-converting enzyme inhibitory peptides in skim milk fermented with *Lactobacillus helveticus* 130B4

- from camel milk in Inner Mongolia, China. *J. Sci. Food Agric.* 88, 2688–2692. doi: 10.1002/jsfa
- Solanki, D., Hati, S., and Sakure, A. (2017). In silico and in vitro analysis of novel Angiotensin I-Converting Enzyme (ACE) inhibitory bioactive peptides derived from fermented camel milk (*Camelus dromedarius*). *Int. J. Pept. Res. Ther.* 23, 441–459. doi: 10.1007/s10989-017-9577-5
- Taleghani, H. G., Ghoreyshi, A. A., and Najafpour, G. (2017). Lactic acid production with in situ extraction in membrane bioreactor. *Appl. Food Biotechnol.* 4, 27–34. doi: 10.22037/afb.v4i1.13686
- Tang, J., Wang, X. C., Hu, Y., Ngo, H. H., and Li, Y. (2017). Dynamic membrane-assisted fermentation of food wastes for enhancing lactic acid production. *Bioresour. Technol.* 234, 40–47. doi: 10.1016/j.biortech.2017.03.019
- Wakai, T., and Yanamoto, N. (2012). “Antihypertensive peptides specific to *Lactobacillus helveticus* fermented milk,” in *Biotechnology - Molecular Studies and Novel Applications for Improved Quality of Human Life*, ed. R. Sammour (London: IntechOpen), 159–172.
- Wu, J., Liao, W., and Udenigwe, C. C. (2017). Revisiting the mechanisms of ACE inhibitory peptides from food proteins. *Trends Food Sci. Technol.* 69, 214–219. doi: 10.1016/j.tifs.2017.07.011
- Wu, S., Qi, W., Li, T., Lu, D., Su, R., and He, Z. (2013). Simultaneous production of multi-functional peptides by pancreatic hydrolysis of bovine casein in an enzymatic membrane reactor via combinational chromatography. *Food Chem.* 141, 2944–2951. doi: 10.1016/j.foodchem.2013.05.050
- Xu, G. Q., Chu, J., Wang, Y. H., Zhuang, Y. P., Zhang, S. L., and Peng, H. Q. (2006). Development of a continuous cell-recycle fermentation system for production of lactic acid by *Lactobacillus paracasei*. *Process Biochem.* 41, 2458–2463. doi: 10.1016/j.procbio.2006.05.022

Conflict of Interest: CR and MF are affiliated with VF Bioscience SAS, France, a company commercializing lactic acid bacteria strains for use as probiotics or dairy starters.

The remaining authors declare that the research was conducted in the absence of any commercial or financial relationships that could be construed as a potential conflict of interest.

Copyright © 2020 Raveschot, Deracinois, Bertrand, Flahaut, Frémont, Drider, Dhulster, Cudennec and Coutte. This is an open-access article distributed under the terms of the Creative Commons Attribution License (CC BY). The use, distribution or reproduction in other forums is permitted, provided the original author(s) and the copyright owner(s) are credited and that the original publication in this journal is cited, in accordance with accepted academic practice. No use, distribution or reproduction is permitted which does not comply with these terms.



Revisiting the Growth Modulon of *Corynebacterium glutamicum* Under Glucose Limited Chemostat Conditions

Michaela Graf^{1†}, Thorsten Haas^{1†}, Attila Teleki¹, André Feith¹, Martin Cerff², Wolfgang Wiechert², Katharina Nöh², Tobias Busche^{3,4}, Jörn Kalinowski³ and Ralf Takors^{1*}

OPEN ACCESS

Edited by:

Christoph Herwig,
Vienna University of Technology,
Austria

Reviewed by:

Zhen Chen,
Tsinghua University, China
Bernhard Elkmanns,
University of Ulm, Germany

*Correspondence:

Ralf Takors
takors@ibvt.uni-stuttgart.de

[†]These authors have contributed
equally to this work

Specialty section:

This article was submitted to
Bioprocess Engineering,
a section of the journal
Frontiers in Bioengineering and
Biotechnology

Received: 17 July 2020

Accepted: 23 September 2020

Published: 15 October 2020

Citation:

Graf M, Haas T, Teleki A, Feith A,
Cerff M, Wiechert W, Nöh K,
Busche T, Kalinowski J and Takors R
(2020) Revisiting the Growth Modulon
of *Corynebacterium glutamicum*
Under Glucose Limited Chemostat
Conditions.
Front. Bioeng. Biotechnol. 8:584614.
doi: 10.3389/fbioe.2020.584614

¹ Institute of Biochemical Engineering, University of Stuttgart, Stuttgart, Germany, ² Institute of Bio- and Geosciences, IBG-1: Biotechnology, Forschungszentrum Jülich GmbH, Jülich, Germany, ³ Center for Biotechnology, Bielefeld University, Bielefeld, Germany, ⁴ Institute for Biology-Microbiology, Freie Universität Berlin, Berlin, Germany

Increasing the growth rate of the industrial host *Corynebacterium glutamicum* is a promising target to rise productivities of growth coupled product formation. As a prerequisite, detailed knowledge about the tight regulation network is necessary for identifying promising metabolic engineering goals. Here, we present comprehensive metabolic and transcriptional analysis of *C. glutamicum* ATCC 13032 growing under glucose limited chemostat conditions with $\mu = 0.2, 0.3$, and 0.4 h^{-1} . Intermediates of central metabolism mostly showed rising pool sizes with increasing growth. ¹³C-metabolic flux analysis (¹³C-MFA) underlined the fundamental role of central metabolism for the supply of precursors, redox, and energy equivalents. Global, growth-associated, concerted transcriptional patterns were not detected giving rise to the conclusion that glycolysis, pentose-phosphate pathway, and citric acid cycle are predominately metabolically controlled under glucose-limiting chemostat conditions. However, evidence is found that transcriptional regulation takes control over glycolysis once glucose-rich growth conditions are installed.

Keywords: *Corynebacterium glutamicum*, growth rate, metabolome, transcriptome, continuous bioprocess, stationary flux analysis

Abbreviations: 2/3PG, 2-/3-phosphoglyceric acid; aKG, alpha ketoglutarate; ASN, L-asparagin; ASP, L-aspartate; ATP, adenosine triphosphate; CDW, cell dry weight; CIT, citrate; CLE, carbon labeling experiment; DEG, differentially expressed gene; DHAP, dihydroxyacetone phosphate; EMP, Emden-Meyerhof-Parnas; F6P, fructose 6-phosphate; FBP, fructose 1,6-bisphosphate; FFC, flux fold change; FUM, fumarate; GAP, glyceraldehyde 3-phosphate; GLC, glucose; GLU, L-glutamate; ICIT, isocitrate; LEU, L-leucine; LFC, log fold change; MAL, L-malate; MET, L-methionine; MFA, metabolic flux analysis; MID, mass isotopomer distribution; NADPH, nicotinamide adenine dinucleotide phosphate; OAA, oxaloacetate; OD₆₀₀, optical density; OED, optimal experimental design; P5P, pentose-5-phosphate; PEP, phosphoenolpyruvate; PCA, protocatechuic acid; PPP, pentose phosphate pathway; PRO, L-proline; RT, residence time; RNA, ribonucleic acid; S7P, sedoheptulose 7-phosphate; SUC, succinate; SSR, sum of squared residuals; TCA, tricarboxylic acid; TIC, total inorganic carbon; TOC, total organic carbon; WT, wild-type.

INTRODUCTION

Corynebacterium glutamicum, discovered in 1957 as a soil bacterium, has gained prominent acceptance in industry for the production of amino acids, organic acids, and even proteins (Hermann, 2003; Wendisch et al., 2006; Freudl, 2017). Beside the broad availability of fine-tuned tools to genetically engineer the strain, *C. glutamicum* offers intrinsic features which are of high interest for use in industrial production. In particular, the robustness for large-scale application is one of its outstanding traits (Vertès et al., 2012).

However, a putative drawback lies in the somewhat reduced growth rates compared to other hosts such as *Escherichia coli*. With about 0.4 h^{-1} wild-type (WT) *C. glutamicum* shows only moderate growth in synthetic media in classical batch cultivations (Blombach et al., 2013; Grünberger et al., 2013; Graf et al., 2018; Haas et al., 2019) compared to about $0.7\text{--}0.8 \text{ h}^{-1}$ maximum growth rate of other prokaryotes such as *E. coli*, 1.7 h^{-1} for the putative future competitors *Vibrio natriegens* (Hoffart et al., 2017) and *Geobacillus* LC300 with 2.15 h^{-1} (Long et al., 2017). Relatively low space-time yields compared to other hosts may be the consequence. Therefore, several authors have tried to boost the growth of *C. glutamicum* applying growth evolution studies aiming for a “natural” selection of a faster growing *C. glutamicum* strain (Pfeifer et al., 2017; Wang et al., 2018; Graf et al., 2019). As a result, several gene mutations were identified serving as putative targets for metabolic engineering toward higher growth under controlled conditions.

Besides these efforts to accelerate the growth rate, other studies aimed to at understand growth regulation of *C. glutamicum* deciphering potential limitations to improve growth coupled productivities (Grünberger et al., 2013; Unthan et al., 2014). More precisely, the cell's intrinsic regulation was analyzed by employing tools from the systems biology toolbox, i.e., metabolomics, transcriptomics, fluxomics, and proteomics. An essential prerequisite for these “omics” disciplines is the establishment of highly reproducible and stable experimental cultivation environments (Hoskisson and Hobbs, 2005; Bull, 2010). Therefore, continuous bioprocess setups are commonly used since they make it possible to grow a cell population in a metabolic steady state by limiting one growth substrate, e.g., the carbon source. Manipulation of the dilution rate translates to an adjustment of limiting substrate supply whereby the growth rate of the investigated strain can be ultimately set to a precise rate. With regard to *C. glutamicum* WT ATCC 17965, continuous chemostat processes were performed by Coccagn-Bousquet et al. (1996) to examine growth kinetics and glucose consumption at $\mu = 0.1\text{--}0.55 \text{ h}^{-1}$. Their results hinted at the presence of a secondary transport system for glucose beside the phosphotransferase system (PTS) which was confirmed by two different groups later (Ikeda et al., 2011; Lindner et al., 2011). Silberbach et al. (2005) were among the first to perform systems biology analysis on *C. glutamicum* ATCC 13032 by analyzing the cell's transcriptional and proteomic response to ammonium limitation at two different growth rates. They identified growth rate dependent expression of ribosomal proteins and of F_0F_1 subunits of ATP-synthase. Another study

with a systems biology viewpoint was recently performed by Noack et al. (2017) conducting chemostat cultivations to record the proteomic response of *C. glutamicum* WT ATCC 13032 within a broad range of growth rates ($\mu = 0.05\text{--}0.35 \text{ h}^{-1}$). Under the tested glucose-limited growth conditions, Noack et al. (2017) concluded that metabolic fluxes within *C. glutamicum*'s central carbon metabolism are likely more affected by concentrations of local substrates and allosteric metabolite effectors than by the concentration of enzymes. Recently, another systems biology study was performed in traditional non-substrate limited batch cultivations to investigate determinants of global regulation orchestrating the growth of *C. glutamicum* (Haas et al., 2019). The so-called growth modulon was discovered by investigating transcriptional dynamics of strains in batch cultivation. Growth control was observed to be well distributed within a tightly networked system of transcriptional regulators controlling different branches of central metabolism.

Based on these recent systems biology insights, the current study tries to broaden knowledge about the strain's metabolic, transcriptional, and fluxomic response to different growth rates. Accordingly, we continuously cultivated *C. glutamicum* under glucose-limited growth conditions setting dilution rates of 0.2, 0.3, and 0.4 h^{-1} , applying the same strain as Haas et al. (2019). We analyzed whether the transcriptional regulatory response identified in glucose-rich batch cultures is similar to the one operational under chemostat conditions at similar growth rates. Thereof we investigated how comparable transcriptional data of batch and continuous culture are. In other words we wonder: How similar are regulatory patterns of *C. glutamicum* growing with equal rates but under different nutrient availability?

MATERIALS AND METHODS

Bacterial Strain and Pre-culture Cultivation

All cultivations of this study were performed with the WT strain *C. glutamicum* ATCC 13032 obtained from the American Type Culture Collection (ATCC, Manassas, VA, United States). Cells from a glycerol stock working cell bank were spread on $2 \times$ tryptone-yeast extract ($2 \times$ TY) medium (Sambrook, 2001) agar plates and incubated for 48–60 h at 30°C . Thereof, extracted colonies served to inoculate 5 mL sterile $2 \times$ TY medium in glass reaction tubes and were incubated for 8 h at 30°C on a bench-top rotary shaker (Infors HT, Bottmingen, Switzerland) at 120 rpm. Subsequently, individual shaking flasks filled with 50 mL of sterile CGXII minimal medium (Grünberger et al., 2013) supplemented with 40 g L^{-1} glucose were inoculated with the pre-culture content of one glass reaction tube, respectively. Shaking flask pre-cultures were incubated overnight at 30°C and 120 rpm.

Continuous Bioreactor Cultivations Bioreactor Setup

Continuous chemostat processes with *C. glutamicum* were conducted in a 3 L steel bioreactor (KLF 2000, Bioengineering, Switzerland) equipped with process control (Lab view 2010,

National Labs). Cooling and heating elements and a temperature sensor (Pt100, Bioengineering, Switzerland) ensured constant cultivation temperature of 30°C. Mixing was realized with a six blade Rushton turbine. A pressure probe (PR-35 X HT, KELLER Druckmesstechnik, Jestetten, Germany) and an automatic exhaust valve were installed at the head of the reactor to regulate pressure (1.5 bar). For aeration, compressed air was channeled through a mass flow controller (MFC GFC171S, Analyt-MTC GmbH, Müllheim, Germany) and filtered aseptically (Midisart® 2000, Sartorius Stedim Biotech, Goettingen, Germany) before entering the bioreactor. Dissolved oxygen was monitored by an amperometric pO₂ electrode (InPro 6800, Mettler-Toledo, Germany) and pH with a conventional pH probe (405-DPAS-SC-K8S, Mettler-Toledo, Germany). Molar fractions of oxygen and carbon dioxide in the exhaust gas were measured by a sensor (BCP-O₂/CO₂, BlueSens, Germany).

To enable continuous processes in chemostat mode at fixed dilution rates (D , h⁻¹) equaling the growth rate (μ , h⁻¹; see section “Determination of Kinetic Parameters”), the advanced controller scheme described in Graf et al. (2019) was employed. Thereby, a defined reaction volume in the bioreactor was maintained and constant feed and harvest rates were ensured. Prior to all cultivations, the reactor was sterilized with 1 mol L⁻¹ K₂HPO₄/KH₂HPO₄ buffer (pH 7) for 20 min at 121°C. Prior removal of the buffer, the drain of the reactor was sterilized *in situ* with pure steam for 10 min.

Chemostat Processes at $\mu = 0.2, 0.3, 0.4$ h⁻¹

All chemostat processes started with an initial batch cultivation. Therefore, sterile CGXII minimal medium (Grünberger et al., 2013) supplemented with 12 g D-glucose L⁻¹ was pumped from a stirred sterile medium feed reservoir (later employed for continuous mode) into the sterile bioreactor until a volume of 1.4 L was reached. The required amount of *C. glutamicum* biomass from pre-culture shaking flasks (see section “Bacterial Strain and Pre-culture Cultivation”) was harvested and resuspended in 100 mL 9 g NaCl L⁻¹ solution yielding an inoculation biomass density of 0.3 g_{CDW} L⁻¹ and a cultivation volume of 1.5 L. During batch and continuous cultivation, pH was controlled at 7.4 by automatically adding 25% (v/v) NH₄OH solution. In batch mode, pO₂ was maintained above 30% by 50 rpm stepwise increase of the impeller speed (initial: 250 rpm) and analogous rise of aeration rate by 0.15 L min⁻¹ (initial: 0.15 L min⁻¹). Antifoam agent (Struktol® J 647, Schill + Seilacher, Hamburg, Germany) was manually added when necessary. After about 7.5 h of exponential growth, the sharp increase of the pO₂ signal indicated glucose depletion.

Thereupon, the continuous mode was initiated by starting the control regime (Graf et al., 2019), adding antifoam agent constantly and fixing impeller speed and aeration rate to 700 rpm and 1 L min⁻¹, respectively. During the course of one continuous experiment, dilution rates of $D = 0.2, 0.3$, and 0.4 h⁻¹ were sequentially installed. Constant antifoam concentrations were achieved by increasing related feed rates proportionally (80, 120, 160 μ L h⁻¹). Sampling of each growth rate was performed after at least five residence

times (RTs), i.e., 25, 16.67, 12.5 h, respectively. Accordingly, the achievement of a metabolic steady state of the culture was ensured (Zamboni et al., 2009). Sampling comprised withdrawing biosuspension for biomass determination [optical density (OD₆₀₀) and cell dry weight (CDW) measurements], providing cell-free filtrates for extracellular metabolite analyses, and determining total inorganic carbon (TIC) and organic carbon (TOC) as described in the **Supplementary Material** section “Analysis of Exometabolome.” Moreover, intracellular metabolome and transcriptome samples were taken and analyzed as described in the same **Supplementary Material** sections “Sampling, Quenching, and Extraction for Absolute Quantification of Intracellular Pool Concentrations” and “Flux Estimation,” respectively. Non-labeled intracellular pools were measured by HILIC-based QQQ-MS/MS analysis (see **Supplementary Material** section “LC-MS-Based Quantification of Intracellular Pool Concentrations and ¹³C-Labeling Dynamics”) and absolutely quantified by isotope dilution mass spectrometry (IDMS) with a constant addition of (U-¹³C)-labeled *C. glutamicum* extracts (see **Supplementary Material** section “Generation of Fully ¹³C-Labeled *C. glutamicum* extracts for IDMS”). Apart from transcriptome samples, conventional and metabolome samples were withdrawn 3× in 1.5 h intervals at each growth rate. Continuous chemostat processes at $D = 0.2, 0.3$, and 0.4 h⁻¹ were conducted in biological triplicates following the described scheme.

¹³C-Labeling Experiment

The ¹³C-carbon labeling experiment (CLE) in chemostat mode ($D = 0.4$ h⁻¹) was initiated with a batch cultivation as described in section “Chemostat Processes at $\mu = 0.2, 0.3, 0.4$ h⁻¹,” but aiming for a working volume of 1.2 L instead of 1.5 L. Therefore, 1.1 L sterile CGXII minimal medium (Grünberger et al., 2013) supplemented with 12 g D-glucose L⁻¹ was retrieved from the sterile feed reservoir and stirrer speed and aeration were set to 600 rpm and 0.8 L min⁻¹, respectively.

Unlimited batch growth prevailed for 7.45 h ($\mu = 0.42$ h⁻¹) until glucose was depleted from the medium. The continuous mode was started by feeding fresh supplemented CGXII medium with a dilution rate of 0.4 h⁻¹ while keeping the working volume constant (1.2 L) and constantly feeding 200 μ L h⁻¹ antifoam agent to prevent excessive foaming. After 12.5 h equaling five RTs, online measurements of O₂ and CO₂ in the exhaust gas indicated a metabolic steady state of the culture. Conventional sampling was performed as described in **Supplementary Material** section “Analysis of Exometabolome.” After five more RTs (12.5 h), the CGXII medium feed containing non-labeled (U-¹²C)-D-glucose was switched to labeled CGXII feed containing 67% (U-¹³C)-D-glucose and 33% (1-¹³C)-D-glucose according to the previously performed tracer design (see section “A priori Tracer Design”). After four RTs (10 h), samples for intracellular isotopologue metabolome analyses were withdrawn (see **Supplementary Material** section “Sampling, Quenching, and Extraction for Quantification of ¹³C-Isotopic Labeling Dynamics”) as a stationary isotopic enrichment in *C. glutamicum*’s intracellular

metabolites was expected at this time. Isotopic distributions of ^{13}C -labeled and non-labeled intracellular pools of analog samples were quantified by HILIC-based QTOF-HRMS analysis (see **Supplementary Material** section “LC-MS-Based Quantification of Intracellular Pool Concentrations and ^{13}C -Labeling Dynamics”). For technical replicates of this measurement, intracellular metabolome samples were withdrawn 30, 20, and 10 min before reaching four RTs, and 10 min afterward.

Transcriptome Analysis

Transcriptome sampling was performed by withdrawing 1 mL biosuspension from the bioreactor, centrifuging at $20,817 \times g$ and 4°C for 30 s (5430 R, Eppendorf, Hamburg, Germany), discarding the supernatant and immediately quenching the biomass pellet in liquid nitrogen. Extraction and isolation of RNA from the samples, whole transcriptome sequencing, read mapping, and raw read count calculation was performed as described in Haas et al. (2019). The raw sequencing data have been deposited in the ArrayExpress database at EMBL-EBI under accession number E-MTAB-9371. Transcript data analysis was performed using R version 3.5.0. Raw read counts were normalized using the Relative Log Expression function of the DESeq2 (Love et al., 2014) package. Differential gene expression was determined using the maSigPro (Nueda et al., 2014) package in “generalized linear model” mode. Clustering of the genes according to expression trend was performed through hclust as implemented in maSigPro.

^{13}C -Metabolic Flux Analysis: Modeling and Computational Procedures

Metabolic Network Model for ^{13}C -MFA

The metabolic network model of *C. glutamicum* WT was taken from Kappelmann et al. (2016) and slightly modified for experimental design and flux fitting (see **Supplementary Material** section “ ^{13}C -MFA”). The models were composed according to the workflow described in Nöh et al. (2015) and formulated in FluxML format (Beyß et al., 2019). The models contain the major pathways of central carbon metabolism such as glycolysis, pentose phosphate pathway (PPP), anaplerotic reactions, tricarboxylic acid (TCA) cycle, and all pathways for amino acid synthesis. In addition, protocatechuic acid (PCA) oxidation into the TCA cycle was taken into account (Unthan et al., 2014). A lumped biomass equation was formulated representing the cellular composition (Eggeling and Bott(eds), 2005). Transport reactions were considered for glucose, PCA and carbon dioxide (CO_2). Carbon atom transitions were formulated for each reaction. For reactions with C-symmetric reactants (in the TCA cycle and lysine synthesis), scrambling reactions were introduced and for each variant equal fluxes assumed. The metabolic model used for flux fitting comprises 45 balanced intracellular and 4 non-balanced extracellular metabolite pools, connected through 87 metabolic reactions (22 bidirectional and 65 unidirectional). The model has 27 degrees of freedom (7 net and 20 exchange fluxes), whereas

the network model used for tracer design was slightly simpler (22 free parameters, 5 net fluxes, and 17 exchange fluxes). Full model specifications are provided in the **Supplementary Data FluxML Files**.

A priori Tracer Design

To determine an informative, yet cost efficient tracer mixture for the CLE at $D = 0.4 \text{ h}^{-1}$, an experimental design study was performed using the high-performance simulation framework 13CFLUX2 (Möllney et al., 1999; Weitzel et al., 2013). To this end, a measurement configuration was formulated on the basis of a previous ^{13}C -tracer quantification study (Feith et al., 2019), and six glucose tracers were considered [(U- ^{12}C)-, (U- ^{13}C)-, (1- ^{13}C)-, (1,2- ^{13}C)-, (6- ^{13}C)-, and (5,6- ^{13}C)-D-glucose]. The model used for the design as well as the assumed measured fragments and rates including their corresponding expected errors are detailed in the **Supplementary Material** section “Model Setup.”

External Rate Estimation

For the CLE at $D = 0.4 \text{ h}^{-1}$, extracellular biomass-specific rates (growth rate μ , glucose consumption rate r_{GLC} , CO_2 -production rate r_{CO_2} , PCA uptake rate r_{PCA}) were estimated using an ODE-based bioprocess model adapted from Cerff et al. (2013) (see details in **Supplementary Material** section “Bioprocess Model Used for External Rate Estimation”). Model parameters were estimated using weighted least squares regression. Standard deviations of model parameters were estimated using Monte-Carlo simulations (1,000 runs with random initial parameter values). Estimates of biomass-specific rates including their errors were used for ^{13}C -metabolic flux analysis (^{13}C -MFA). The bioprocess model was implemented in Matlab (Mathworks, Natick, MA, United States). Monte Carlo simulations were performed with custom Matlab scripts.

Intracellular Flux Estimation

After measurements became available, metabolic fluxes were estimated by minimizing the variance-weighted sum of squared residual (SSR) between the simulated quantities and the measurements, i.e., the extracellular biomass specific rates (**Supplementary Table 3**) and mass isotopomer distributions (MIDs; see **Supplementary Material** section “Flux Estimation”). Prior to ^{13}C -MFA, raw MIDs were corrected for natural isotope abundance using the ICT-toolbox (Jungreuthmayer et al., 2016). Corrected MIDs were derived for the sample taken at $t = 10.17 \text{ h}$ after introduction of ^{13}C -label. MID standard deviations were set to 2.5 mol%, based on analytical experience and supported by the analysis of four samples drawn in the isotopic quasi-stationary regime (9.67–10.17 h after introduction of ^{13}C -tracer). In total 170 measurements (164 labeling data for 28 metabolites and 6 biomass-specific extracellular rates) were used to determine 55 model parameters (27 free fluxes and 28 measurement group scale factors).

Flux estimation was performed using 13CFLUX2 using the optimizer LINCOA (Powell, 2015) and the NAG

optimization toolbox (National Algorithms Group, Oxford, United Kingdom). To minimize the risk of suboptimal local regression solutions, a multi-start heuristic was applied combining gradient-free (LINCOA) and gradient-based (NAG) optimizers, which was initialized 1,000 times from random starting flux distributions. The set of fluxes that resulted in the minimum weighted deviation between experimentally observed (MID and extracellular rates) and simulated data was reported as best flux estimate for the *in vivo* flux distribution. Statistical analysis was performed according to the method described in Wiechert et al. (1997), yielding simultaneous flux confidence intervals.

Determination of Kinetic Parameters

Growth Rate

According to the continuous mass balance (cf. Eq. 1 in **Supplementary Material** section “Bioprocess Model Used for External Rate Estimation”) and under the assumption of metabolic stationarity of the culture, the set dilution rate D (in h^{-1}) equals the exponential growth rate μ (in h^{-1}) of the culture:

$$\mu = D$$

Metabolic steady states were ensured by employing the controller scheme described in Graf et al. (2019).

Biomass Specific Glucose Consumption Rate and Biomass-Glucose Yield

According to the continuous glucose mass balance (cf. Eq. 2 in **Supplementary Material** section “Bioprocess Model Used for External Rate Estimation”) and under the assumption of metabolic stationarity of the culture, the biomass-specific glucose consumption rate q_{GLC} (in $\text{g gCDW}^{-1} \text{h}^{-1}$) is:

$$q_{\text{GLC}} = D \cdot \frac{c_{\text{GLC,feed}}}{c_X}$$

where $c_{\text{GLC,feed}}$ (in g L^{-1}) is the glucose concentration of the feed medium and c_X (in g L^{-1}) is the biomass concentration of the culture. Residual glucose in cell free biosuspension samples was below the detection limit and was therefore neglected in the calculation.

Furthermore, the biomass-glucose yield ($Y_{X,\text{GLC}}$) was determined by:

$$Y_{X,\text{GLC}} = \frac{D}{q_{\text{GLC}}} = \frac{c_X}{c_{\text{GLC,feed}}}$$

Respiratory Rates

Biomass-specific respiratory rates (q_{O_2} , q_{CO_2}) were calculated by dividing volumetric oxygen consumption or carbon dioxide emission rates by the biomass concentration determined at set dilution rate (cf. Eq. 9 in **Supplementary Material** section “Bioprocess Model Used for External Rate Estimation”). The carbon dioxide emission rate was corrected by TIC-measurements using a total carbon-analyzer (Multi N/C 2100s, Analytik Jena, Jena, Germany).

RESULTS

Chemostat Cultivations at $\mu = 0.2, 0.3$, and 0.4 h^{-1}

Continuous Processes and Kinetic Parameters

Three biological replicates (A–C, **Figure 1**) were conducted in chemostat mode employing CGXII minimal medium (Grünberger et al., 2013) supplemented with 12 g D-glucose L^{-1} . After about 7.5 h batch phase [$\mu_{\text{max}} = (0.44 \pm 0.01) \text{ h}^{-1}$] the continuous mode was started with a dilution rate $D = 0.2 \text{ h}^{-1}$ (process time = 0), which was increased to 0.3 h^{-1} after ca. 28 h and to $D = 0.4 \text{ h}^{-1}$ after ca. 49 h. Three independent samples for OD, CDW, filtrate TC/TIC, metabolome, and transcriptome were withdrawn after five RTs within 1.5 h-intervals to monitor the respective metabolic steady-states at $D = 0.2, 0.3$, and 0.4 h^{-1} .

As illustrated in **Figure 1**, only minor differences occurred between the triplicates mirroring slightly varying feed glucose concentrations ($c_{\text{GLC,feed}} = 12.47 \pm 0.35 \text{ g L}^{-1}$). Biomass levels elevated from 5.87 ± 0.13 to $6.43 \pm 0.18 \text{ g L}^{-1}$ with rising D . By analogy, glucose-to-biomass yields rose from 0.47 ± 0.01 to $0.52 \pm 0.00 \text{ g gCDW}^{-1}$ (**Table 1**) which caused partially growth coupled changes of q_{GLC} , q_{O_2} , and q_{CO_2} . Respiratory quotients (RQ) remained at 1. All carbon balances closed well with 99 ± 1 , 98 ± 2 , and $96 \pm 3\%$ for the growth rates $\mu = 0.2, 0.3$, and 0.4 h^{-1} , respectively (data not shown). No residual glucose or *C. glutamicum* typical by-products such as acetate or pyruvate (Yokota and Lindley, 2005; Han et al., 2008a), lactate or alanine (Blombach et al., 2013) were detectable in biomass-free filtrates analyzed with non-targeted HILIC-QTOF-HRMS (Feith et al., 2019). The growth decoupled maintenance parameters $m_S = (0.44 \pm 0.04) \text{ mmol D-glucose gCDW}^{-1} \text{h}^{-1}$ and the growth coupled real glucose-to-biomass yield $1/Y_{X\text{GLC,real}} = 9.73 \pm 0.08 \text{ mmol gCDW}^{-1}$ (Pirt, 1982) are illustrated in **Figure 2**.

Metabolomics

To account for slightly increasing biomass concentrations, the volumes of extraction solution were adjusted for each sample yielding equal amounts of extracted biomass. Mean values and variances are listed in the **Supplementary Material** Excel File reflecting the analysis of technical and biological replicates (see **Figure 1**). As indicated in **Table 2**, biomass specific pools ranged between $0.01 \mu\text{mol gCDW}^{-1}$ [L-asparagin (ASN)] and $250 \mu\text{mol gCDW}^{-1}$ [L-glutamate (GLU)]. Very good reproducibility of pool sizes was found in biological replicates with low standard errors between 2 and 8%. Few exceptions are the cumulated citrate/isocitrate (CIT/ICIT) and L-proline (PRO) pools revealing standard errors of 13 and 25% at $\mu = 0.2 \text{ h}^{-1}$. Noteworthy, most pool sizes changed proportionally with growth assigning $\mu = 0.2 \text{ h}^{-1}$ either minimum or maximum contents (see **Figures 3, 4** and **Supplementary Figure 1**). The majority of metabolite pools increased with rising μ resulting in 1.2 to 11 times higher concentrations at $\mu = 0.4 \text{ h}^{-1}$ compared to $\mu = 0.2 \text{ h}^{-1}$.

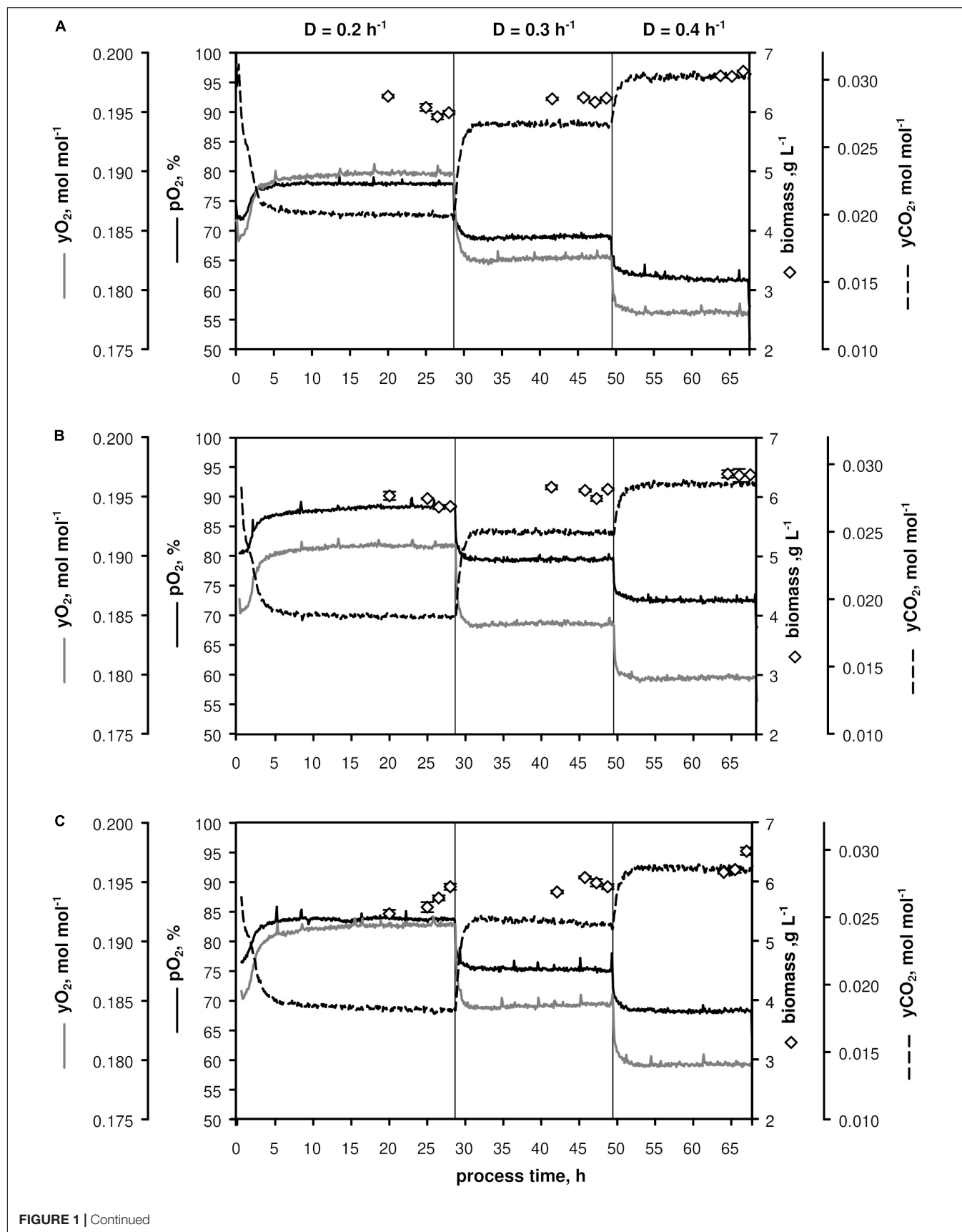


FIGURE 1 | Continued

FIGURE 1 | Process parameters of triplicate chemostats (A–C) with *C. glutamicum* WT: dissolved oxygen (pO_2), off-gas molar oxygen (y_{O_2}) and carbon dioxide (y_{CO_2}), biomass concentration (black diamonds). The dilution rate (D) was set to 0.2, 0.3, and 0.4 h^{-1} and sampling was performed after five residence times. Stirrer speed and aeration remained at 700 min^{-1} and 0.67 vvm, respectively. Depicted standard deviations of biomass measurements were calculated from three technical replicates per sample.

TABLE 1 | Listing of kinetic process parameters \pm standard deviation calculated from three individual chemostat processes (A, B, C; **Figure 1**) with *C. glutamicum* cultivated in CGXII medium supplemented with (12.47 ± 0.35) g D-glucose L^{-1} .

D, h^{-1}	$c_X, g L^{-1}$	$q_{Glc}, g g^{-1} h^{-1}$	$Y_{X, Glc}, g g^{-1}$	$q_{O_2}, mmol g^{-1} h^{-1}$	$q_{CO_2}, mmol g^{-1} h^{-1}$
0.20 ± 0.01	5.87 ± 0.13	0.42 ± 0.01	0.47 ± 0.01	5.36 ± 0.10	5.64 ± 0.14
0.30 ± 0.01	6.09 ± 0.12	0.62 ± 0.01	0.49 ± 0.01	7.16 ± 0.14	7.30 ± 0.18
0.40 ± 0.01	6.43 ± 0.18	0.77 ± 0.01	0.52 ± 0.01	8.15 ± 0.15	7.94 ± 0.10

c_X , biomass concentration; q_{Glc} , biomass specific glucose uptake rate; $Y_{X, Glc}$, biomass-glucose-yield; q_{O_2} , molar biomass specific oxygen uptake rate; q_{CO_2} , carbon dioxide evolution rate.

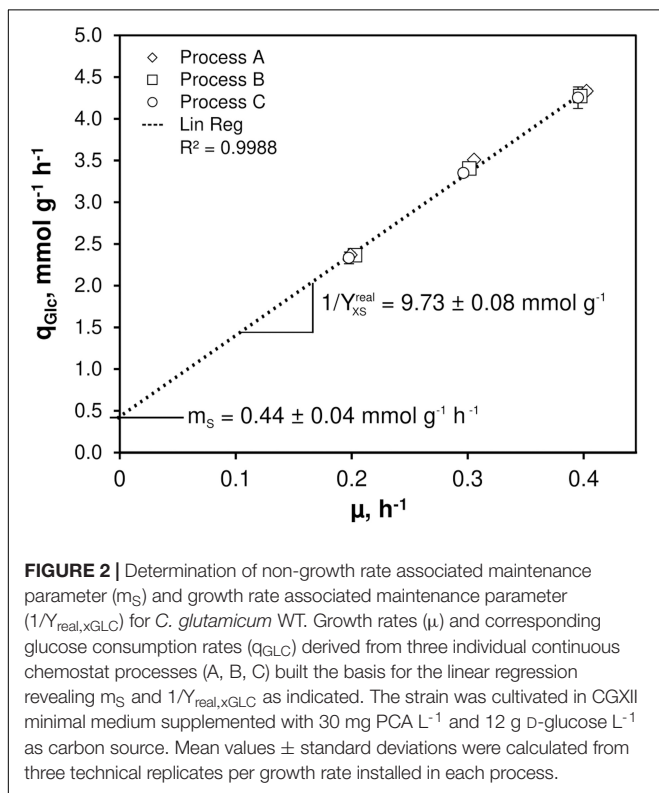


FIGURE 2 | Determination of non-growth rate associated maintenance parameter (m_s) and growth rate associated maintenance parameter ($1/Y_{real, X, Glc}$) for *C. glutamicum* WT. Growth rates (μ) and corresponding glucose consumption rates (q_{Glc}) derived from three individual continuous chemostat processes (A, B, C) built the basis for the linear regression revealing m_s and $1/Y_{real, X, Glc}$ as indicated. The strain was cultivated in CGXII minimal medium supplemented with 30 mg PCA L^{-1} and 12 g D-glucose L^{-1} as carbon source. Mean values \pm standard deviations were calculated from three technical replicates per growth rate installed in each process.

To be precise, metabolites of upper glycolysis [glucose 6-phosphate (G6P), fructose 6-phosphate (F6P), fructose 1,6-bisphosphate (FBP), dihydroxyacetone phosphate (DHAP)] linearly increased 5- to 11-fold from $\mu = 0.2$ to $0.4 h^{-1}$ which is contrasted by intermediates of lower glycolysis [pool of 2-/3-phosphoglyceric acid (2/3PG), phosphoenolpyruvate (PEP)] decreasing about 40% in pool size (**Figure 3**). In PPP, the summed pool of pentose 5-phosphate sugars (P5P), i.e., ribose 5-phosphate and ribulose 5-phosphate, showed comparably stable pool concentrations (10% decrease at $\mu = 0.3 h^{-1}$, 10% increase at $\mu = 0.4 h^{-1}$ compared to pool at $\mu = 0.2 h^{-1}$), whereas sedoheptulose 7-phosphate (S7P) revealed a steady rise.

In the TCA cycle (**Figure 4**), remaining trends are observed for alpha ketoglutarate (aKG) and succinate (SUC). In contrast, fumarate (FUM) and L-malate (MAL) showed linear increases between 1.5- and 2-fold over μ . By trend, amino acids, building blocks of protein synthesis, predominately showed rising pool sizes with increasing growth (**Supplementary Figure 1**). Few exceptions were L-aspartate (ASP), ASN, and GLU which persisted and L-leucine (LEU) and L-methionine (MET) with even decreased concentrations.

Transcriptomics

Metabolic studies were complemented by transcript analysis identifying differentially expressed genes (DEGs) at $\mu = 0.2$, 0.3, and $0.4 h^{-1}$. Noteworthy, the low growth rate served as reference. In total, 547 DEGs were found grouping in 257 with rising and 290 with decreasing DEGs (**Figure 5**). By trend, rather proportional correlations with μ were identified.

Differentially expressed genes assigned to genes coding for central metabolism reactions are considered in **Figures 3** and **4**. **Figure 3** comprises reactions of glycolysis and PPP. Notably, only *pgi* was identified as DEG mirroring that expression levels of all other genes persisted despite growth rise from 0.2 to $0.4 h^{-1}$. In case of *pgi* falling expression levels with increasing growth were detected.

By analogy, of the 28 genes presented in **Figure 4** comprising the “extended TCA cycle,” 18 (64%) did not reveal any transcription dynamics with changing growth. Only four were up and six downregulated. Downregulation occurred for genes coding for the formation of MAL, PEP, pyruvate, acetate, and SUC via reducing expression levels of *aceB*, *mdh*, *pck*, *pqo*, *sucC*, and *sucD*, respectively. In particular, *sucC* and *sucD* showed strongest log fold changes (logFCs) with $\log FC = -1.5$ whereas the majority of other DEGs reduction was $-0.5 \leq LFC_{max} \leq -1$. For comparison, upregulation of *ackA*, *pta*, *gltA*, and *lpdA* was less pronounced revealing $0.4 \leq LFC_{max} \leq 0.9$. Those genes somehow encode the pathway from acetate to citrate.

Further transcript analysis focused on genes encoding glucose uptake and regulation in *C. glutamicum* (**Figure 6**). Noteworthy, published data of Haas et al. (2019) serve as reference. The expression profiles mirror transcript dynamics of the same strain in the same synthetic medium after its exposure to glucose

TABLE 2 | Biomass specific metabolite pool concentrations obtained with the fast-centrifugation treatment and hot-water-extraction from three biological replicates of *C. glutamicum* cultures cultivated in chemostat mode (processes A, B, C) at growth rates of 0.2, 0.3, and 0.4 h⁻¹ (Figure 1).

Metabolites	Intracellular pool size, $\mu\text{mol gCDW}^{-1}$		
	$\mu = 0.2\text{ h}^{-1}$	$\mu = 0.3\text{ h}^{-1}$	$\mu = 0.4\text{ h}^{-1}$
G6P	1.32 ± 0.04	4.32 ± 0.16	6.65 ± 0.29
F6P	0.64 ± 0.03	2.16 ± 0.06	3.24 ± 0.08
FBP	0.85 ± 0.07	4.54 ± 0.09	9.33 ± 0.64
DHAP	0.16 ± 0.02	0.52 ± 0.03	0.63 ± 0.04
2/3PG	1.05 ± 0.04	0.96 ± 0.07	0.65 ± 0.02
PEP	1.48 ± 0.04	1.27 ± 0.04	0.90 ± 0.03
CIT/ICIT	0.00 ± 0.00	0.01 ± 0.01	0.01 ± 0.00
aKG	0.75 ± 0.05	0.58 ± 0.01	0.58 ± 0.02
SUC	7.12 ± 0.53	9.27 ± 0.14	8.71 ± 0.52
FUM	0.06 ± 0.00	0.09 ± 0.00	0.11 ± 0.00
MAL	0.34 ± 0.01	0.60 ± 0.01	0.75 ± 0.03
P5P	0.89 ± 0.02	0.82 ± 0.03	1.00 ± 0.04
S7P	0.44 ± 0.03	0.76 ± 0.02	0.83 ± 0.02
ALA	5.19 ± 0.41	5.59 ± 0.23	6.37 ± 0.81
LEU	0.66 ± 0.03	0.64 ± 0.01	0.41 ± 0.01
VAL	2.25 ± 0.01	3.04 ± 0.07	2.63 ± 0.05
ASP	5.44 ± 0.25	4.87 ± 0.20	5.86 ± 0.12
ASN	0.01 ± 0.00	0.01 ± 0.00	0.01 ± 0.00
LYS	0.78 ± 0.06	1.20 ± 0.06	1.45 ± 0.12
THR	0.86 ± 0.02	1.11 ± 0.02	1.35 ± 0.02
ILE	0.50 ± 0.03	0.73 ± 0.02	0.64 ± 0.01
MET	0.61 ± 0.03	0.48 ± 0.01	0.31 ± 0.00
SER	0.99 ± 0.03	1.46 ± 0.04	1.61 ± 0.04
GLY	1.43 ± 0.04	1.98 ± 0.05	3.13 ± 0.06
GLU	255.35 ± 4.06	253.23 ± 5.02	248.58 ± 3.98
GLN	6.22 ± 0.16	6.79 ± 0.14	10.13 ± 0.15
ARG	0.24 ± 0.01	0.25 ± 0.00	0.28 ± 0.00
PRO	0.73 ± 0.19	1.09 ± 0.01	3.89 ± 0.08
TYR	0.03 ± 0.00	0.06 ± 0.00	0.09 ± 0.00
PHE	0.05 ± 0.00	0.08 ± 0.00	0.13 ± 0.00
TRP	0.02 ± 0.00	0.03 ± 0.00	0.03 ± 0.00

Values represent means ± standard deviations of the biological triplicates.

limitation (highlighted in red in Figure 6). By trend, *iolT1* (coding for glucose specific EII permease; Ikeda et al., 2011; Lindner et al., 2011) and *glk* (encoding glucokinase; Park et al., 2000) showed rising expression with growth in chemostat mode although *glk* levels in continuous culture were below those of all batch studies. On contrary, *iolT1* expression in chemostat was stronger than in batch cultures. By analogy *iolT2*, the second glucose permease (Ikeda et al., 2011; Lindner et al., 2011), also revealed high expression levels in continuous culture but falling levels with rising growth rate. The same holds true for *ppgK* (polyphosphate glucokinase, Lindner et al., 2010) which phosphorylates glucose to G6P utilizing poly-phosphate pools. *iolR*, *ramA*, *cg3388*, and *sugR* are putative regulator genes. *iolR* is the known regulator of *iolT1* (Klafl et al., 2013), whereas *cg3388* may exert control on *iolT2* (Brinkrolf et al., 2006). *sugR* represents a transcriptional regulator of sugar metabolism which is likely to

be controlled by *ramA*, a “master” regulator in *C. glutamicum* (Cramer and Eikmanns, 2007; Shah et al., 2018). Interestingly, all putative regulators disclosed only moderate expression changes with *ramA* showing the lowest expression level at all.

¹³C-Labeling Experiment at $\mu = 0.4\text{ h}^{-1}$

To further investigate the intracellular flux distribution at $\mu = 0.4\text{ h}^{-1}$ – the maximum growth rate typically observed under non-limited glucose batch conditions in minimal medium – a CLE was performed in chemostat mode after a non-labeled metabolic steady-state was installed by switching to ¹³C-labeled feed [mixture of 33% (1-¹³C)- and 67% (U-¹³C)-D-glucose, see section “A priori Tracer Design”]. Figure 7 illustrates the CLE that ran with the same operating conditions as shown in Figure 1.

After five RTs, non-labeled metabolic steady-state was reached (biomass concentration $c_X = 6.09 \pm 0.03\text{ g L}^{-1}$, $pO_2 = 67\%$, $yO_2 = 0.18\text{ mol mol}^{-1}$, $yCO_2 = 0.03\text{ mol mol}^{-1}$) as evidenced by four fold sampling revealing low standard deviations (Figure 2 and Table 3). A fully closed carbon balance was measured for this phase of the experiment (no data shown).

As indicated in Figure 7, ¹³C-labeled feeding started after 39.5 h causing dropping yCO_2 signals as a well-known interference between newly produced isotopic CO₂ and near-infrared exhaust gas measurements. Because of slightly higher glucose feed concentrations in the labeling phase compared to the non-labeled period ($11.88 \pm 0.20\text{ g L}^{-1}$ vs. $11.32 \pm 0.10\text{ g L}^{-1}$), c_X values proportionally increased to $6.20 \pm 0.11\text{ g L}^{-1}$. However, microbial kinetics remained constant compared to the non-labeled state (Table 3). Labeling samples were taken after 3.8 RTs in 10 min intervals to document the expected isotopic stationarity. Sample processing followed the protocol given in the Supplementary Material sections “Sampling, Quenching, and Extraction for Quantification of ¹³C-Isotopic Labeling Dynamics” and “LC-MS-Based Quantification of Intracellular Pool Concentrations and ¹³C-Labeling Dynamics.”

Biomass-specific extracellular rates were furthermore estimated using a bioprocess model (see Supplementary Material section “Bioprocess Model Used for External Rate Estimation”). The rate of glucose consumption was estimated to be $r_{GLC} = 4,130 \pm 150\text{ }\mu\text{mol gCDW}^{-1}\text{ h}^{-1}$, the specific growth rate as $\mu = 0.40 \pm 0.03\text{ h}^{-1}$, CO₂ production and PCA uptake rates were determined as $r_{CO_2} = 8,240 \pm 760\text{ }\mu\text{mol gCDW}^{-1}\text{ h}^{-1}$ and $r_{PCA} = 13 \pm 1\text{ }\mu\text{mol gCDW}^{-1}\text{ h}^{-1}$, respectively.

From these rates and the (corrected) MIDs, extracellular and intracellular fluxes were estimated with the ¹³C-MFA model at hand (see section “Metabolic Network Model for ¹³C-MFA”), following the procedure described in section “External Rate Estimation.” For the best fit obtained, measured and simulated data agreed very well (Supplementary Figures 3,4), as indicated by a SSR of approximately 31. Therewith the SSR was lower than the maximally acceptable SSR of 114 at 95% significance level. The estimated absolute fluxes including flux standard deviations are provided in the Supplementary Table 2.

Figure 8 shows the central metabolic carbon fluxes, normalized to glucose consumption rate $v_{GLC} = 4,086\text{ }\mu\text{mol gCDW}^{-1}\text{ h}^{-1}$ for the specific growth rate $\mu = 0.41 \pm 0.02\text{ h}^{-1}$. Two-thirds ($66.4 \pm 7.6\%$) of the incoming

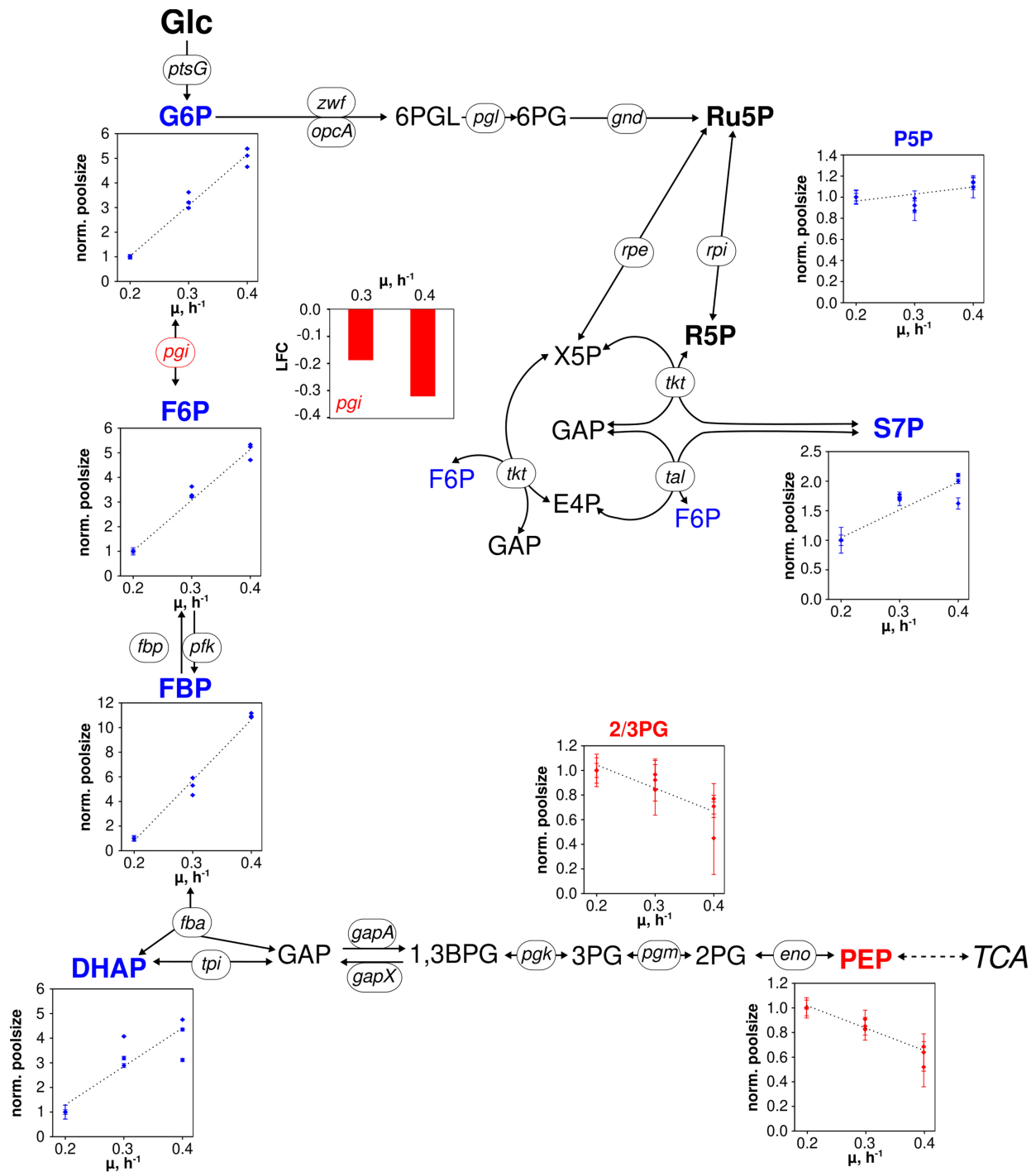
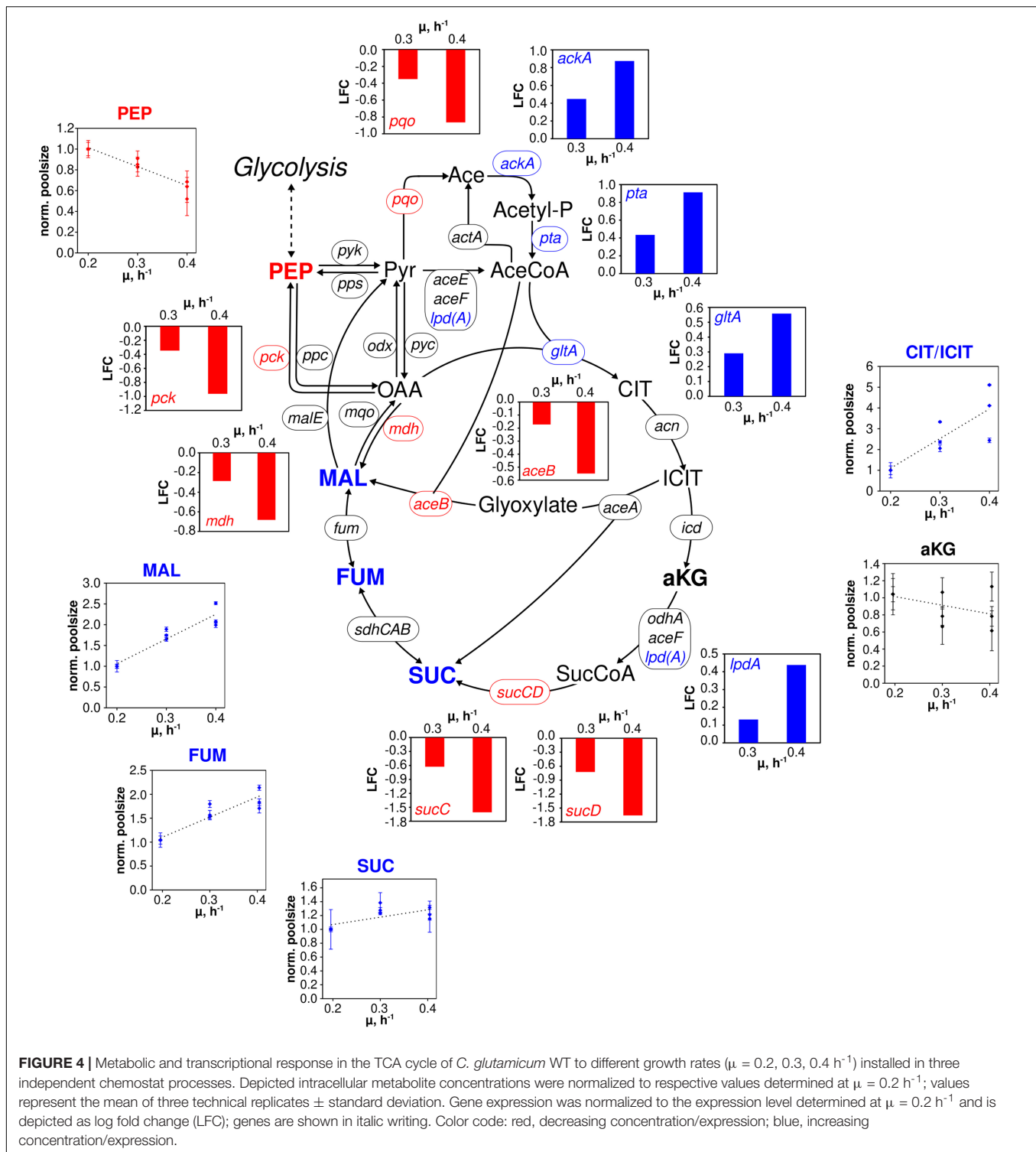


FIGURE 3 | Metabolic and transcriptional response in glycolysis and pentose phosphate pathway of *C. glutamicum* WT to different growth rates ($\mu = 0.2, 0.3, 0.4 \text{ h}^{-1}$) installed in three independent chemostat processes. Depicted intracellular metabolite concentrations were normalized to respective values determined at $\mu = 0.2 \text{ h}^{-1}$; values represent the mean of three technical replicates \pm standard deviation. Gene expression was normalized to the expression level determined at $\mu = 0.2 \text{ h}^{-1}$ and is depicted as log fold change (LFC); genes are shown in italic writing. Color code: red, decreasing concentration/expression; blue, increasing concentration/expression.

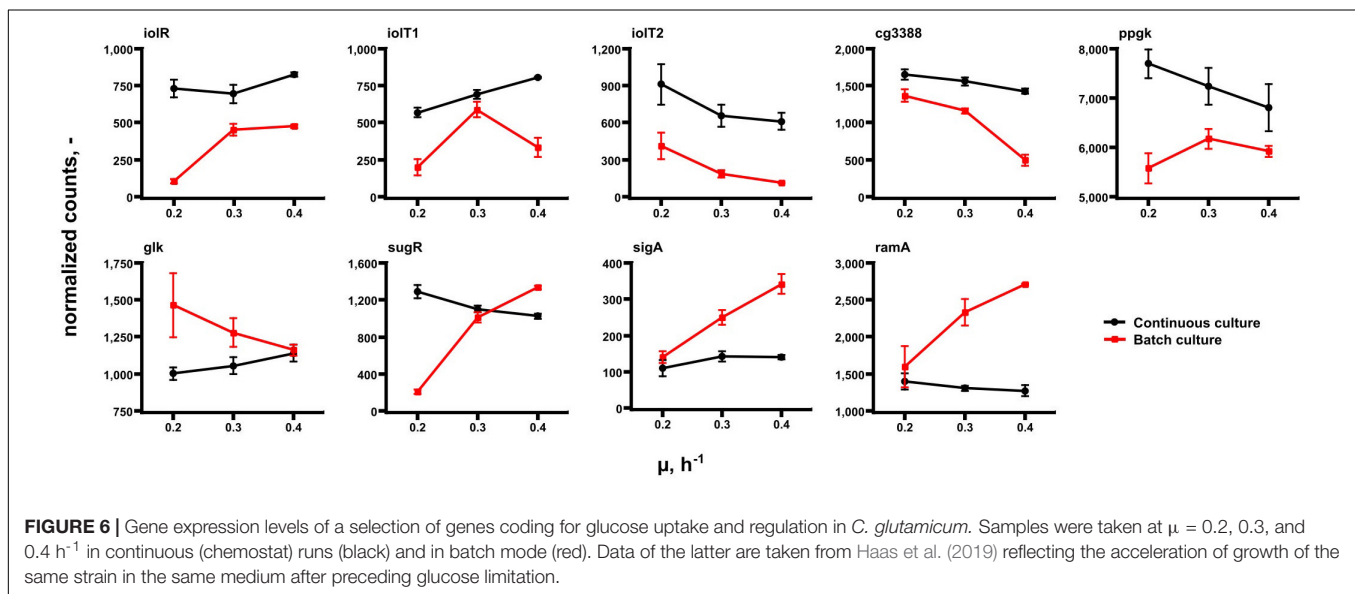
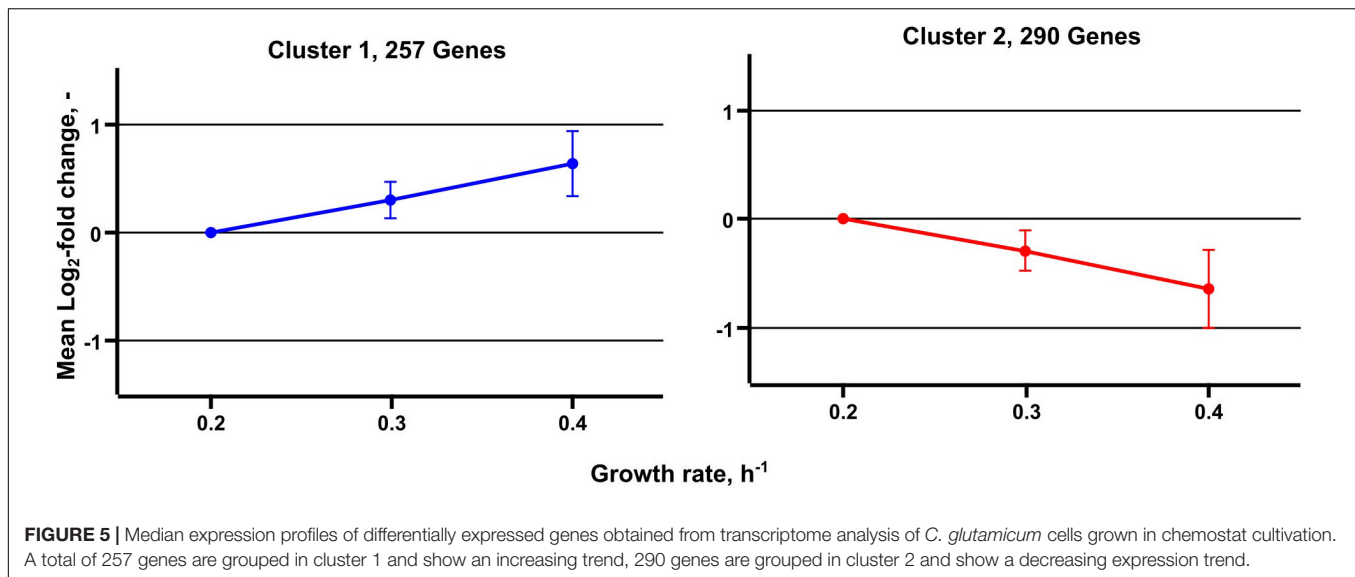
glucose flux were metabolized via the EMP pathway through G6P isomerase (reaction *pgi*), whereas one-third ($31.6 \pm 7.6\%$) of the glucose was metabolized via the PPP through G6P

dehydrogenase and phosphogluconate dehydrogenase (*gnd*) to regenerate nicotinamide adenine dinucleotide phosphate (NADPH) and accomplish P5P-precursor production for



nucleotides and amino acids. A considerable portion of the input flux, namely $25.1 \pm 1.2\%$, was utilized for acetyl-CoA precursors, e.g., the synthesis of fatty acids and to satisfy the demand for biomass. A relatively high proportion ($58.3 \pm 4.2\%$) of the incoming glucose was channeled into the TCA cycle via citrate synthase (*glta*) to generate ATP via the respiratory

chain and to satisfy the demand of amino acids of the ASP and GLU branches, whereas the contribution of the PCA flux to the TCA cycle via the β -keto-adipate pathway was negligibly small ($v_{\text{PCA}} = 0.3 \pm 0.0\%$). Best fit results suggest that the anaplerotic net flux mainly goes through *pyc*, which channels 31.3% of the glucose uptake flux into the TCA cycle



via oxaloacetate (OAA). In *C. glutamicum*, three reactions in central carbon metabolism, namely, isocitrate dehydrogenase (*icd*), *gnd*, and malic enzyme (*mez*) contribute to regeneration of NADP^+ to NADPH (Marx et al., 1996). According to the flux map (Figure 8), *gnd* ($1,290 \pm 309 \mu\text{mol g}_{\text{CDW}}^{-1} \text{s}^{-1}$) and *icd* ($2,380 \pm 169 \mu\text{mol g}_{\text{CDW}}^{-1} \text{s}^{-1}$) contribute in a roughly 1:2 proportion to NADPH generation. Because the TCA cycle contributes 1 NADPH molecule per CIT molecule and the oxidative PPP contributes 2 NADPH molecules per G6P molecule, flux estimations suggest that NADPH demands were equally met by *icd* (48% of NADPH) and the lumped reactions of the oxidative PPP (52% of NADPH), recognizing that the contribution of *mez* is negligible. From the flux map in Figure 8 it follows that the total relative flux of NADPH synthesis is approximately 121.5% of the glucose consumption rate. Assuming the coefficient for NADPH required for growth to

be $14,849 \mu\text{mol g}_{\text{CDW}}^{-1}$ (Neidhardt et al., 1990), NADP^+ has to be regenerated at a relative rate of 149.0%, leaving a gap of 27.5% molar flux relative to the glucose consumption rate. Notice that the net *mez* flux is statistically non-identifiable (Supplementary Table 2). A value of approximately $1,144 \mu\text{mol g}_{\text{CDW}}^{-1} \text{s}^{-1}$ suffices to close the gap, whereas any larger value results in excess NADPH production. Finally, the analysis showed that the total carbon flux into the biomass and CO_2 was 65.6 and 34.4%, respectively, where 1 mol of glucose was converted into 2.06 mol CO_2 . Therewith, trends of relative fluxes are similar to those reported by previous studies at slightly higher specific growth rates ($\mu = 0.42, 0.46 \text{ h}^{-1}$) and glucose uptake rates ($v_{\text{GLC}} = 4,800, 5,100 \mu\text{mol g}_{\text{CDW}}^{-1} \text{h}^{-1}$) conducted under batch conditions (Becker et al., 2011; Wang et al., 2018; see Supplementary Figure 5). Accordingly, biomass yields per glucose obtained in these studies are comparable with this study

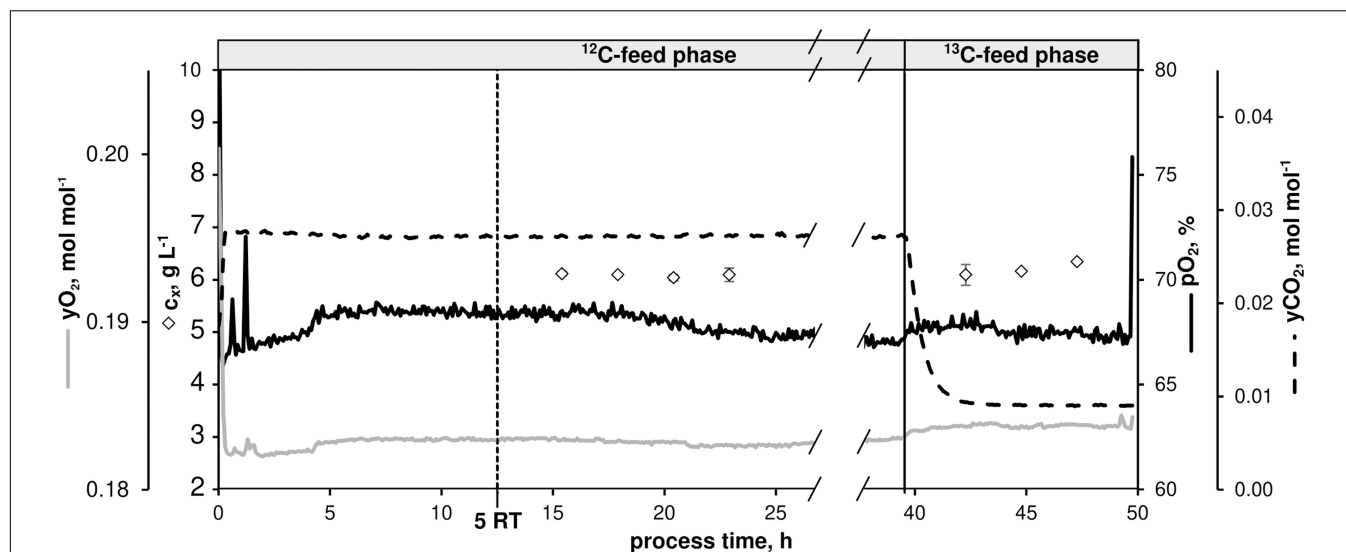


FIGURE 7 | Process parameters of the continuous ^{13}C -labeling experiment with *C. glutamicum* WT: dissolved oxygen ($p\text{O}_2$), off-gas molar oxygen ($y\text{O}_2$) and carbon dioxide ($y\text{CO}_2$), biomass concentration (black diamonds). The dilution rate (D) was set to 0.4 h^{-1} . Sampling in the ^{12}C -phase was initiated after five residence times (RT, 12.5 h). After 39.5 h, feed was switched to isotopic CGXII medium containing a $12\text{ g D-glucose L}^{-1}$ mixture [67% ($\text{U-}^{13}\text{C}$)-D-glucose and 33% (^{13}C)-D-glucose]. Residual process parameters were kept constant. Depicted standard deviations of biomass measurements were calculated from three technical replicates per sample.

TABLE 3 | Kinetic process parameters from the ^{13}C -labeling experiment with *C. glutamicum* (Figure 7) using CGXII minimal medium supplemented with $12\text{ g D-glucose L}^{-1}$ [^{13}C -phase: 67% ($\text{U-}^{13}\text{C}$)-D-glucose and 33% (^{13}C)-D-glucose] at a dilution rate of 0.4 h^{-1} .

Phase	q_{GLC} , $\text{g gCDW}^{-1}\text{ h}^{-1}$	q_{O_2} , $\text{mmol gCDW}^{-1}\text{ h}^{-1}$	q_{CO_2} , $\text{mmol gCDW}^{-1}\text{ h}^{-1}$
^{12}C -feed	0.74 ± 0.01	9.26 ± 0.09	9.86 ± 0.10
^{13}C -feed	0.77 ± 0.02	9.77 ± 0.14	n.a.

Listed results are the means of four (^{12}C -phase) or three (^{13}C -phase) technical replicates. q_{GLC} , biomass specific glucose uptake rate; $Y_{\text{X,GLC}}$, biomass-glucose-yield; q_{O_2} , molar biomass specific oxygen uptake rate; q_{CO_2} , carbon dioxide evolution rate; n.a., not available.

($Y_{\text{X,GLC}} = 0.49$ and 0.50 g gCDW^{-1} , respectively; see also Eq. 10 in **Supplementary Material** section “Bioprocess Model Used for External Rate Estimation”).

DISCUSSION

Kinetic Studies

Figures 1, 2 together with Tables 1, 3 give evidence to the high repeatability of biological and technical replicates qualifying the data sets as sound and representative. The growth de-coupled maintenance coefficient, m_s is identified as $(0.44 \pm 0.04)\text{ mmol D-glucose gCDW}^{-1}\text{ h}^{-1}$ and the growth-coupled maintenance coefficient $Y_{\text{XS}}^{\text{real}}$ as $(0.103 \pm 0.01)\text{ gCDW mmol}^{-1}$ which indicates about 9 and 1% standard deviation, respectively. Surprisingly, the m_s value exceeds measurements of Koch-Koerfges et al. (2013) by factor 5.5 whereas $Y_{\text{XS}}^{\text{real}}$ of the current study is about 21% lower. Accordingly, results of the current study hint to

higher cellular maintenance needs which consequently lead to reduced glucose-to-biomass conversion. As strains and media compositions are similar, no apparent reason is found for the discrepancy. However, determined growth kinetics which built the basis for maintenance calculations in this study agree well with kinetics determined by Coccagn-Bousquet et al. (1996) investigating *C. glutamicum* WT ATCC 17965 in chemostat tests.

Metabolic and Transcriptional Regulation of Central Metabolism in Chemostat

The metabolic flux map of Figure 8 mirrors cellular efforts to provide sufficient metabolic precursors, reduction equivalents, and ATP at a growth rate of 0.4 h^{-1} that represents growth conditions typically observed under non-limited batch conditions (Blombach et al., 2013; Grünberger et al., 2013; Graf et al., 2018; Haas et al., 2019). Apparently, the central metabolism of *C. glutamicum* serves the pivotal need of precursor supply for biomass formation which is mirrored by the strong activity of glycolysis fueling the TCA cycle. Somewhat inferior are cellular needs for NADPH which is disclosed by only 1/3 of consumed glucose branching into the PPP thereby meeting half of the demands required for nucleotide precursors, biomass, and growth.

Pool sizes of upper glycolysis and PPP rise with the growth rate (G6P, F6P, FBP, DHAP) whereas intracellular concentrations of 2,3PG and PEP show opposite trends (see Figure 3). Notably, 2/3PG assigns the lumped pool of 2PG + 3PG of low total size which may be discarded from further discussion. Glycolytic fluxes are expected to increase with growth considering raising biomass specific glucose consumption rates of Table 1. Noack et al. (2017) found constant enzyme concentrations in central

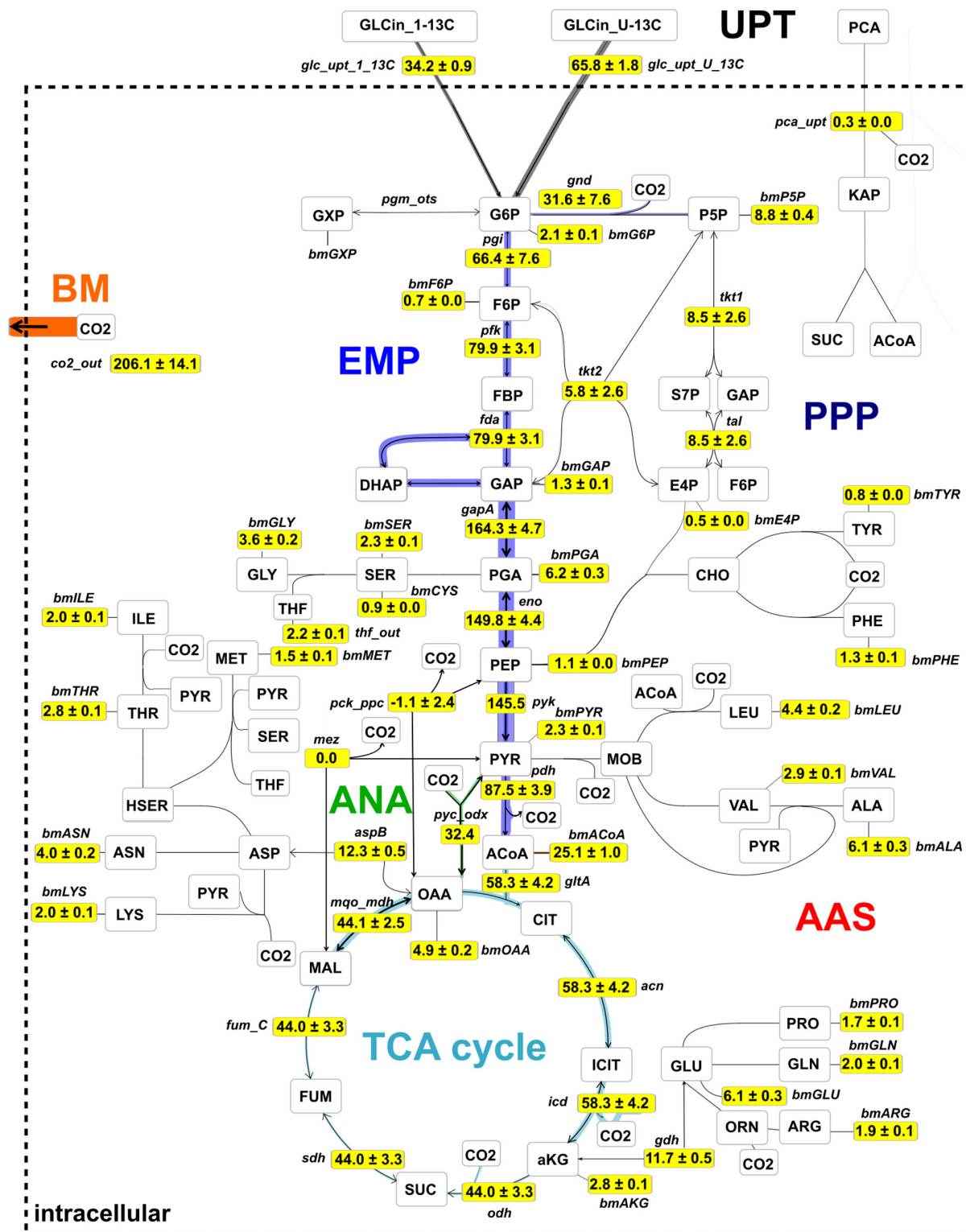


FIGURE 8 | Metabolic flux map for *C. glutamicum* WT cultivated under continuous conditions at growth rate $\mu = 0.41 \text{ h}^{-1}$ using glucose as main carbon source. Fluxes were estimated using isotopic stationary ^{13}C -MFA with a data set generated in a CLE with 33% ($1\text{-}^{13}\text{C}$)- and 67% ($\text{U-}^{13}\text{C}$)-D-glucose. Shown are net flux values, normalized to glucose uptake rate ($v_{\text{GLC}} = 4,086 \mu\text{mol g}_{\text{CDW}}^{-1} \text{ h}^{-1}$), together with their standard deviations. The complete absolute and relative flux distributions are provided in the **Supplementary Table 2**. The flux map is drawn using the network editor and visualization tool Omix (Omix Visualization GmbH, Lennestadt, Germany, www.omix-visualization.com). UPT, uptake; PPP, pentose-phosphate pathway; ANA, anaplerotic section; BM, biomass; EMP, Embden-Meyerhof-Parnas; AAS, amino acid synthesis; TCA, tricarboxylic acid.

metabolism of *C. glutamicum* ATCC 13032 cultivated in the same CGXII minimal medium and under the same process conditions in chemostat mode ($D = 0.05, 0.1, 0.2$, and 0.35 h^{-1}) as employed in this study. Our findings agree with the previous study because only gene *pgi* showed minor reduction of transcript levels of genes encoding enzymes in glycolysis and in PPP. Consequently, increasing glycolytic fluxes should be enabled by elevated intracellular pool concentrations fairly assuming Michaelis–Menten type kinetics for said enzymes. Because extracellular glucose concentrations were limiting under chemostat operation, the majority of glucose consumption is expected to happen via the PTS. PEP is dephosphorylated stoichiometrically to pyruvate (not measured) activating glucose to G6P. Accordingly, increasing PEP consumption coincides with raising glucose consumption rates and growth. Observing falling PEP pools anticipate limited PEP regeneration with increasing growth rate. In general, glycolytic metabolite dynamics agree with independent studies of Noack et al. (2017) hinting to metabolically controlled glycolytic fluxes in glucose-limited chemostats.

In the TCA cycle, metabolite dynamics are less pronounced than in glycolysis and PPP. The strongest increase found in the lumped CIT/ICIT pool might be misleading as the low pool sizes reflect the particular instability of these metabolites using the leakage-reduced fast centrifugation treatment and hot-water extraction protocol for separation and metabolite extraction. However, elevating pools with growth may also mirror increased citrate synthase catalyzed flux (indicated by amplified *glcA* expression; van Ooyen et al., 2011) which is not passed on to aKG because of missing *icd* amplification (Figure 4). Rising MAL and FUM levels may mirror rising fluxes catalyzed via Michaelis–Menten type kinetics of fumarate hydratase, malic enzyme and malate:quinone oxidoreductase whose corresponding genes (*fum*, *malE*, *mgo*; Han et al., 2008b) did not show any changes of expression levels. Interesting enough the expression of *pck*, encoding phosphoenolpyruvate carboxykinase (Riedel et al., 2001), reduces with growth which agrees with the hypothesis of limited PEP regeneration from OAA.

In general, the identification of only a few DEGs in TCA cycle agrees with findings of Noack et al. (2017) analyzing the enzyme content of *C. glutamicum*. Similar to glycolysis, growth dependent TCA cycle activity appears to be mostly metabolically controlled under chemostat conditions. Rising *glcA* expression, however, may thus be qualified as one example of transcriptional control. In case of the other DEGs, a coherent regulatory scheme is missing so far. Furthermore, putative regulator genes such as *ramA* and *sugR* are unlikely to exert additional control as they show only moderate dynamics with increasing growth rate (Figure 6).

Most of the amino acid pools show rising sizes with increasing growth (Supplementary Figure 1) which reflects increasing needs of said precursors for protein synthesis using the assumption of Michaelis–Menten type enzyme kinetics. Frankly speaking, there are no obvious reasons why MET and LEU pools fall. However, the observation of growth rate independent intracellular pool sizes of ASP, ASN, and GLU agrees with findings of Graf et al. (2018). The authors outlined that those amino acids were consumed non-proportionally with the strain's

amino acid biomass composition under non-limited glucose and amino acid conditions (batch cultivations). They concluded that most likely, these compounds serve as central amino donors for multiple acceptors explaining why their uptake outnumbers stoichiometric biomass needs by far.

Comparability of Chemostat and Batch Observations

Haas et al. (2019) identified the so-called “growth modulon” of *C. glutamicum* analyzing the growth in the same medium as in this study, but after preceding installation of carbon, nitrogen, and phosphate limitation. The intersection analysis of DEGs changing with accelerating growth rates after previous stress exposure yielded a set of 447 genes belonging to the growth modulon. Noteworthy, the batch study of Haas et al. (2019) differs from chemostat tests by installing saturating nutrient levels including glucose whereas glucose limitation and low extracellular glucose concentrations occur in the continuous runs. Interesting enough, Haas et al. (2019) analyzed transcriptional patterns at the growth rates 0.2, 0.3, and 0.4 h^{-1} which are identical to the chemostat growth rates of the current study. This allows the direct comparison of transcriptional patterns associated to equal growth but under different glucose levels.

A primary observation is that changes of gene expression levels are more pronounced under batch conditions (Haas et al., 2019) than in chemostat mode. On average, log fold changes (LFCs) of batch DEGs are twice as large as those of the continuous culture. Apparently, non-transcriptional control of cellular growth is more prominent in chemostat than in glucose-rich batch conditions. Interestingly, most of the genes coding for TCA cycle reactions are not members of the “growth modulon” which agrees well with the proteome measurements of Noack et al. (2017) and with the chemostat transcript results of this study. In contrast, acetate kinase (encoded by *ackA*) and phosphate acetyltransferase (encoded by *pta*) showed amplifying trends (Figure 4) and are part of the growth modulon. Consequently, both conditions, chemostat, and batch, assigned those genes identical functions, either as part of the non- or as member of the growth correlated fractions.

Contrary, *aceA* (isocitrate lyase), *pqo* (pyruvate:quinone oxidoreductase), and *sucCD* (succinate CoA ligase) revealed opposite expression trends in chemostat runs compared to the expectations as members of the growth modulon derived from batch observations. Even more striking, the entire glycolysis was assigned to the growth modulon anticipating increasing transcripts with rising growth. However, transcriptome (Figure 5) and proteome (Noack et al., 2017) studies of chemostats did not depict such dynamics. Apparently, findings of batch studies may not be transferred one-by-one to chemostat conditions, *vice versa*.

For explanation, Figure 6 should be discussed: considering that extracellular glucose levels were below the detection limit in chemostats, cells may require stronger amplification of *iolT1* (coding for glucose specific EII permease; Ikeda et al., 2011; Lindner et al., 2011) than under high-glucose batch conditions.

Notably, early studies of Coccagn-Bousquet et al. (1996) followed by glucose uptake engineering works of Xu et al. (2019) outlined that PTS-based glucose imports dominate glucose uptake by 70–85% in *C. glutamicum*. Accordingly, non-PTS glucose import may account for roughly 15–30%. Nevertheless, the finding of increasing *iolT1* levels with chemostat growth supports the hypothesis that non-PTS glucose uptake may have gained importance. *iolT1* is under control of *iolR* (Klafl et al., 2013), *iolT2* is supposed to be regulated by cg3388 (Brinkrolf et al., 2006). By trend, the second correlation is observed whereas the first is not. Maybe, *iolT1* expression is co-controlled by another regulator not discovered yet. Glucose entering the cell via *IolT1* requires activation by glucokinase either encoded by *glk* (Park et al., 2000) or by *ppgk* (Lindner et al., 2010). The ATP dependent glucokinase reveals slightly rising gene expression with growth whereas expression levels of the PolyP/ATP-dependent glucokinase reduce in continuous culture. Interestingly, *glk* levels in chemostat are mostly below those of glucose-rich batch conditions anticipating that permease-driven import of glucose is higher when extracellular levels are elevated too. Most remarkably, *ramA*, encoding one of the key regulators of the growth modulon (Haas et al., 2019) revealed only low expression in each chemostat environment whereas higher, amplifying trends were found in batch tests. As RamA controls expression of glycolytic genes (Auchter et al., 2011; Shah et al., 2018; Haas et al., 2019) their missing amplification in chemostats may be explained as the missing activation of *ramA*. Most likely, extracellular glucose levels somehow stimulate *ramA* activation but this remains to be shown.

CONCLUSION

Investigating *C. glutamicum* WT under nutrient limiting conditions in chemostat, we found that pool sizes of glycolysis predominately rise with growth. Although not measured explicitly, rising intracellular fluxes are likely to follow the experimentally observed increasing, growth coupled glucose uptake rates. In particular, the scenario pinpoints to a predominant metabolic control of glycolysis because indications for transcriptional control could not be detected in chemostat. By analogy, growth coupled metabolic control of PPP and TCA cycle is anticipated. Again, concerted trends in transcriptional patterns could not be found. The picture is complemented by ^{13}C -studies underlining the central function of central metabolism as supplier of precursors, redox, and energy equivalents.

As such, the study consolidates previous findings outlining a particularity: glycolysis apparently is transcriptionally controlled under glucose-rich batch condition whereas metabolic control dominates in glucose limited chemostats. The important player may be RamA, a key transcriptional regulator of glycolysis.

REFERENCES

- Auchter, M., Cramer, A., Hüser, A., Rückert, C., Emer, D., Schwarz, P., et al. (2011). RamA and RamB are global transcriptional regulators in *Corynebacterium glutamicum* and control genes for enzymes of the central metabolism. *J. Biotechnol.* 154, 126–139. doi: 10.1016/j.jbiotec.2010.07.001
- Becker, J., Zelder, O., Häfner, S., Schröder, H., and Wittmann, C. (2011). From zero to hero—design-based systems metabolic engineering of *Corynebacterium glutamicum* Under Limited Chemostat Conditions
- Brinkrolf, M., and Knebel, A. (2006). The *iolT2* gene of *Corynebacterium glutamicum* is involved in iron uptake. *FEBS Lett.* 580, 105–110. doi: 10.1016/j.febslet.2006.01.011
- Coccagn, B., and Bousquet, M. (1996). Glucose uptake and growth of *Corynebacterium glutamicum* in continuous culture. *Biotechnol. Bioeng.* 50, 105–110. doi: 10.1002/(SICI)1097-4644(199605)50:1<105::AID-BT105>3.0.CO;2-1
- Haas, S., and Knebel, A. (2019). The growth modulon of *Corynebacterium glutamicum*. *Front. Bioeng. Biotechnol.* 7, 1–10. doi: 10.3389/fbioe.2019.00001
- Klafl, M., and Knebel, A. (2013). The *iolR* gene of *Corynebacterium glutamicum* is involved in iron uptake. *FEBS Lett.* 580, 105–110. doi: 10.1016/j.febslet.2006.01.011
- Lindner, M., and Knebel, A. (2010). The *ppgk* gene of *Corynebacterium glutamicum* is involved in glucose uptake. *FEBS Lett.* 580, 105–110. doi: 10.1016/j.febslet.2006.01.011
- Park, J., and Knebel, A. (2000). The *glk* gene of *Corynebacterium glutamicum* is involved in glucose uptake. *FEBS Lett.* 478, 105–110. doi: 10.1016/S0014-5794(00)00105-1
- Shah, S., and Knebel, A. (2018). The *glk* gene of *Corynebacterium glutamicum* is involved in glucose uptake. *FEBS Lett.* 580, 105–110. doi: 10.1016/j.febslet.2006.01.011
- Xu, J., and Knebel, A. (2019). The *glk* gene of *Corynebacterium glutamicum* is involved in glucose uptake. *FEBS Lett.* 580, 105–110. doi: 10.1016/j.febslet.2006.01.011

Obviously, it is a highly attractive goal of future studies to unravel the metabolic effector interacting with RamA, one of the remaining puzzle pieces to complete the growth regulation picture of *C. glutamicum*.

DATA AVAILABILITY STATEMENT

The datasets presented in this study can be found in online repositories. The names of the repository/repositories and accession number(s) can be found below: <https://www.ebi.ac.uk/arrayexpress/>, E-MTAB-9371.

AUTHOR CONTRIBUTIONS

MG designed the study, carried out the bioreactor experiments, analyzed the metabolic datasets, and drafted and corrected the manuscript. TH designed the study, analyzed the transcriptomic data sets and, drafted and corrected the manuscript. AT and AF conceptualized and performed metabolic analysis and corrected the manuscript. TB and JK measured the transcript samples and corrected the manuscript. MC and KN designed the flux study, performed the MFA, and drafted and corrected the manuscript together with WW. RT conceptualized the whole study and drafted and corrected the manuscript. All authors read and approved the final manuscript.

FUNDING

This work was supported by the German Federal Ministry of Education and Research (BMBF; Grant 031A302A and 031A302C).

ACKNOWLEDGMENTS

We thank Anna-Lena Mayer, Salaheddine Laghrami, and Andreas Freund for excellent support with bioreactor fermentations. Moreover, we thank all members of the 0.6 plus project group for valuable comments on the topic and for their great cooperation. Parts of this contribution previously appeared online in the doctoral thesis of Graf (2019).

SUPPLEMENTARY MATERIAL

The Supplementary Material for this article can be found online at: <https://www.frontiersin.org/articles/10.3389/fbioe.2020.584614/full#supplementary-material>

- glutamicum* for l-lysine production. *Metab. Eng.* 13, 159–168. doi: 10.1016/j.ymben.2011.01.003
- Beyß, M., Azzouzi, S., Weitzel, M., Wiechert, W., and Nöh, K. (2019). The design of fluxml: a universal modeling language for ^{13}C metabolic flux analysis. *Front. Microbiol.* 10:1022. doi: 10.3389/fmicb.2019.01022
- Blombach, B., Buchholz, J., Busche, T., Kalinowski, J., and Takors, R. (2013). Impact of different $\text{CO}_2/\text{HCO}_3^-$ levels on metabolism and regulation in *Corynebacterium glutamicum*. *J. Biotechnol.* 168, 331–340. doi: 10.1016/j.jbiotec.2013.10.005
- Brinkrolf, K., Brune, I., and Tauch, A. (2006). Transcriptional regulation of catabolic pathways for aromatic compounds in *Corynebacterium glutamicum*. *Genet. Mol. Res.* 5, 773–789.
- Bull, A. T. (2010). The renaissance of continuous culture in the post-genomics age. *J. Indust. Microbiol. Biotechnol.* 37, 993–1021. doi: 10.1007/s10295-010-0816-4
- Cerff, M., Scholz, A., Käßler, T., Ottow, K. E., Hobley, T. J., and Posten, C. (2013). Semi-continuous in situ magnetic separation for enhanced extracellular protease production—modeling and experimental validation. *Biotechnol. Bioeng.* 110, 2161–2172. doi: 10.1002/bit.24893
- Cocaign-Bousquet, M., Guyonvarch, A., and Lindley, N. D. (1996). Growth rate-dependent modulation of carbon flux through central metabolism and the kinetic consequences for glucose-limited chemostat cultures of *Corynebacterium glutamicum*. *Appl. Environ. Microbiol.* 62, 429–436. doi: 10.1128/aem.62.2.429-436.1996
- Cramer, A., and Eikmanns, B. J. (2007). RamA, the transcriptional regulator of acetate metabolism in *Corynebacterium glutamicum*, is subject to negative autoregulation. *J. Mol. Microbiol. Biotechnol.* 12, 51–59. doi: 10.1128/JB.01061-06
- Eggeling, L., and Bott, M. (eds) (2005). *Handbook of Corynebacterium Glutamicum*, 1st Edn. Boca Raton: CRC Press, doi: 10.1201/9781420039696
- Feith, A., Teleki, A., Graf, M., Favilli, L., and Takors, R. (2019). HILIC-Enabled ^{13}C metabolomics strategies: comparing quantitative precision and spectral accuracy of QTOF high- and QQQ low-resolution mass spectrometry. *Metabolites* 9, 63. doi: 10.3390/metabo9040063
- Freudl, R. (2017). Beyond amino acids: use of the *Corynebacterium glutamicum* cell factory for the secretion of heterologous proteins. *J. Biotechnol.* 258, 101–109. doi: 10.1016/j.jbiotec.2017.02.023
- Graf, M. (2019). *Investigation of Growth Limitations in (Pseudo-)Steady States with Corynebacterium Glutamicum*. Dissertation, University of Stuttgart, Stuttgart.
- Graf, M., Haas, T., Müller, F., Harm-Bekbenbetova, J., Freund, A., Nieß, A., et al. (2019). Continuous adaptive evolution of a fast-growing *Corynebacterium glutamicum* strain independent of protocatechuate. *Front. Microbiol.* 10:1648. doi: 10.3389/fmicb.2019.01648
- Graf, M., Zieringer, J., Haas, T., Nieß, A., Blombach, B., and Takors, R. (2018). Physiological response of *Corynebacterium glutamicum* to increasingly nutrient-rich growth conditions. *Front. Microbiol.* 9:2058. doi: 10.3389/fmicb.2018.02058
- Grünberger, A., van Ooyen, J., Paczia, N., Rohe, P., Schiendzielorz, G., Eggeling, L., et al. (2013). Beyond growth rate 0.6: corynebacterium glutamicum cultivated in highly diluted environments. *Biotechnol. Bioeng.* 110, 220–228. doi: 10.1002/bit.24616
- Haas, T., Graf, M., Nieß, A., Busche, T., Kalinowski, J., Blombach, B., et al. (2019). Identifying the Growth Modulon of *Corynebacterium glutamicum*. *Front. Microbiol.* 10:974. doi: 10.3389/fmicb.2019.00974
- Han, S. O., Inui, M., and Yukawa, H. (2008a). Effect of carbon source availability and growth phase on expression of *Corynebacterium glutamicum* genes involved in the tricarboxylic acid cycle and glyoxylate bypass. *Microbiology* 154, 3073–3083. doi: 10.1099/mic.0.2008/019828-0
- Han, S. O., Inui, M., and Yukawa, H. (2008b). Transcription of *Corynebacterium glutamicum* genes involved in tricarboxylic acid cycle and glyoxylate cycle. *J. Mol. Microbiol. Biotechnol.* 15, 264–276. doi: 10.1159/000117614
- Hermann, T. (2003). Industrial production of amino acids by coryneform bacteria. *J. Biotechnol.* 104, 155–172. doi: 10.1016/S0168-1656(03)00149-4
- Hoffart, E., Grenz, S., Lange, J., Nitschel, R., Müller, F., Schwentner, A., et al. (2017). High substrate uptake rates empower *Vibrio natriegens* as production host for industrial biotechnology. *Appl. Environ. Microbiol.* 83:AEM.1614-17. doi: 10.1128/AEM.01614-17
- Hoskisson, P. A., and Hobbs, G. (2005). Continuous culture—making a comeback? *Microbiology* 151, 3153–3159. doi: 10.1099/mic.0.27924-0
- Ikedo, M., Mizuno, Y., Awane, S. I., Hayashi, M., Mitsunashi, S., and Takeno, S. (2011). Identification and application of a different glucose uptake system that functions as an alternative to the phosphotransferase system in *Corynebacterium glutamicum*. *Appl. Microbiol. Biotechnol.* 90, 1443–1451. doi: 10.1007/s00253-011-3210-x
- Jungreuthmayer, C., Neubauer, S., Mairinger, T., Zanghellini, J., and Hann, S. (2016). ICT: isotope correction toolbox. *Bioinformatics* 32, 154–156. doi: 10.1093/bioinformatics/btv514
- Kappelmann, J., Wiechert, W., and Noack, S. (2016). Cutting the gordian knot: identifiability of anaplerotic reactions in *Corynebacterium glutamicum* by means of ^{13}C -metabolic flux analysis. *Biotechnol. Bioeng.* 113, 661–674. doi: 10.1002/bit.25833
- Klaffl, S., Brocker, M., Kalinowski, J., Eikmanns, B. J., and Bott, M. (2013). Complex regulation of the phosphoenolpyruvate carboxykinase gene *pck* and characterization of its GntR-type regulator IolR as a repressor of *myo*-inositol utilization genes in *Corynebacterium glutamicum*. *J. Bacteriol.* 195, 4283–4296. doi: 10.1128/JB.00265-13
- Koch-Koerfges, A., Pfler, N., Platzen, L., Oldiges, M., and Bott, M. (2013). Conversion of *Corynebacterium glutamicum* from an aerobic respiring to an aerobic fermenting bacterium by inactivation of the respiratory chain. *Biochim. Biophys. Acta* 1827, 699–708. doi: 10.1016/j.bbabo.2013.02.004
- Lindner, S. N., Knebel, S., Pallerla, S. R., Schoberth, S. M., and Wendisch, V. F. (2010). Cg2091 encodes a polyphosphate/ATP-dependent glucokinase of *Corynebacterium glutamicum*. *Appl. Microbiol. Biotechnol.* 2010 87, 703–713. doi: 10.1007/s00253-010-2568-5
- Lindner, S. N., Seibold, G. M., Henrich, A., Krämer, R., and Wendisch, V. F. (2011). Phosphotransferase system-independent glucose utilization in *Corynebacterium glutamicum* by inositol permeases and glucokinases. *Appl. Environ. Microbiol.* 77, 3571–3581. doi: 10.1128/AEM.02713-10
- Long, C. P., Gonzalez, J. E., Cipolla, R. M., and Antoniewicz, M. R. (2017). Metabolism of the fast-growing bacterium *Vibrio natriegens* elucidated by ^{13}C metabolic flux analysis. *Metab. Eng.* 44, 191–197. doi: 10.1016/j.ymben.2017.10.008
- Love, M. I., Huber, W., Anders, S., Lönnstedt, I., Speed, T., Robinson, M., et al. (2014). Moderated estimation of fold change and dispersion for RNA-seq data with DESeq2. *Genome Biol.* 15:550. doi: 10.1186/s13059-014-0550-8
- Marx, A., de Graaf, A. A., Wiechert, W., Eggeling, L., and Sahm, H. (1996). Determination of the fluxes in the central metabolism of *Corynebacterium glutamicum* by nuclear magnetic resonance spectroscopy combined with metabolite balancing. *Biotechnol. Bioeng.* 49, 111–129. doi: 10.1002/(sici)1097-0290(19960120)49:2<111::aid-bit1>3.0.co;2-t
- Möllney, M., Wiechert, W., Kownatzki, D., and de Graaf, A. A. (1999). Bidirectional reaction steps in metabolic networks: IV. Optimal design of isotopomer labeling experiments. *Biotechnol. Bioeng.* 66, 86–103. doi: 10.1002/(sici)1097-0290(1999)66:2<86::aid-bit2>3.0.co;2-a
- Neidhardt, F. C., Ingraham, J. L., and Schaechter, M. (1990). *Physiology of the Bacterial Cell — A Molecular Approach*. Sunderland, MA: Sinauer Associates.
- Noack, S., Voges, R., Gätgens, J., and Wiechert, W. (2017). The linkage between nutrient supply, intracellular enzyme abundances and bacterial growth: new evidences from the central carbon metabolism of *Corynebacterium glutamicum*. *J. Biotechnol.* 258, 13–24. doi: 10.1016/j.jbiotec.2017.06.407
- Nöh, K., Droste, P., and Wiechert, W. (2015). Visual workflows for ^{13}C -metabolic flux analysis. *Bioinformatics* 31, 346–354. doi: 10.1093/bioinformatics/btu585
- Nueda, M. J., Tarazona, S., and Conesa, A. (2014). Next maSigPro: updating maSigPro bioconductor package for RNA-seq time series. *Bioinformatics* 30, 2598–2602. doi: 10.1093/bioinformatics/btu333
- Park, S. Y., Kim, H. K., Yoo, S. K., Oh, T. K., and Lee, J. K. (2000). Characterization of *glk*, a gene coding for glucose kinase of *Corynebacterium glutamicum*. *FEMS Microbiol. Lett.* 188, 209–215. doi: 10.1111/j.1574-6968.2000.tb09195.x
- Pfeifer, E., Gätgens, C., Polen, T., and Frunzke, J. (2017). Adaptive laboratory evolution of *Corynebacterium glutamicum* towards higher growth rates on glucose minimal medium. *Sci. Rep.* 7:16780. doi: 10.1038/s41598-017-17014-9
- Pirt, S. J. (1982). Maintenance energy: a general model for energy-limited and energy-sufficient growth. *Arch. Microbiol.* 133, 300–302. doi: 10.1007/bf00521294
- Powell, M. J. (2015). On fast trust region methods for quadratic models with linear constraints. *Math. Program. Comput.* 7, 237–267. doi: 10.1007/s12532-015-0084-4

- Riedel, C., Rittmann, D., Dangel, P., Möckel, B., Petersen, S., Sahm, H., et al. (2001). Characterization of the phosphoenolpyruvate carboxykinase gene from *Corynebacterium glutamicum* and significance of the enzyme for growth and amino acid production. *J. Mol. Microbiol. Biotechnol.* 3, 573–583.
- Sambrook, J. (2001). *Molecular Cloning: A Laboratory Manual*. Cold Spring Harbor, NY: Cold Spring Harbor Laboratory Press.
- Shah, A., Blombach, B., Gauttam, R., and Eikmanns, B. J. (2018). The RamA regulon: complex regulatory interactions in relation to central metabolism in *Corynebacterium glutamicum*. *Appl. Microbiol. Biotechnol.* 102, 5901–5910. doi: 10.1007/s00253-018-9085-3
- Silberbach, M., Schäfer, M., Hüser, A. T., Kalinowski, J., Pühler, A., Krämer, R., et al. (2005). Adaptation of *Corynebacterium glutamicum* to ammonium limitation: a global analysis using transcriptome and proteome techniques. *Appl. Environ. Microbiol.* 71, 2391–2402. doi: 10.1128/AEM.71.5.2391-2402.2005
- Unthan, S., Grünberger, A., van Ooyen, J., Gätgens, J., Heinrich, J., Paczia, N., et al. (2014). Beyond growth rate 0.6: what drives *Corynebacterium glutamicum* to higher growth rates in defined medium. *Biotechnol. Bioeng.* 111, 359–371. doi: 10.1002/bit.25103
- van Ooyen, J., Emer, D., Bussmann, M., Bott, M., Eikmanns, B. J., and Eggeling, L. (2011). Citrate synthase in *Corynebacterium glutamicum* is encoded by two gltA transcripts which are controlled by RamA, RamB, and GlxR. *J. Biotechnol.* 154, 140–148. doi: 10.1016/j.jbiotec.2010.07.004
- Vertès, A. A., Inui, M., and Yukawa, H. (2012). Postgenomic approaches to using corynebacteria as biocatalysts. *Annu. Rev. Microbiol.* 66, 521–550. doi: 10.1146/annurev-micro-010312-105506
- Wang, Z., Liu, J., Chen, L., Zeng, A. P., Solem, C., and Jensen, P. R. (2018). Alterations in the transcription factors GntR1 and RamA enhance the growth and central metabolism of *Corynebacterium glutamicum*. *Metab. Eng.* 48, 1–12. doi: 10.1016/j.ymben.2018.05.004
- Weitzel, M., Nöh, K., Dalman, T., Niedenführ, S., Stute, B., and Wiechert, W. (2013). 13CFLUX2—high-performance software suite for ¹³C-metabolic flux analysis. *Bioinformatics* 29, 143–145. doi: 10.1093/bioinformatics/bts646
- Wendisch, V. F., Bott, M., and Eikmanns, B. J. (2006). Metabolic engineering of *Escherichia coli* and *Corynebacterium glutamicum* for biotechnological production of organic acids and amino acids. *Curr. Opin. Microbiol.* 9, 268–274. doi: 10.1016/j.mib.2006.03.001
- Wiechert, W., Siefke, C., de Graaf, A. A., and Marx, A. (1997). Bidirectional reaction steps in metabolic networks: ii. flux estimation and statistical analysis. *Biotechnol. Bioeng.* 55, 118–135. doi: 10.1002/(sici)1097-0290(19970705)55:1<118::aid-bit13>3.0.co;2-i
- Xu, J.-Z., Yu, H. B., Han, M., Liu, L.-M., and Zhang, W.-G. (2019). Metabolic engineering of glucose uptake systems in *Corynebacterium glutamicum* for improving the efficiency of L-Lysine production. *J. Indust. Microbiol. Biotechnol.* 46, 937–949. doi: 10.1007/s10295-019-02170-w
- Yokota, A., and Lindley, N. D. (2005). “10 Central Metabolism: Sugar Uptake and Conversion,” in *Handbook of Corynebacterium Glutamicum*, Vol. 2005, eds L. Eggeling and M. Bott (Boca Raton: Taylor & Francis), 215–242. doi: 10.1201/9781420039696.pt5
- Zamboni, N., Fendt, S. M., Rühl, M., and Sauer, U. (2009). ¹³C-based metabolic flux analysis. *Nat. Prot.* 4:878. doi: 10.1038/nprot.2009.58

Conflict of Interest: The authors declare that the research was conducted in the absence of any commercial or financial relationships that could be construed as a potential conflict of interest.

Copyright © 2020 Graf, Haas, Teleki, Feith, Cerff, Wiechert, Nöh, Busche, Kalinowski and Takors. This is an open-access article distributed under the terms of the Creative Commons Attribution License (CC BY). The use, distribution or reproduction in other forums is permitted, provided the original author(s) and the copyright owner(s) are credited and that the original publication in this journal is cited, in accordance with accepted academic practice. No use, distribution or reproduction is permitted which does not comply with these terms.



Intrinsically Magnetic Cells: A Review on Their Natural Occurrence and Synthetic Generation

Alexander Pekarsky and Oliver Spadiut*

Institute of Chemical, Environmental and Bioscience Engineering, Research Area Biochemical Engineering, Technische Universität Wien, Vienna, Austria

OPEN ACCESS

Edited by:

Peter Neubauer,
Technical University of Berlin,
Germany

Reviewed by:

Robert Kourist,
Graz University of Technology, Austria
Claire Wilhelm,
UMR 7057 Laboratoire Matière et
Systèmes Complexes (MSC), France

*Correspondence:

Oliver Spadiut
oliver.spadiut@tuwien.ac.at

Specialty section:

This article was submitted to
Bioprocess Engineering,
a section of the journal
Frontiers in Bioengineering and
Biotechnology

Received: 16 June 2020

Accepted: 29 September 2020

Published: 19 October 2020

Citation:

Pekarsky A and Spadiut O (2020)
Intrinsically Magnetic Cells: A Review
on Their Natural Occurrence
and Synthetic Generation.
Front. Bioeng. Biotechnol. 8:573183.
doi: 10.3389/fbioe.2020.573183

The magnetization of non-magnetic cells has great potential to aid various processes in medicine, but also in bioprocess engineering. Current approaches to magnetize cells with magnetic nanoparticles (MNPs) require cellular uptake or adsorption through *in vitro* manipulation of cells. A relatively new field of research is “magnetogenetics” which focuses on *in vivo* production and accumulation of magnetic material. Natural intrinsically magnetic cells (IMCs) produce intracellular, MNPs, and are called magnetotactic bacteria (MTB). In recent years, researchers have unraveled function and structure of numerous proteins from MTB. Furthermore, protein engineering studies on such MTB proteins and other potentially magnetic proteins, like ferritins, highlight that *in vivo* magnetization of non-magnetic hosts is a thriving field of research. This review summarizes current knowledge on recombinant IMC generation and highlights future steps that can be taken to succeed in transforming non-magnetic cells to IMCs.

Keywords: intrinsic magnetism, magnetic cells, magnetotactic bacteria, magnetic protein, ferritin, encapsulin, continuous cultivation

INTRODUCTION

Magnetic nanoparticles (MNPs) have been of importance since the successful use of magnetically labeled antibodies for cell separation (Whitesides et al., 1983; Kemsheadl and Ugelstad, 1985). Since then, magnet-assisted cell separation (MACS) has been frequently used for detection and isolation of cells from complex mixtures [e.g., (McCloskey et al., 2003; Kuhara et al., 2004; Zborowski and Chalmers, 2011)]. The use of MNPs is also of great interest as magnetic resonance imaging (MRI; Li et al., 2016) and magnetic particle imaging (MPI) contrast agent (Kraupner et al., 2017), for targeted drug delivery (Huang et al., 2016; Price et al., 2018), stem cell-based regenerative medicine (Van de Walle et al., 2020), targeted cell delivery (Wu L. et al., 2018), hyperthermia treatment (Kobayashi, 2011; Liu et al., 2020), and magneto-mechanical cell fate regulation (Wu C. et al., 2018). In these

Abbreviations: DCW, dry cell weight; hHf, human H-chain ferritin; IMCs, intrinsically magnetic cells; M6A, charged C-terminal region of the MTB Mms6 protein; MACS, magnet-assisted cell separation; mam, magnetosome membrane; mms, magnetic-particle-membrane specific; MNPs, magnetic nanoparticles; MPI, magnetic particle imaging; MRI, magnetic resonance imaging; MTB, magnetotactic bacteria; P + MNP, protein coupled to magnetic nanoparticles; SQUID, superconducting quantum interference device; T_C , Curie-temperature; TEM, transmission electron microscopy; T_N , Néel-temperature; VSM, vibrating sample mode; XRD, X-ray diffraction.

approaches, cells take up or adhere MNPs (**Figure 1A**). Recent research showed that internalized MNPs can undergo degradation (Van de Walle et al., 2019; Curcio et al., 2020). Interestingly, cells showed re-magnetization after MNP degradation, which demonstrated that some cells might contain quiescent abilities to magnetize *in vivo*. Furthermore, there exist prokaryotic organisms that naturally magnetize themselves through intracellular MNP formation (Blakemore, 1975). This existence of natural, cellular magnetization initiated research to uncover important prerequisites for cell magnetization. “Magnetogenetics” focuses on intracellular production and accumulation of magnetic material in non-magnetic cells *in vivo* (Meister, 2016; Nimpf and Keays, 2017; **Figure 1B**). Several reviews describe the accumulation (Li et al., 2011; Singh et al., 2016; Gorobets et al., 2017; Gahlawat and Choudhury, 2019) and current applications of MNPs (Plouffe et al., 2015; Li et al., 2016; Mohammed et al., 2017; Vargas et al., 2018; Wu et al., 2019; Van de Walle et al., 2020). However, no overview on the generation and application of whole magnetic cells is available. This review specifically discusses intrinsically magnetic cells (IMCs) and recombinant approaches to generate them.

MAGNETISM

Intrinsically magnetic cells are magnetic cells, therefore a brief overview on magnetism and important characteristics in the nano- and micrometer range is given. Due to availability, biocompatibility and magnetic properties, we focus on the element iron. There are different types of magnetism: depending on the magnetic moments that arise from electrons and their two spin states, a material can show ferromagnetism, antiferromagnetism and ferrimagnetism through unpaired electrons (unpaired spins; **Figure 2A**) or diamagnetism through paired electrons (paired opposite spins). Diamagnetic molecules, like water, are commonly classified as non-magnetic materials and are repelled by strong magnetic fields. In paramagnetic materials, randomly oriented spins are found (**Figure 2A**; O’Handley, 2000).

Above a certain temperature, called Curie-temperature (T_C) and Néel-temperature (T_N), the magnetic behavior of materials can change to paramagnetism. Metallic iron is ferromagnetic at room temperature and shows equal and aligned magnetic moments below T_C . In antiferromagnetic materials, like hematite ($\alpha\text{-Fe}_2\text{O}_3$), the spins show opposing directions, but equal magnetic moments. In ferrimagnetic materials, like magnetite (Fe_3O_4), maghemite ($\gamma\text{-Fe}_2\text{O}_3$) or greigite (Fe_3S_4), unequal magnetic moments and opposing directions are present (**Figure 2A**; O’Handley, 2000). Greigite has a similar structure to magnetite, but with sulfur instead of oxygen ions (Roberts et al., 2011). Reported saturation magnetization values at room temperature are $218 \text{ Am}^2 \text{ kg}^{-1}$ for ferromagnetic iron (Wohlfarth, 1986), $92\text{--}100 \text{ Am}^2 \text{ kg}^{-1}$ for magnetite, $60\text{--}80 \text{ Am}^2 \text{ kg}^{-1}$ for maghemite, $59 \text{ Am}^2 \text{ kg}^{-1}$ for greigite and $0.3 \text{ Am}^2 \text{ kg}^{-1}$ for hematite (Cornell and Schwertmann, 2003; Chang et al., 2008).

The magnetic behavior is not only affected by temperature, but also by particle size. Above a critical particle size, an energetically favorable division of ferro-, ferri-, and antiferromagnetic materials into microscopic domains occurs, called Weiss domains (**Figure 2B**). These domains show different spin orientations, which result in a low net magnetic field of a macroscopic sample (O’Handley, 2000). When an external magnetic field is applied, these Weiss domains broaden and the spins align, which leads to magnetic attraction and dissipation of the domains (**Figure 2B**). Additionally, below a certain particle size, the Weiss domains also dissipate to form one single domain (single-domain state). This size-dependency is also visible through coercivity (demagnetization point) measurements in sensitive magnetometry experiments. In the single-domain state not only Weiss domains dissipate, but the external magnetic field required for demagnetization also decreases (**Figure 2C**). The characteristic size for a certain magnetic material to form a single-domain state differs. For example, a switch to single-domain state was reported below 73 nm for synthetic magnetite crystals (Li et al., 2017). Additionally, some materials exhibit superparamagnetism below 20 nm and above a certain temperature (blocking temperature). Exemplary sizes for superparamagnetic particles are 10 nm for cube-like magnetite (Li et al., 2017), 15–18 nm for maghemite (Ali K. et al., 2015), 16 nm for hematite (Bødker et al., 2000), and 9–14 nm for greigite (Lyubutin et al., 2013). Superparamagnetic particles show a fixed magnetic moment that varies only in direction, have no coercivity and a sample of such particles will have an overall zero net magnetization without an external magnetic field, due to random orientation of particles (**Figure 2D**). Since superparamagnetic particles also show high initial magnetic susceptibility, only low fields are needed for magnetization, making these particles valuable in medical and biotechnological approaches (Huber, 2005).

Several techniques are currently employed to investigate magnetic materials (Nisticò et al., 2020): superconducting quantum interference device (SQUID) magnetometry (Jenks et al., 1997; Sawicki et al., 2011) and vibrating sample mode (VSM) magnetometry (Foner, 1959) to gain magnetization curves, X-ray diffraction (XRD) to identify the atomic and molecular structure of crystals (Warren, 1990; Mos et al., 2018), and Mössbauer spectroscopy to gain valence state of iron, type of coordination polyhedron occupied by iron atoms and identification of iron oxide phases (Gütlich and Schröder, 2012; Keune, 2012; Kamnev and Tugarova, 2017). SQUID magnetometry is often the method of choice to determine if a sample is ferro-, ferri-, antiferro-, para-, or diamagnetic through measurement at different temperatures and external magnetic field strengths (Jenks et al., 1997; Sawicki et al., 2011). A schematic depiction of SQUID graphs and their extractable magnetic information is given in **Figure 2E**. For example, variation in temperature allows to distinguish between ferro-/ ferri-, antiferro-, and paramagnetic samples (inlet; **Figure 2E**). A variation in external magnetic field strength allows one to distinguish between ferro-/ ferri-, para-, dia-, and superparamagnetic samples

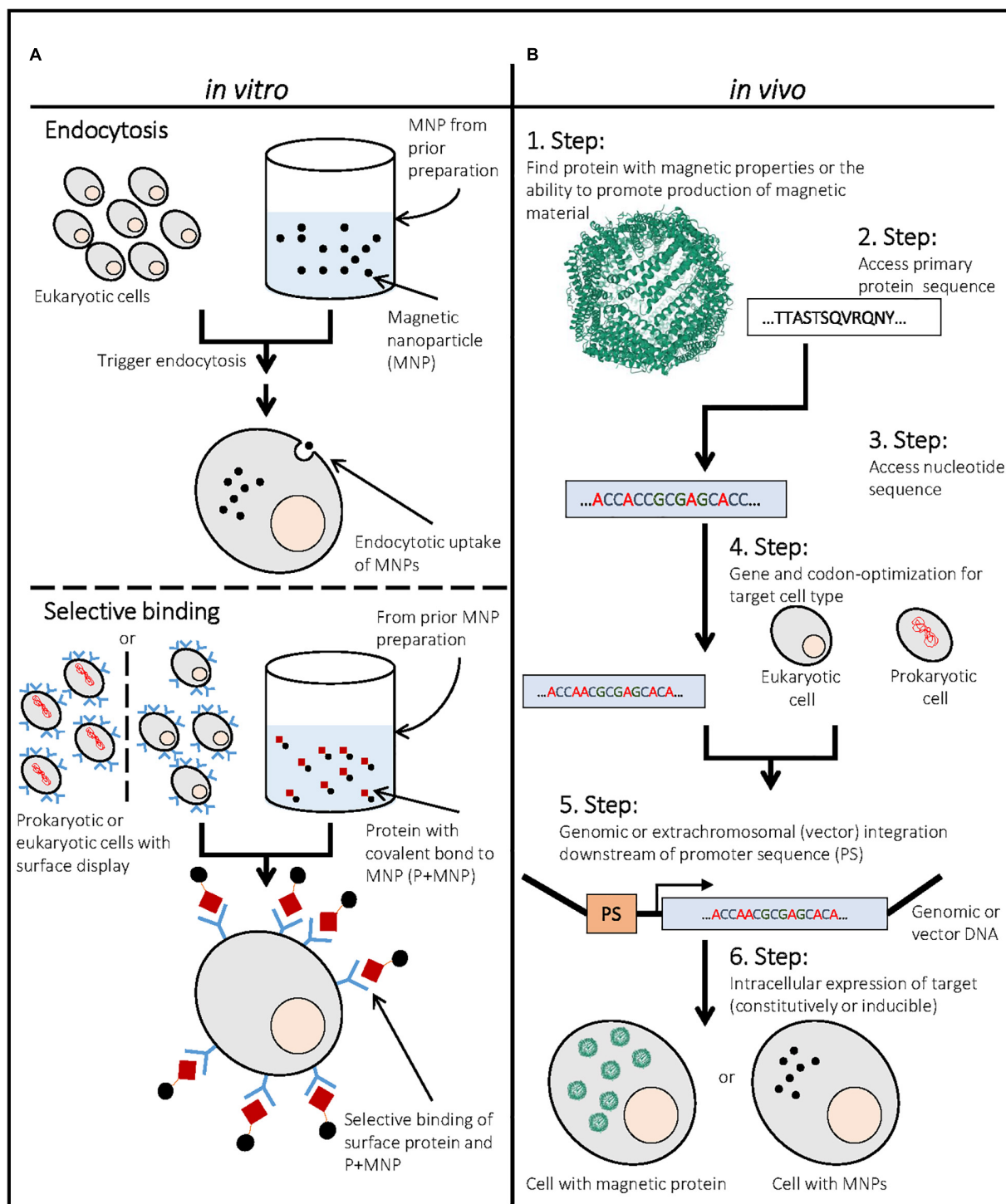


FIGURE 1 | Generation of magnetic cells by *in vitro* and *in vivo* approaches. **(A)** Upper part: Example for the generation of magnetic cells by endocytosis of magnetic nanoparticles (MNPs) with eukaryotic cells. MNPs have to be prepared in a prior step to promote endocytosis. **(A)** Lower part: Example for the generation of magnetic cells through the selective binding of a protein with covalently bound MNP to another cell surface protein (e.g., surface display of antibody that binds MNP-bound antigen). This approach can be performed for eukaryotic and prokaryotic cells by expressing and targeting a respective protein to the cell surface. The MNPs have to be chemically modified to covalently bind a respective antigen, preferably through a covalent bond. **(B)** Example for the generation of intrinsically magnetic cells through expression of a respective protein in the cell. In this case, the iron oxide containing protein ferritin [PDB ID: 1FHA (Lawson et al., 1991)] is seen as an example. First, a respective protein that confers a magnetic moment or is able to generate magnetic precipitates in the cell has to be identified. Further its primary sequence and nucleotide sequence have to be assessed and optimized. Finally, the respective protein can be integrated in a vector or genomic DNA of the cell and expressed to yield intrinsically magnetic cells that contain high amounts of the respective magnetic protein or a magnetic precipitate.

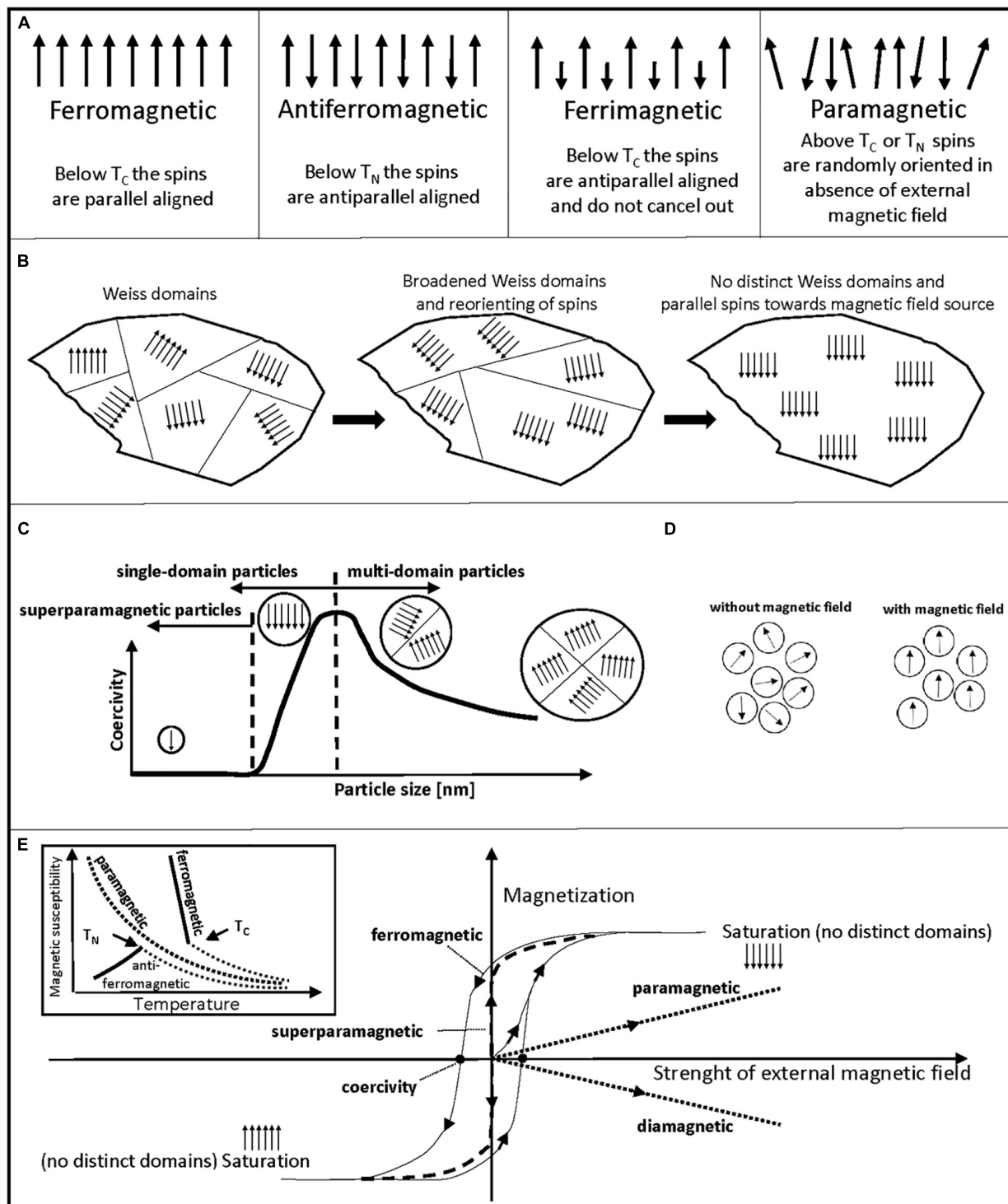


FIGURE 2 | Schematic description of different magnetic properties. **(A)** Schematic orientation of magnetic moments (spins) of ferromagnetic, antiferromagnetic, ferrimagnetic, and paramagnetic materials are shown. **(B)** Broadening and dissipation of Weiss domains of a ferromagnetic material through an increasing external magnetic field is shown from left to right. **(C)** Schematic graph of coercivity versus particle size. Superparamagnetic particles show no coercivity, coercivity increases for single-domain particles with increasing size until a maximum, when a switch to the energetically more favorable multi-domain state occurs. **(D)** Schematic sample of superparamagnetic particles is shown. Without an external magnetic field, particles show random orientation that leads to no net magnetization of the sample. With an external magnetic field, magnetic moments orient parallel toward the source of the magnetic field. **(E)** Schematic depiction of magnetization curves and their extractable information on magnetic properties of a sample. Temperature (inlet) and magnetic field strength dependency in SQUID magnetometry measurements is (Continued)

FIGURE 2 | Continued

shown. Ferro- and ferrimagnetic materials usually show similar curves, only ferromagnetism is shown. Inlet: Magnetic susceptibility versus temperature graph is shown. Based on the changing magnetic susceptibility at rising temperature, one can differentiate antiferromagnetic, ferromagnetic, or paramagnetic properties of a sample. Magnetic susceptibility decreases exponentially with increasing temperature for paramagnetic samples. Until T_N , antiferromagnetic samples show an increase in magnetic susceptibility with temperature. Near T_C , ferro- and ferrimagnetic samples show a steep decrease in magnetic susceptibility with temperature. Then, above T_N and T_C paramagnetic behavior is visible for ferro-, ferri-, and antiferromagnetic samples. Main graph: Sample magnetization versus strength of external magnetic field. Non-magnetized samples start at zero magnetization without an external magnetic field. Measurement allows to find coercivity points as marked for hysteresis curve of ferro- and ferrimagnetic samples that arises from moving/dissipating Weiss domains with magnetic field strength. No coercivity and hysteresis is usually visible for superparamagnetic particles. A linear course of sample magnetization is common for paramagnetic and diamagnetic samples. Plateau of sample magnetization marks saturation magnetization of sample, where no distinct Weiss domains exist in multi-domain state particles and is used as a mean to compare magnetic potency of a sample.

(Figure 2E). This magnetization to field strength analysis can be also used to determine coercivity points and the saturation magnetization of ferro- and ferrimagnetic samples (Sorensen, 2001).

GENERAL CONSIDERATIONS FOR *in vivo* MAGNETIZATION OF CELLS

We define an IMC as a cell that (i) exhibits a measurable magnetic moment, (ii) changes its flow direction in a magnetic field, and (iii) has not acquired these properties through uptake of – or surface modification with – MNPs. Living cells mainly consist of water, thus they are usually classified as diamagnetic. However, diamagnetism can be overcome (O’Handley, 2000). One might ask (1) the type and (2) the amount of magnetic material to overcome diamagnetism.

In respect of type, iron is the element of choice, due to its availability, biocompatibility, and magnetic properties. Furthermore, prokaryotic and eukaryotic cells have integrated iron homeostasis (Crichton et al., 2002; Konhauser et al., 2011). In a cell, iron is never present in its metallic form, but in its cationic forms [ferrous (Fe^{2+}), ferric (Fe^{3+})] with critical functions in cellular processes. Under physiological conditions only 10^{-18} M soluble Fe^{3+} , but 10^{-1} M soluble Fe^{2+} can be accumulated (Bou-Abdallah, 2010). Unpaired electrons are needed for magnetic attraction and a brief look on the electron configuration of Fe^{2+} ($[\text{Ar}]3d^6$) with 4 unpaired electrons and Fe^{3+} ($[\text{Ar}]3d^5$) with 5 unpaired electrons might indicate that generation of IMCs is already feasible by intracellular accumulation of soluble iron cations. However, most intracellular iron is complexed by proteins, since accumulation of soluble iron is cytotoxic (Imlay, 2008; Yamada et al., 2012). Since iron cofactor proteins present limited options for cell magnetization, MNPs are a better strategy to magnetize cells – through uptake [e.g., (Van de Walle et al., 2020)] or adsorption [e.g., (McCloskey et al., 2003)]. However, IMCs need to produce MNPs *in vivo* through precipitation and crystallization of magnetic iron oxides (e.g., magnetite) or sulfides (e.g., greigite). Due to its strong magnetization, magnetite has been the material of choice for that purpose.

In respect to the required amount of magnetic material to overcome diamagnetism, it is difficult to state generally valid minimum quantities. The magnetic force and three additional forces are directly proportional to the radius of the respective

cell (McCloskey et al., 2003; Plouffe et al., 2015; Zahn et al., 2017). Opposite to the direction of the magnetic force, a viscous drag force slows the cell down. Additionally, the gravitational force and the buoyancy force act on the cell. Calculations for MNP uptake (Plouffe et al., 2015) and adsorption (McCloskey et al., 2003) showed that increasing cell size requires more magnetic material to gain comparable magnetic properties. Furthermore, concerning the size of the intracellular magnetic material the characteristics of superparamagnetic and single-domain state magnetic behavior have to be considered. Recent calculations showed that MNP arrangements influence the magnetic state (Muxworthy and Williams, 2009). The authors showed that chain-like arrangement increases the range of the single-domain state to 12–197 nm for touching cubic-like magnetite particles.

Many molecules and ions that are of utmost importance for the cellular machinery, have small molecular magnetic moments, due to their nuclear spins. Despite the small value of these magnetic moments, a high gradient magnetic field might act on them (Zablotskii et al., 2016a). Thus, magnetic forces might compete and interfere with electrical forces (Zablotskii et al., 2016a). Several studies were performed on a variety of cells to analyze the impact of magnetism on cells. For example, it was long hoped to use high magnetic fields to reduce microbial growth for sanitization. However, neither static nor pulsed magnetic fields showed a significant impact on microbial growth (Harte et al., 2001), viability (László and Kutasi, 2010), or endospore germination (Wu et al., 2017). It is still noteworthy that transposition and heat shock protein activity was induced in *Escherichia coli* cells when exposed to magnetic fields (Chow and Tung, 2000; Potenza et al., 2004; Del Re et al., 2006). Low-level static magnetic fields significantly increased superoxide dismutase and peroxidase activity in suspension-cultured tobacco plant cells (Abdolmaleki et al., 2007; Sahebamei et al., 2007). A variety of effects were found for mammalian cells. An *in vitro* study on human lymphocytes and macrophages showed morphological changes in an inhomogeneous static magnetic field (Vergallo et al., 2014). In an *in vivo* study with human endothelial cells, proliferation was inhibited and angiogenesis impaired by magnetic field gradients around 2 T m^{-1} (Wang et al., 2009). However, a static homogenous magnetic field (370 mT) showed no impact on human lung fibroblast cells (Romeo et al., 2016). Recent reviews (Zablotskii et al., 2016a,b) highlight that cellular parameters are rather dependent on the value

of the magnetic field gradient, but not on the strength of the magnetic field.

CURRENTLY KNOWN NATURAL IMCs

Magnetotactic Bacteria

Magnetotactic bacteria (MTB) form intracellular liposomes, called magnetosomes, filled with crystalline MNPs [mostly magnetite (Blakemore, 1975) or greigite (Mann et al., 1990; Lefèvre et al., 2011)]. MTB also show a chain-like arrangement of the magnetosomes, often positioned mid-cell (Figures 3A,B; Matsunaga et al., 1991; Williams et al., 2012; Bazylinski et al., 2013; Silva et al., 2013), which helps them to passively align their swimming to magnetic field lines (i.e., magnetotaxis; Blakemore, 1975; Bazylinski and Frankel, 2004; Müller et al., 2020). Magnetosomes make MTB susceptible to magnetic fields as low as the earth's magnetic field (~ 0.5 Gauss = 0.05 mT; Blakemore, 1975). It has been also shown that single MTB cells have magnetic moments around 2×10^{-16} A m² in magnetic fields below 23 mT (Reufer et al., 2014; Zahn et al., 2017) and can be efficiently sorted and enriched with high-throughput microfluidic methods (Tay et al., 2018). Most magnetosome crystal sizes are between 35 and 120 nm (Bazylinski and Frankel, 2004; Araujo et al., 2015). This results in single-domain states with measureable coercivity rather than superparamagnetism. Furthermore, the linear arrangement and distance of magnetosomes increases the possible range of single-domain particles (Muxworthy and Williams, 2009) and increases cellular motility within external magnetic fields (Pfeiffer and Schüler, 2020).

Most MTB are found in micro-oxic and anoxic environments with an abundance of soluble iron ($6\text{--}60$ μM Fe²⁺; Flies et al., 2005) and show species-specific shape and size properties of MNPs (Lefèvre et al., 2013; Araujo et al., 2015; Uebe and Schüler, 2016; Figures 3C,D). Frequently described species of MTB are *Magnetospirillum* (Blakemore et al., 1979; Matsunaga et al., 1991), *Magnetovibrio* (Silva et al., 2013), *Magnetospira* (Zhu et al., 2010; Williams et al., 2012), *Magnetofaba* (Morillo et al., 2014), and *Magnetococcus* (Lefèvre et al., 2009; Bazylinski et al., 2013). *Magnetospirillum gryphiswaldense* and *Magnetospirillum magneticum* AMB-1 are frequently used to study magnetosome formation and magnetotaxis (Müller et al., 2020).

Magnetotactic bacteria accumulate magnetite up to 2–4% of their dry cell weight (DCW; Blakemore, 1982). It is thought that crystal nucleation proceeds through co-precipitation of soluble Fe²⁺ and Fe³⁺ with subsequent transformation to magnetite (Faivre and Godec, 2015). The thought precursor mineral is ferrihydrite (Faivre and Godec, 2015) that naturally forms nanocrystals below 10 nm (Michel et al., 2007, 2010a), can transform to ordered ferrimagnetic ferrihydrite (Michel et al., 2010a) and is found in the ubiquitous iron-storage protein ferritin (Chasteen and Harrison, 1999; Lewin et al., 2005; Michel et al., 2010b). MTB have a reservoir of special proteins that are located in or close to the magnetosome membrane with up to 120 copies per magnetosome particle (Raschdorf et al., 2018). These proteins are necessary for iron transport

(Nies, 2011; Uebe and Schüler, 2016; Uebe et al., 2018; Keren-Khadmy et al., 2020), crystal growth and shape (Arakaki et al., 2010, 2014, 2016; Lopez-Moreno et al., 2017; Nudelman et al., 2018), and intracellular magnetosome arrangement (Scheffel et al., 2006; Abreu et al., 2014; Toro-Nahuelpan et al., 2019). Additionally, some exhibit peroxidase-like activity (Guo et al., 2012; Li et al., 2015), which help to reduce reactive oxygen species from Fenton reactions (Hongping et al., 2015), or prevent accumulation of free radicals (Amor et al., 2020). MTB have magnetosome gene clusters, often with *mam* (magnetosome membrane) and *mms* (magnetic-particle-membrane specific) genes that regulate magnetosome formation (Schübbe et al., 2003; Fukuda et al., 2006). In magnetotactic alphaproteobacteria, magnetosome-related genes are often abbreviated with *mam* or *mms*, in other recently characterized MTB of deltaproteobacteria, nitrospirae and omnitrophica, magnetosome-related genes can be denoted as *mad* or *man* genes (Barber-Zucker and Zarivach, 2017). The magnetosome genes are organized in operons and cluster in a single region, called magnetosome island (Uebe and Schüler, 2016; Barber-Zucker and Zarivach, 2017; McCausland and Komeili, 2020).

In general, magnetosome production requires large amounts of adenosine triphosphate (Yang et al., 2013) and leads to a strong increase of intracellular NADH/NAD⁺ ratio (~ 15 after 40 h; Yang et al., 2013). MNP formation is a sensitive process that requires numerous protein-protein interactions and specific environmental conditions. MTB cultivation requires precise media and culture conditions (Ali et al., 2017). A major milestone was the first detailed analysis of magnetosome production in the controlled, microaerobic environment of a bioreactor (Heyen and Schüler, 2003). A maximum magnetite yield of 6.3 mg L⁻¹ day⁻¹ was found during batch cultivation of *M. gryphiswaldense* with a medium supplemented with 40 μM of iron. However, a cell density of only 0.40 g DCW L⁻¹ was achieved. Later, researchers were able to produce the current maximum of 9.16 g DCW L⁻¹ and 178.26 mg magnetite L⁻¹ day⁻¹ with *M. gryphiswaldense* (Zhang et al., 2011). It is also noteworthy to mention that defined growth media were recently developed that are devoid of uncharacterized and toxic products and yield magnetosome cores with higher iron content (99.8%) compared to common growth media [93.8% (Zhang et al., 2011)] for MTB (Berny et al., 2020).

Magnetic Non-magnetotactic Cells Erythrocytes

Erythrocytes (red blood cells) are crucial for delivery of O₂ in the body. They achieve this through their high intracellular hemoglobin content [$\leq 96\%$ of DCW (Weed et al., 1963) or 5.5 mM (Spees et al., 2001)]. Hemoglobin is made of four monomers, each with a covalently bound, Fe²⁺-containing prosthetic heme group (Khoshouei et al., 2017). Three hemoglobin forms are characterized by the state of the iron cation: Deoxyhemoglobin has no bound O₂ and is paramagnetic due to unpaired electrons of Fe²⁺ (Kurokawa et al., 2018), Oxyhemoglobin has a diamagnetic character due to its bond of Fe²⁺ and O₂ (Kurokawa et al., 2018), and Methemoglobin contains oxidized Fe³⁺, has paramagnetic behavior and is not

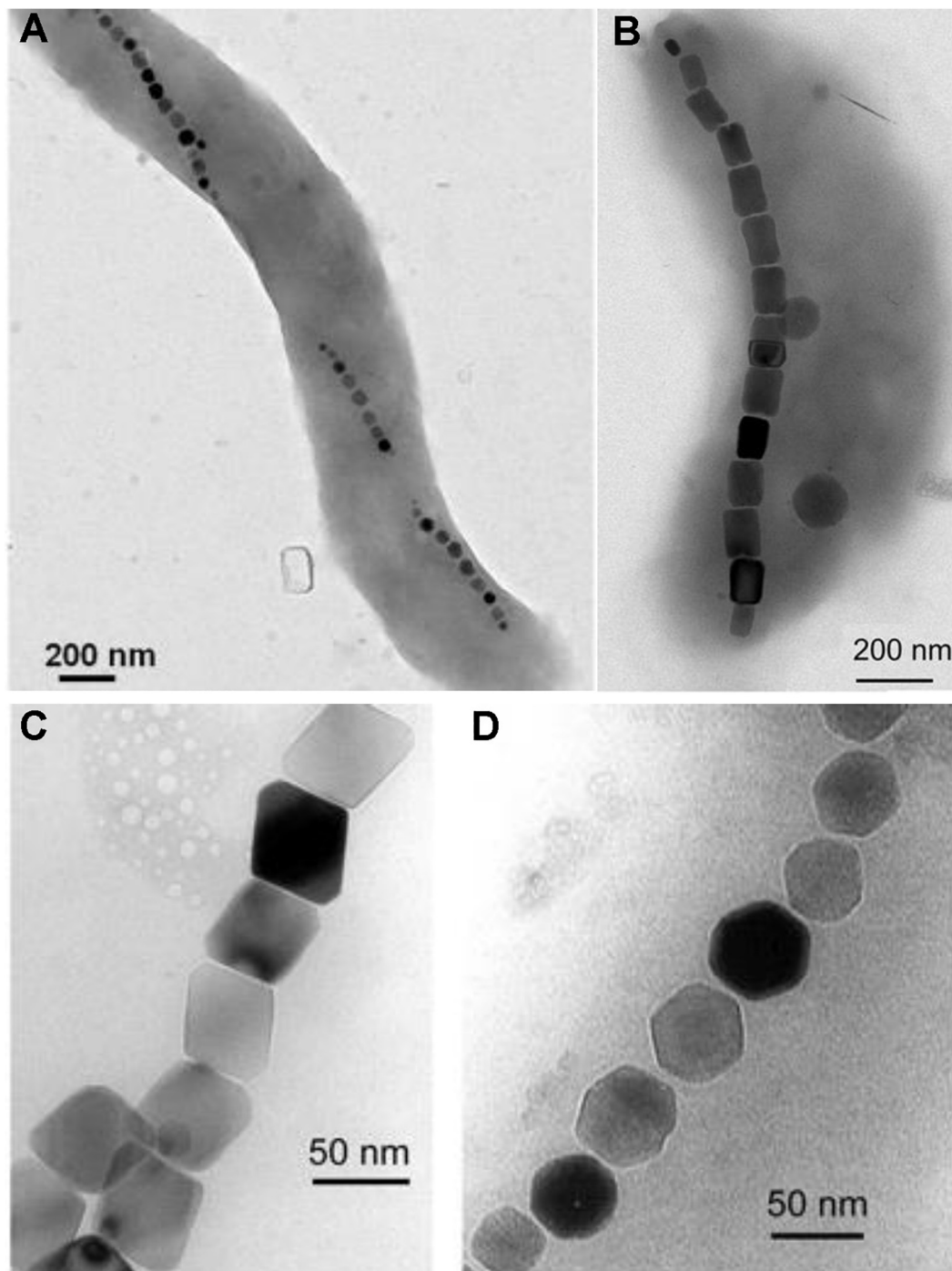


FIGURE 3 | Exemplary transmission electron microscope images of magnetotactic bacteria with magnetosome chains and different magnetosome shapes.

(A) Example of a magnetotactic *Magnetospirillum* species with chain-like magnetosome arrangement. **(B)** Example of a magnetotactic *Magnetovibrio* species with chain-like magnetosome arrangement. **(C)** Magnetite magnetosomes with octahedral and **(D)** cuboctahedral morphologies. Image in part **(A)** was adapted from Alphandéry (2014). Images in part **(B–D)** were adapted from Pósfai et al. (2013).

able to bind O_2 . Erythrocytes rich in Deoxyhemoglobin or Methemoglobin can be characterized as natural IMCs, because they can be separated from a complex matrix through high magnetic fields (Melville et al., 1975). In fact, erythrocytes are

usually separated by intense magnetic field gradients (Toner and Irimia, 2005). It is also worth mentioning that malaria-infected patients show an astonishingly high content in magnetic erythrocytes, which is also used to diagnose the infection with

the malaria parasite *Plasmodium falciparum* [e.g., (Zimmerman et al., 2006)]. In its blood stage, *P. falciparum* resides in erythrocytes and digests up to 80% of the present hemoglobin. During the degradation, heme is released into the digestive vacuole, Fe^{2+} is oxidized and after further modifications, cyclic ferriprotoporphyrin IX [Fe(III)PPIX] dimers are produced. The dimers are linked to each other to form a brown, insoluble, crystalline and paramagnetic malaria pigment, called hemozoin (Egan, 2008).

PROTEINS AND APPROACHES FOR THE GENERATION OF IMCs

Iron Importers

Uncontrolled import of iron without a specific intracellular recipient will likely result in disturbances in iron homeostasis (Crichton et al., 2002; Konhauser et al., 2011) and an increase in damaging Fenton reactions (Imlay, 2008; Yamada et al., 2012). However, we want to mention a recent study that showed successful magnetization of algae through overexpression of iron importers (Buck et al., 2015). Although separation of magnetic algae was demonstrated, the researchers highlighted this approach as economically unfeasible, due to low magnetization of algae.

MTB Proteins

In a hallmark study, researchers generated a recombinant IMC through genomic engineering of the non-magnetic, photosynthetic alphaproteobacterium *Rhodospirillum rubrum* with genes from the magnetotactic alphaproteobacterium *M. gryphiswaldense* (Kolinko et al., 2014). Their final strain harbored 29 relevant magnetosome genes of *M. gryphiswaldense* and was attracted to permanent magnets. The respective intracellular magnetic particles were crystalline magnetite with an average diameter of 24 nm and strongly resembled the magnetosomes of the donor strain. Based on this work, researchers recently aimed to (re)magnetize three non-magnetic *Magnetospirillum* species through a single-step transfer of a vector with > 30 major magnetosome genes from *M. gryphiswaldense* (Dziuba et al., 2020). However, only one strain genomically integrated the vector and produced small, unaligned magnetosomes that hindered efficient magnetotaxis under conditions similar to the geomagnetic field. It is evident that genomic integration of 29 genes and more requires tedious work and single MTB specific vectors have limited applicability for other hosts. In this respect, researchers have identified a possible pool of magnetite interacting MTB proteins. The proteins Mms6 of the *mms6* operon, MamD (Mms7), MamC (Mms13), and MamG (Mms5) of the *mamGFDC* operon strongly bind to magnetite crystals through a charged, hydrophilic C-terminal region, rich in amino acids Glu, Asp, Tyr, Ser, and Thr (Arakaki et al., 2010). Furthermore, this C-terminal region can initiate crystal nucleation and shape of magnetite crystals (Arakaki et al., 2003; Ubago-Rodríguez et al., 2019). The proteins MamG and MamC contain a loop, rich in charged residues that interact with magnetite crystals, which was also

found in MmsF and its homologue MamF of the *mamGFDC* operon (Nudelman and Zarivach, 2014; Rawlings et al., 2014; Valverde-Tercedor et al., 2015). Additionally, all contain a hydrophobic glycine-leucine repeat motif, which is common for self-assembling proteins, like silk fibroin (Zhou et al., 2001; Nudelman and Zarivach, 2014).

MamD

MamD is a 30.2 kDa magnetosome membrane protein that controls crystal size (Scheffel et al., 2008) and has its Leu-Gly repeat containing N-terminus inside the magnetosome lumen (Arakaki et al., 2003; Nudelman and Zarivach, 2014). However, studies on MamD are scarce and its highly hydrophobic character makes it a hard-to-express protein (Nudelman and Zarivach, 2014).

MamG

Similarly to MamD, studies on MamG are scarce and the 8 kDa MamG protein mostly contains hydrophobic transmembrane helices and charged amino acids residues at its ends (Lang and Schüller, 2008; Nudelman and Zarivach, 2014), which makes it also hard to express.

MamF/MmsF

The 12.3 kDa MamF protein has a 61% identity with the MmsF protein (Lohße et al., 2011). Both have an integral membrane character with three predicted hydrophobic helices, with the first connecting loop in the magnetosome lumen that contains charged residues for magnetite interaction (Nudelman and Zarivach, 2014). Surprisingly, it was possible to produce both proteins recombinantly in *E. coli* (Rawlings et al., 2014). Even more interesting, the authors found that almost all protein was found in the soluble fraction with an apparent 2-fold mass of 26 kDa under denaturing conditions. They hypothesized extremely stable dimers to be the reason. Cultivation of transfected mesenchymal stem cells that expressed the codon-optimized *mmsF* gene in 35 mM ferric quinate supplemented medium successfully yielded cells with intracellular MNPs (Elfick et al., 2017).

MamC

The MamC protein is found in magnetosome membranes and regulates the size of magnetite crystals (Scheffel et al., 2008; Valverde-Tercedor et al., 2015; Peigneux et al., 2016). Due to the hydrophobic character, whole MamC has only been produced as inclusion bodies in *E. coli* (Valverde-Tercedor et al., 2015; Lopez-Moreno et al., 2017). Although the 12.4 kDa protein has two transmembrane helices with a helical connecting loop, rich in charged residues (Nudelman and Zarivach, 2014; Nudelman et al., 2016), it could be a proper candidate for *in vivo* IMC generation. The two acidic residues (Glu66 and Asp70) of the loop match the distance between iron cations in magnetite (Nudelman et al., 2016) and *in vitro* studies on MamC and protein constructs that contained the helical MamC loop resulted in better magnetite size control (Nudelman et al., 2016; Ubago-Rodríguez et al., 2019). This highlighted that only parts of MTB proteins can be used to induce magnetite formation through fusion proteins.

Mms6

Mms6 represents an astonishing and heavily studied magnetosome-associated protein (Staniland and Rawlings, 2016). In *M. magneticum* AMB-1, the native Mms6 protein occurs in two distinct sizes 14.5 kDa and 6 kDa (Nguyen et al., 2016). The smaller 6 kDa version is tightly associated to magnetite crystals in magnetosomes and contains one transmembrane helix between N- and C-terminus (Arakaki et al., 2003; Grünberg et al., 2004; Nudelman and Zarivach, 2014). In addition to magnetite binding, the 14.5 kDa Mms6 version was found to be a binding partner of the important MamA (Nguyen et al., 2016). MamA surrounds magnetosomes and facilitates important protein-protein interactions (Komeili et al., 2004; Yamamoto et al., 2010; Zeytuni et al., 2011). Mms6 is also able to form micelles *in vitro* (200–400 kDa) with a diameter of approximately 10 nm in aqueous solution and the C-terminal, hydrophilic regions exposed (Wang et al., 2012). Astonishingly, addition of iron caused the micelles to form higher order structures (Zhang et al., 2015). Purified Mms6 improved MNP homogeneity during *in vitro* magnetite precipitation (Arakaki et al., 2003; Amemiya et al., 2007; Galloway et al., 2011; Staniland and Rawlings, 2016). Furthermore, experiments with Mms6 and MamC showed that magnetite formation was increased compared to the single protein approaches (Peigneux et al., 2019). Nevertheless, recombinant production of Mms6 in *E. coli* results in inclusion body formation (Amemiya et al., 2007; Prozorov et al., 2007; Bird et al., 2015). However, expression of codon-optimized *mms6* is possible in eukaryotic cells (Zhang et al., 2014; Elflick et al., 2017). Cultivation of *mms6* transfected mouse gliosarcoma 9L cells (Zhang et al., 2014) in 200 μ M ferric citrate supplemented medium resulted in formation of intracellular, dark particles as seen by transmission electron microscopy (TEM) images (Zhang et al., 2014). The authors stated an increased iron content of transfected cells together with an increased MRI contrast, but without a decrease in viability. Furthermore, after inoculation of cells into mice, the resulting tumors showed an increased MRI contrast. However, further magnetic studies or iron oxide identification analyses were not performed. A more detailed analysis of *mms6* transfected human mesenchymal stem cells also revealed dark aggregates between 10 and 500 nm when cultivated in 34 mM ferric quinate supplemented medium (Elflick et al., 2017; **Figures 4A,B**). SQUID magnetometry measurements of whole cells highlighted a superparamagnetic character with a saturation magnetization of $23.5 \text{ Am}^2 \text{ kg}^{-1}$ at 310.15 K (37°C). Based on their measurements, the authors hypothesized the particles to be superparamagnetic magnetite with an average diameter of 12 nm after 2 weeks and approximately 6×10^6 particles per gram biomass after 3 weeks. Thus, Mms6 seems to be a proper candidate for eukaryotic IMC generation. Interestingly, a recent review mentioned unpublished data of this study on the co-transfection of codon-optimized *mms6* and *mmsF* that resulted in less magnetism compared to *mms6* transfection alone (Kerans et al., 2018).

MagA

The *magA* gene encodes a putative 46.8 kDa transmembrane iron transporter (Nakamura et al., 1995). Studies with recombinant

MagA have focused on increasing MRI contrast of mammalian cells (Zurkiya et al., 2008; Goldhawk et al., 2009; Cho et al., 2014; Rohani et al., 2014; Sengupta et al., 2014). All studies stated that iron supplementation was crucial to achieve MRI contrast and all but one (Cho et al., 2014) reported no adverse effects on cell proliferation and/or cytotoxicity. Interestingly, it was reported that MagA is definitely not involved in magnetosome formation in *M. magneticum* AMB-1 and *M. gryphiswaldense* (Uebe et al., 2012). However, a detailed study with human embryonic kidney (HEK) 293FT-derived clonal cells, that expressed the *magA* gene in 200 μ M ferric citrate supplemented medium, described 3–5 nm intracellular particles (Zurkiya et al., 2008). The particles were visualized by TEM and a further extraction and analysis by XRD highlighted similarities to magnetite. An increase in MRI contrast was stated, but faded back to normal values, when induction of the *magA* expression was stopped. The authors hypothesized that the particles were diluted through cell division. However, formation of magnetite through MagA was questioned (Uebe et al., 2012). Magnetite formation could result randomly from high intracellular iron concentrations, due to the ability of MagA to transport iron (Uebe et al., 2012). Recent studies also questioned the general use of MagA to increase MRI contrast. One study reported strong toxic effects of MagA production in murine mesenchymal/stromal cells and kidney-derived stem cells (Pereira et al., 2016). This study also showed that *magA* transfected HEK293TN cells showed comparable accumulation of 5 nm particles, increased intracellular iron concentration and MRI contrast when cultivated in 200 μ M ferric citrate supplemented medium. Another study reported an increased intracellular iron content, but no increased MRI contrast of *magA* transfected undifferentiated embryonic mouse teratocarcinoma, multipotent P19 cells when cultured in 250 μ M ferric nitrate supplemented medium (Liu et al., 2019). Summarizing, MagA seems to be usable to increase MRI contrast in some mammalian cells, but definite generation of IMCs has not been achieved yet.

Magnetite Interacting Scaffolds

All of the mentioned MTB proteins (MagA, MamC, MamD, MamF, MmsF, MamG, and Mms6) contain transmembrane regions that limit their usability and overall expression levels. As recently reviewed (Rawlings, 2016), the problems that come with transmembrane regions could be bypassed through *in-silico* methods and protein fusions. This was recently shown for MTB peptides in Adhiron (Rawlings et al., 2015), which represent non-antibody scaffold proteins with high thermal stability (melting temperature $\sim 101^\circ\text{C}$) and high soluble expression in *E. coli* (Tiede et al., 2014). The authors used phage display to display Adhiron with two variable binding loops and screened their interaction with cubic magnetite nanoparticles (Rawlings et al., 2015). Through several selection rounds, they identified lysine and histidine residues as key amino acids for magnetite interaction. Furthermore, they showed that only one loop with the sequence QKFVPKSTN was crucial for magnetite interaction and modestly improved magnetite particle appearance in magnetite precipitation reactions. Another study reported the generation of a new non-antibody scaffold protein that resembled an antiparallel, coiled-coil hairpin (Rawlings et al., 2019). The

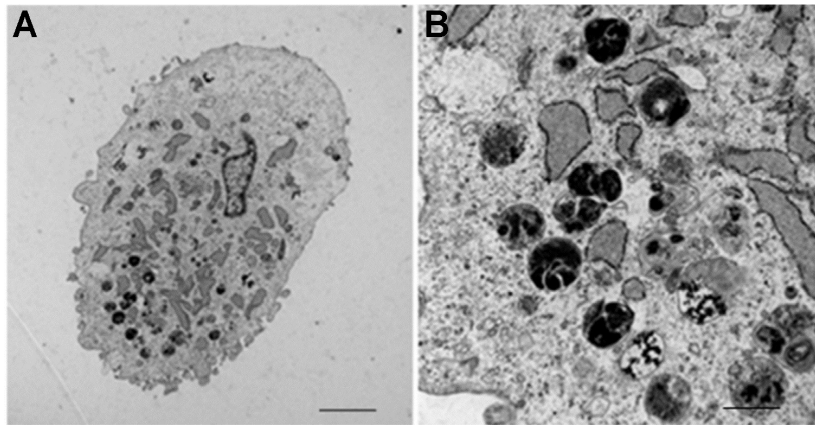


FIGURE 4 | Transmission electron microscope images of *mms6*-transfected mesenchymal stem cells. Pictures were taken after 15 days of cultivation in ferric quinate supplemented medium and show accumulation of membrane-bound, intracytoplasmic electron-dense nanoparticles. **(A)** scale bar = 10 μ m. **(B)** scale bar = 100 nm. Images in part **(A,B)** are adapted from Kerans et al. (2018).

authors further identified magnetite interacting regions of the MTB proteins MamC and MmsF and engineered the scaffold protein to display these regions. Unfortunately, the protein was produced as inclusion body in *E. coli* and needed on-column refolding. In *in vitro* magnetite precipitation experiments, the MmsF construct, but not the MamC construct, produced magnetite particles in size and shape comparable to the native MmsF protein. More studies on such magnetite interacting scaffolds are definitely needed.

Hemoglobin and Myoglobin

The paramagnetic forms of hemoglobin, namely deoxyhemoglobin, methemoglobin and the crystalline hemozoin, are naturally occurring in erythrocytes, although hemozoin only during malaria infection (Egan, 2008). The paramagnetic behavior can be explained by unpaired electrons of the respective iron cations. When occurring in high amounts, hemoglobins can render the whole cell magnetic (Melville et al., 1975; Egan, 2008). Similarly, myoglobin can become paramagnetic metmyoglobin under oxidizing conditions (Sofla et al., 2013). Myoglobin and each of the four hemoglobin subunits contain a porphyrin ring with an iron at its center (Khoshouei et al., 2017). The rather small size and simple folding pattern of myoglobin and the single hemoglobin subunits make them suitable for recombinant expression. Cytosolic expression of active myoglobin from sperm whale to approximately 10% of total protein was successful in *E. coli* (Springer and Sligar, 1987). Cytosolic production of recombinant hemoglobin above 5% and 7% of total protein content in *E. coli* and *Saccharomyces cerevisiae*, respectively, was also reported (Hoffman et al., 1990; Martínez et al., 2015). However, given the high natural hemoglobin content of erythrocytes, even higher expression levels are needed. Astonishingly, a total intracellular, soluble protein yield of 65% was reported for recombinant overexpression of leghemoglobin (LegH) from soy bean in a proprietary methylotrophic *Komagataella phaffii* MXY0291 strain (Fraser et al., 2018). LegH shows structural similarities

to myoglobin (Singh and Varma, 2017). Aside from the *legH* gene, the respective strain also overexpressed all 8 genes of the heme biosynthesis pathway and the transcriptional activator Mxr1 (Fraser et al., 2018) that has been shown to be crucial for the yeast's methanol pathway and peroxisomal enzymes (Lin-Cereghino et al., 2006). Unfortunately, data on the strain's physiology, cultivation and magnetic behavior is not available. However, this proves that active folding and high titers of heme-containing globins are not limited to mammalian cells as long as the necessary genetic prerequisites are given. Nevertheless, high intracellular heme-protein content for cell magnetization might be rather limited to erythrocytes. Furthermore, based on magnetic properties, heme proteins will never result in cell magnetization comparable to *in vivo* magnetite production. However, it must be mentioned that extracellular triggers can be used to increase magnetic susceptibility of heme-protein-rich cells, as shown for myoglobin-rich cardiomyocytes (Sofla et al., 2013). Naturally, the cytoplasmic protein fraction of these cells consists only of 5–10% of the heme-protein myoglobin (Berridge et al., 2013). The use of the highly oxidizing agent NaNO_2 transformed all myoglobin to paramagnetic metmyoglobin to generate magnetic cardiomyocytes (Sofla et al., 2013).

Ferritin

Ferritins are a family of highly conserved protein nanostructures that hold and sequester iron atoms. Theoretically, ferritins store up to 4,500 iron atoms as iron oxides in their inner cavity, but typically an average of 2,000 iron atoms are present (Jutz et al., 2015). All ferritins have an α -helix structure with strong helix-helix interactions that make the proteins very stable (Theil, 1987; Martsev et al., 1998). Ferritins usually consist of 24 subunits and have a size around 450 kDa in the apo-ferritin state (Theil, 1987). Ferritin cavities can have diameters between 5 and 8 nm (Theil, 2012). Mammalian and plant ferritins consist of a certain ratio of H- and L-subunits and are soluble in the cytoplasm and plastids. The H-subunit has an iron center, where fast conversion of Fe^{2+} to Fe^{3+} by O_2 or hydrogen peroxide occurs (Lawson et al., 1989).

The L-subunit contributes to the nucleation of the iron core and protein stability (Santambrogio et al., 1992). Bacteria have two types of ferritins, the archetypal ferritins with 24 identical H-type subunits and the heme containing bacterioferritins, also consisting of 24 H-subunits. Bacterioferritins (~450 kDa) and bacterial non-heme ferritins (~470 kDa) from *E. coli* are essential for growth and store around 2,500–2,700 iron atoms (Andrews et al., 2003). The iron oxide core structure and crystallinity can vary from amorphous to nanocrystalline and often contains a material similar to ferrihydrite (Lewin et al., 2005; Michel et al., 2010b) that naturally forms nanocrystals below 10 nm (Michel et al., 2007).

Due to their iron oxide storage capacity, ferritins have been studied as intrinsic MRI contrast agents (Naumova and Vande Velde, 2018). Researchers have been also eager to use ferritin for *in vitro* production of MNPs. Early *in vitro* studies mainly produced maghemite MNPs with horse spleen ferritin (Meldrum et al., 1992; Wong et al., 1998) and human H-chain ferritin (hHf; Uchida et al., 2006). Later, studies with hHf succeeded in magnetite MNP production (Cao et al., 2010; Walls et al., 2013). The authors found a surprisingly high number of iron atoms (8,400) in the hHf cavity (Walls et al., 2013). Convincingly, they argued that magnetite is denser than other iron oxides and that the 7.5 nm wide cavity of hHf would fit nearly 9,000 Fe atoms (Walls et al., 2013). Based on these successful *in vitro* results, *in vivo* formation of magnetic ferritins to increase intrinsic cellular MRI contrast and to generate IMCs seems possible. This was tried with mammalian HEK293T cells (Kim et al., 2012). First, the authors found that cultivation in 3 mM ferrous ammonium sulfate supplemented medium and recombinant expression of hHf resulted only in minor intracellular iron accumulation and no cell magnetization. However, additional co-expression of the divalent metal transporter 1 (DMT1) increased intracellular iron content significantly. Only then, the cells were attracted to permanent magnets by $30 \mu\text{m s}^{-1}$. The engineered cells were also retained to 25% on a MACS column, but unfortunately no further analyses were performed to characterize the source of cellular magnetism. Another study reported an almost 3-fold increase in magnetic binding of *S. cerevisiae* cells through expression of a mutated form of the thermostable, homo-multimeric ferritin of *Pyrococcus furiosus* (Matsumoto et al., 2015). The authors assumed that higher ferritin iron content would increase ferritin magnetization, as recently shown *in vitro* for hHf (Walls et al., 2013) and therefore selected ferritin mutants with increased iron binding. Their most promising mutant ferritin candidate, L55P, induced an almost 2-fold greater iron accumulation than the wild-type (Matsumoto et al., 2015). Although their mutant ferritin showed paramagnetic behavior at 5 K in SQUID magnetometry measurements and around 60% of mutant-expressing yeast cells were retained on a magnetic column, MRI analysis of the respective yeast cells showed no significant difference of the signals when normalized to the intracellular iron content. This implied no formation of a distinct magnetic iron oxide form, but rather an increase of magnetization through intracellular iron. Similar results were found for an *E. coli* knockout strain without the native ferritin-clan genes (*ftnA*, *bfr*, and *dps*) and iron exporters (*rcnA*, *fieF*, and

zntA) that overexpressed a ferritin (FtnA) double-mutant (H34L, T64I) together with iron importers (Liu et al., 2016). SQUID magnetometry measurements of the mutant cells indicated a paramagnetic character and around 70% of cells were retained on a MACS column. However, no distinct formation of magnetic iron oxides in the ferritin cores was stated.

Together, these results highlight that overexpression of ferritins and mutant ferritins with higher iron binding capacity is a promising starting point, but more sophisticated methods to induce *in vivo* magnetite formation with ferritins are needed. One possible approach was recently shown with a ferritin-M6A chimera (Radoul et al., 2016). The authors fused the charged C-terminal region (M6A) of the MTB Mms6 protein that strongly binds magnetite and is crucial for magnetite biomineralization (Arakaki et al., 2003; Ubago-Rodríguez et al., 2019) to the mouse H-ferritin subunit (Radoul et al., 2016). Ferritin-M6A formed ~440 kDa structures that were found to be ~12 nm protein particles with 24 (~25.8 kDa) monomers able to bind iron. Expression of ferritin-M6A in rat glioma C6 cells resulted in increased iron content, and *in vivo* analysis of tumor xenografts in mice that expressed ferritin-M6A showed also increased MRI contrast. Summarizing, engineered ferritins have the potential to magnetize cells, their easy expression in various hosts increases their applicability, but definite magnetite formation for strong magnetization of cells requires further research.

Encapsulins

Prokaryotic, proteinaceous proteins, called encapsulins, were structurally described to form large icosahedral shells by intracellular self-assembly of monomers that function as a minimal compartment (Sutter et al., 2008). These nanocompartments are suggested to play an important role in many microbial organisms and form capsids around 25–35 nm in diameter (Nichols et al., 2017). Similar to ferritin, they are pH resistant and temperature stable. However, they have a native set of cargo molecules that are packaged into the shells via a specific short terminal peptide tag that can be used to target other proteins to the shell (Cassidy-Amstutz et al., 2016). Encapsulins were not only successfully produced in prokaryotes (McHugh et al., 2014; Lagoutte et al., 2018), but also in eukaryotes (Lau et al., 2018; Sigmund et al., 2018), which makes them versatile tools for localized reactions. An interesting candidate for the generation of IMCs could be the encapsulin of the gram-negative bacterium *Myxococcus xanthus*. The *M. xanthus* encapsulin consists of a shell protein (EncA; 32.5 kDa) and contains three internal proteins (EncB; 17 kDa; EncC; 13 kDa; EncD; 11 kDa; McHugh et al., 2014). Built from 180 EncA monomers, the final encapsulin has an average diameter of 32 nm with an internal diameter of 26 nm. Furthermore, the authors showed that EncB and EncC contain ferritin-like domains attached to the inner encapsulin surface. They further found ~5 nm electron-dense granules inside the encapsulin and calculated that it could potentially hold up to 30,000 iron atoms, which marks an approximate 10-fold increase compared to ferritin. However, the authors gave no indication on the iron phase inside the encapsulin (McHugh et al., 2014). In a recent study, the authors expressed the EncA protein of *M. xanthus* together

with EncB or EncC in mammalian HEK293T cells (Sigmund et al., 2018). They reported efficient iron encapsulation for MRI contrast and MACS. Cell viability was not negatively affected. Unfortunately, the authors performed no further magnetometry investigations on the cells. Interestingly, they tried to use the beneficial magnetite interacting ability of Mms6 and MamD (Mms7) through fusion of the C-terminal regions to EncA, B, or C. However, they reported no beneficial impact on iron loading compared to the native encapsulin proteins. Nevertheless, they demonstrated that encapsulins are potential candidates for recombinant IMC generation.

Iron-Sulfur Cluster Proteins

Iron-sulfur cluster proteins have a crucial role in various physiological processes. In the oxidized state, [2Fe-2S] cluster proteins have Fe^{3+} atoms, leading to 5 unpaired electrons at each iron. It has been shown that the two spin-bearing iron centers are coupled to each other through an exchange-driven antiferromagnetic coupling mechanism (Ali M.E. et al., 2015). Some iron-sulfur cluster proteins can be expressed to high titers of 30% total soluble protein (Ta and Vickery, 1992; Gubernator et al., 2003). However to our knowledge, magnetic separation techniques have not been performed with iron-sulfur cluster proteins until recently. Migratory animals are thought to have special, magnetically sensitive receptors that help in navigation on their journeys. Recently, a potential protein candidate was found (Qin et al., 2016). The authors demonstrated that the protein MagR (magnetic receptor), a homologue of the Iron-Sulfur Cluster Assembly 1 (Isca1) protein, when in complex with another protein, cryptochrome (Cry), formed a multimeric protein complex that responded to magnetic fields *in vitro*. Based on a structural analysis of MagR multimers and the MagR/Cry complex, the authors argued that the magnetic behavior could result from alignment of MagR monomers (Qin et al., 2016). Additionally, they were able to enrich the MagR protein and MagR/Cry complex, respectively, from a complex matrix with a magnet and non-magnetized iron beads (Qin et al., 2016). Later, this method was also shown to be effective to capture MagR fusion proteins from a complex matrix (Jiang et al., 2017; Wang L. et al., 2019). However, the physical capabilities of this protein complex were recently questioned (Meister, 2016; Winklhofer and Mouritsen, 2016) and the putative magnetic properties have been still under review. When MagR-membrane channel constructs were subjected to magnetic stimuli in HEK cells, they were not able to induce significant membrane channel activity in a magnetic field (Pang et al., 2017; Wang G. et al., 2019). Therefore, usability of MagR for IMC generation might be farfetched at this point and research on MagR and similar iron-sulfur cluster proteins is needed.

ENVISIONED APPLICATIONS OF IMCS

Recombinant Production of Magnetosomes and MNPs

Magnetic nanoparticles have a wide application range in medicine (Li et al., 2016), but their production has to be

cost-efficient. Although research on the mass production of MTB has brought fruitful results, common industrially relevant cellular organisms, like *E. coli* or *S. cerevisiae*, are easier to cultivate to high cell densities. Therefore, transformation of non-magnetic cells to magnetosome-producing cells is a quest (Kolinko et al., 2014; Uebe and Schüller, 2016). Recently, a patent has been granted (US9913918B2) that protects the heterologous expression of gene cassettes that comprise several MTB operons (Kolinko et al., 2014). Another set of patents describing the introduction of MTB into eukaryotic cells as artificial endosymbionts was recently granted (e.g., US8828681B2). Briefly, it is stated that MTB are genetically modified to survive conditions in the eukaryotic cytosol that further provides sufficient nutrients and micro-oxic conditions for magnetosome formation. Technically, the resulting eukaryotic cell has to be regarded as an IMC. Although not stated specifically, successful generation of MTB-endosymbiotic yeasts could be one way to facilitate mass production. Given the production of superparamagnetic MNPs with an estimated size of 12 nm in *mms6* transfected human mesenchymal stem cells (Elfick et al., 2017), production of MNPs, as side products in costly mammalian cell cultures, could be also envisioned, especially in pharmaceutically-relevant mammalian antibody production cell lines.

MRI Contrast

In recent years concerns have arisen surrounding the long-term safety of current Gadolinium(III)-based MRI contrast compounds (Runge, 2017), and this has spurred research into alternatives. It was shown that MTB can produce positive MRI contrast (Benoit et al., 2009). Additionally, although application in humans will be a future challenge, a number of studies focused on the improvement of cellular MRI contrast through genetic engineering of cells through MTB proteins (Zurkiya et al., 2008; Goldhawk et al., 2009; Cho et al., 2014; Rohani et al., 2014; Sengupta et al., 2014; Elfick et al., 2017) and ferritins (Cohen et al., 2005; Matsumoto et al., 2015; Liu et al., 2016; Radoul et al., 2016).

Magnetic Drug and Cell Delivery

Targeted drug delivery refers to predominant drug accumulation at a target zone (Torchilin, 2000). A small number of publications dealt with the use of MTB for magnetic drug and cell delivery in cancer treatment (Martel et al., 2009; Felfoul et al., 2016). In tissue engineering, intrinsically magnetic mesenchymal stem cells could be used to repair tissue damage by tracking, targeting and local long-term retention of cells at the specific site of damage (Kerans et al., 2018).

Magnetic Hyperthermia in Cancer Treatment

Magnetic hyperthermia is based on the concept that MNPs generate heat when exposed to an external, alternating magnetic field (Carrey et al., 2011; Beik et al., 2016). In hyperthermia therapy, heat is increased within or near a tumor to induce cellular changes including protein denaturation, damage to the cytoskeleton and disruption of DNA repair that lead to cell

death (Jha et al., 2016). Studies with *M. gryphiswaldense* and *M. magneticum* AMB-1 showed that IMCs present proper tools for magnetic hyperthermia (Alphandéry et al., 2011; Gandia et al., 2019). Additionally, a recent review mentioned the potential use of intrinsically magnetic mesenchymal stem cells for localized magnetic hyperthermia treatment, but also highlighted that future studies have to generate a sufficient amount of intracellular MNPs (Kerans et al., 2018).

IMCs in Bioprocess Engineering

Intrinsically magnetic cells are interesting for immobilized, whole cell catalysis that often uses magnetic beads for cell immobilization (Al-Qodah et al., 2018). With IMCs, immobilization of cells can be solely done through magnetic fields, which eliminates chemical coupling to bead surfaces.

Some cells, especially mammalian cells, are very sensitive to shear forces, which could be minimized through magnetic harvesting. Once mammalian cells exhibit magnetic behavior, they can be simply harvested through a magnetic field that attracts cells to the walls or bottom of the vessel, rather than using stressful centrifugation and filtration. The same approach might be applied for cell retention in continuous bioprocessing.

OUTLOOK

Simple overexpression of iron importers to increase intracellular iron concentrations is not the method of choice to magnetize cells. Free iron cations induce Fenton reactions and disturb iron homeostasis and show only little magnetic properties (Buck et al., 2015). Also the use of heme-proteins to magnetize cells seems to be limited. Researchers showed that heme-proteins can be expressed to high intracellular titers, but their magnetic character is only sufficiently present under oxygen-free or highly oxidizing conditions (Sofla et al., 2013). Moreover, the example of erythrocytes shows that extensive amounts of heme-proteins must be present for cell magnetization, which clearly limits recombinant approaches. Similarly, MagR might not be usable for IMC generation, since current *in vivo* studies failed. Better prospects for IMC generation are clearly envisioned for MTB proteins, ferritins and encapsulins.

Magnetotactic bacteria accumulate magnetic minerals to around 3% of their DCW, their magnetosomes show single-domain magnetic behavior, have sizes between 35 and 120 nm and are chain-like arranged. MTB present the golden standard of an IMC. Genetic engineering of non-magnetic hosts like *R. rubrum* with 29 magnetosome genes from *M. gryphiswaldense* yielded a magnetic cell (Kolinko et al., 2014). This study also yielded the largest recombinantly produced MNPs (~24 nm) in an initially non-magnetic cell. However, transferring a large pool of MTB proteins to non-magnetic hosts does not necessarily yield IMCs, as shown for non-magnetic *Magnetospirillum* species (Dziuba et al., 2020). We also argue that expression of MTB proteins might be tricky in common industrial hosts, like the bacterium *E. coli*. The work of Juodeikis in 2016 presents a good overview on soluble and insoluble production of various MTB proteins in *E. coli* (Juodeikis, 2016). Although recombinant

overexpression of MTB proteins (e.g., MagA, MmsF, or Mms6) showed better results in eukaryotic hosts, probably due to the better equipped protein folding machinery and posttranslational protein modifications (Barber and Rinehart, 2018), we argue that increasing the soluble protein expression must be a priority to successfully generate IMCs with MTB proteins. The amino acid sequence QKFVPKSTN, crucial for magnetite interaction and improvement of magnetite particle appearance, seems to be especially promising for these approaches (Rawlings et al., 2015). Furthermore, we hypothesize that the Mms6 protein marks a proper starting point for IMC generation (Elfick et al., 2017).

Compared to MTB proteins, ferritins are limited in their possible MNP size (~5–8 nm). Therefore, ferritins could be the proteins of choice for *in vivo* production of superparamagnetic MNPs. Their ubiquitous occurrence and soluble character makes them perfect for recombinant expression. Native ferritins naturally contain no magnetite, but rather amorphous or crystalline ferrihydrite that forms crystals below 10 nm. However, it was already proven that ferritins can form relatively pure magnetite *in vitro* (Walls et al., 2013). Weak cell magnetization with ferritins was already achieved in bacteria (Liu et al., 2016), yeasts (Matsumoto et al., 2015), and mammalian cells (Kim et al., 2012), but unfortunately no study reported magnetite *in vivo*. Radoul et al. (2016) presented a promising ferritin-M6A fusion to increase *in vivo* magnetite formation. It would be interesting to investigate how this ferritin-M6A fusion can be improved in iron loading through mutagenesis.

Similar to ferritins, encapsulins provide a protecting shell for iron oxide formation, but research on encapsulins has only started. Through their ability to form >20 nm nanocompartments, good expression levels in prokaryotes and eukaryotes and protein targeting inside these nanocompartments, their usability for localized magnetite forming reactions seems promising. Native *M. xanthus* encapsulin weakly magnetized mammalian cells *in vivo* only through the amount of iron stored in its inner core (Sigmund et al., 2018). The authors also tried to improve the encapsulin's iron storage abilities through fusions of MTB protein peptides, but this resulted in no improvement. However, we argue that further studies should be performed with encapsulins. It might be interesting to investigate how hypoxic conditions affect iron oxide content of encapsulins and if engineered encapsulin proteins could be used to produce rather big, single-domain iron oxide particles.

AUTHOR CONTRIBUTIONS

AP read the literature and drafted the manuscript. OS supervised and corrected the manuscript draft. All authors contributed to the article and approved the submitted version.

FUNDING

The authors acknowledge the TU Wien Bibliothek for financial support through its Open Access Funding Program.

REFERENCES

- Abdolmaleki, P., Ghanati, F., Sahebamei, H., and Sarvestani, A. S. (2007). Peroxidase activity, lignification and promotion of cell death in tobacco cells exposed to static magnetic field. *Environmentalist* 27, 435–440. doi: 10.1007/s10669-007-9080-1
- Abreu, N., Mannoubi, S., Ozyamak, E., Pignol, D., Ginet, N., and Komeili, A. (2014). Interplay between two bacterial actin homologs, MamK and MamK-like, is required for the alignment of magnetosome organelles in *Magnetospirillum magneticum* AMB-1. *J. Bacteriol.* 196, 3111–3121. doi: 10.1128/jb.01674-14
- Ali, I., Peng, C., Khan, Z. M., and Naz, I. (2017). Yield cultivation of magnetotactic bacteria and magnetosomes: a review. *J. Basic Microbiol.* 57, 643–652. doi: 10.1002/jobm.201700052
- Ali, K., Sarfraz, A. K., Mirza, I. M., Bahadur, A., Iqbal, S., and ul Haq, A. (2015). Preparation of superparamagnetic maghemite (γ -Fe₂O₃) nanoparticles by wet chemical route and investigation of their magnetic and dielectric properties. *Curr. Appl. Phys.* 15, 925–929. doi: 10.1016/j.cap.2015.04.030
- Ali, M. E., Staemmler, V., and Marx, D. (2015). Magnetostructural dynamics of rieske versus ferredoxin iron–sulfur cofactors. *Phys. Chem. Chem. Phys.* 17, 6289–6296. doi: 10.1039/C4CP05465B
- Alphandéry, E. (2014). Applications of magnetosomes synthesized by magnetotactic bacteria in medicine. *Front. Bioeng. Biotechnol.* 2:5. doi: 10.3389/fbioe.2014.00005
- Alphandéry, E., Faure, S., Raison, L., Duguet, E., Howse, P. A., and Bazylinski, D. A. (2011). Heat production by bacterial magnetosomes exposed to an oscillating magnetic field. *J. Phys. Chem. C* 115, 18–22. doi: 10.1021/jp104580t
- Al-Qodah, Z., Al-Shannag, M., Al-Bosoul, M., Penchev, I., Al-Ahmadi, H., and Al-Qodah, K. (2018). On the performance of immobilized cell bioreactors utilizing a magnetic field. *Rev. Chem. Eng.* 34:385. doi: 10.1515/revce-2016-0059
- Amemiya, Y., Arakaki, A., Staniland, S. S., Tanaka, T., and Matsunaga, T. (2007). Controlled formation of magnetite crystal by partial oxidation of ferrous hydroxide in the presence of recombinant magnetotactic bacterial protein Mms6. *Biomaterials* 28, 5381–5389. doi: 10.1016/j.biomaterials.2007.07.051
- Amor, M., Mathon, F. P., Monteil, C. L., Busigny, V., and Lefevre, C. T. (2020). Iron-biomineralizing organelle in magnetotactic bacteria: function, synthesis and preservation in ancient rock samples. *Environ. Microbiol.* doi: 10.1111/1462-2920.15098 [Epub ahead of print].
- Andrews, S. C., Robinson, A. K., and Rodríguez-Quiriones, F. (2003). Bacterial iron homeostasis. *FEMS Microbiol. Rev.* 27, 215–237. doi: 10.1016/s0168-6445(03)00055-x
- Arakaki, A., Kikuchi, D., Tanaka, M., Yamagishi, A., Yoda, T., and Matsunaga, T. (2016). Comparative subcellular localization analysis of magnetosome proteins reveals a unique localization behavior of Mms6 protein onto magnetite crystals. *J. Bacteriol.* 198, 2794–2802. doi: 10.1128/jb.00280-16
- Arakaki, A., Masuda, F., Amemiya, Y., Tanaka, T., and Matsunaga, T. (2010). Control of the morphology and size of magnetite particles with peptides mimicking the Mms6 protein from magnetotactic bacteria. *J. Colloid Interface Sci.* 343, 65–70. doi: 10.1016/j.jcis.2009.11.043
- Arakaki, A., Webb, J., and Matsunaga, T. (2003). A novel protein tightly bound to bacterial magnetic particles in *Magnetospirillum magneticum* strain AMB-1. *J. Biol. Chem.* 278, 8745–8750. doi: 10.1074/jbc.M211729200
- Arakaki, A., Yamagishi, A., Fukuyo, A., Tanaka, M., and Matsunaga, T. (2014). Co-ordinated functions of Mms proteins define the surface structure of cubo-octahedral magnetite crystals in magnetotactic bacteria. *Mol. Microbiol.* 93, 554–567. doi: 10.1111/mmi.12683
- Araujo, A. C., Abreu, F., Silva, K. T., Bazylinski, D. A., and Lins, U. (2015). Magnetotactic bacteria as potential sources of bioproducts. *Mar. Drugs* 13, 389–430. doi: 10.3390/md13010389
- Barber, K. W., and Rinehart, J. (2018). The ABCs of PTMs. *Nat. Chem. Biol.* 14, 188–192. doi: 10.1038/nchembio.2572
- Barber-Zucker, S., and Zarivach, R. (2017). A look into the biochemistry of magnetosome biosynthesis in magnetotactic bacteria. *ACS Chem. Biol.* 12, 13–22. doi: 10.1021/acscchembio.6b01000
- Bazylinski, D. A., and Frankel, R. B. (2004). Magnetosome formation in prokaryotes. *Nat. Rev. Microbiol.* 2, 217–230. doi: 10.1038/nrmicro842
- Bazylinski, D. A., Williams, T. J., Lefèvre, C. T., Berg, R. J., Zhang, C. L., Bowser, S. S., et al. (2013). *Magnetococcus marinus* gen. nov., sp. nov., a marine, magnetotactic bacterium that represents a novel lineage (*Magnetococcaceae* fam. nov., *Magnetococcales* ord. nov.) at the base of the *Alphaproteobacteria*. *Int. J. Syst. Evol. Microbiol.* 63, 801–808. doi: 10.1099/ijss.0.038927-0
- Beik, J., Abed, Z., Ghoreishi, F. S., Hosseini-Nami, S., Mehrzadi, S., Shakeri-Zadeh, A., et al. (2016). Nanotechnology in hyperthermia cancer therapy: from fundamental principles to advanced applications. *J. Control. Release* 235, 205–221. doi: 10.1016/j.jconrel.2016.05.062
- Benoit, M. R., Mayer, D., Barak, Y., Chen, I. Y., Hu, W., Cheng, Z., et al. (2009). Visualizing implanted tumors in mice with magnetic resonance imaging using magnetotactic bacteria. *Clin. Cancer Res.* 15, 5170–5177. doi: 10.1158/1078-0432.ccr-08-3206
- Berny, C., Le Fèvre, R., Guyot, F., Blondeau, K., Guizonne, C., Rousseau, E., et al. (2020). A method for producing highly pure magnetosomes in large quantity for medical applications using *Magnetospirillum gryphiswaldense* MSR-1 magnetotactic bacteria amplified in minimal growth media. *Front. Bioeng. Biotechnol.* 8:16. doi: 10.3389/fbioe.2020.00016
- Berridge, B. R., Van Vleet, J. F., and Herman, E. (2013). “Chapter 46 - cardiac, vascular, and skeletal muscle systems,” in *Haschek and Rousseaux's Handbook of Toxicologic Pathology*, 3rd Edn, eds W. M. Haschek, C. G. Rousseaux, and M. A. Wallig (Boston, MA: Academic Press), 1567–1665. doi: 10.1016/b978-0-12-415759-0.00046-7
- Bird, S. M., Galloway, J. M., Rawlings, A. E., Bramble, J. P., and Staniland, S. S. (2015). Taking a hard line with biotemplating: cobalt-doped magnetite magnetic nanoparticle arrays. *Nanoscale* 7, 7340–7351. doi: 10.1039/c5nr00651a
- Blakemore, R. (1975). Magnetotactic bacteria. *Science* 190, 377–379. doi: 10.1126/science.170679
- Blakemore, R. P. (1982). Magnetotactic bacteria. *Annu. Rev. Microbiol.* 36, 217–238. doi: 10.1146/annurev.mi.36.100182.001245
- Blakemore, R. P., Maratea, D., and Wolfe, R. S. (1979). Isolation and pure culture of a freshwater magnetic spirillum in chemically defined medium. *J. Bacteriol.* 140, 720–729. doi: 10.1128/jb.140.2.720-729.1979
- Bodker, F., Hansen, M. F., Koch, C. B., Lefmann, K., and Mørup, S. (2000). Magnetic properties of hematite nanoparticles. *Phys. Rev. B* 61, 6826–6838. doi: 10.1103/PhysRevB.61.6826
- Bou-Abdallah, F. (2010). The iron redox and hydrolysis chemistry of the ferritins. *Biochim. Biophys. Acta* 1800, 719–731. doi: 10.1016/j.bbagen.2010.03.021
- Buck, A., Moore, L. R., Lane, C. D., Kumar, A., Stroff, C., White, N., et al. (2015). Magnetic separation of algae genetically modified for increased intracellular iron uptake. *J. Magn. Magn. Mater.* 380, 201–204. doi: 10.1016/j.jmmm.2014.09.008
- Cao, C., Tian, L., Liu, Q., Liu, W., Chen, G., and Pan, Y. (2010). Magnetic characterization of noninteracting, randomly oriented, nanometer-scale ferrimagnetic particles. *J. Geophys. Res. Solid Earth* 115:B07103. doi: 10.1029/2009jb006855
- Carrey, J., Mehdaoui, B., and Respaud, M. (2011). Simple models for dynamic hysteresis loop calculations of magnetic single-domain nanoparticles: application to magnetic hyperthermia optimization. *J. Appl. Phys.* 109:083921. doi: 10.1063/1.3551582
- Cassidy-Amstutz, C., Oltrogge, L., Going, C. C., Lee, A., Teng, P., Quintanilla, D., et al. (2016). Identification of a minimal peptide tag for *in vivo* and *in vitro* loading of encapsulin. *Biochemistry* 55, 3461–3468. doi: 10.1021/acs.biochem.6b00294
- Chang, L., Roberts, A. P., Tang, Y., Rainford, B. D., Muxworthy, A. R., and Chen, Q. (2008). Fundamental magnetic parameters from pure synthetic greigite (Fe₃S₄). *J. Geophys. Res. Solid Earth* 113:B06104. doi: 10.1029/2007jb005502
- Chasteen, N. D., and Harrison, P. M. (1999). Mineralization in ferritin: an efficient means of iron storage. *J. Struct. Biol.* 126, 182–194. doi: 10.1006/jsbi.1999.4118
- Cho, I. K., Moran, S. P., Paudyal, R., Piotrowska-Nitsche, K., Cheng, P.-H., Zhang, X., et al. (2014). Longitudinal monitoring of stem cell grafts in vivo using magnetic resonance imaging with inducible magA as a genetic reporter. *Theranostics* 4, 972–989. doi: 10.7150/thno.9436
- Chow, K.-C., and Tung, W. L. (2000). Magnetic field exposure stimulates transposition through the induction of DnaK/J synthesis. *Biochem. Biophys. Res. Commun.* 270, 745–748. doi: 10.1006/bbrc.2000.2496
- Cohen, B., Dafni, H., Meir, G., Harmelin, A., and Neeman, M. (2005). Ferritin as an endogenous MRI reporter for noninvasive imaging of gene expression in C6 glioma tumors. *Neoplasia* 7, 109–117. doi: 10.1593/neo.04436

- Cornell, R. M., and Schwertmann, U. (2003). *The Iron Oxides: Structure, Properties, Reactions, Occurrences and Uses*. Hoboken, NJ: John Wiley & Sons.
- Crichton, R. R., Wilmet, S., Leggsy, R., and Ward, R. J. (2002). Molecular and cellular mechanisms of iron homeostasis and toxicity in mammalian cells. *J. Inorg. Biochem.* 91, 9–18. doi: 10.1016/s0162-0134(02)00461-0
- Curcio, A., Van de Walle, A., Serrano, A., Preveral, S., Péchoux, C., Pignol, D., et al. (2020). Transformation cycle of magnetosomes in human stem cells: from degradation to biosynthesis of magnetic nanoparticles anew. *ACS Nano* 14, 1406–1417. doi: 10.1021/acsnano.9b08061
- Del Re, B., Bersani, F., Mesirca, P., and Giorgi, G. (2006). Synthesis of DnaK and GroEL in *Escherichia coli* cells exposed to different magnetic field signals. *Bioelectrochemistry* 69, 99–103. doi: 10.1016/j.bioelechem.2005.11.006
- Dziuba, M. V., Zwiener, T., Uebe, R., and Schüler, D. (2020). Single-step transfer of biosynthetic operons endows a non-magnetotactic *Magnetospirillum* strain from wetland with magnetosome biosynthesis. *Environ. Microbiol.* 22, 1603–1618. doi: 10.1111/1462-2920.14950
- Egan, T. J. (2008). Haemozoin formation. *Mol. Biochem. Parasitol.* 157, 127–136. doi: 10.1016/j.molbiopara.2007.11.005
- Elflick, A., Rischitor, G., Mouras, R., Azfer, A., Lungaro, L., Uhlarz, M., et al. (2017). Biosynthesis of magnetic nanoparticles by human mesenchymal stem cells following transfection with the magnetotactic bacterial gene *mms6*. *Sci. Rep.* 7:39755. doi: 10.1038/srep39755
- Faivre, D., and Godec, T. U. (2015). From bacteria to mollusks: the principles underlying the biomineralization of iron oxide materials. *Angew. Chem. Int. Ed. Engl.* 54, 4728–4747. doi: 10.1002/anie.201408900
- Felfoul, O., Mohammadi, M., Taherkhani, S., de Lanaue, D., Zhong Xu, Y., Loghin, D., et al. (2016). Magneto-aerotactic bacteria deliver drug-containing nanoliposomes to tumour hypoxic regions. *Nat. Nanotechnol.* 11, 941–947. doi: 10.1038/nnano.2016.137
- Flies, C. B., Jonkers, H. M., de Beer, D., Bosselmann, K., Böttcher, M. E., and Schüler, D. (2005). Diversity and vertical distribution of magnetotactic bacteria along chemical gradients in freshwater microcosms. *FEMS Microbiol. Ecol.* 52, 185–195. doi: 10.1016/j.femsec.2004.11.006
- Foner, S. (1959). Versatile and sensitive vibrating-sample magnetometer. *Rev. Sci. Instrum.* 30, 548–557. doi: 10.1063/1.1716679
- Fraser, R. Z., Shitut, M., Agrawal, P., Mendes, O., and Klapholz, S. (2018). Safety evaluation of soy leghemoglobin protein preparation derived from *Pichia pastoris*, intended for use as a flavor catalyst in plant-based meat. *Int. J. Toxicol.* 37, 241–262. doi: 10.1177/1091581818766318
- Fukuda, Y., Okamura, Y., Takeyama, H., and Matsunaga, T. (2006). Dynamic analysis of a genomic island in *Magnetospirillum* sp. strain AMB-1 reveals how magnetosome synthesis developed. *FEBS Lett.* 580, 801–812. doi: 10.1016/j.febslet.2006.01.003
- Gahlawat, G., and Choudhury, A. R. (2019). A review on the biosynthesis of metal and metal salt nanoparticles by microbes. *RSC Adv.* 9, 12944–12967. doi: 10.1039/C8RA10483B
- Galloway, J. M., Arakaki, A., Masuda, F., Tanaka, T., Matsunaga, T., and Staniland, S. S. (2011). Magnetic bacterial protein Mms6 controls morphology, crystallinity and magnetism of cobalt-doped magnetite nanoparticles in vitro. *J. Mater. Chem.* 21, 15244–15254. doi: 10.1039/C1JM12003D
- Gandia, D., Gandarias, L., Rodrigo, I., Robles-García, J., Das, R., Garaio, E., et al. (2019). Unlocking the potential of magnetotactic bacteria as magnetic hyperthermia agents. *Small* 15:1902626. doi: 10.1002/sml.201902626
- Goldhawk, D. E., Lemaire, C., McCreary, C. R., McGirr, R., Dhanvantari, S., Thompson, R. T., et al. (2009). Magnetic resonance imaging of cells overexpressing MagA, an endogenous contrast agent for live cell imaging. *Mol. Imaging* 8, 129–139. doi: 10.2310/7290.2009.00006
- Gorobets, O., Gorobets, S., and Koralewski, M. (2017). Physiological origin of biogenic magnetic nanoparticles in health and disease: from bacteria to humans. *Int. J. Nanomed.* 12, 4371–4395. doi: 10.2147/IJN.S130565
- Grünberg, K., Müller, E.-C., Otto, A., Reszka, R., Linder, D., Kube, M., et al. (2004). Biochemical and proteomic analysis of the magnetosome membrane in *Magnetospirillum gryphiswaldense*. *Appl. Environ. Microbiol.* 70, 1040–1050. doi: 10.1128/aem.70.2.1040-1050.2004
- Gubernator, B., Seidler, A., Rögner, M., and Szczepaniak, A. (2003). Overexpression and reconstitution of a Rieske iron-sulfur protein from the higher plant. *Protein Expr. Purif.* 29, 8–14. doi: 10.1016/s1046-5928(03)00016-0
- Guo, F. F., Yang, W., Jiang, W., Geng, S., Peng, T., and Li, J. L. (2012). Magnetosomes eliminate intracellular reactive oxygen species in *Magnetospirillum gryphiswaldense* MSR-1. *Environ. Microbiol.* 14, 1722–1729. doi: 10.1111/j.1462-2920.2012.02707.x
- Gütlich, P., and Schröder, C. (2012). “Mössbauer spectroscopy,” in *Methods in Physical Chemistry*, eds R. Schäfer and P. C. Schmidt (Weinheim: Wiley-VCH), 351–389.
- Harte, F., Martin, M. F. S., Lacerda, A. H., Lelieveld, H. L. M., Swanson, B. G., and Barbosa-Cánovas, G. V. (2001). Potential use of 18 tesla static and pulsed magnetic fields on *Escherichia coli* and *Saccharomyces cerevisiae*. *J. Food Process. Preserv.* 25, 223–235. doi: 10.1111/j.1745-4549.2001.tb00456.x
- Heyen, U., and Schüler, D. (2003). Growth and magnetosome formation by microaerophilic *Magnetospirillum* strains in an oxygen-controlled fermentor. *Appl. Microbiol. Biotechnol.* 61, 536–544. doi: 10.1007/s00253-002-1219-x
- Hoffman, S. J., Looker, D. L., Roehrich, J. M., Cozart, P. E., Durfee, S. L., Tedesco, J. L., et al. (1990). Expression of fully functional tetrameric human hemoglobin in *Escherichia coli*. *Proc. Natl. Acad. Sci. U.S.A.* 87, 8521–8525. doi: 10.1073/pnas.87.21.8521
- Hongping, H., Zhong, Y., Liang, X., Wei, T., Jianxi, Z., and Wang, C. Y. (2015). Natural magnetite: an efficient catalyst for the degradation of organic contaminant. *Sci. Rep.* 5:10139.
- Huang, J., Li, Y., Orza, A., Lu, Q., Guo, P., Wang, L., et al. (2016). Magnetic nanoparticle facilitated drug delivery for cancer therapy with targeted and image-guided approaches. *Adv. Funct. Mater.* 26, 3818–3836. doi: 10.1002/adfm.201504185
- Huber, D. L. (2005). Synthesis, properties, and applications of iron nanoparticles. *Small* 1, 482–501. doi: 10.1002/sml.200500006
- Imlay, J. A. (2008). Cellular defenses against superoxide and hydrogen peroxide. *Annu. Rev. Biochem.* 77, 755–776. doi: 10.1146/annurev.biochem.77.061606.161055
- Jenks, W., Sadeghi, S., and Wikswo, J. P. Jr. (1997). SQUIDS for nondestructive evaluation. *J. Phys. D Appl. Phys.* 30, 293–323.
- Jha, S., Sharma, P. K., and Malviya, R. (2016). Hyperthermia: role and risk factor for cancer treatment. *Achiev. Life Sci.* 10, 161–167. doi: 10.1016/j.als.2016.11.004
- Jiang, M., Zhang, L., Wang, F., Zhang, J., Liu, G., Gao, B., et al. (2017). Novel application of magnetic protein: convenient one-step purification and immobilization of proteins. *Sci. Rep.* 7:13329. doi: 10.1038/s41598-017-13648-x
- Juodeikis, R. (2016). *Engineering Membranes in Escherichia coli: The Magnetosome, LemA Protein Family and Outer Membrane Vesicles*. Canterbury: University of Kent.
- Jutz, G., van Rijn, P., Santos Miranda, B., and Böker, A. (2015). Ferritin: a versatile building block for bionanotechnology. *Chem. Rev.* 115, 1653–1701. doi: 10.1021/cr400011b
- Kamnev, A. A., and Tugarova, A. V. (2017). Sample treatment in Mössbauer spectroscopy for protein-related analyses: nondestructive possibilities to look inside metal-containing biosystems. *Talanta* 174, 819–837. doi: 10.1016/j.talanta.2017.06.057
- Kemsheadl, J. T., and Ugelstad, J. (1985). Magnetic separation techniques: their application to medicine. *Mol. Cell. Biochem.* 67, 11–18. doi: 10.1007/BF00220980
- Kerans, F. F. A., Lungaro, L., Azfer, A., and Salter, D. M. (2018). The potential of intrinsically magnetic mesenchymal stem cells for tissue engineering. *Int. J. Mol. Sci.* 19:3159. doi: 10.3390/ijms19103159
- Keren-Khadmy, N., Zeytuni, N., Kutnowski, N., Perriere, G., Monteil, C., and Zarivach, R. (2020). From conservation to structure, studies of magnetosome associated cation diffusion facilitators (CDF) proteins in *Proteobacteria*. *PLoS One* 15:e0231839. doi: 10.1371/journal.pone.0231839
- Keune, W. (2012). Application of Mössbauer spectroscopy in magnetism. *Hyperfine Interact.* 204, 13–45. doi: 10.1007/978-94-007-4762-3_5
- Khoshouei, M., Danev, R., Plitzko, J. M., and Baumeister, W. (2017). Revisiting the structure of hemoglobin and myoglobin with cryo-electron microscopy. *J. Mol. Biol.* 429, 2611–2618. doi: 10.1016/j.jmb.2017.07.004
- Kim, T., Moore, D., and Fussenegger, M. (2012). Genetically programmed superparamagnetic behavior of mammalian cells. *J. Biotechnol.* 162, 237–245. doi: 10.1016/j.jbiotec.2012.09.019
- Kobayashi, T. (2011). Cancer hyperthermia using magnetic nanoparticles. *Biotechnol. J.* 6, 1342–1347. doi: 10.1002/biot.201100045

- Kolinko, I., Lohße, A., Borg, S., Raschdorf, O., Jogler, C., Tu, Q., et al. (2014). Biosynthesis of magnetic nanostructures in a foreign organism by transfer of bacterial magnetosome gene clusters. *Nat. Nanotechnol.* 9, 193–197. doi: 10.1038/nnano.2014.13
- Komeili, A., Vali, H., Beveridge, T. J., and Newman, D. K. (2004). Magnetosome vesicles are present before magnetite formation, and MamA is required for their activation. *Proc. Natl. Acad. Sci. U.S.A.* 101, 3839–3844. doi: 10.1073/pnas.0400391101
- Konhauser, K. O., Kappler, A., and Roden, E. E. (2011). Iron in microbial metabolisms. *Elements* 7, 89–93. doi: 10.2113/gselements.7.2.89
- Kraupner, A., Eberbeck, D., Heinke, D., Uebe, R., Schüler, D., and Briel, A. (2017). Bacterial magnetosomes – nature's powerful contribution to MPI tracer research. *Nanoscale* 9, 5788–5793. doi: 10.1039/C7NR01530E
- Kuhara, M., Takeyama, H., Tanaka, T., and Matsunaga, T. (2004). Magnetic cell separation using antibody binding with protein a expressed on bacterial magnetic particles. *Anal. Chem.* 76, 6207–6213. doi: 10.1021/ac0493727
- Kurokawa, D., Gueriba, J. S., and Diño, W. A. (2018). Spin-dependent O₂ binding to hemoglobin. *ACS Omega* 3, 9241–9245. doi: 10.1021/acsomega.8b00879
- Lagoutte, P., Mignon, C., Stadthagen, G., Potisopon, S., Donnat, S., Mast, J., et al. (2018). Simultaneous surface display and cargo loading of encapsulin nanocompartments and their use for rational vaccine design. *Vaccine* 36, 3622–3628. doi: 10.1016/j.vaccine.2018.05.034
- Lang, C., and Schüler, D. (2008). Expression of green fluorescent protein fused to magnetosome proteins in microaerophilic magnetotactic bacteria. *Appl. Environ. Microbiol.* 74, 4944–4953. doi: 10.1128/aem.00231-08
- László, J., and Kutasi, J. (2010). Static magnetic field exposure fails to affect the viability of different bacteria strains. *Bioelectromagnetics* 31, 220–225. doi: 10.1002/bem.20551
- Lau, Y. H., Giessen, T. W., Altenburg, W. J., and Silver, P. A. (2018). Prokaryotic nanocompartments form synthetic organelles in a eukaryote. *Nat. Commun.* 9:1311. doi: 10.1038/s41467-018-03768-x
- Lawson, D. M., Artymiuk, P. J., Yewdall, S. J., Smith, J. M. A., Livingstone, J. C., Treffry, A., et al. (1991). Solving the structure of human H ferritin by genetically engineering intermolecular crystal contacts. *Nature* 349, 541–544. doi: 10.1038/349541a0
- Lawson, D. M., Treffry, A., Artymiuk, P. J., Harrison, P. M., Yewdall, S. J., Luzzago, A., et al. (1989). Identification of the ferroxidase centre in ferritin. *FEBS Lett.* 254, 207–210. doi: 10.1016/0014-5793(89)81040-3
- Lefèvre, C. T., Bernadac, A., Yu-Zhang, K., Pradel, N., and Wu, L.-F. (2009). Isolation and characterization of a magnetotactic bacterial culture from the Mediterranean Sea. *Environ. Microbiol.* 11, 1646–1657. doi: 10.1111/j.1462-2920.2009.01887.x
- Lefèvre, C. T., Menguy, N., Abreu, F., Lins, U., Pósai, M., Prozorov, T., et al. (2011). A cultured greigite-producing magnetotactic bacterium in a novel group of sulfate-reducing bacteria. *Science* 334, 1720–1723. doi: 10.1126/science.1212596
- Lefèvre, C. T., Trubitsyn, D., Abreu, F., Kolinko, S., Jogler, C., de Almeida, L. G. P., et al. (2013). Comparative genomic analysis of magnetotactic bacteria from the *Deltaproteobacteria* provides new insights into magnetite and greigite magnetosome genes required for magnetotaxis. *Environ. Microbiol.* 15, 2712–2735. doi: 10.1111/1462-2920.12128
- Lewin, A., Moore, G. R., and Le Brun, N. E. (2005). Formation of protein-coated iron minerals. *Dalton Trans.* 22, 3597–3610. doi: 10.1039/B506071K
- Li, K., Chen, C., Chen, C., Wang, Y., Wei, Z., Pan, W., et al. (2015). Magnetosomes extracted from *Magnetospirillum magneticum* strain AMB-1 showed enhanced peroxidase-like activity under visible-light irradiation. *Enzyme Microb. Technol.* 72, 72–78. doi: 10.1016/j.enzmictec.2015.02.009
- Li, Q., Kartikowati, C. W., Horie, S., Ogi, T., Iwaki, T., and Okuyama, K. (2017). Correlation between particle size/domain structure and magnetic properties of highly crystalline Fe₃O₄ nanoparticles. *Sci. Rep.* 7:9894.
- Li, X., Wei, J., Aifantis, K. E., Fan, Y., Feng, Q., Cui, F.-Z., et al. (2016). Current investigations into magnetic nanoparticles for biomedical applications. *J. Biomed. Mater. Res. Part A* 104, 1285–1296. doi: 10.1002/jbm.a.35654
- Li, X., Xu, H., Chen, Z.-S., and Chen, G. (2011). Biosynthesis of nanoparticles by microorganisms and their applications. *J. Nanomater.* 2011:270974. doi: 10.1155/2011/270974
- Lin-Cereghino, G. P., Godfrey, L., de la Cruz, B. J., Johnson, S., Khuongsathiene, S., Tolstourkov, I., et al. (2006). Mxr1p, a key regulator of the methanol utilization pathway and peroxisomal genes in *Pichia pastoris*. *Mol. Cell. Biol.* 26, 883–897. doi: 10.1128/MCB.26.3.883-897.2006
- Liu, D., Hong, Y., Li, Y., Hu, C., Yip, T.-C., Yu, W.-K., et al. (2020). Targeted destruction of cancer stem cells using multifunctional magnetic nanoparticles that enable combined hyperthermia and chemotherapy. *Theranostics* 10, 1181–1196. doi: 10.7150/thno.38989
- Liu, L., Alizadeh, K., Donnelly, S. C., Dassanayake, P., Hou, T. T., McGirr, R., et al. (2019). MagA expression attenuates iron export activity in undifferentiated multipotent P19 cells. *PLoS One* 14:e0217842. doi: 10.1371/journal.pone.0217842
- Liu, X., Lopez, P. A., Giessen, T. W., Giles, M., Way, J. C., and Silver, P. A. (2016). Engineering genetically-encoded mineralization and magnetism via directed evolution. *Sci. Rep.* 6:38019. doi: 10.1038/srep38019
- Lohße, A., Ullrich, S., Katzmann, E., Borg, S., Wanner, G., Richter, M., et al. (2011). Functional analysis of the magnetosome island in *Magnetospirillum gryphiswaldense*: the mamAB operon is sufficient for magnetite biomineralization. *PLoS One* 6:e25561. doi: 10.1371/journal.pone.0025561
- Lopez-Moreno, R., Fernández-Vivas, A., Valverde-Tercedor, C., Azuaga Fortes, A. I., Casares Atienza, S., Rodríguez-Navarro, A. B., et al. (2017). Magnetite nanoparticles biomineralization in the presence of the magnetosome membrane protein MamC: effect of protein aggregation and protein structure on magnetite formation. *Cryst. Growth Des.* 17, 1620–1629. doi: 10.1021/acs.cgd.6b01643
- Lyubutin, I. S., Starchikov, S. S., Lin, C.-R., Lu, S.-Z., Shaikh, M. O., Funtov, K. O., et al. (2013). Magnetic, structural, and electronic properties of iron sulfide FeS₄ nanoparticles synthesized by the polyol mediated process. *J. Nanopart. Res.* 15:1397.
- Mann, S., Sparks, N. H., Frankel, R. B., Bazylinski, D. A., and Jannasch, H. W. (1990). Biomineralization of ferrimagnetic greigite (Fe₃S₄) and iron pyrite (FeS₂) in a magnetotactic bacterium. *Nature* 343, 258–261. doi: 10.1038/343258a0
- Martel, S., Mohammadi, M., Felfoul, O., Lu, Z., and Pouponneau, P. (2009). Flagellated magnetotactic bacteria as controlled MRI-trackable propulsion and steering systems for medical nanorobots operating in the human microvasculature. *Int. J. Robot. Res.* 28, 571–582. doi: 10.1177/0278364908100924
- Martínez, J. L., Liu, L., Petranovic, D., and Nielsen, J. (2015). Engineering the oxygen sensing regulation results in an enhanced recombinant human hemoglobin production by *Saccharomyces cerevisiae*. *Biotechnol. Bioeng.* 112, 181–188. doi: 10.1002/bit.25347
- Martsev, S. P., Vlasov, A. P., and Arosio, P. (1998). Distinct stability of recombinant L and H subunits of human ferritin: calorimetric and ANS binding studies. *Protein Eng. Des. Sel.* 11, 377–381. doi: 10.1093/protein/11.5.377
- Matsumoto, Y., Chen, R., Anikeeva, P., and Jasanoff, A. (2015). Engineering intracellular biomineralization and biosensing by a magnetic protein. *Nat. Commun.* 6:8721. doi: 10.1038/ncomms9721
- Matsunaga, T., Sakaguchi, T., and Tadakoro, F. (1991). Magnetite formation by a magnetic bacterium capable of growing aerobically. *Appl. Microbiol. Biotechnol.* 35, 651–655. doi: 10.1007/BF00169632
- McCausland, H. C., and Komeili, A. (2020). Magnetic genes: studying the genetics of biomineralization in magnetotactic bacteria. *PLoS Genet.* 16:e1008499. doi: 10.1371/journal.pgen.1008499
- McCloskey, K. E., Chalmers, J. J., and Zborowski, M. (2003). Magnetic cell separation: characterization of magnetophoretic mobility. *Anal. Chem.* 75, 6868–6874. doi: 10.1021/ac034315j
- McHugh, C. A., Fontana, J., Nemecek, D., Cheng, N., Aksyuk, A. A., Heymann, J. B., et al. (2014). A virus capsid-like nanocompartment that stores iron and protects bacteria from oxidative stress. *EMBO J.* 33, 1896–1911. doi: 10.15252/emboj.201488566
- Meister, M. (2016). Physical limits to magnetogenetics. *eLife* 5:e17210. doi: 10.7554/eLife.17210
- Meldrum, F., Heywood, B., and Mann, S. (1992). Magnetoferritin: in vitro synthesis of a novel magnetic protein. *Science* 257, 522–523. doi: 10.1126/science.1636086
- Melville, D., Paul, F., and Roath, S. (1975). Direct magnetic separation of red cells from whole blood. *Nature* 255:706. doi: 10.1038/255706a0
- Michel, F. M., Barrón, V., Torrent, J., Morales, M. P., Serna, C. J., Boily, J.-F., et al. (2010a). Ordered ferrimagnetic form of ferrihydrite reveals links

- among structure, composition, and magnetism. *Proc. Natl. Acad. Sci. U.S.A.* 107, 2787–2792. doi: 10.1073/pnas.0910170107
- Michel, F. M., Hosein, H.-A., Hausner, D. B., Debnath, S., Parise, J. B., and Strongin, D. R. (2010b). Reactivity of ferritin and the structure of ferritin-derived ferrihydrite. *Biochim. Biophys. Acta* 1800, 871–885. doi: 10.1016/j.bbagen.2010.05.007
- Michel, F. M., Ehm, L., Antao, S. M., Lee, P. L., Chupas, P. J., Liu, G., et al. (2007). The structure of ferrihydrite, a nanocrystalline material. *Science* 316, 1726–1729. doi: 10.1126/science.1142525
- Mohammed, L., Gomaa, H. G., Ragab, D., and Zhu, J. (2017). Magnetic nanoparticles for environmental and biomedical applications: a review. *Particuology* 30, 1–14. doi: 10.1016/j.partic.2016.06.001
- Morillo, V., Abreu, F., Araujo, A. C., de Almeida, L. G. P., Enrich-Prast, A., Farina, M., et al. (2014). Isolation, cultivation and genomic analysis of magnetosome biomineralization genes of a new genus of South-seeking magnetotactic cocci within the *Alphaproteobacteria*. *Front. Microbiol.* 5:72. doi: 10.3389/fmicb.2014.00072
- Mos, Y. M., Vermeulen, A. C., Buisman, C. J. N., and Weijma, J. (2018). X-ray diffraction of iron containing samples: the importance of a suitable configuration. *Geomicrobiol. J.* 35, 511–517. doi: 10.1080/01490451.2017.1401183
- Müller, F. D., Schüler, D., and Pfeiffer, D. (2020). A compass to boost navigation: cell biology of bacterial magnetotaxis. *J. Bacteriol.* doi: 10.1128/JB.00398-20
- Muxworthy, A. R., and Williams, W. (2009). Critical superparamagnetic/single-domain grain sizes in interacting magnetite particles: implications for magnetosome crystals. *J. R. Soc. Interface* 6, 1207–1212. doi: 10.1098/rsif.2008.0462
- Nakamura, C., Burgess, J. G., Sode, K., and Matsunaga, T. (1995). An iron-regulated gene, magA, encoding an iron transport protein of *Magnetospirillum* sp. strain AMB-1. *J. Biol. Chem.* 270, 28392–28396. doi: 10.1074/jbc.270.47.28392
- Naumova, A. V., and Vande Velde, G. (2018). Genetically encoded iron-associated proteins as MRI reporters for molecular and cellular imaging. *Wiley Interdiscip. Rev. Nanomed. Nanobiotechnol.* 10:e1482. doi: 10.1002/wnan.1482
- Nguyen, H. V., Suzuki, E., Oestreicher, Z., Minamide, H., Endoh, H., Fukumori, Y., et al. (2016). A protein-protein interaction in magnetosomes: TPR protein MamA interacts with an Mms6 protein. *Biochem. Biophys. Rep.* 7, 39–44. doi: 10.1016/j.bbrep.2016.05.010
- Nichols, R. J., Cassidy-Amstutz, C., Chaijarasphong, T., and Savage, D. F. (2017). Encapsulins: molecular biology of the shell. *Crit. Rev. Biochem. Mol. Biol.* 52, 583–594. doi: 10.1080/10409238.2017.1337709
- Nies, D. H. (2011). How iron is transported into magnetosomes. *Mol. Microbiol.* 82, 792–796. doi: 10.1111/j.1365-2958.2011.07864.x
- Nimpf, S., and Keays, D. A. (2017). Is magnetogenetics the new optogenetics? *EMBO J.* 36, 1643–1646. doi: 10.15252/embj.201797177
- Nisticò, R., Cesano, F., and Garello, F. (2020). Magnetic materials and systems: domain structure visualization and other characterization techniques for the application in the materials science and biomedicine. *Inorganics* 8:6. doi: 10.3390/inorganics8010006
- Nudelman, H., Perez Gonzalez, T., Kolushiva, S., Widdrat, M., Reichel, V., Peigneux, A., et al. (2018). The importance of the helical structure of a MamC-derived magnetite-interacting peptide for its function in magnetite formation. *Acta Crystallogr. D Struct. Biol.* 74, 10–20. doi: 10.1107/S2059798317017491
- Nudelman, H., Valverde-Tercedor, C., Kolushiva, S., Perez Gonzalez, T., Widdrat, M., Grimberg, N., et al. (2016). Structure-function studies of the magnetite-biomineralizing magnetosome-associated protein MamC. *J. Struct. Biol.* 194, 244–252. doi: 10.1016/j.jsb.2016.03.001
- Nudelman, H., and Zarivach, R. (2014). Structure prediction of magnetosome-associated proteins. *Front. Microbiol.* 5:9. doi: 10.3389/fmicb.2014.00009
- O'Handley, R. C. (2000). *Modern Magnetic Materials: Principles and Applications*. New York, NY: John Wiley.
- Pang, K., You, H., Chen, Y., Chu, P., Hu, M., Shen, J., et al. (2017). MagR alone is insufficient to confer cellular calcium responses to magnetic stimulation. *Front. Neural Circuits* 11:11. doi: 10.3389/fncir.2017.00011
- Peigneux, A., Jabalera, Y., Vivas, M. A. F., Casares, S., Azuaga, A. I., and Jimenez-Lopez, C. (2019). Tuning properties of biomimetic magnetic nanoparticles by combining magnetosome associated proteins. *Sci. Rep.* 9:8804.
- Peigneux, A., Valverde-Tercedor, C., López-Moreno, R., Pérez-González, T., Fernández-Vivas, M. A., and Jiménez-López, C. (2016). Learning from magnetotactic bacteria: a review on the synthesis of biomimetic nanoparticles mediated by magnetosome-associated proteins. *J. Struct. Biol.* 196, 75–84. doi: 10.1016/j.jsb.2016.06.026
- Pereira, S. M., Williams, S. R., Murray, P., and Taylor, A. (2016). MS-1 magA: revisiting its efficacy as a reporter gene for MRI. *Mol. Imaging* 15:1536012116641533. doi: 10.1177/1536012116641533
- Pfeiffer, D., and Schüler, D. (2020). Quantifying the benefit of a dedicated “Magnetoskeleton” in bacterial magnetotaxis by live-cell motility tracking and soft agar swimming assay. *Appl. Environ. Microbiol.* 86:e01976-19.
- Plouffe, B. D., Murthy, S. K., and Lewis, L. H. (2015). Fundamentals and application of magnetic particles in cell isolation and enrichment: a review. *Rep. Prog. Phys.* 78:016601. doi: 10.1088/0034-4885/78/1/016601
- Pósfai, M., Lefèvre, C., Trubitsyn, D., Bazylinski, D., and Frankel, R. (2013). Phylogenetic significance of composition and crystal morphology of magnetosome minerals. *Front. Microbiol.* 4:344. doi: 10.3389/fmicb.2013.00344
- Potenza, L., Ubaldi, L., De Sanctis, R., De Bellis, R., Cucchiari, L., and Dachà, M. (2004). Effects of a static magnetic field on cell growth and gene expression in *Escherichia coli*. *Mutat. Res. Genet. Toxicol. Environ. Mutagen.* 561, 53–62. doi: 10.1016/j.mrgentox.2004.03.009
- Price, P. M., Mahmoud, W. E., Al-Ghamdi, A. A., and Bronstein, L. M. (2018). Magnetic drug delivery: where the field is going. *Front. Chem.* 6:619. doi: 10.3389/fchem.2018.00619
- Prozorov, T., Mallapragada, S. K., Narasimhan, B., Wang, L., Palo, P., Nilsen-Hamilton, M., et al. (2007). Protein-mediated synthesis of uniform superparamagnetic magnetite nanocrystals. *Adv. Funct. Mater.* 17, 951–957. doi: 10.1002/adfm.200600448
- Qin, S., Yin, H., Yang, C., Dou, Y., Liu, Z., Zhang, P., et al. (2016). A magnetic protein biocompass. *Nat. Mater.* 15, 217–226. doi: 10.1038/nmat4484
- Radoul, M., Lewin, L., Cohen, B., Oren, R., Popov, S., Davidov, G., et al. (2016). Genetic manipulation of iron biomineralization enhances MR relaxivity in a ferritin-M6A chimeric complex. *Sci. Rep.* 6:26550. doi: 10.1038/srep26550
- Raschdorf, O., Bonn, F., Zeytuni, N., Zarivach, R., Becher, D., and Schüler, D. (2018). A quantitative assessment of the membrane-integral sub-proteome of a bacterial magnetic organelle. *J. Proteomics* 172, 89–99. doi: 10.1016/j.jprot.2017.10.007
- Rawlings, A. E. (2016). Membrane proteins: always an insoluble problem? *Biochem. Soc. Trans.* 44, 790–795. doi: 10.1042/BST20160025
- Rawlings, A. E., Bramble, J. P., Tang, A. A. S., Somner, L. A., Monnington, A. E., Cooke, D. J., et al. (2015). Phage display selected magnetite interacting Adhirons for shape controlled nanoparticle synthesis. *Chem. Sci.* 6, 5586–5594. doi: 10.1039/C5SC01472G
- Rawlings, A. E., Bramble, J. P., Walker, R., Bain, J., Galloway, J. M., and Staniland, S. S. (2014). Self-assembled MmsF proteinosomes control magnetite nanoparticle formation in vitro. *Proc. Natl. Acad. Sci. U.S.A.* 111, 16094–16099. doi: 10.1073/pnas.1409256111
- Rawlings, A. E., Somner, L. A., Fitzpatrick-Milton, M., Roebuck, T. P., Gwyn, C., Liravi, P., et al. (2019). Artificial coiled coil biomineralisation protein for the synthesis of magnetic nanoparticles. *Nat. Commun.* 10:2873.
- Reufer, M., Besseling, R., Schwarz-Linek, J., Martinez, V. A., Morozov, A. N., Arlt, J., et al. (2014). Switching of swimming modes in *Magnetospirillum gryphiswaldense*. *Biophys. J.* 106, 37–46. doi: 10.1016/j.bpj.2013.10.038
- Roberts, A. P., Chang, L., Rowan, C. J., Horng, C.-S., and Florindo, F. (2011). Magnetic properties of sedimentary greigite (Fe₃S₄): an update. *Rev. Geophys.* 49:RG1002. doi: 10.1029/2010rg000336
- Rohani, R., Figueredo, R., Bureau, Y., Koropatnick, J., Foster, P., Thompson, R. T., et al. (2014). Imaging tumor growth non-invasively using expression of MagA or modified ferritin subunits to augment intracellular contrast for repetitive MRI. *Mol. Imaging Biol.* 16, 63–73. doi: 10.1007/s11307-013-0661-8
- Romeo, S., Sannino, A., Scarfi, M. R., Massa, R., d'Angelo, R., and Zeni, O. (2016). Lack of effects on key cellular parameters of MRC-5 human lung fibroblasts exposed to 370 mT static magnetic field. *Sci. Rep.* 6:19398. doi: 10.1038/srep19398
- Runge, V. M. (2017). Critical questions regarding gadolinium deposition in the brain and body after injections of the gadolinium-based contrast agents, safety, and clinical recommendations in consideration of the EMA's pharmacovigilance and risk assessment committee recommendation for suspension of the marketing authorizations for 4 linear agents. *Invest. Radiol.* 52, 317–323. doi: 10.1097/rli.0000000000000374

- Sahebamei, H., Abdolmaleki, P., and Ghanati, F. (2007). Effects of magnetic field on the antioxidant enzyme activities of suspension-cultured tobacco cells. *Bioelectromagnetics* 28, 42–47. doi: 10.1002/bem.20262
- Santambrogio, P., Levi, S., Arosio, P., Palagi, L., Vecchio, G., Lawson, D. M., et al. (1992). Evidence that a salt bridge in the light chain contributes to the physical stability difference between heavy and light human ferritins. *J. Biol. Chem.* 267, 14077–14083.
- Sawicki, M., Stefanowicz, W., and Ney, A. (2011). Sensitive SQUID magnetometry for studying nanomagnetism. *Semicond. Sci. Technol.* 26:064006. doi: 10.1088/0268-1242/26/6/064006
- Scheffel, A., Gärdes, A., Grünberg, K., Wanner, G., and Schüler, D. (2008). The major magnetosome proteins MamGFDC are not essential for magnetite biomineralization in *Magnetospirillum gryphiswaldense* but regulate the size of magnetosome crystals. *J. Bacteriol.* 190, 377–386. doi: 10.1128/jb.01371-07
- Scheffel, A., Gruska, M., Faivre, D., Linaroudis, A., Plitzko, J. M., and Schüler, D. (2006). An acidic protein aligns magnetosomes along a filamentous structure in magnetotactic bacteria. *Nature* 440, 110–114. doi: 10.1038/nature04382
- Schübbe, S., Kube, M., Scheffel, A., Wawer, C., Heyen, U., Meyerdiere, A., et al. (2003). Characterization of a spontaneous nonmagnetic mutant of *Magnetospirillum gryphiswaldense* reveals a large deletion comprising a putative magnetosome island. *J. Bacteriol.* 185, 5779–5790. doi: 10.1128/jb.185.19.5779-5790.2003
- Sengupta, A., Quiaoi, K., Thompson, R. T., Prato, F. S., Gelman, N., and Goldhawk, D. E. (2014). Biophysical features of MagA expression in mammalian cells: implications for MRI contrast. *Front. Microbiol.* 5:29. doi: 10.3389/fmicb.2014.00029
- Sigmund, F., Massner, C., Erdmann, P., Stelzl, A., Rolbieski, H., Desai, M., et al. (2018). Bacterial encapsulins as orthogonal compartments for mammalian cell engineering. *Nat. Commun.* 9:1990.
- Silva, K. T., Leao, P. E., Abreu, F., Lopez, J. A., Gutarra, M. L., Farina, M., et al. (2013). Optimization of magnetosome production and growth by the magnetotactic vibrio *Magnetovibrio blakemorei* strain MV-1 through a statistics-based experimental design. *Appl. Environ. Microbiol.* 79, 2823–2827. doi: 10.1128/aem.03740-12
- Singh, P., Kim, Y.-J., Zhang, D., and Yang, D.-C. (2016). Biological synthesis of nanoparticles from plants and microorganisms. *Trends Biotechnol.* 34, 588–599. doi: 10.1016/j.tibtech.2016.02.006
- Singh, S., and Varma, A. (2017). “Structure, function, and estimation of leghemoglobin,” in *Rhizobium Biology and Biotechnology*, eds A. P. Hansen, D. K. Choudhary, P. K. Agrawal, and A. Varma (Cham: Springer International Publishing), 309–330. doi: 10.1007/978-3-319-64982-5_15
- Sofla, A., Cirkovic, B., Hsieh, A., Miklas, J. W., Filipovic, N., and Radisic, M. (2013). Enrichment of live unlabelled cardiomyocytes from heterogeneous cell populations using manipulation of cell settling velocity by magnetic field. *Biomedfluidics* 7:14110. doi: 10.1063/1.4791649
- Sorensen, C. M. (2001). “Magnetism,” in *Nanoscale Materials in Chemistry*, ed. K. J. Klabunde (Hoboken, NJ: John Wiley & Sons, Inc).
- Spees, W. M., Yablonskiy, D. A., Oswald, M. C., and Ackerman, J. J. H. (2001). Water proton MR properties of human blood at 1.5 Tesla: magnetic susceptibility, T₁, T₂, T₂* and non-Lorentzian signal behavior. *Magn. Reson. Med.* 45, 533–542. doi: 10.1002/mrm.1072
- Springer, B. A., and Sligar, S. G. (1987). High-level expression of sperm whale myoglobin in *Escherichia coli*. *Proc. Natl. Acad. Sci. U.S.A.* 84, 8961–8965. doi: 10.1073/pnas.84.24.8961
- Staniland, S. S., and Rawlings, A. E. (2016). Crystallizing the function of the magnetosome membrane mineralization protein Mms6. *Biochem. Soc. Trans.* 44, 883–890. doi: 10.1042/BST20160057
- Sutter, M., Boehringer, D., Gutmann, S., Günther, S., Prangishvili, D., Loessner, M. J., et al. (2008). Structural basis of enzyme encapsulation into a bacterial nanocompartment. *Nat. Struct. Mol. Biol.* 15, 939–947. doi: 10.1038/nsmb.1473
- Ta, D. T., and Vickery, L. E. (1992). Cloning, sequencing, and overexpression of a [2Fe-2S] ferredoxin gene from *Escherichia coli*. *J. Biol. Chem.* 267, 11120–11125.
- Tay, A., Pfeiffer, D., Rowe, K., Tannenbaum, A., Popp, F., Strangeway, R., et al. (2018). High-throughput microfluidic sorting of live magnetotactic bacteria. *Appl. Environ. Microbiol.* 84:e01308-18.
- Theil, E. C. (1987). Ferritin: structure, gene regulation, and cellular function in animals, plants, and microorganisms. *Annu. Rev. Biochem.* 56, 289–315. doi: 10.1146/annurev.bi.56.070187.001445
- Theil, E. C. (2012). Ferritin protein nanocages-the story. *Nanotechnol. Percept.* 8, 7–16. doi: 10.4024/n03th12a.ntp.08.01
- Tiede, C., Tang, A. A., Deacon, S. E., Mandal, U., Netteship, J. E., Owen, R. L., et al. (2014). Adhiron: a stable and versatile peptide display scaffold for molecular recognition applications. *Protein Eng. Des. Sel.* 27, 145–155. doi: 10.1093/protein/gzu007
- Toner, M., and Irimia, D. (2005). Blood-on-a-chip. *Annu. Rev. Biomed. Eng.* 7, 77–103. doi: 10.1146/annurev.bioeng.7.011205.135108
- Torchilin, V. P. (2000). Drug targeting. *Eur. J. Pharm. Sci.* 11, S81–S91.
- Toro-Nahuelpan, M., Giacomelli, G., Raschdorf, O., Borg, S., Plitzko, J. M., Bramkamp, M., et al. (2019). MamY is a membrane-bound protein that aligns magnetosomes and the motility axis of helical magnetotactic bacteria. *Nat. Microbiol.* 4, 1978–1989. doi: 10.1038/s41564-019-0512-8
- Ubago-Rodríguez, A., Casares Atienza, S., Fernández-Vivas, A., Peigneux, A., Jabalera, Y., de la Cuesta-Rivero, M., et al. (2019). Structure-function of MamC loop and its effect on the in vitro precipitation of biomimetic magnetite nanoparticles. *Cryst. Growth Des.* 19, 2927–2935. doi: 10.1021/acs.cgd.9b00150
- Uchida, M., Flenniken, M. L., Allen, M., Willits, D. A., Crowley, B. E., Brumfield, S., et al. (2006). Targeting of cancer cells with ferrimagnetic ferritin cage nanoparticles. *J. Am. Chem. Soc.* 128, 16626–16633. doi: 10.1021/ja0655690
- Uebe, R., Henn, V., and Schüler, D. (2012). The MagA protein of magnetospirilla is not involved in bacterial magnetite biomineralization. *J. Bacteriol.* 194, 1018–1023. doi: 10.1128/jb.06356-11
- Uebe, R., Keren-Khadmy, N., Zeytuni, N., Katzmann, E., Navon, Y., Davidov, G., et al. (2018). The dual role of MamB in magnetosome membrane assembly and magnetite biomineralization. *Mol. Microbiol.* 107, 542–557. doi: 10.1111/mmi.13899
- Uebe, R., and Schüler, D. (2016). Magnetosome biogenesis in magnetotactic bacteria. *Nat. Rev. Microbiol.* 14, 621–637. doi: 10.1038/nrmicro.2016.99
- Valverde-Tercedor, C., Montalbán-López, M., Perez-Gonzalez, T., Sanchez-Quesada, M. S., Prozorov, T., Pineda-Molina, E., et al. (2015). Size control of in vitro synthesized magnetite crystals by the MamC protein of *Magnetococcus marinus* strain MC-1. *Appl. Microbiol. Biotechnol.* 99, 5109–5121. doi: 10.1007/s00253-014-6326-y
- Van de Walle, A., Perez, J. E., Abou-Hassan, A., Hémadi, M., Luciani, N., and Wilhelm, C. (2020). Magnetic nanoparticles in regenerative medicine: what of their fate and impact in stem cells? *Mater. Today Nano* 11:100084. doi: 10.1016/j.mtnano.2020.100084
- Van de Walle, A., Plan Sangnier, A., Abou-Hassan, A., Curcio, A., Hémadi, M., Menguy, N., et al. (2019). Biosynthesis of magnetic nanoparticles from nano-degradation products revealed in human stem cells. *Proc. Natl. Acad. Sci. U.S.A.* 116, 4044–4053. doi: 10.1073/pnas.1816792116
- Vargas, G., Cypriano, J., Correa, T., Leão, P., Bazylinski, D. A., and Abreu, F. (2018). Applications of magnetotactic bacteria, magnetosomes and magnetosome crystals in biotechnology and nanotechnology: mini-review. *Molecules* 23:2438. doi: 10.3390/molecules23102438
- Vergallo, C., Ahmadi, M., Mobasheri, H., and Dini, L. (2014). Impact of inhomogeneous static magnetic field (31.7–232.0 mT) exposure on human neuroblastoma SH-SY5Y cells during cisplatin administration. *PLoS One* 9:e113530. doi: 10.1371/journal.pone.0113530
- Walls, M. G., Cao, C., Yu-Zhang, K., Li, J., Che, R., and Pan, Y. (2013). Identification of ferrous-ferric Fe₃O₄ nanoparticles in recombinant human ferritin cages. *Microsc. Microanal.* 19, 835–841. doi: 10.1017/S1431927613001724
- Wang, G., Zhang, P., Mendu, S. K., Wang, Y., Zhang, Y., Kang, X., et al. (2019). Revaluation of magnetic properties of Magneto. *Nat. Neurosci.* 23, 1047–1050. doi: 10.1038/s41593-019-0473-5
- Wang, L., Prozorov, T., Palo, P. E., Liu, X., Vaknin, D., Prozorov, R., et al. (2012). Self-assembly and biphasic iron-binding characteristics of Mms6, a bacterial protein that promotes the formation of superparamagnetic magnetite nanoparticles of uniform size and shape. *Biomacromolecules* 13, 98–105. doi: 10.1021/bm201278u
- Wang, L., Xu, H., Liu, Z., Sun, T., Yuan, C., Yang, Y., et al. (2019). Magnetic immobilization of a quorum sensing signal hydrolase, AiiA. *Microbiologyopen* 8:e00797. doi: 10.1002/mbo3.797
- Wang, Z., Yang, P., Xu, H., Qian, A., Hu, L., and Shang, P. (2009). Inhibitory effects of a gradient static magnetic field on normal angiogenesis. *Bioelectromagnetics* 30, 446–453. doi: 10.1002/bem.20501

- Warren, B. E. (1990). *X-Ray Diffraction*. Chelmsford, MA: Courier Corporation.
- Weed, R. I., Reed, C. F., and Berg, G. (1963). Is hemoglobin an essential structural component of human erythrocyte membranes? *J. Clin. Invest.* 42, 581–588. doi: 10.1172/JCI104747
- Whitesides, G. M., Kazlauskas, R. J., and Josephson, L. (1983). Magnetic separations in biotechnology. *Trends Biotechnol.* 1, 144–148. doi: 10.1016/0167-7799(83)90005-7
- Williams, T. J., Lefèvre, C. T., Zhao, W., Beveridge, T. J., and Bazylinski, D. A. (2012). *Magnetospira thiophila* gen. nov., sp. nov., a marine magnetotactic bacterium that represents a novel lineage within the *Rhodospirillaceae* (*Alphaproteobacteria*). *Int. J. Syst. Evol. Microbiol.* 62, 2443–2450. doi: 10.1099/ijs.0.037697-0
- Winklhofer, M., and Mouritsen, H. (2016). A room-temperature ferrimagnet made of metallo-proteins? *bioRxiv* [Preprint]. doi: 10.1101/094607
- Wohlfarth, E. P. (1986). *Handbook of Magnetic Materials*. Amsterdam: Elsevier.
- Wong, K. K., Douglas, T., Gider, S., Awschalom, D. D., and Mann, S. (1998). Biomimetic synthesis and characterization of magnetic proteins (magnetoferritin). *Chem. Mater.* 10, 279–285. doi: 10.1021/cm970421o
- Wu, C., Shen, Y., Chen, M., Wang, K., Li, Y., and Cheng, Y. (2018). Recent advances in magnetic-nanomaterial-based mechanotransduction for cell fate regulation. *Adv. Mater.* 30:e1705673. doi: 10.1002/adma.201705673
- Wu, K., Su, D., Liu, J., Saha, R., and Wang, J.-P. (2019). Magnetic nanoparticles in nanomedicine: a review of recent advances. *Nanotechnology* 30:502003. doi: 10.1088/1361-6528/ab4241
- Wu, L., Zhang, F., Wei, Z., Li, X., Zhao, H., Lv, H., et al. (2018). Magnetic delivery of Fe₃O₄@polydopamine nanoparticle-loaded natural killer cells suggest a promising anticancer treatment. *Biomater. Sci.* 6, 2714–2725. doi: 10.1039/C8BM00588E
- Wu, W. J., Liu, S. L., and Yung, P. T. (2017). Effect of static magnetic field on endospore germination. *Bioelectromagnetics* 38, 121–127. doi: 10.1002/bem.22017
- Yamada, M., Shimizu, M., Katafuchi, A., Grúz, P., Fujii, S., Usui, Y., et al. (2012). *Escherichia coli* DNA polymerase III is responsible for the high level of spontaneous mutations in mutT strains. *Mol. Microbiol.* 86, 1364–1375. doi: 10.1111/mmi.12061
- Yamamoto, D., Taoka, A., Uchihashi, T., Sasaki, H., Watanabe, H., Ando, T., et al. (2010). Visualization and structural analysis of the bacterial magnetic organelle magnetosome using atomic force microscopy. *Proc. Natl. Acad. Sci. U.S.A.* 107, 9382–9387. doi: 10.1073/pnas.1001870107
- Yang, J., Li, S., Huang, X., Tang, T., Jiang, W., Zhang, T., et al. (2013). A key time point for cell growth and magnetosome synthesis of *Magnetospirillum gryphiswaldense* based on real-time analysis of physiological factors. *Front. Microbiol.* 4:210. doi: 10.3389/fmicb.2013.00210
- Zablotskii, V., Lunov, O., Kubinova, S., Polyakova, T., Sykova, E., and Dejneka, A. (2016a). Effects of high-gradient magnetic fields on living cell machinery. *J. Phys. D Appl. Phys.* 49:493003. doi: 10.1088/0022-3727/49/49/493003
- Zablotskii, V., Polyakova, T., Lunov, O., and Dejneka, A. (2016b). How a high-gradient magnetic field could affect cell life. *Sci. Rep.* 6:37407. doi: 10.1038/srep37407
- Zahn, C., Keller, S., Toro-Nahuelpan, M., Dorscht, P., Gross, W., Laumann, M., et al. (2017). Measurement of the magnetic moment of single *Magnetospirillum gryphiswaldense* cells by magnetic tweezers. *Sci. Rep.* 7:3558. doi: 10.1038/s41598-017-03756-z
- Zborowski, M., and Chalmers, J. J. (2011). Rare cell separation and analysis by magnetic sorting. *Anal. Chem.* 83, 8050–8056. doi: 10.1021/ac200550d
- Zeytuni, N., Ozyamak, E., Ben-Harush, K., Davidov, G., Levin, M., Gat, Y., et al. (2011). Self-recognition mechanism of MamA, a magnetosome-associated TPR-containing protein, promotes complex assembly. *Proc. Natl. Acad. Sci. U.S.A.* 108, E480–E487. doi: 10.1073/pnas.1103367108
- Zhang, H., Liu, X., Feng, S., Wang, W., Schmidt-Rohr, K., Akinc, M., et al. (2015). Morphological transformations in the magnetite biomineralizing protein Mms6 in iron solutions: a small-angle X-ray scattering study. *Langmuir* 31, 2818–2825. doi: 10.1021/la5044377
- Zhang, X. Y., Robledo, B. N., Harris, S. S., and Hu, X. P. (2014). A bacterial gene, mms6, as a new reporter gene for magnetic resonance imaging of mammalian cells. *Mol. Imaging* 13, 1–12. doi: 10.2310/7290.2014.00046
- Zhang, Y., Zhang, X., Jiang, W., Li, Y., and Li, J. (2011). Semicontinuous culture of *Magnetospirillum gryphiswaldense* MSR-1 cells in an autofermentor by nutrient-balanced and isosmotic feeding strategies. *Appl. Environ. Microbiol.* 77, 5851–5856. doi: 10.1128/aem.05962-11
- Zhou, C. Z., Confalonieri, F., Jacquet, M., Perasso, R., Li, Z. G., and Janin, J. (2001). Silk fibroin: structural implications of a remarkable amino acid sequence. *Proteins* 44, 119–122. doi: 10.1002/prot.1078
- Zhu, K., Pan, H., Li, J., Yu-Zhang, K., Zhang, S.-D., Zhang, W.-Y., et al. (2010). Isolation and characterization of a marine magnetotactic spirillum axenic culture QH-2 from an intertidal zone of the China Sea. *Res. Microbiol.* 161, 276–283. doi: 10.1016/j.resmic.2010.02.003
- Zimmerman, P. A., Thomson, J. M., Fujioka, H., Collins, W. E., and Zborowski, M. (2006). Diagnosis of malaria by magnetic deposition microscopy. *Am. J. Trop. Med. Hyg.* 74, 568–572. doi: 10.4269/ajtmh.2006.74.568
- Zurkiya, O., Chan, A. W. S., and Hu, X. (2008). MagA is sufficient for producing magnetic nanoparticles in mammalian cells, making it an MRI reporter. *Magn. Reson. Med.* 59, 1225–1231. doi: 10.1002/mrm.21606

Conflict of Interest: The authors declare that the research was conducted in the absence of any commercial or financial relationships that could be construed as a potential conflict of interest.

Copyright © 2020 Pekarsky and Spadiut. This is an open-access article distributed under the terms of the Creative Commons Attribution License (CC BY). The use, distribution or reproduction in other forums is permitted, provided the original author(s) and the copyright owner(s) are credited and that the original publication in this journal is cited, in accordance with accepted academic practice. No use, distribution or reproduction is permitted which does not comply with these terms.



Repetitive Fed-Batch: A Promising Process Mode for Biomanufacturing With *E. coli*

Julian Kopp[†], Stefan Kittler[†], Christoph Slouka, Christoph Herwig, Oliver Spadiut and David J. Wurm*

Research Area Biochemical Engineering, Institute of Chemical Engineering, TU Wien, Vienna, Austria

OPEN ACCESS

Edited by:

Pau Ferrer,
Autonomous University of Barcelona,
Spain

Reviewed by:

Dongming Xie,
University of Massachusetts Lowell,
United States
Stefan Junne,
Technical University of Berlin,
Germany

*Correspondence:

David J. Wurm
david.wurm@tuwien.ac.at

[†] These authors have contributed
equally to this work

Specialty section:

This article was submitted to
Bioprocess Engineering,
a section of the journal
Frontiers in Bioengineering and
Biotechnology

Received: 17 June 2020

Accepted: 21 October 2020

Published: 10 November 2020

Citation:

Kopp J, Kittler S, Slouka C,
Herwig C, Spadiut O and Wurm DJ
(2020) Repetitive Fed-Batch:
A Promising Process Mode
for Biomanufacturing With *E. coli*.
Front. Bioeng. Biotechnol. 8:573607.
doi: 10.3389/fbioe.2020.573607

Recombinant protein production with *Escherichia coli* is usually carried out in fed-batch mode in industry. As set-up and cleaning of equipment are time- and cost-intensive, it would be economically and environmentally favorable to reduce the number of these procedures. Switching from fed-batch to continuous biomanufacturing with microbials is not yet applied as these cultivations still suffer from time-dependent variations in productivity. Repetitive fed-batch process technology facilitates critical equipment usage, reduces the environmental fingerprint and potentially increases the overall space-time yield. Surprisingly, studies on repetitive fed-batch processes for recombinant protein production can be found for yeasts only. Knowledge on repetitive fed-batch cultivation technology for recombinant protein production in *E. coli* is not available until now. In this study, a mixed feed approach, enabling repetitive fed-batch technology for recombinant protein production in *E. coli*, was developed. Effects of the cultivation mode on the space-time yield for a single-cycle fed-batch, a two-cycle repetitive fed-batch, a three-cycle repetitive fed batch and a chemostat cultivation were investigated. For that purpose, we used two different *E. coli* strains, expressing a model protein in the cytoplasm or in the periplasm, respectively. Our results demonstrate that a repetitive fed-batch for *E. coli* leads to a higher space-time yield compared to a single-cycle fed-batch and can potentially outperform continuous biomanufacturing. For the first time, we were able to show that repetitive fed-batch technology is highly suitable for recombinant protein production in *E. coli* using our mixed feeding approach, as it potentially (i) improves product throughput by using critical equipment to its full capacity and (ii) allows implementation of a more economic process by reducing cleaning and set-up times.

Keywords: *E. coli*, repetitive fed-batch, process understanding, process intensification, recombinant protein production, continuous biomanufacturing

INTRODUCTION

Escherichia coli serves as a beloved workhorse for the production of many recombinant proteins. Fast doubling times, little risk of contamination, cheap media and easy upscale are the most prominent benefits (Casali, 2003; Baeshen et al., 2015; Gupta and Shukla, 2017). The *E. coli* strain BL21(DE3) is the most commonly applied strain in industry with outstanding low acetate secretion and high product concentrations (Rosano and Ceccarelli, 2014; Wurm et al., 2017a; Rosano et al., 2019). The strain is regularly used for recombinant protein production with pET-plasmids, making use of the

integrated T7-promotor system (Wurm et al., 2016; Kopp et al., 2017; Rosano et al., 2019). For many applications IPTG (Isopropyl- β -D-thiogalactopyranosid) is the inducer of choice, which leads to high levels of recombinant protein. Even though IPTG induction is described as tunable, toxic effects can be observed (Wurm et al., 2016; Hausjell et al., 2018). Several studies showed that the use of IPTG throughout long induction times leads to increased stress levels and thus to low viability (Dvorak et al., 2015; Slouka et al., 2018). Promotor systems, like araBAD and rhamBAD are not described to show any toxic effects (Marschall et al., 2016). The utilization of arabinose or rhamnose might enable long-term cultivation with *E. coli* (Marschall et al., 2016), however they are rarely used in industry due to the high price of these inducers (Kopp et al., 2019b). Thus, it is of great importance to find a suitable inducer that is affordable in large scale and shows no signs of toxicity onto host cells (Malakar and Venkatesh, 2012; Mühlmann et al., 2018). The disaccharide lactose is taken up via lactose permease. Upon uptake, lactose is either cleaved to glucose and galactose or converted to allolactose via β -galactosidase (Deutscher et al., 2006). Allolactose can then bind to the lac repressor and enable induction as described in various previous publications (Wurm et al., 2016; Kopp et al., 2017). Due to the non-toxicity and low cost of lactose compared to other inducers, this induction mechanism is tuneable and also economically feasible (9.39 €/g IPTG vs. 0.02 €/g lactose) (Yan et al., 2004; Briand et al., 2016). For mixed feed systems using lactose, an established mechanistic knowledge platform, which explains the correlation between sugar and inducer uptake by physiological parameters can be used (Wurm et al., 2017a). Furthermore, lactose has shown to boost productivity in soluble recombinant protein production when compared to IPTG (Wurm et al., 2016, 2017a). For periplasmic recombinant protein production soft induction by lactose is especially important as translocation to the periplasm is the rate limiting step (Gupta and Shukla, 2017; Karyolaimos et al., 2019; Hausjell et al., 2020).

Independent of product location, recombinant protein production in *E. coli* is commonly carried out in fed-batch cultivation mode (Slouka et al., 2018; Kopp et al., 2019b). However, in fed-batch cultivation sterilization, cleaning and biomass formation take up the majority of process time (Slouka et al., 2018). As industry is always aiming to increase the space-time yield, a continuous production system would be desirable to reduce down-times (Rathore, 2015; Tan et al., 2019; Zobel-Roos et al., 2019). Regulations of continuously produced products used to be an issue, however regulatory authorities have defined to separate production into diverse lot numbers according to ICH Q7: "The batch size can be defined either by a fixed quantity or by the amount produced in a fixed time interval" (EU GMP Guide, Part II). Compared to a batch system, continuous systems enable maximum utilization of equipment. By reducing down-times, production scale can be decreased or amounts of product can be gained within less time, or a combination of both factors (Glaser, 2015; Herwig et al., 2015; Rathore, 2015). Continuous production processes would allow increased product yields in smaller production facilities while obtaining the same amounts of

product (Allison et al., 2015; Konstantinov and Cooney, 2015; Nasr et al., 2017).

Aiming to establish time-independent microbial cultivation systems, evolutionary mechanisms, such as mutations (Rugbjerg and Sommer, 2019) and shifts in transcriptome and proteome (Peebo et al., 2015; Peebo and Neubauer, 2018) spoiled expectations of industry.

Repetitive fed-batch cultivation mode offers the chance of an immense down-time reduction, with multiple production cycles performed within one cultivation run (Bergmann and Trösch, 2016; Kuo et al., 2017; Zagrodnik and Łaniecki, 2017). While in fed-batch processes a complete harvest of the fermenter is performed at the end of cultivation, repetitive fed batch processing differs by performing only a partial harvest (Martens et al., 2011). Afterwards, the spared fermentation broth is diluted with fresh media and a new induction cycle can be started right away (Fricke et al., 2013). Repetitive fed-batch has proven to be a suitable cultivation mode to improve many processes in biotechnology and conducted studies and literature concerning repetitive fed-batch cultivations up to date are given in **Table 1**. However, studies on repetitive fed-batch using *E. coli* are scarce.

Repetitive fed-batch technology has shown promising effects in recombinant protein production mainly using *Pichia pastoris* (Ohya et al., 2005; Martens et al., 2011; Fricke et al., 2013). To our knowledge, a repetitive fed-batch cultivation mode using *E. coli* has only been implemented for pyruvate production (Zelić et al., 2004). However, the potential of using *E. coli* in repetitive fed-batch mode for recombinant protein production has not been investigated yet.

In this study we performed repetitive fed-batch cultivations for recombinant protein production using the production host *E. coli* in combination with lactose induction. In previous studies, the negative side effects of IPTG induction onto recombinant protein production in long-term fermentations were shown, whereas lactose was found to have a beneficial effect on productivity (Malakar and Venkatesh, 2012; Dvorak et al., 2015; Kopp et al., 2019a). We believe that no studies on repetitive fed-batch cultivation with *E. coli* for recombinant protein production have been published yet, either due to toxic effects of IPTG and the consequent decreasing productivity over time (Dvorak et al., 2015; Kopp et al., 2019b) or due to the absence of an induction strategy comparable to the established yeast system (Fricke et al., 2013). The goal of this study was to compare productivities and space-time yields of different production modes for *E. coli*. The assessment of changes in product quality and purity was not in the scope of this study. For the first time, we were able to show that a repetitive fed-batch cultivation mode using our developed lactose induction strategy is able to outperform conventional fed-batches and chemostat cultivations regarding the overall space-time yield.

MATERIALS AND METHODS

Strains

All cultivations were carried out with the strain *E. coli* BL21(DE3), transformed with a pET30a⁺ plasmid carrying the gene for the cytoplasmic protein (CP) and periplasmic

TABLE 1 | Summary of studies about repetitive fed-batch cultivations.

Microorganism	Product	Process description	Ref.
<i>Cryptocodinium cohnii</i>	docosahexaenoic acid	4 cycles, 80% medium replacement	Liu et al., 2020
<i>Aspergillus terreus</i>	Lovastatin	3 cycles, 37% yield in crease	Novak et al., 1997; Kumar et al., 2000
<i>Gluconobacter oxydans</i>	Dihydroxyacetone	4 cycles, repeated fed-batch process using two spatially separated vessels	Bauer et al., 2005
<i>Kluyveromyces marxianus</i>	Ethanol	5 cycles, product yield constant	Ozmihci and Kargi, 2007
<i>Kitasatospora</i>	ε-Poly-L-lysine	5 cycles	Zhang et al., 2010
<i>Yarrowia lipolytica</i>	Citric acid	10 cycles, productivity decrease over cultivation time	Moeller et al., 2011
<i>Pichia pastoris</i>	human serum albumin (rHSA)	4 cycles, 47% yield increase	Ohya et al., 2005
<i>Pichia pastoris</i>	Malaria vaccine candidates	stable productivity for 2-8 cycles, methanol induction	Martens et al., 2011; Fricke et al., 2013
<i>Escherichia coli</i>	Pyruvate	5 cycles, q_p increased fivefold	Zelić et al., 2004

protein (PP), respectively. The cytoplasmic protein contained no disulfide bonds, had a isoelectric point (PI) of 5.62 and a protein size of 26.9 kDa. PI and protein size of the periplasmic protein were 5.42 and 32 kDa, respectively and it contained a single disulfide bond.

Media

All cultivations were conducted using a defined minimal medium by DeLisa et al. (1999), supplemented with different amounts of glucose and lactose. 0.02 g/L kanamycin was added to prevent plasmid loss.

Bioreactor Setup

All cultivations were performed in a Minifors 2 bioreactor system (max. working volume: 1 L; Infors HT, Bottmingen, Switzerland). The cultivation offgas was analyzed in online mode using gas sensors – IR for CO₂ and ZrO₂ based for Oxygen (Blue Sens Gas analytics, Herten, Germany).

Process control and exponential feeding was established using the process control system PIMS Lucullus (Securecell, Urdorf Switzerland). pH was monitored using an EasyFerm Plus pH-sensor (Hamilton, Reno, NV, United States) and was kept constant at 6.7 throughout all cultivations and controlled using a base only control (12.5% NH₄OH), while acid (5% H₃PO₄) was added manually, if necessary. Stirrer speed was set to 1400 rpm. Dissolved oxygen (dO₂) was kept above 30% oxygen saturation by supplying 2 vvm of a mixture of pressurized air and pure oxygen. The dO₂ was monitored using a Visiferm fluorescence dissolved oxygen electrode (Hamilton, Reno, NV, United States). Feed medium was added by using a PRECIFLOW pump (Lambda, Laboratory Instruments, Baar, Switzerland). Reactor weight and the depleted feed weight were monitored to determine exact feeding rates using a feed forward control as described here (Slouka et al., 2018). Harvest and fill-up step were conducted using a peristaltic pump (Watson-Marlow, Guntramsdorf, Austria).

Cultivation Procedure

The pre-culture and batch phase was equivalent for all performed cultivations, followed by a single-cycle fed-batch, a two-cycle

fed-batch, a three-cycle fed-batch or a chemostat cultivation (**Supplementary Figure 1**).

Pre-culture

Pre-culture was prepared using 2500 mL high yield flasks. 500 milliliter of DeLisa medium (DeLisa et al., 1999) supplemented with 8.8 g/L glucose were inoculated with 1.5 mL of bacteria solution stored in cryos at –80°C and subsequently cultivated for 16 h at 230 rpm in an Infors HR Multitron shaker (Infors, Bottmingen Switzerland) at 37°C.

Batch Cultivation

Batch medium [DeLisa medium supplement with 20 g/L glucose (DeLisa et al., 1999)] was inoculated with 1/10th of the reactor volume using the previously described pre-culture. Batch process was carried out at 37°C and took approximately 6–7 h until sugar was depleted, monitored via a drop in the CO₂ signal or a pO₂ peak, respectively.

Fed-Batch for Biomass Generation

After the batch phase, a non-induced fed-batch was carried out at 35°C over-night using carbon-limited feeding approaches. Non-induced fed-batch was carried out at a constant specific feeding rate ($=q_s$) of 0.25 g/g/h to achieve a biomass concentration of approximately 35 g/L prior to induction (**Supplementary Figures 3a,b**). For exponential feeding, DeLisa medium (DeLisa et al., 1999) supplemented with 300 g/L glucose was used as feed medium. Equation 1 was used for the feed controller to calculate the feed-rate for maintaining a constant q_s in feed forward mode (Kopp et al., 2017; Wurm et al., 2017a). Dry cell weight of biomass and feeding rates were determined as described here (Hausjell et al., 2018; Slouka et al., 2018). In short, triplicate at-line optical density (OD) measurements and a previously established OD to biomass correlation were used for calculation of the exponential feeding profile.

$$F(t) = \frac{q_s \times X(t) \times \rho_f}{c_f} \quad (1)$$

F, feed-rate (g/h); q_s , specific glucose uptake rate (g/g/h); X(t), biomass (g); ρ_f , feed density (g/L); c_f , feed concentration (g/L).

Single-Cycle Fed-Batch

Prior to induction, temperature was decreased to 30°C, to reduce stress onto host cells and enhance soluble protein formation (Wurm et al., 2016). The induction phase was conducted for 12 h using a glucose–lactose mixed feed system according to a previous study (Slouka et al., 2018). For induction, DeLisa medium (DeLisa et al., 1999) supplemented with 250 g/L glucose and 141.2 g/L lactose, was fed at a constant specific feeding rate of 0.25 g/g/h, as these mixing ratios were found to show better results in previous cultivations (Wurm et al., 2017a). For single-cycle fed-batch cultivations, the cultivation was terminated after 12 h of induction and a full reactor harvest was conducted (Figure 1 and Supplementary Figure 1a), whereas for two-cycle and three-cycle fed-batches only a partial harvest was performed.

Two-Cycle Repetitive Fed-Batch

Prior to the repetitive fed-batch the process cycles preculture, batch cultivation, fed-batch for biomass generation and the single-cycle fed-batch were performed. However, after the induction phase feeding was stopped and only a partial harvest was conducted leaving half of the initial volume for the ongoing process steps. In order to achieve the same biomass concentration as before induction, biomass was determined at-line and diluted to approximately 35 g/L using sterile DeLisa medium (DeLisa et al., 1999). Dilution media contained no carbon source but was double concentrated in salt and trace element concentration to avoid nutrient limitation throughout the following repeated cycles. Antibiotic was also added to the sterile medium to achieve the initial start concentration. After the refilling the feeding was started analogous to the single-cycle fed-batch for another 12 h. Complete harvest was conducted after the second cycle.

Three-Cycle Repetitive Fed-Batch

Cultivation was carried out analog to the description in section “Two-Cycle Repetitive Fed-Batch.” However, after the second cycle was finished, again only a partial harvest was conducted. The refilling step was conducted analog to the procedure for the two-cycle repetitive fed-batch and the total fermentation broth was harvested after cycle 3 was finished.

Chemostat Cultivation

After batch cultivation the continuous process mode was started. Dilution rate was set to $D = 0.1 \text{ h}^{-1}$ and the volume in the reactor was kept constant at 750 mL using an immersion tube adjusted to the right height of the stirred liquid surface in the reactor which was connected to a bleed pump (Watson-Marlow, Guntramsdorf, Austria). Medium for chemostat cultivation was prepared as described by DeLisa (DeLisa et al., 1999) supplemented with 50 g/L glucose and 25 g/L lactose. To keep the growth rates of the performed repetitive fed-batch processes comparable to the performed chemostat processes, only dilution rates of 0.1 h^{-1} were investigated within this study. The overall induction time of the chemostat process was 90 h.

Ideal Chemostat

In order to test advantages of a continuous cultivation system, an ideal chemostat was simulated. We calculated the ideal chemostat

with stable product formation at maximum specific productivity as shown in Figures 2B,3B.

Sampling

Samples were taken at the end of the batch phase, after the fed-batch phase and regularly during the induced cycles of all cultivation modes. Biomass, optical density, viability and metabolite accumulation were determined for every sample taken. All samples taken during induction phase were additionally analyzed for product formation.

Samples during repetitive fed-batch cultivations were taken every three hours during the first and the third cycle, while the second cycle was conducted over night and therefore only the harvest sample was taken.

For the chemostat cultivation, samples were taken 3 h after start of the induced chemostat and from then on twice a day.

Biomass, Viability, Substrate and Metabolite Analysis

Biomass was measured by optical density (OD_{600}) and gravimetrically by dry cell weight (DCW), while flow cytometry analysis (FCM) was used for the determination of viability.

OD_{600} was measured in triplicates using a Genesys 20 photometer (Thermo Scientific, Waltham, MA, United States). Since the linear range of the used photometer was between 0.2 and 0.8 (AU), samples were diluted with dH_2O to stay within the given range.

The DCW was determined by centrifugation (10,000 rpm for 10 min at 4°C) of 1 mL of homogenous sample solution in a pre-tared 2 mL Eppendorf-Safe-Lock Tube (Eppendorf, Hamburg, Germany). After centrifugation, the supernatant was withdrawn, frozen at -20°C and used to determine sugar concentrations by HPLC measurements. The pellet was re-suspended with 1 mL of 0.9% NaCl solution and centrifuged again (10,000 rpm for 10 min at 4°C). Afterward, the pellet was dried for at least 48 h at 105°C and DCW was evaluated gravimetrically in triplicates.

For FCM, cultivation broth was diluted 1:100 with 0.9% NaCl solution, stored at 4°C and measured every day. The measurement was performed using a Cyflow® Cube 8 flow cytometer (Sysmex, Görlitz, Germany) according to Langemann et al. (2016) using DiBAC4(3) (bis-(1,3-dibutylbarbituric acid-trimethineoxonol) and Rh414 dye. Both dyes were purchased from AnaSpec (Fremont, CA, United States).

Sugar concentrations of feed and clarified fermentation broth were measured via anion exchange HPLC (Thermo Scientific, Waltham, MA, United States) using a Supelcogel-column (Sigma-Aldrich, St. Louis, MO, United States) and a refractive index detector (Agilent Technologies, Santa Clara, CA, United States). The mobile phase was 0.1% H_3PO_4 with a constant flow rate of 0.5 mL/min, and the system was run isocratically at 30°C. Glucose, lactose, galactose, and acetate accumulation was monitored using calibration standards with a concentration of 1, 5, 10, 25, and 50 g/L of each analyte. Chromatograms were analyzed using Chromeleon Software (Thermo Scientific, Waltham, MA, United States).

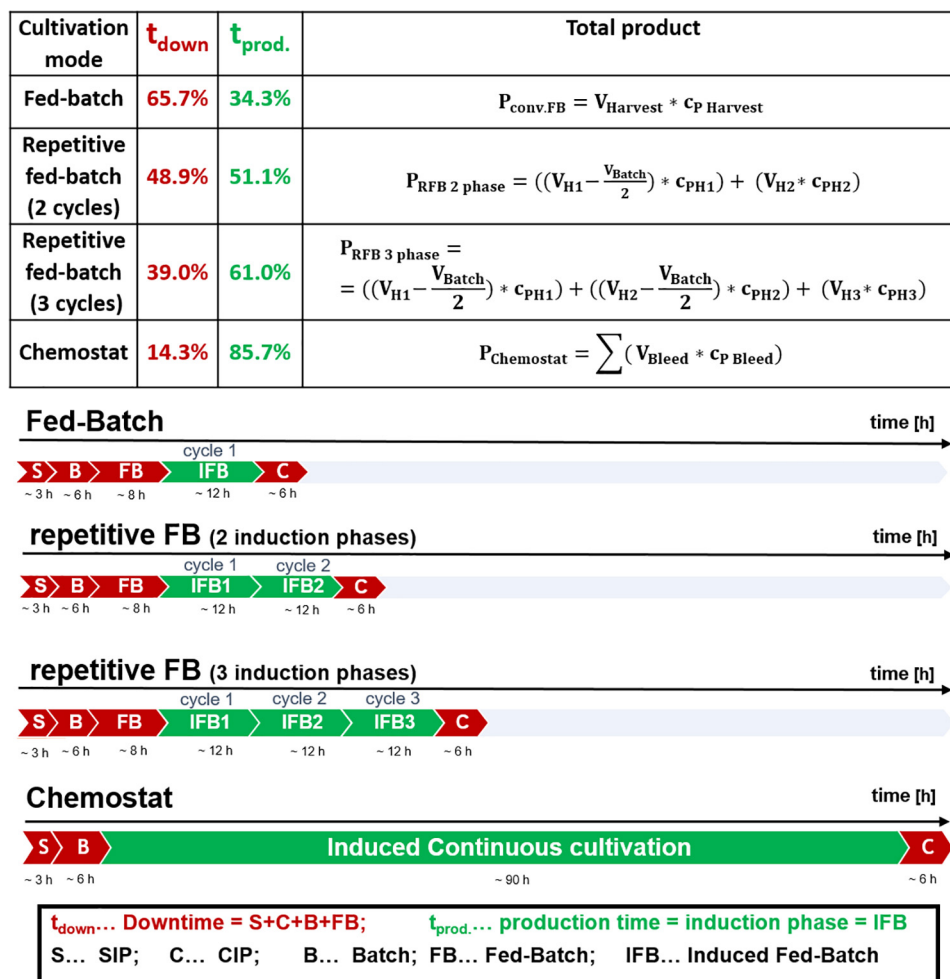


FIGURE 1 | Comparison of cultivation durations of a fed-batch, a repetitive fed-batch consisting of two cycles, a repetitive fed-batch consisting of three cycles and a chemostat process; effective production time vs. downtime for a 10 m³ fermenter scale is given for each process in percent relative to total process time; steam in place (SIP), cleaning in place (CIP).

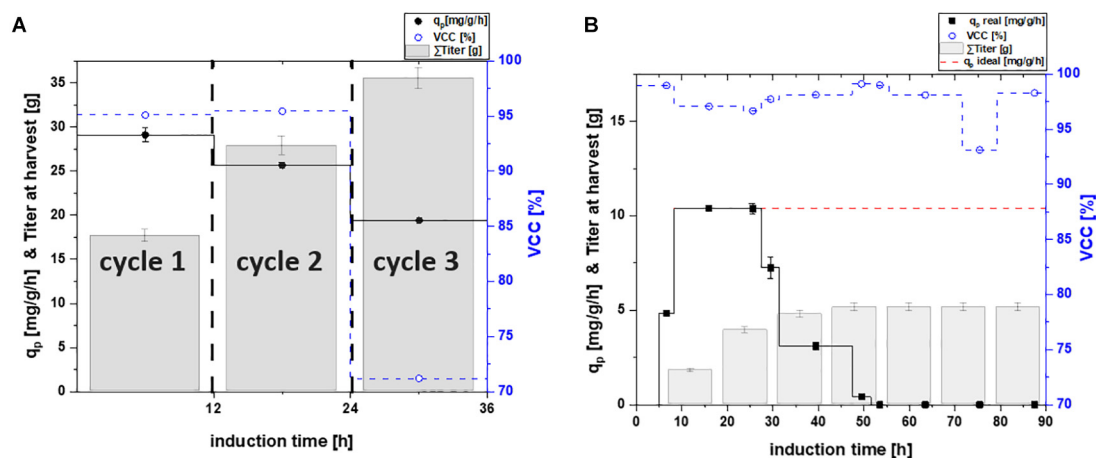


FIGURE 2 | Specific productivity q_p (mg/g/h), viable cell concentration (=VCC) [%] and the harvested product titer for **(A)** a repetitive fed-batch cultivation and **(B)** a chemostat process; a theoretical ideal chemostat was simulated at $q_{p,\text{max.}}$; VCC was evaluated by flow cytometry analysis with an average standard deviation of 2%.

Product Quantification

Product samples were taken after the start of the induction phase. Five milliliter of cultivation broth were pipetted in a 50 mL falcon tube and centrifuged for 10 min at 5000 rpm at 4°C. The supernatant was discarded and the pellet was frozen at −20°C. Afterward, the samples were disrupted by homogenization as follows: The pellets were re-suspended in a buffer (0.1 M TRIS, 10 mM EDTA, pH 7.4) according to their dry cell weight to reach a biomass of 10 g/L prior to homogenization. After suspending the cells with a disperser (T10 basic ULTRA-TURRAX®, Staufen, Germany) they were treated with an EmusiflexC3 Homogenizer (Avestin, Ottawa, ON, United States) at 1400 bar for 4 passages, ensuring complete cell disruption. After homogenization the broth was centrifuged (14,000 rpm, 10 min, 4°C) and the supernatant was used immediately for HPLC quantification.

For soluble titer measurements of the cytoplasmic target protein, the supernatant derived after centrifugation of homogenized broth was filtered and then quantified via UHPLC (Thermo Scientific, Waltham, MA, USA). For quantification of cytoplasmic soluble protein, a size exclusion (=SEC) chromatography principle was applied, using a X-bridge column (Waters, Milford, DE, United States). The mobile phase was composed of 250 mM KCl and 50 mM of each KH₂PO₄ and K₂HPO₄ dissolved in Ultrapure water as describe elsewhere (Goyon et al., 2018). A constant flow rate of 0.5 mL/min was applied with an isocratic elution at 25°C for 18 min. BSA standards (50, 140, 225, 320, 500, 1000, and 2000 mg/mL; Sigma Aldrich, St. Louis, MO, United States) were used for quantification.

For soluble titer measurements of the periplasmic protein, clarified cultivation broth was analyzed by a BioResolve RP mAb Polyphenyl column (Waters, Milford, DE, United States), using a reversed-phase HPLC method published elsewhere (Kopp et al., 2020). Product was quantified with a UV detector (Thermo Fisher, Waltham, MA, United States) at 214 nm, using BSA as standard reference.

Specific productivity was calculated as a rate between two sampling points using Eq. 2:

$$q_p = \frac{\frac{c_i + c_{i-1}}{2}}{\frac{x_i + x_{i-1}}{2}} \times \frac{1}{t_i - t_{i-1}}. \quad (2)$$

q_p specific productivity (mg/g/h); c_i , product concentration of sample at timepoint i (mg/L); X_i , biomass concentration of sample at timepoint i (g/L); t_i , cultivation time at timepoint of sample i (h).

The experimentally evaluated q_p values were used for the calculation of the real chemostat. For the simulated ideal chemostat, stable product formation at maximum specific productivity was assumed, once the maximum productivity was reached, as shown in **Figures 2B,3B**.

Reproducibility

To test the reproducibility of the equipment described in section “Bioreactor Setup,” triplicates of a fed-batch cultivation were assessed by the same operator for one target protein. Found errors were not higher than ±0.35 g/L for titer determination

[resulting in a maximum relative standard deviation (RSD) below 10%]. Specific feeding rates were found to be within a deviation of ± 0.03 g/g/h (max. RSD below 11%). Dry cell weights deviations between replicates were below 3.8 g/L (below a max. RSD of 9%). Set specific feeding rates require at-line OD₆₀₀ determination to estimate the biomass, before the exponential feeding ramp is calculated. Variances (i.e., due to dilution) in OD₆₀₀-signals thus may cause differences in the resulting biomass and titer, as previously shown (Slouka et al., 2018).

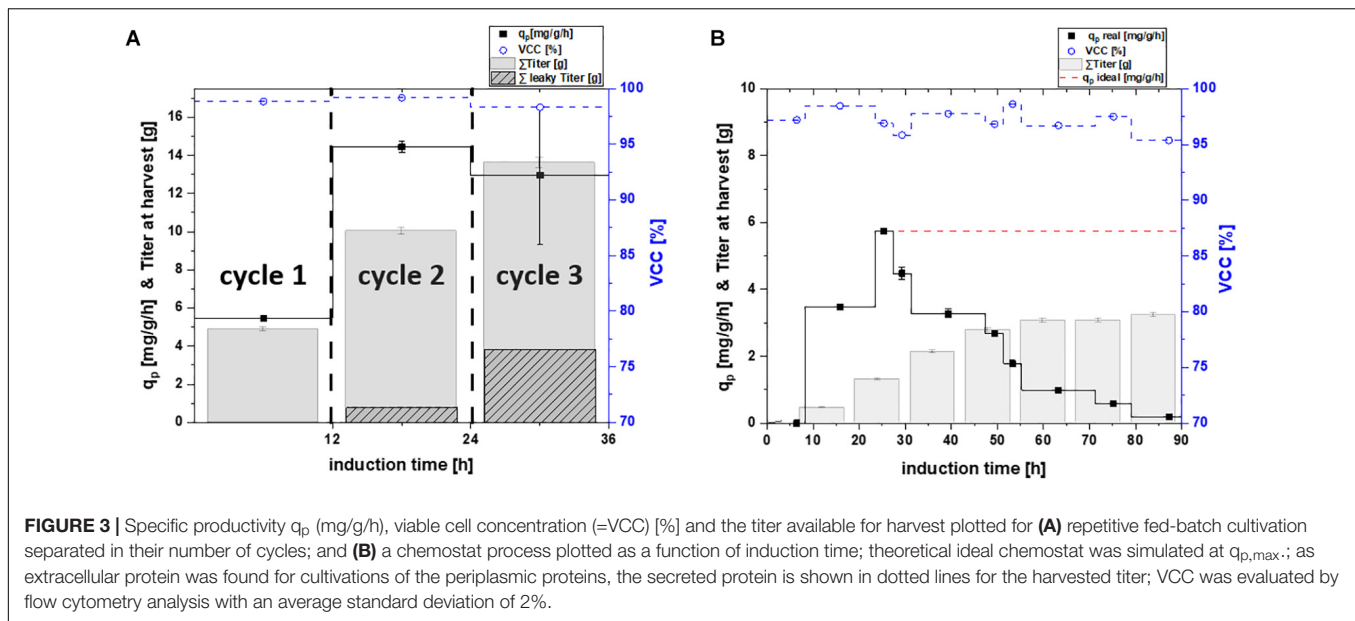
RESULTS AND DISCUSSION

Experimental Design

The potential of achieving high recombinant protein titers in repetitive fed-batch cultivation mode was shown by Luttmann et al. for *P. pastoris* as production host (Martens et al., 2011). However, repetitive fed-batch technology for recombinant protein production using *E. coli* has not been investigated yet. As methanol was continuously fed throughout the repetitive fed-batch studies with *P. pastoris* (Martens et al., 2011; Fricke et al., 2013), we established a similar feeding strategy for the inducer lactose and *E. coli*. Hence a feed-forward feeding strategy according to Eq. 1 was applied throughout all cycles. Furthermore, we tested whether a single-cycle fed batch, a two-cycle repetitive fed-batch, a three-cycle repetitive fed-batch or a chemostat is the cultivation mode of choice regarding overall space-time yield. We tested the cultivation modes for two different recombinant products: one produced in the cytoplasm and one secreted to the periplasm. Establishing such a process is of high interest for industry, to reduce downtime. For the calculations within this study the duration of the cycles and downtimes of the cultivation were chosen as regularly applied in industry (Slouka et al., 2018). Downtime, production time as well as calculation of total product titer are depicted in **Figure 1**.

The fermenter scale for the calculations was assumed with 10 m³, which is a common scale for *E. coli* in industry. Thus, time for steam in place (SIP) and cleaning in place (CIP) takes 3 and 6 h, respectively (communication with industrial partner). Batch phase on glucose was 6 h (Slouka et al., 2018). Non-induced fed-batch time was 8 h, to achieve a biomass of 35–40 g/L before induction using a growth rate of $\mu = 0.1 \text{ h}^{-1}$ (equivalent to a q_s of 0.25 g/g/h using a biomass/substrate yield of 0.4 g/g for calculation, Kopp et al., 2017). Previous results indicate, that a q_s of 0.25 g/g/h, a cultivation temperature of 30°C and an induction time of 10–12 h is beneficial for the production of many recombinant proteins and was thus chosen for this study (Wurm et al., 2016; Wurm et al., 2017b; Slouka et al., 2018; Schein, 2019). As fed-batch cultivations were conducted at $q_s = 0.25 \text{ g/g/h}$ (equivalent to $\mu = 0.1 \text{ h}^{-1}$), dilution rates in chemostat cultivation were investigated for the same $\mu = D = 0.1 \text{ h}^{-1}$.

The final product titer for the different cultivations modes was calculated according to **Figure 1**. Space-time yield was calculated according to Equation 3 to allow comparison of the different



diversification (Kittler et al., 2020). Hence we believe effects causing the decrease in productivity derive from subpopulation diversification. Shifts in the transcriptome in combination with point mutations (Rugbjerg and Sommer, 2019), are known to cause the formation of non-producing subpopulations (Basan, 2018). Recent publications (Schreiber et al., 2016; Binder et al., 2017) showed that carbon limited feeding increases probability of phenotypic subpopulation diversification. These effects are described to increase with generation time (Rugbjerg et al., 2018). As cells in chemostat processes are cultivated for longer time-spans than fed-batch and repeated fed-batch processes, long-term cultures face a higher chance of being affected (Buerger et al., 2019). We believe that a fitter subpopulation, having altered levels of transcription, is avoiding the burden of production. As recombinant protein expression is referred to cause decreasing biomass yields, a non-productive subpopulation, showing no decrease in biomass yield thus could overgrow the initial population. Hence we believe that the productive subpopulation is washed-out over the time-course of the induction phase and a non-productive subpopulation takes over, explaining the decline in productivity (Peebo and Neubauer, 2018; Kopp et al., 2019b).

In order to test the applicability of continuous cultivations for industry, a theoretical “ideal” chemostat with constant productivity at maximum specific productivity was simulated. However, the maximum specific productivity during the chemostat cultivation is significantly lower compared to the repetitive fed-batch cultivation (2.9 times lower compared to productivity of cycle two, **Figures 2A,B**). Furthermore, higher biomass concentrations and thus higher volumetric titers can be achieved in fed-batch and repetitive fed-batch mode. As biomass yield is decreasing upon production of recombinant proteins, this can potentially lead to washout (Lis et al., 2019). Hence, trying to achieve “fed-batch like” biomass concentrations in chemostat cultivation is highly difficult. Our results are in favor of fed-batch and repetitive fed-batch cultivation for the cytoplasmic target

protein and will be compared in section “Targeting Maximum Space-Time Yield: The Cultivation Mode to Choose” regarding their space-time yield.

Cultivation Strategies and Their Results for Periplasmic Protein Formation

In order to test and verify the effects monitored for the cytoplasmic protein, we investigated the same cultivation techniques for periplasmic protein production (**Figure 3** and **Table 3**).

The measured cell specific productivity in the single-cycle fed-batch was $q_p = 5.47$ mg/g/h, which was significantly lower compared to the cytoplasmic product. Production of the periplasmic protein started only 6 h post induction and low uptake rates of the inducer lactose potentially explain the low specific productivity during the single-cycle fed-batch. As production of periplasmic products depends on several factors (i.e., translocation to the periplasm), generally lower specific productivity can be expected, compared to protein expression in the cytoplasm (Kleiner-Grote et al., 2018; Karyolaimos et al., 2019). No decrease in viability could be observed throughout cycle one, as for the cytoplasmic product.

Cell specific productivity in the two-cycle repeated fed-batch cultivation was much higher compared to the first cycle ($q_p = 14.44$ mg/g/h). Even though viability did not decrease in cycle two, leaky product (7.7% of total product) could be detected in the supernatant. This behavior has been observed for periplasmic proteins in literature before (Chen et al., 2014; Hausjell et al., 2020).

For repeated fed-batch technology carried out for three cycles, a minor decrease in productivity was found compared to cycle two, resulting in a q_p of 12.96 mg/g/h. The uptake rate of the inducer lactose increased during cycle two and three (**Supplementary Figure 4b**). Thus, we hypothesize that longer

TABLE 3 | Comparing specific productivity and the product titer at harvest for the production of a periplasmic protein; each cycle is investigated separately for fed-batch and repeated fed-batch cultivation; values for chemostat and theoretical “ideal” chemostat cultivations are given every 12 h (i.e., one cycle); calculation for q_p represents instantaneous values whereas titers are calculated as accumulated values.

Induction time (h)	12		24		36		48		60		72		84	
periplasmic protein	q _p (mg/g/h)	Titer (g/L)	q _p (mg/g/h)	Titer (g/L)	q _p (mg/g/h)	Titer (g/L)	q _p (mg/g/h)	Titer (g/L)	q _p (mg/g/h)	Titer (g/L)	q _p (mg/g/h)	Titer (g/L)	q _p (mg/g/h)	Titer (g/L)
Fed-batch (1 cycle)	5.47 ± 0.06	4.87 ± 0.09												
Repeated fed-batch (2 cycles)			14.44 ± 0.30	10.03 ± 0.19										
Repeated fed-batch (3 cycles)					12.96 ± 3.65	13.61 ± 0.26								
Chemostat cultivation	1.98 ± 0.03	0.45 ± 0.01	5.26 ± 0.08	1.30 ± 0.02	3.76 ± 0.06	2.12 ± 0.04	2.32 ± 0.04	2.78 ± 0.05	1.31 ± 0.02	3.06 ± 0.06	0.69 ± 0.01	3.07 ± 0.06	0.34 ± 0.01	3.22 ± 0.06
Theoretical "ideal" chemostat	1.98 ± 0.03	0.45 ± 0.01	5.26 ± 0.08	1.30 ± 0.02	5.75 ± 0.04	3.16 ± 0.05	5.75 ± 0.04	5.02 ± 0.07	5.75 ± 0.04	6.88 ± 0.10	5.75 ± 0.04	8.74 ± 0.12	5.75 ± 0.04	10.6 ± 0.14

timespans of full lactose induction were the reason for the increase in specific productivity compared to cycle one. No cell death was monitored throughout cycle three, however higher amounts of leakiness were found (28.1% of total product). No fourth cycle was conducted, in order to make repetitive fed-batch cultivations for both target proteins comparable in their number of cycles. Moreover, levels of leakiness increased over the timespan of the cultivation, which was a further reason to terminate the process after cycle three.

For the chemostat cultivation no product formation was found for the first 8 h of induction. Product formation started after 8 h of induction and increased until reaching a peak of 5.75 mg/g/h after 20–25 h. The timespan until full induction was comparable for repetitive fed batch cultivations and chemostat cultivations (Figure 3). Therefore, it seems like the expression of the periplasmic protein required an adaption time after the start of induction, to establish protein translocation toward the periplasm (Kopp et al., 2017). Throughout chemostat cultivation maximum specific productivity was lower compared to repetitive fed-batch cultivation by a factor of 2.9 (which is in accordance with results obtained for the cytoplasmic product). However, we could not monitor any secretion of periplasmic protein during continuous cultivation. Chemostat cultivation was terminated after 90 h of induction as productivity was below the LOD for both products.

Again, a theoretical ideal chemostat was simulated, exhibiting time-independent productivity once cell specific productivity reached $q_{p,max}$ (Figure 3B). Our results favor repetitive fed-batch cultivation mode for the periplasmic target protein over single cycle fed-batch and chemostat cultivations regarding the specific productivity. Achieved space-time yields of each cultivation mode will be compared in section “Targeting Maximum Space-Time Yield: The Cultivation Mode to Choose.”

Targeting Maximum Space-Time Yield: The Cultivation Mode to Choose

The goal of this study was to determine the cultivation strategy giving the highest space-time yield with recombinant *E. coli*. Thus, we calculated the overall space-time yield in $g_{product}/L_{reactor}/day$, including “downtimes” for each cultivation mode. Results are shown in Figure 4 and Supplementary Figure 2 for recombinant cytoplasmic and periplasmic protein production.

In fed-batch cultivations, cleaning and set-up take up a severe amount of time. Generally, this leads to a much shorter production time in comparison to the total process time. For repetitive fed-batch cultivations and continuous cultivations these downtimes can be reduced compared to single-cycle fed batches (Figure 1). Even though fed-batch cultivations usually give a high q_p , cultivation modes with a lower q_p in combination with a lower downtime might still result in an increase of the overall space-time yield.

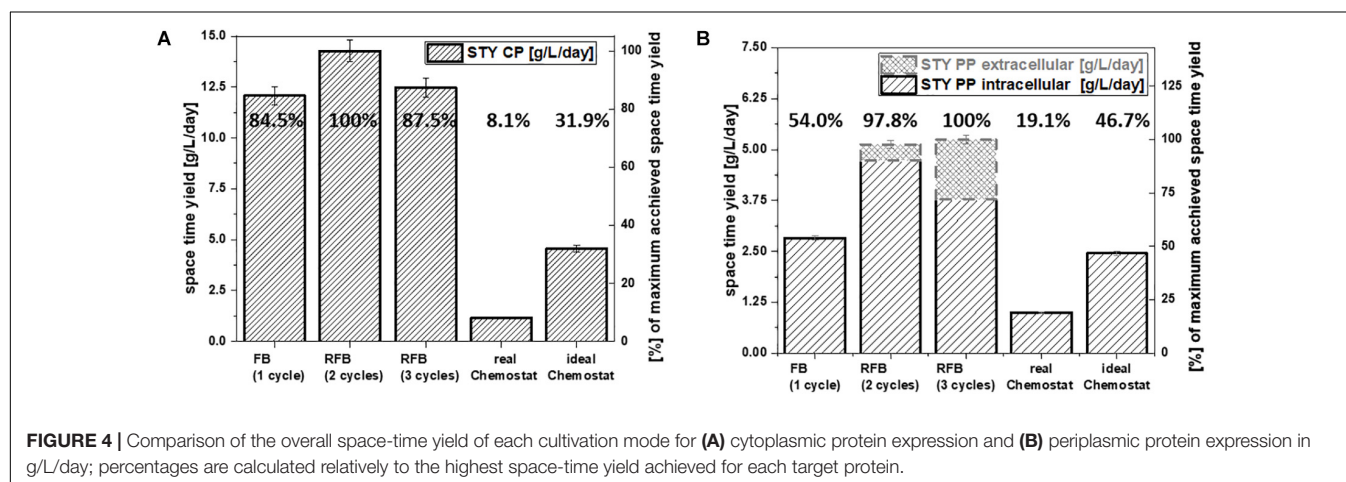
For repetitive fed-batch cultivations and the cytoplasmic target protein, the highest space-time yield was found for a two-cycle process (Figure 4A). Even though q_p declined during cycles two and three (Figure 2A), the space-time yield for all repetitive fed batch cultivations was superior to a single-cycle fed batch.

TABLE 4 | Comparing substrate per product yield for the production of a cytoplasmic protein; each cycle is investigated separately for fed-batch and repeated fed-batch cultivation; chemostat cultivation is calculated as a rate every 12 h (i.e., one cycle).

induction time (h)	12	24	36	48	60	72	84
cytoplasmic protein	$Y_{P/S}$ (mg/g)						
Fed-batch (1 cycle)	86.8 ± 4.3						
Repeated fed-batch (2 cycles)		84.6 ± 4.2					
Repeated fed-batch (3 cycles)			77.9 ± 3.4				
Chemostat cultivation	241.7 ± 12.1	280.8 ± 14.0	176.3 ± 8.8	11.6 ± 0.6	0	0	0
Theoretical "ideal" chemostat	241.7 ± 12.1	280.8 ± 14.0	280.8 ± 14.0	280.8 ± 14.0	280.8 ± 14.0	280.8 ± 14.0	280.8 ± 14.0

TABLE 5 | Comparing substrate per product yield in mg/g for the production of a periplasmic protein; each cycle is investigated separately for fed-batch and repeated fed-batch cultivation; chemostat cultivation is calculated as a rate every 12 h (i.e., one cycle).

induction time (h)	12	24	36	48	60	72	84
periplasmic protein	$Y_{P/S}$ (mg/g)						
Fed-batch (1 cycle)	24.5 ± 0.9						
Repeated fed-batch (2 cycles)		135.4 ± 4.8					
Repeated fed-batch (3 cycles)			133.5 ± 4.7				
Chemostat cultivation	94.9 ± 3.3	133.6 ± 4.7	99.3 ± 3.5	58.4 ± 2.1	32.3 ± 1.1	7.8 ± 1.2	5.2 ± 0.8
Theoretical "ideal" chemostat	94.9 ± 3.3	133.6 ± 4.7	133.6 ± 4.7	133.6 ± 4.7	133.6 ± 4.7	133.6 ± 4.7	133.6 ± 4.7



For processes conducted with the periplasmic target protein, q_p in cycle two and three was higher than productivity in cycle one (Figure 3A). Hence, it was obvious that repetitive fed-batch would be superior to a single-cycle cultivation regarding space-time yield. Even though the total space-time yield (Figure 4B) differed only by 2.2% when harvesting after cycle two or cycle three for the periplasmic protein, we want to highlight that by applying three induction cycles, total downtime can be reduced compared to the two-cycle repeated fed-batch.

A reduction of downtimes leads to reduced costs for chemicals and energy needed throughout SIP and CIP. Taking into account that CO₂-taxes for industry will potentially be realized in near future, a reduction of energy consumption could also lead to higher profits (Kettner et al., 2018).

Continuous processes are generally described to lead to higher space-time yields (Lee et al., 2015). However, the monitored

space-time yield for the chemostat cultivations within this study was beneath 1/5th of the space-time yield received by the repetitive fed-batch cultivations, independent of the target product (Figures 4A,B). As (i) cell specific productivity and (ii) set biomass concentrations are lower in chemostat cultivation compared to repetitive fed-batch cultivation, this implies an overall reduction of space-time yield for chemostat processes. Product per Substrate Yield at the beginning of the continuous cultivation might compete with repetitive fed-batch cultivations (Tables 4, 5, and Supplementary Table 1). However, a severe decrease in productivity over time was monitored for chemostat cultivations, as microbial chemostat cultivations are known to result in fluctuating productivity (Peebo and Neubauer, 2018; Kopp et al., 2019a).

In order to simulate a steady state upon recombinant protein in chemostat cultivation, a stable productivity at $q_{p,max}$ was

assumed for more than 6 residence times. The simulated space-time yield however was not superior compared to the repetitive fed batch cultivation. This is because q_p of chemostat cultivations was significantly lower compared to repeated fed-batch cultivations (Figures 2, 3). Hence, in this study chemostat cultivation led to a lower productivity and a lower space-time yield and would still need further investigation to achieve the high demands needed for recombinant protein formation.

CONCLUSION

The goal of this study was to find out, whether a single-cycle fed-batch, a repetitive fed-batch consisting of two cycles or three cycles or a chemostat is the most suitable cultivation technique to achieve the highest space-time yield of soluble recombinant protein within *E. coli* BL21 (DE3). The impact of the cultivation technology on soluble protein formation was investigated for a cytoplasmic and a periplasmic model protein.

The results of this study show that a repetitive fed-batch approach leads to higher space-time yields compared to single-cycle fed-batches and chemostat cultures. For the cytoplasmic protein a two-cycle repetitive fed-batch was the most efficient cultivation mode, whereas for the periplasmic product a three-cycle repetitive fed-batch was found to be the most efficient cultivation method. Chemostat cultivations suffered from a low maximum specific productivity, which further decreased over time. Therefore, overall product throughput of the chemostat cultivations was much lower compared to other cultivation modes. Furthermore, a single-cycle fed batch was always outperformed by repeated fed-batch independent of the target product and number of applied cycles.

Production processes for recombinant proteins in large-scale are cost-intensive. Here, we were able to show that a repetitive

fed-batch cultivation leads to a higher space-time yield compared to a single-cycle fed-batch or a chemostat process. We can promote the developed mixed feeding approach in combination with the repetitive fed-batch cultivation mode, as it leads toward a more economic fingerprint and an increased space-time yield.

DATA AVAILABILITY STATEMENT

The raw data supporting the conclusions of this article will be made available by the authors, without undue reservation.

AUTHOR CONTRIBUTIONS

JK planned the experimental design and carried out the data treatment. SK performed the cultivations and analytics. CS, CH, and OS gave major scientific input. DW founded the idea of this study. JK and DW wrote the manuscript. OS critically reviewed the manuscript. All authors contributed to the article and approved the submitted version.

ACKNOWLEDGMENTS

The authors acknowledge the TU Wien Bibliothek for financial support through its Open Access Funding Program.

SUPPLEMENTARY MATERIAL

The Supplementary Material for this article can be found online at: <https://www.frontiersin.org/articles/10.3389/fbioe.2020.573607/full#supplementary-material>

REFERENCES

- Allison, G., Cain, Y. T., Cooney, C., Garcia, T., Bizjak, T. G., Holte, O., et al. (2015). Regulatory and Quality Considerations for Continuous Manufacturing. May 20–21, 2014 Continuous Manufacturing Symposium. *J. Pharm. Sci.* 104, 803–812. doi: 10.1002/jps.24324
- Baeshen, M. N., Al-Hejin, A. M., Bora, R. S., Ahmed, M. M., Ramadan, H. A., Saini, K. S., et al. (2015). Production of Biopharmaceuticals in *E. coli*: Current Scenario and Future Perspectives. *J. Microbiol. Biotechnol.* 25, 953–962. doi: 10.4014/jmb.1412.12079
- Basan, M. (2018). Resource allocation and metabolism: the search for governing principles. *Curr. Opin. Microbiol.* 45, 77–83. doi: 10.1016/j.mib.2018.02.008
- Bauer, R., Katsikis, N., Varga, S., and Hekmat, D. (2005). Study of the inhibitory effect of the product dihydroxyacetone on *Gluconobacter oxydans* in a semi-continuous two-stage repeated-fed-batch process. *Bioprocess. Biosyst. Eng.* 28, 37–43. doi: 10.1007/s00449-005-0009-0
- Bergmann, P., and Trösch, W. (2016). Repeated fed-batch cultivation of *Thermosynechococcus elongatus* BP-1 in flat-panel airlift photobioreactors with static mixers for improved light utilization: Influence of nitrate, carbon supply and photobioreactor design. *Algal Res.* 17, 79–86. doi: 10.1016/j.algal.2016.03.040
- Binder, D., Drepper, T., Jaeger, K.-E., Delvigne, F., Wiechert, W., Kohlheyer, D., et al. (2017). Homogenizing bacterial cell factories: analysis and engineering of phenotypic heterogeneity. *Metab. Eng.* 42, 145–156. doi: 10.1016/j.ymben.2017.06.009
- Briand, L., Marcion, G., Kriznik, A., Heydel, J. M., Artur, Y., Garrido, C., et al. (2016). A self-inducible heterologous protein expression system in *Escherichia coli*. *Sci. Rep.* 6:33037. doi: 10.1038/srep33037
- Buerger, J., Gronenberg, L. S., Genee, H. J., and Sommer, M. O. A. (2019). Wiring cell growth to product formation. *Curr. Opin. Biotechnol.* 59, 85–92. doi: 10.1016/j.copbio.2019.02.014
- Casali, N. (2003). *Escherichia coli* host strains. *Methods Mol. Biol.* 235, 27–48. doi: 10.1385/1-59259-409-3:27
- Chen, Z.-Y., Cao, J., Xie, L., Li, X.-F., Yu, Z.-H., and Tong, W.-Y. (2014). Construction of leaky strains and extracellular production of exogenous proteins in recombinant *Escherichia coli*. *Microb. Biotechnol.* 7, 360–370. doi: 10.1111/1751-7915.12127
- DeLisa, M. P., Li, J., Rao, G., Weigand, W. A., and Bentley, W. E. (1999). Monitoring GFP-operon fusion protein expression during high cell density cultivation of *Escherichia coli* using an on-line optical sensor. *Biotechnol. Bioeng.* 65, 54–64.
- Deutscher, J., Francke, C., and Postma, P. W. (2006). How phosphotransferase system-related protein phosphorylation regulates carbohydrate metabolism in bacteria. *Microbiol. Mol. Biol. Rev.* 70, 939–1031. doi: 10.1128/MMBR.00024-06
- Dvorak, P., Chrast, L., Nikel, P. I., Fedr, R., Soucek, K., Sedlackova, M., et al. (2015). Exacerbation of substrate toxicity by IPTG in *Escherichia coli* BL21(DE3) carrying a synthetic metabolic pathway. *Microb. Cell. Fact.* 14:201. doi: 10.1186/s12934-015-0393-3
- Fricke, J., Pohlmann, K., Vefghi, E., Drews, M., Scheffler, U., and Luttmann, R. (2013). Advanced automation strategies for reliable, reproducible cultivation

- runs in a sequential/parallel operated multi-bioreactor plant. *IFAC Proc.* 46, 54–59. doi: 10.3182/20131216-3-IN-2044.00042
- Glaser, J. A. (2015). Continuous chemical production processes. *Clean Technol. Environ. Policy* 17, 309–316. doi: 10.1007/s10098-015-0903-3
- Goyon, A., Sciascera, L., Clarke, A., Guillaume, D., and Pell, R. (2018). Extending the limits of size exclusion chromatography: Simultaneous separation of free payloads and related species from antibody drug conjugates and their aggregates. *J. Chromatogr. A* 1539, 19–29. doi: 10.1016/j.chroma.2018.01.039
- Gupta, S. K., and Shukla, P. (2017). Microbial platform technology for recombinant antibody fragment production: A review. *Crit. Rev. Microbiol.* 43, 31–42. doi: 10.3109/1040841X.2016.1150959
- Hausjell, J., Kutscha, R., Gesson, D. J., Reinisch, D., and Spadiut, O. (2020). The Effects of Lactose Induction on a Plasmid-Free *E. coli* T7 Expression System. *Bioengineering* 7:8. doi: 10.3390/bioengineering7010008
- Hausjell, J., Weissensteiner, J., Molitor, C., Halbwirth, H., and Spadiut, O. (2018). *E. coli* HMS174(DE3) is a sustainable alternative to BL21(DE3). *Microb. Cell Fact.* 17:169. doi: 10.1186/s12934-018-1016-6
- Herwig, C., Garcia-Aponte, O. F., Golabgir, A., and Rathore, A. S. (2015). Knowledge management in the QbD paradigm: manufacturing of biotech therapeutics. *Trends Biotechnol.* 33, 381–387. doi: 10.1016/j.tibtech.2015.04.004
- Karyolaimos, A., Ampah-Korsah, H., Hillenaar, T., Mestre Borrás, A., Dolata, K. M., Sievers, S., et al. (2019). Enhancing Recombinant Protein Yields in the *E. coli* Periplasm by Combining Signal Peptide and Production Rate Screening. *Front. Microbiol.* 10:1511. doi: 10.3389/fmicb.2019.01511
- Kettner, C., Kletzan-Slamanig, D., Kirchner, M., Sommer, M., Kratena, K., Weishaar, S. E., et al. (2018). CATs—Carbon Taxes in Austria. *Implementation Issues and Impacts*. Vienna: WIFO.
- Kittler, S., Kopp, J., Veelenturf, P. G., Spadiut, O., Delvigne, F., Herwig, C., et al. (2020). The Lazarus *Escherichia coli* Effect: Recovery of Productivity on Glycerol/Lactose Mixed Feed in Continuous Biomanufacturing. *Front. Bioeng. Biotechnol.* 8:993. doi: 10.3389/fbioe.2020.00993
- Kleiner-Grote, G. R. M., Risse, J. M., and Friehs, K. (2018). Secretion of recombinant proteins from *E. coli*. *Eng. Life Sci.* 18, 532–550. doi: 10.1002/elsc.201700200
- Konstantinov, K. B., and Cooney, C. L. (2015). White Paper on Continuous Bioprocessing. May 20–21, 2014 Continuous Manufacturing Symposium. *J. Pharm. Sci.* 104, 813–820. doi: 10.1002/jps.24268
- Kopp, J., Kolkman, A.-M., Veelenturf, P. G., Spadiut, O., Herwig, C., and Slouka, C. (2019a). Boosting recombinant inclusion body production—from classical fed-batch approach to continuous cultivation. *Front. Bioeng. Biotechnol.* 7:297. doi: 10.3389/fbioe.2019.00297
- Kopp, J., Slouka, C., Spadiut, O., and Herwig, C. (2019b). The rocky road from fed-batch to continuous processing with *E. coli*. *Front. Bioeng. Biotechnol.* 7:328. doi: 10.3389/fbioe.2019.00328
- Kopp, J., Slouka, C., Ulonka, S., Kager, J., Fricke, J., Spadiut, O., et al. (2017). Impact of Glycerol as Carbon Source onto Specific Sugar and Inducer Uptake Rates and Inclusion Body Productivity in *E. coli* BL21(DE3). *Bioengineering* 5:1. doi: 10.3390/bioengineering5010001
- Kopp, J., Zauner, F. B., Pell, A., Hausjell, J., Humer, D., Ebner, J., et al. (2020). Development of a generic reversed-phase liquid chromatography method for protein quantification using analytical quality-by-design principles. *J. Pharm. Biomed. Anal.* 188:113412. doi: 10.1016/j.jpba.2020.113412
- Kumar, M. S., Jana, S. K., Senthil, V., Shashanka, V., Kumar, S. V., and Sadhukhan, A. K. (2000). Repeated fed-batch process for improving lovastatin production. *Process Biochem.* 36, 363–368. doi: 10.1016/S0032-9592(00)00222-3
- Kuo, H.-P., Wang, R., Lin, Y.-S., Lai, J.-T., Lo, Y.-C., and Huang, S.-T. (2017). Pilot scale repeated fed-batch fermentation processes of the wine yeast *Dekkera bruxellensis* for mass production of resveratrol from *Polygonum cuspidatum*. *Bioresour. Technol.* 243, 986–993. doi: 10.1016/j.biortech.2017.07.053
- Langemann, T., Mayr, U. B., Meitz, A., Lubitz, W., and Herwig, C. (2016). Multi-parameter flow cytometry as a process analytical technology (PAT) approach for the assessment of bacterial host production. *Appl. Microbiol. Biotechnol.* 100, 409–418. doi: 10.1007/s00253-015-7089-9
- Lee, S. L., O'Connor, T. F., Yang, X., Cruz, C. N., Chatterjee, S., Madurawe, R. D., et al. (2015). Modernizing Pharmaceutical Manufacturing: from Batch to Continuous Production. *J. Pharm. Innov.* 10, 191–199. doi: 10.1007/s12247-015-9215-8
- Lis, A. V., Schneider, K., Weber, J., Keasling, J. D., Jensen, M. K., and Klein, T. (2019). Exploring small-scale chemostats to scale up microbial processes: 3-hydroxypropionic acid production in *S. cerevisiae*. *Microb. Cell Fact.* 18, 50–50. doi: 10.1186/s12934-019-1101-5
- Liu, L., Wang, F., Pei, G., Cui, J., Diaio, J., Lv, M., et al. (2020). Repeated fed-batch strategy and metabolomic analysis to achieve high docosahexaenoic acid productivity in *Cryptocodinium cohnii*. *Microb. Cell Fact.* 19:91. doi: 10.1186/s12934-020-01349-6
- Malakar, P., and Venkatesh, K. V. (2012). Effect of substrate and IPTG concentrations on the burden to growth of *Escherichia coli* on glycerol due to the expression of Lac proteins. *Appl. Microbiol. Biotechnol.* 93, 2543–2549. doi: 10.1007/s00253-011-3642-3
- Marshall, L., Sagmeister, P., and Herwig, C. (2016). Tunable recombinant protein expression in *E. coli*: enabler for continuous processing? *Appl. Microbiol. Biotechnol.* 100, 5719–5728. doi: 10.1007/s00253-016-7550-4
- Martens, S., Borchert, S.-O., Faber, B. W., Cornelissen, G., and Luttmann, R. (2011). Fully automated production of potential Malaria vaccines with *Pichia pastoris* in integrated processing. *Eng. Life Sci.* 11, 429–435. doi: 10.1002/elsc.201000163
- Moeller, L., Grünberg, M., Zehnsdorf, A., Aurich, A., Bley, T., and Strehlitz, B. (2011). Repeated fed-batch fermentation using biosensor online control for citric acid production by *Yarrowia lipolytica*. *J. Biotechnol.* 153, 133–137. doi: 10.1016/j.biotech.2011.03.013
- Mühlmann, M. J., Forsten, E., Noack, S., and Büchs, J. (2018). Prediction of recombinant protein production by *Escherichia coli* derived online from indicators of metabolic burden. *Biotechnol. Prog.* 34, 1543–1552. doi: 10.1002/btpr.2704
- Nasr, M. M., Krumme, M., Matsuda, Y., Trout, B. L., Badman, C., Mascia, S., et al. (2017). Regulatory Perspectives on Continuous Pharmaceutical Manufacturing: Moving From Theory to Practice: September 26–27, 2016, International Symposium on the Continuous Manufacturing of Pharmaceuticals. *J. Pharm. Sci.* 106, 3199–3206. doi: 10.1016/j.xphs.2017.06.015
- Neubauer, P., Lin, H. Y., and Mathisizik, B. (2003). Metabolic load of recombinant protein production: inhibition of cellular capacities for glucose uptake and respiration after induction of a heterologous gene in *Escherichia coli*. *Biotechnol. Bioeng.* 83, 53–64. doi: 10.1002/bit.10645
- Novak, N., Gerdin, S., and Berovic, M. (1997). Increased lovastatin formation by *Aspergillus terreus* using repeated fed-batch process. *Biotechnol. Lett.* 19, 947–948. doi: 10.1023/A:1018322628333
- Ohya, T., Ohyama, M., and Kobayashi, K. (2005). Optimization of human serum albumin production in methylotrophic yeast *Pichia pastoris* by repeated fed-batch fermentation. *Biotechnol. Bioeng.* 90, 876–887. doi: 10.1002/bit.20507
- Ozmihci, S., and Kargi, F. (2007). Ethanol fermentation of cheese whey powder solution by repeated fed-batch operation. *Enzyme Microb. Technol.* 41, 169–174. doi: 10.1016/j.enzmictec.2006.12.016
- Peebo, K., and Neubauer, P. (2018). Application of Continuous Culture Methods to Recombinant Protein Production in Microorganisms. *Microorganisms* 6:56. doi: 10.3390/microorganisms6030056
- Peebo, K., Valgepea, K., Maser, A., Nahku, R., Adamberg, K., and Vilu, R. (2015). Proteome reallocation in *Escherichia coli* with increasing specific growth rate. *Mol. Biosyst.* 11, 1184–1193.
- Rathore, A. S. (2015). Continuous Processing for Production of Biotech Therapeutics. *PDA J. Pharm. Sci. Technol.* 69:333. doi: 10.5731/pdajpst.2015.01072
- Rosano, G. L., and Ceccarelli, E. A. (2014). Recombinant protein expression in *Escherichia coli*: advances and challenges. *Front. Microbiol.* 5:172. doi: 10.3389/fmicb.2014.00172
- Rosano, G. L., Morales, E. S., and Ceccarelli, E. A. (2019). New tools for recombinant protein production in *Escherichia coli*: A 5-year update. *Protein Sci.* 28, 1412–1422. doi: 10.1002/pro.3668
- Rugbjerg, P., and Sommer, M. O. A. (2019). Overcoming genetic heterogeneity in industrial fermentations. *Nat. Biotechnol.* 37, 869–876. doi: 10.1038/s41587-019-0171-6
- Rugbjerg, P., Myling-Petersen, N., Porse, A., Sarup-Lytzen, K., and Sommer, M. O. A. (2018). Diverse genetic error modes constrain large-scale bio-based production. *Nat. Commun.* 9:787. doi: 10.1038/s41467-018-03232-w
- Schein, C. H. (2019). Production of Soluble Recombinant Proteins in Bacteria. *Biotechnology* 7:1141. doi: 10.1038/nbt1189-1141

- Schreiber, F., Littmann, S., Lavik, G., Escrig, S., Meibom, A., Kuypers, M. M. M., et al. (2016). Phenotypic heterogeneity driven by nutrient limitation promotes growth in fluctuating environments. *Nat. Microbiol.* 1:16055. doi: 10.1038/nmicrobiol.2016.55
- Sieben, M., Steinhorn, G., Müller, C., Fuchs, S., Chin, L. A., Regestein, L., et al. (2016). Testing plasmid stability of *Escherichia coli* using the continuously operated shaken BIOreactor system. *Biotechnol. Prog.* 32, 1418–1425. doi: 10.1002/btpr.2341
- Slouka, C., Kopp, J., Hutwimmer, S., Strahammer, M., Strohmer, D., Eitenberger, E., et al. (2018). Custom Made Inclusion Bodies: Impact of classical process parameters and physiological parameters on Inclusion Body quality attributes. *Microb. Cell Fact.* 17:148. doi: 10.1186/s12934-018-0997-5
- Tan, Z. L., Zheng, X., Wu, Y., Jian, X., Xing, X., and Zhang, C. (2019). In vivo continuous evolution of metabolic pathways for chemical production. *Microb. Cell Fact.* 18:82. doi: 10.1186/s12934-019-1132-y
- Wurm, D. J., Hausjell, J., Ulonska, S., Herwig, C., and Spadiut, O. (2017a). Mechanistic platform knowledge of concomitant sugar uptake in *Escherichia coli* BL21 (DE3) strains. *Sci. Rep.* 7:45072.
- Wurm, D. J., Quehenberger, J., Mildner, J., Eggenreich, B., Slouka, C., Schwaighofer, A., et al. (2017b). Teaching an old pET new tricks: tuning of inclusion body formation and properties by a mixed feed system in *E. coli*. *Appl. Microbiol. Biotechnol.* 102, 667–676. doi: 10.1007/s00253-017-8641-6
- Wurm, D. J., Veiter, L., Ulonska, S., Eggenreich, B., Herwig, C., and Spadiut, O. (2016). The *E. coli* pET expression system revisited—mechanistic correlation between glucose and lactose uptake. *Appl. Microbiol. Biotechnol.* 100, 8721–8729. doi: 10.1007/s00253-016-7620-7
- Yan, J., Zhao, S. F., Mao, Y. F., and Luo, Y. H. (2004). Effects of lactose as an inducer on expression of *Helicobacter pylori* rUreB and rHpaA, and *Escherichia coli* rLTKA63 and rLTB. *World J. Gastroenterol.* 10, 1755–1758. doi: 10.3748/wjg.v10.i12.1755
- Zagrodnik, R., and Łaniecki, M. (2017). Hydrogen production from starch by co-culture of *Clostridium acetobutylicum* and *Rhodobacter sphaeroides* in one step hybrid dark- and photofermentation in repeated fed-batch reactor. *Bioresour. Technol.* 224, 298–306. doi: 10.1016/j.biortech.2016.10.060
- Zelić, B., Gostović, S., Vuorilehto, K., Vasić-Rački, , and Takors, R. (2004). Process strategies to enhance pyruvate production with recombinant *Escherichia coli*: From repetitive fed-batch to in situ product recovery with fully integrated electrodialysis. *Biotechnol. Bioeng.* 85, 638–646. doi: 10.1002/bit.10820
- Zhang, Y., Feng, X., Xu, H., Yao, Z., and Ouyang, P. (2010). ϵ -Poly-L-lysine production by immobilized cells of *Kitasatospora* sp. MY 5-36 in repeated fed-batch cultures. *Bioresour. Technol.* 101, 5523–5527. doi: 10.1016/j.biortech.2010.02.021
- Zobel-Roos, S., Schmidt, A., Mestmäcker, F., Mouellef, M., Huter, M., Uhlenbrock, L., et al. (2019). Accelerating Biologics Manufacturing by Modeling or: Is Approval under the QbD and PAT Approaches Demanded by Authorities Acceptable without a Digital-Twin? *Processes* 7:94. doi: 10.3390/pr7020094

Conflict of Interest: The authors declare that the research was conducted in the absence of any commercial or financial relationships that could be construed as a potential conflict of interest.

Copyright © 2020 Kopp, Kittler, Slouka, Herwig, Spadiut and Wurm. This is an open-access article distributed under the terms of the Creative Commons Attribution License (CC BY). The use, distribution or reproduction in other forums is permitted, provided the original author(s) and the copyright owner(s) are credited and that the original publication in this journal is cited, in accordance with accepted academic practice. No use, distribution or reproduction is permitted which does not comply with these terms.



Single-Cell Technologies to Understand the Mechanisms of Cellular Adaptation in Chemostats

Naia Risager Wright^{1,2}, Nanna Petersen Rønne¹ and Nikolaus Sonnenschein^{2*}

¹ Novo Nordisk A/S, Bagsvaerd, Denmark, ² Department of Biotechnology and Biomedicine, Technical University of Denmark, Kongens Lyngby, Denmark

OPEN ACCESS

Edited by:

Peter Neubauer,
Technical University of Berlin,
Germany

Reviewed by:

Nuno F. Azevedo,
University of Porto, Portugal
Alexander Grünberger,
Bielefeld University, Germany

*Correspondence:

Nikolaus Sonnenschein
niso@dtu.dk

Specialty section:

This article was submitted to
Bioprocess Engineering,
a section of the journal
Frontiers in Bioengineering and
Biotechnology

Received: 03 July 2020

Accepted: 30 November 2020

Published: 18 December 2020

Citation:

Wright NR, Rønne NP and
Sonnenschein N (2020) Single-Cell
Technologies to Understand
the Mechanisms of Cellular
Adaptation in Chemostats.
Front. Bioeng. Biotechnol. 8:579841.
doi: 10.3389/fbioe.2020.579841

There is a growing interest in continuous manufacturing within the bioprocessing community. In this context, the chemostat process is an important unit operation. The current application of chemostat processes in industry is limited although many high yielding processes are reported in literature. In order to reach the full potential of the chemostat in continuous manufacture, the output should be constant. However, adaptation is often observed resulting in changed productivities over time. The observed adaptation can be coupled to the selective pressure of the nutrient-limited environment in the chemostat. We argue that population heterogeneity should be taken into account when studying adaptation in the chemostat. We propose to investigate adaptation at the single-cell level and discuss the potential of different single-cell technologies, which could be used to increase the understanding of the phenomena. Currently, none of the discussed single-cell technologies fulfill all our criteria but in combination they may reveal important information, which can be used to understand and potentially control the adaptation.

Keywords: chemostat cultivation, continuous biomanufacturing, adaptation, population heterogeneity, microbes, single-cell technologies

INTRODUCTION

Today, production of biological products is primarily based on batch operations where each unit operation is completed in sequence. The transition from these constitutive batch processes to continuous manufacture in which the product moves directly from one unit operation to the next, has been of growing interest within the bioprocessing community in recent years (Farid, 2019). Several benefits of moving to continuous processes can be listed due to the possibility of keeping production organisms in high producing states for longer time. These include a reduction in equipment costs, increased productivity, greater flexibility, and improved product quality (Zydney, 2016).

Continuous cell culture technologies have existed for several decades and include among others chemostat processes (Monod, 1950; Novick and Szilard, 1950). In a chemostat, the cells in the bioreactor are kept in a steady-state growth environment by a continuous addition of medium with one or more cell-density-limiting nutrients and simultaneous removal of spent culture medium at a defined rate (Peebo and Neubauer, 2018). Ideally, the chemostat should operate at a true steady state with a constant productivity. Although, the chemostat establishes a well-controlled and

constant environment for production processes, it imposes selective pressure on cells, which may result in cellular adaptation. These alterations can affect productivity and the output of the cultivation. It is therefore important to understand the mechanisms behind the adaptation in order to control them and realize the full potential of chemostats in industrial production.

This article focuses on chemostat cultivations of microbes, the reported adaptation, and discuss how development of continuous biomanufacturing and chemostat processes can benefit from single-cell technologies.

ADAPTATION IN THE CHEMOSTAT

The chemostat imposes a steady nutrient limited environment forcing cells to grow at a constant growth rate. These conditions result in an ongoing selective pressure driving the adaptation of cells with growth advantages. Cells which are not able to adapt will be washed out. Adaptive processes in chemostats are illustrated in several studies for many different microorganisms at both the RNA, protein, metabolite, and morphological level (Adams et al., 1985; Ferea et al., 1999; Wick et al., 2001; Robin et al., 2003; Jansen et al., 2004, 2005; Mashego et al., 2005; Franchini and Egli, 2006; Wu et al., 2006; Douma et al., 2011; Paulová et al., 2012; Wang et al., 2018). The adaptation covers the differential expression of thousands of genes and proteins, but some general trends, which confer fitness in a nutrient limited environment, can be extracted (**Figure 1A**). This includes an improved affinity for the limiting substrate (Wick et al., 2001; Jansen et al., 2005). Any adaptation which increases the specific growth rate under low external concentrations of the limiting nutrient will improve the competitiveness of the cell compared to non-adapted cells (Jansen et al., 2005). Moreover, decreased (over)capacity of the main carbon metabolism including the glycolysis and TCA cycle is observed and has been suggested as a way to get an energetical advantage (Mashego et al., 2005). Cellular stress-responses are in many cases also differentially expressed between early and late cultivation stages including proteins involved in heat shock, oxidative stress, and damage resistance (Jansen et al., 2005; Franchini and Egli, 2006; Wright et al., 2020). Morphological changes toward filamentous and pseudo-hyphal growth are known effects of chemostat growth (Brown and Hough, 1965; Adams et al., 1985; Rebnegger et al., 2014; Rai et al., 2019) and also a known adaptive response to nutrient poor environments (Gimeno et al., 1992). The productivity of industrially relevant strains often decreases over time during chemostat growth (Douma et al., 2011; Paulová et al., 2012; Kazemi Seresht et al., 2013; Wright et al., 2016, 2020). A reduced productivity can be construed as a clear growth advantage over cells that are not able to reduce the burden of heterologous production.

Stochastic, regulatory, epigenetic, and mutational changes can contribute to increased fitness and adaptation is therefore a comprehensive process (Ryall et al., 2012). The underlying functional mechanisms of the adaptive processes in chemostats often remain unknown but many studies couple changed

phenotypes to specific genetic mutations (Brown et al., 1998; Dunham et al., 2002; Wenger et al., 2011; Kvittek and Sherlock, 2013; Gresham and Hong, 2015; Hope et al., 2017). Hope et al. (2017) related morphological changes in *S. cerevisiae* after hundreds of generations to genetic mutations in known flocculation genes such as the cell wall protein FLO1. Clones with mutations in nutrient signaling and regulation of glucose transport have also been isolated from *S. cerevisiae* evolved for more than 200 generations in glucose-limited conditions (Wenger et al., 2011). This illustrates that some of the observed adaptive phenomena can be related to genetic alterations. Whether and when a given mutation will dominate a culture depends on the relative fitness of the mutant compared to other clones in the population (Gresham and Hong, 2015). For industrial strains, studies report reproducible adaptive changes in transcriptome, proteome, and heterologous product already after 22 generations of chemostat growth (Douma et al., 2011; Kazemi Seresht et al., 2013; Wright et al., 2020). The observed changes cannot always be coupled to genetic instability (Douma et al., 2011) and may therefore be related to other adaptive mechanisms, e.g., epigenetics.

Population heterogeneity is a cellular response to nutrient limitation and is reported for chemostat growth (Lieder et al., 2014; Kopf et al., 2015; Schreiber et al., 2016). Here we refer to population heterogeneity as the phenotypic diversity occurring between genetically identical individuals (Davis and Isberg, 2016). Nikolic et al. (2017) showed cell-to-cell variations in gene expression and substrate specialization for *E. coli* growing simultaneously on glucose and arabinose under chemostat conditions. Population heterogeneity with respect to growth and cell robustness was observed in glucose-limited chemostats of both *S. cerevisiae*, *E. coli*, and *P. putida* (Carlquist et al., 2012; Heins et al., 2019; Sassi et al., 2019) and also *Arthrobacter* evolves subpopulations with respect to nucleic acid content and metabolic activity (Kundu et al., 2020). The subpopulation ratios reported, strongly depend on the cultured strains, the cultivation conditions and the parameters analyzed. Ratios up to 1:2 between non-growing and growing subpopulations are reported (Kundu et al., 2020).

When bioprocesses are scaled up to manufacturing scale, the cells will often be exposed to a heterogeneous environment, for example, gradients in substrate and oxygen (Oosterhuis and Kossen, 1984; Larsson and Enfors, 1988). Fluctuations in the extracellular environment affect metabolism including product yield and by-product formation (George et al., 1993, 1998; Neubauer et al., 1995; Bylund et al., 1998, 1999, 2000; Lin and Neubauer, 2000; Enfors et al., 2001; Sandoval-Basurto et al., 2005). The gradients can also influence population heterogeneity. Differences in transcription levels between cells located in different zones of reactors have been found (Schweder et al., 1999; Lara et al., 2006). Schweder et al. (1999) measured different mRNA levels of stress genes between cells taken from the top and bottom of a production reactor. Nonetheless, other studies have shown that the heterogeneous environment can also result in a more homogeneous population for example when measured by viability and membrane damage (Hewitt et al., 2000, 2007; Han et al., 2013; Brognaux et al., 2014).

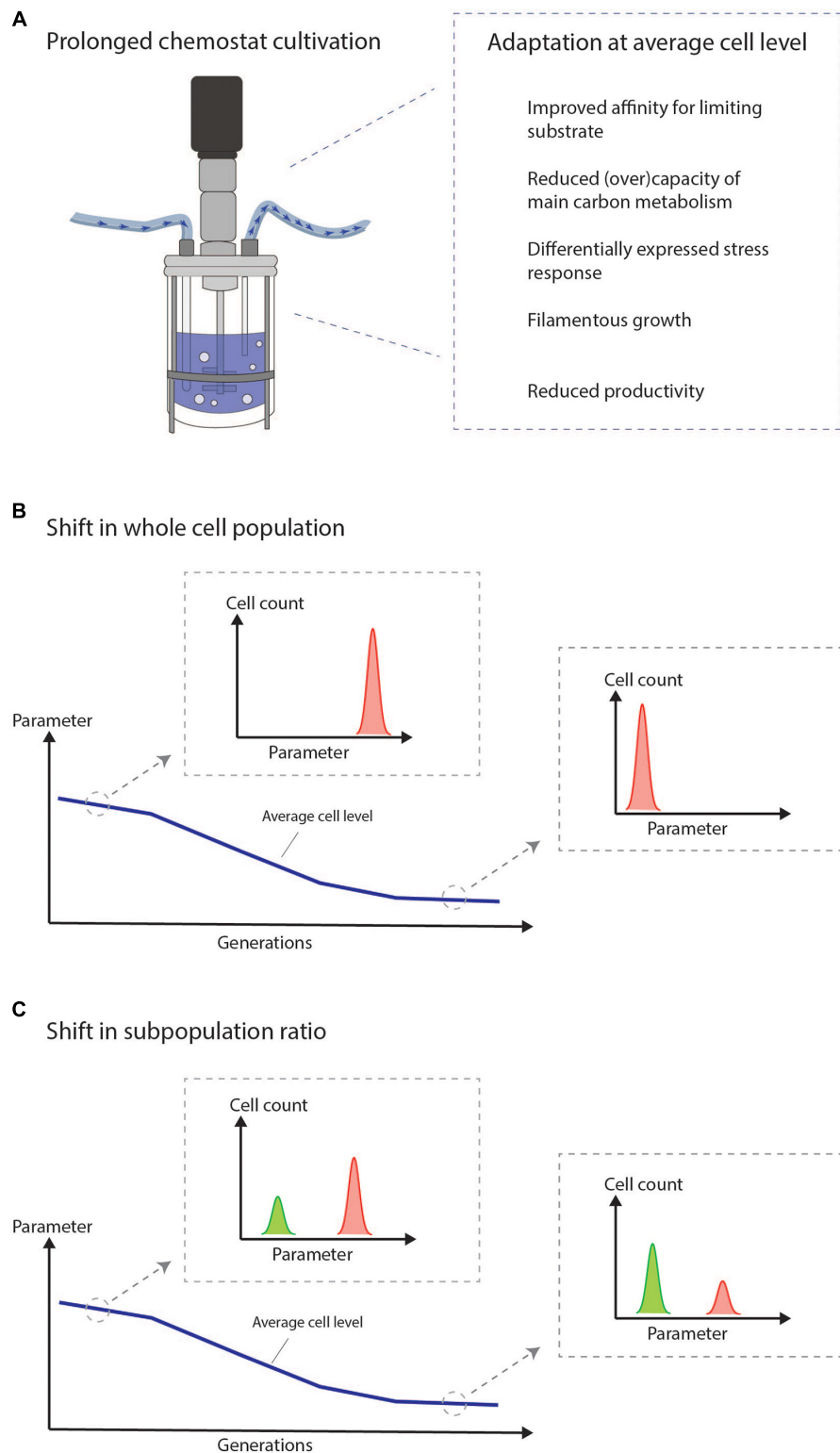


FIGURE 1 | The chemostat imposes a selective pressure on the cultured cells, which drives cellular adaptation. We suggest to intensify the efforts on combining the study of adaptation at the average cell level with the current knowledge of population heterogeneity in chemostats to study the mechanisms of adaptation at the single cell level. **(A)** General trends observed at average cell level during prolonged adaptation in chemostat cultivation of microbes. **(B)** Illustration of adaptation measured in the bulk. The figure illustrates how it may look at the single-cell level if the adaptation is a result of a shift in the whole cell population. **(C)** Illustration of adaptation measured in the bulk. The figure illustrates how it may look at the single-cell level if the adaptation is a result of a shift in subpopulation ratios.

Population heterogeneity can therefore arise due to external influences such as gradients in manufacturing scale and nutrient limitation. It can also originate from intracellular events not influenced by the environment such as stochastic gene expression, e.g., random variations in the abundance of intracellular molecules with important regulatory functions (Elowitz et al., 2002; Blake et al., 2003). The population heterogeneity can have important functional consequences, which is beneficial for the entire population. It has been suggested that heterogeneity emerges as a consequence of metabolic cooperation between cells (Campbell et al., 2016) and that the population as a whole benefits from division of labor between individuals (Reuven and Eldar, 2011; Ackermann, 2015). We speculate that this can also occur in chemostats. Bet-hedging is another strategy resulting in phenotypic heterogeneity and can be seen as a way to cope with unforeseen conditions in fluctuating environments (Thattai and van Oudenaarden, 2004; Kussell and Leibler, 2005). Acar et al. (2008) suggested that isogenic populations can improve fitness by optimizing the phenotypic diversity to an ideal fraction. As a recent example Kundu et al. (2020) showed how cells in a chemostat divide into growing and non-growing subpopulations and propose that the isogenic population in this way improves its fitness to sudden increases in nutrient concentrations. Due to the selective nature of the chemostat, this strategy requires that cells with the less beneficial growth advantage continuously emerge, as they would otherwise be washed out (Kundu et al., 2020). Alternative mechanisms causing phenotypic heterogeneity can be related to aging and the asymmetrical division of exponentially growing cells. Recently, Li Y. et al. (2020) showed that genetically identical yeast cells age at different rates and toward different phenotypes in a constant glucose-limited environment, for example.

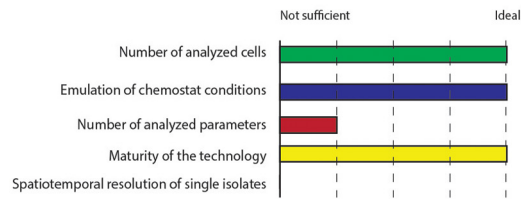
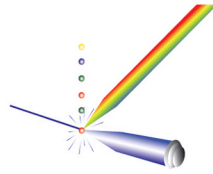
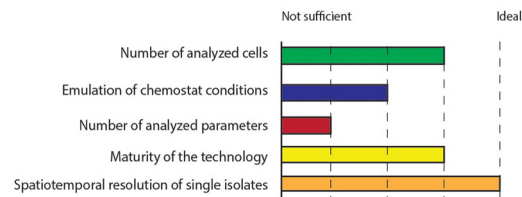
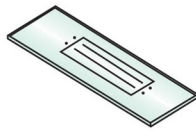
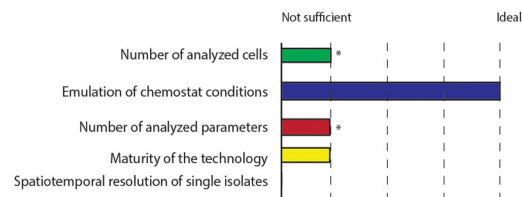
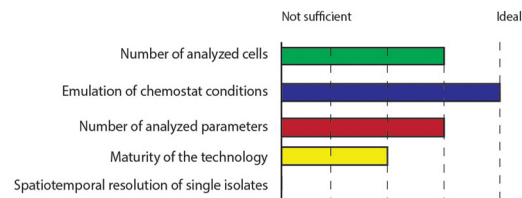
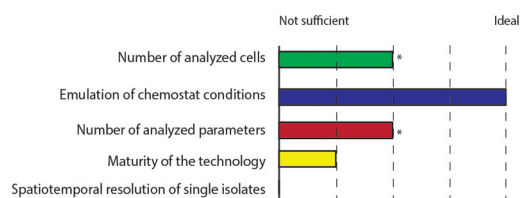
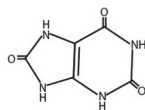
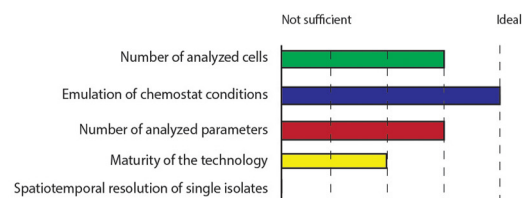
DISCUSSION OF SINGLE-CELL TECHNOLOGIES FOR THE STUDY OF ADAPTATION IN CHEMOSTATS

It is essential to understand the functional molecular basis of adaptation in prolonged chemostats in order to utilize the full potential of the chemostat process in continuous biomanufacturing. We suggest to intensify the efforts on combining the study of adaptation at the average cell level with the current knowledge of population heterogeneity in chemostat cultivations to study mechanisms of adaption at the single-cell level. This could reveal important differences between subpopulations potentially hidden in bulk measurements (Figures 1B,C). For this endeavor, single-cell technologies are needed.

Traditionally, flow cytometry has been used to address heterogeneity in bioprocesses including chemostats (Hewitt et al., 1998, 1999; Delvigne et al., 2015; Heins et al., 2019; Vees et al., 2020). Populations differentiated by structural or physiological cell parameters can be revealed based on optical signals from, e.g., staining dyes or biosensors. Online flow cytometers exist and can be applied for regulation of bioreactors (Sassi et al., 2019). If the adaptation observed in chemostats

is grounded in population heterogeneity, real-time monitoring of heterogeneity can potentially be used to control adaptation. However, more knowledge about how to control the processes are needed. Fluorescence-activated cell sorting in combination with proteomics or transcriptomics allow for the sorting of cells into subpopulations, which can afterward be analyzed by subpopulation omics (Achilles et al., 2007; Jehmlich et al., 2010; Jahn et al., 2013; Lieder et al., 2014). This method can be used to gain knowledge about changes in gene and protein expression leading to the development of subpopulations (Jahn et al., 2013). The method is limited by the time it takes to obtain enough cells to detect sufficient amounts of proteins or transcripts for the omics characterization.

Microfluidic single-cell cultivation systems enable time-resolved analysis of individual cells in accurately controlled environments by application of, e.g., online fluorescent readouts or phase contrast images. These systems are typically used to study cell division, morphology, aging, or gene expression (Elowitz and Leibler, 2000; Wang et al., 2010; Ullman et al., 2013; Grünberger et al., 2015; Li Y. et al., 2020). Contrary to studies in bioreactors, it is possible to follow phenotypic development and regulation of isolated cells with spatiotemporal resolution and to distinguish contributions from intrinsic stochastic processes and environmental factors (Weibel et al., 2007; Dusny and Schmid, 2015). On this basis, the systems can reveal fundamental insight into cellular regulation strategies to nutrient-limited conditions (Lindemann et al., 2019). Several microfluidic cultivation concepts exist where cells are trapped by different physical principles. This includes systems with contactless trapping of single cells by a non-uniform electric field (Kortmann et al., 2009; Fritzsche et al., 2013) and mechanical trapping of cells in chambers (Wang et al., 2010; Long et al., 2013). 1D chamber systems can accurately reproduce the dynamic nutrient variations observed by cells in a large-scale production reactor (Ho et al., 2019). We find the contactless cultivation systems most interesting for the study of adaptation to nutrient limited growth. In these systems cell-to-surface and cell-to-cell interactions are avoided (Fritzsche et al., 2013). However, cell-to-cell interactions may play important roles in bioreactors. Cross-scale studies have, e.g., revealed differences in growth rates of *C. glutamicum* due to density differences (Grünberger et al., 2013). 2D-chamber systems exist where cell-to-cell interactions can be examined (Burmeister et al., 2019). However, growth is restricted to two spatial dimensions in the 2D systems and gradients of nutrients and excreted metabolites can occur (Ho et al., 2019). Droplet microfluidics is another example of single-cell cultivation systems that enable high-throughput studies of adaptation. Jakiela et al. (2013) developed a micro-droplet chemostat to study bacterial growth and adaptation. However, it is hard to control the environment in the droplets (Schmitz et al., 2019). Recent examples show how microfluidic cultivation systems can be coupled to mass spectrometry (MS) for label-free analysis of extracellular proteins or metabolites (Dusny et al., 2019; Haidas et al., 2020; Schirmer et al., 2020). These setups are promising as they expand the window of molecules, which can be analyzed in microfluidic cultivation systems. However, the cultivation medium needs to satisfy the MS used for analysis

Flow cytometry**Microfluidics****Single-cell proteomics****Single-cell transcriptomics****Single-cell metabolomics****Single-cell genomics**

* The number of analysed parameters/cells are the current status. With the rapid advancement in the field we envision that it will approach the ideal number.

FIGURE 2 | Single-cell technologies are compared on a scale from not sufficient to ideal with respect to how suited they are for the study of adaptation in chemostats. The parameters used for the comparison are: the number of analyzed cells, how well the technologies emulate chemostat conditions, the number of parameters which can be analyzed, how mature the technologies are and whether the technologies can be used to study individual cells by precise spatial and temporal control. None of the technologies *fulfill* all these criteria at the moment.

(Schirmer et al., 2020). Therefore, it is hard to precisely match the bioreactor conditions in these setups.

Single-cell omics technologies covering single-cell proteomics, single-cell transcriptomic (scRNA-seq), single-cell genomics (SCG), and single-cell metabolomics are successfully applied to mammalian cells in areas such as health and disease (Baslan and Hicks, 2017; Stubbington et al., 2017). We envision a transfer of this success to microbial bioprocesses enabling the study of adaption in chemostats on all hierarchical levels by a systems biology approach (Joyce and Palsson, 2006). Methods for analysis of unicellular microorganisms lag behind mainly due to the small size of the microorganisms, the low number of molecules per cell, and their resistant cell walls (Saint et al., 2019). scRNA-seq and SCG are the most evolved methods, mainly because DNA and mRNA signals can be amplified. SCG has been used to study genomic heterogeneity in both monocultures and microbial communities by analyzing thousands of single cells (de Bourcy et al., 2014; Hosokawa et al., 2017; Lan et al., 2017). Recent promising studies have applied scRNA-seq for investigation of microbes (Gasch et al., 2017; Kuchina et al., 2019; Saint et al., 2019; Geoghegan et al., 2020; Jackson et al., 2020; Jariani et al., 2020). The newest technologies identified more than half of the transcriptome of yeast per cell for 285 individuals (Nadal-Ribelles et al., 2019). Methods for label-free, single-cell analysis of proteins, and metabolites from microbes are limited. Single-cell MS has been used to measure in the region of 25 intracellular metabolites from up to a thousand single cells from microbial cultures (Ibanez et al., 2013; Walker et al., 2013; Krismer et al., 2017; Li Z. et al., 2020). To our knowledge, only few methods for unlabeled single-cell proteomics of microorganisms exist in literature. Armbrrecht et al. (2019) published a single-cell proteomics method for mammalian cells and claimed that it also works for microbes. Sensitivity for detection, technical noise and the wide range of expression levels have been highlighted as main challenges for MS techniques (Zhang and Vertes, 2018). To speed up the progress toward suitable single-cell omics methods one could focus the development on more efficient sample preparation methods, e.g., based on microfluidics or droplets that lead to less loss of material due to adsorption to plastic etc. (Dou et al., 2019). Moreover, to increase the coverage of the methods, we see computational approaches, which impute missing data, as important tools (Li and Li, 2018; Peng et al., 2019).

The ideal technology for the study of single-cell adaptation in chemostats should be high-throughput with respect to the number of phenotypic parameters that can be analyzed and in terms of the number of cells investigated in order to be statistically significant for the high cell density cultures applied in industry. Moreover, the cells should be analyzed in an environment, which emulates chemostat conditions and the analysis should not interfere with the studied mechanisms. Ideally, the technology should enable a spatiotemporal resolution of individual cells. None of the technologies described in this perspective article fulfill all these criteria (Figure 2), but together they can be used to reveal the underlying mechanisms thus enabling control of adaptation in chemostats, e.g., by bioprocess control strategies or metabolic engineering. Flow cytometry is well established, high-throughput in terms of the number of

cells analyzed and has already proven its worth for the study of chemostats (Hewitt et al., 1998; Sassi et al., 2019). The online versions can be coupled directly to bioreactors making it possible to perform the analysis in a relevant environment. Microfluidic cultivation systems are the only technology, which enables the study of individual cells by precise spatial and temporal control. However, the systems have to emulate bioprocess conditions. The number of available biosensors and reporter strains are rapidly increasing. Recently, a biosensor for the measure of glycolytic flux in yeast was developed (Monteiro et al., 2019). Combined with flow cytometry and/or microfluidics, the increase in reporter strains and biomarkers will enable the study of new phenomena and mechanisms on the single-cell level. Technologies, which rely on fluorescent readouts, are restricted by the number of dyes, which can be applied simultaneously. Moreover, genetic modifications of host strains for incorporation of biosensors can be work intensive and might interfere with the metabolism of the host. Due to the cost of large-scale production reactors, potential GMP and safety regulations, we find it hard to imagine that reporter strains can be used to investigate adaptation in actual production scale. Single-cell metabolomics and proteomics are still not suitable for the analysis of microbial bioprocesses. SCG technologies are more matured but will only reveal mutational mechanisms. scRNA-seq has advanced rapidly but can be costly and labor intensive (Nadal-Ribelles et al., 2019), which may explain the limited application in microbial bioprocesses. Further development of the technologies are therefore needed. Adaptation in chemostats affects both the genome, transcriptome, metabolome, and proteome (Dunham et al., 2002; Kazemi Seresht et al., 2013; Wright et al., 2020). We envision the application of single-cell omics for the holistic study of the adaptive mechanisms, as the omics technologies have the potential to measure large amounts of parameters at all regulatory levels. Therefore, if the rapid advancements of the technologies continue, single-cell omics can become important supplements to flow cytometry and microfluidic cultivation systems.

DATA AVAILABILITY STATEMENT

The original contributions presented in the study are included in the article/supplementary material, further inquiries can be directed to the corresponding author.

AUTHOR CONTRIBUTIONS

NW and NS conceived the idea for the article. NW reviewed the literature and wrote the manuscript. NS and NR critically commented on the manuscript and contributed their perspectives. All authors contributed to the article and approved the submitted version.

FUNDING

This work received funding from Innovation Fund Denmark and the Novo Nordisk R&D STAR Fellowship Programme.

REFERENCES

- Acar, M., Mettetal, J. T., and van Oudenaarden, A. (2008). Stochastic switching as a survival strategy in fluctuating environments. *Nat. Genet.* 40, 471–475. doi: 10.1038/ng.110
- Achilles, J., Stahl, F., Harms, H., and Müller, S. (2007). Isolation of intact RNA from cytometrically sorted *Saccharomyces cerevisiae* for the analysis of intrapopulation diversity of gene expression. *Nat. Protoc.* 2, 2203–2211. doi: 10.1038/nprot.2007.322
- Ackermann, M. (2015). A functional perspective on phenotypic heterogeneity in microorganisms. *Nat. Rev. Microbiol.* 13, 497–508. doi: 10.1038/nrmicro3491
- Adams, J., Paquin, C., Oeller, P. W., and Lee, L. W. (1985). Physiological characterization of adaptive clones in evolving populations of the yeast, *Saccharomyces cerevisiae*. *Genetics* 110, 173–185.
- Armbrrecht, L., Müller, R. S., Nikoloff, J., and Dittrich, P. S. (2019). Single-cell protein profiling in microchambers with barcoded beads. *Microsyst. Nanoeng.* 5:55. doi: 10.1038/s41378-019-0099-5
- Baslan, T., and Hicks, J. (2017). Unravelling biology and shifting paradigms in cancer with single-cell sequencing. *Nat. Rev. Cancer* 17, 557–569. doi: 10.1038/nrc.2017.58
- Blake, W. J., Kærn, M., Cantor, C. R., and Collins, J. J. (2003). Noise in eukaryotic gene expression. *Nature* 422, 633–637. doi: 10.1038/nature01546
- Brognaux, A., Francis, F., Twizere, J. C., Thonart, P., and Delvigne, F. (2014). Scale-down effect on the extracellular proteome of *Escherichia coli*: correlation with membrane permeability and modulation according to substrate heterogeneities. *Bioprocess. Biosyst. Eng.* 37, 1469–1485. doi: 10.1007/s00449-013-1119-8
- Brown, C. J., Todd, K. M., and Rosenzweig, R. F. (1998). Multiple duplications of yeast hexose transport genes in response to selection in a glucose-limited environment. *Mol. Biol. Evol.* 15, 931–942. doi: 10.1093/oxfordjournals.molbev.a026009
- Brown, C. M., and Hough, J. S. (1965). Elongation of yeast cells in continuous culture. *Nature* 206, 676–678. doi: 10.1038/206676a0
- Burmeister, A., Hilgers, F., Langner, A., Westerwalbesloh, C., Kerkhoff, Y., Tenhaef, N., et al. (2019). A microfluidic co-cultivation platform to investigate microbial interactions at defined microenvironments. *Lab Chip* 19, 98–110. doi: 10.1039/C8LC00977E
- Bylund, F., Castan, A., Mikkola, R., Veide, A., and Larsson, G. (2000). Influence of scale-up on the quality of recombinant human growth hormone. *Biotechnol. Bioeng.* 69, 119–128. doi: 10.1002/(SICI)1097-0290(20000720)69:2<119::AID-BIT1>3.0.CO;2-9
- Bylund, F., Collet, E., Enfors, S.-O., and Larsson, G. (1998). Substrate gradient formation in the large-scale bioreactor lowers cell yield and increases by-product formation. *Bioprocess Eng.* 18, 171–180. doi: 10.1007/s004490050427
- Bylund, F., Guillard, F., Enfors, S.-O., Trägårdh, C., and Larsson, G. (1999). Scale down of recombinant protein production: a comparative study of scaling performance. *Bioprocess Eng.* 20, 377–389. doi: 10.1007/s004490050606
- Campbell, K., Vowinkel, J., and Ralser, M. (2016). Cell-to-cell heterogeneity emerges as consequence of metabolic cooperation in a synthetic yeast community. *Biotechnol. J.* 11, 1169–1178. doi: 10.1002/biot.201500301
- Carlquist, M., Fernandes, R. L., Helmark, S., Heins, A.-L., Lundin, L., Sørensen, S. J., et al. (2012). Physiological heterogeneities in microbial populations and implications for physical stress tolerance. *Microb. Cell Fact.* 11:94. doi: 10.1186/1475-2859-11-94
- Davis, K. M., and Isberg, R. R. (2016). Defining heterogeneity within bacterial populations via single cell approaches. *Bioessays* 38, 782–790. doi: 10.1002/bies.201500121
- de Bourcy, C. F. A., De Vlaminck, I., Kanbar, J. N., Wang, J., Gawad, C., and Quake, S. R. (2014). A quantitative comparison of single-cell whole genome amplification methods. *PLoS One* 9:e105585. doi: 10.1371/journal.pone.0105585
- Delvigne, F., Baert, J., Gofflot, S., Lejeune, A., Telek, S., Johanson, T., et al. (2015). Dynamic single-cell analysis of *Saccharomyces cerevisiae* under process perturbation: comparison of different methods for monitoring the intensity of population heterogeneity. *J. Chem. Technol. Biotechnol.* 90, 314–323. doi: 10.1002/jctb.4430
- Dou, M., Clair, G., Tsai, C.-F., Xu, K., Chrisler, W. B., Sontag, R. L., et al. (2019). High-throughput single cell proteomics enabled by multiplex isobaric labeling in a nanodroplet sample preparation platform. *Anal. Chem.* 91, 13119–13127. doi: 10.1021/acs.analchem.9b03349
- Douma, R. D., Batista, J. M., Touw, K. M., Kiel, J. A. K. W., Krikken, A. M., Zhao, Z., et al. (2011). Degeneration of penicillin production in ethanol-limited chemostat cultivations of *Penicillium chrysogenum*: a systems biology approach. *BMC Syst. Biol.* 5:132. doi: 10.1186/1752-0509-5-132
- Dunham, M. J., Badrane, H., Ferea, T., Adams, J., Brown, P. O., Rosenzweig, F., et al. (2002). Characteristic genome rearrangements in experimental evolution of *Saccharomyces cerevisiae*. *Proc. Natl. Acad. Sci. U.S.A.* 99, 16144–16149. doi: 10.1073/pnas.242624799
- Dusny, C., and Schmid, A. (2015). Microfluidic single-cell analysis links boundary environments and individual microbial phenotypes. *Environ. Microbiol.* 17, 1839–1856. doi: 10.1111/1462-2920.12667
- Dusny, C., Lohse, M., Reemtsma, T., Schmid, A., and Lechtenfeld, O. J. (2019). Quantifying a biocatalytic product from a few living microbial cells using microfluidic cultivation coupled to FT-ICR-MS. *Anal. Chem.* 91, 7012–7018. doi: 10.1021/acs.analchem.9b00978
- Elowitz, M. B., and Leibler, S. (2000). A synthetic oscillatory network of transcriptional regulators. *Nature* 403, 335–338. doi: 10.1038/35002125
- Elowitz, M. B., Levine, A. J., Siggia, E. D., and Swain, P. S. (2002). Stochastic gene expression in a single cell. *Science (New York, N. Y.)* 297, 1183–1186. doi: 10.1126/science.1070919
- Enfors, S. O., Jahic, M., Rozkov, A., Xu, B., Hecker, M., Jürgen, B., et al. (2001). Physiological responses to mixing in large scale bioreactors. *J. Biotechnol.* 85, 175–185. doi: 10.1016/S0168-1656(00)00365-5
- Farid, S. S. (2019). Integrated continuous biomanufacturing: industrialization on the horizon. *Biotechnol. J.* 14:e1800722. doi: 10.1002/biot.201800722
- Ferea, T. L., Botstein, D., Brown, P. O., and Rosenzweig, R. F. (1999). Systematic changes in gene expression patterns following adaptive evolution in yeast. *Proc. Natl. Acad. Sci. U.S.A.* 96, 9721–9726. doi: 10.1073/pnas.96.17.9721
- Franchini, A. G., and Egli, T. (2006). Global gene expression in *Escherichia coli* K-12 during short-term and long-term adaptation to glucose-limited continuous culture conditions. *Microbiology* 152, 2111–2127. doi: 10.1099/mic.0.28939-0
- Fritsch, F. S. O., Rosenthal, K., Kampert, A., Howitz, S., Dusny, C., Blank, L. M., et al. (2013). Picoliter NDEP traps enable time-resolved contactless single bacterial cell analysis in controlled microenvironments. *Lab Chip* 13, 397–408. doi: 10.1039/C2LC41092C
- Gasch, A. P., Yu, F. B., Hose, J., Escalante, L. E., Place, M., Bacher, R., et al. (2017). Single-cell RNA sequencing reveals intrinsic and extrinsic regulatory heterogeneity in yeast responding to stress. *PLoS Biol.* 15:e2004050. doi: 10.1371/journal.pbio.2004050
- Geoghegan, I. A., Emes, R. D., Archer, D. B., and Avery, S. V. (2020). Method for RNA extraction and transcriptomic analysis of single fungal spores. *MethodsX* 7:100760. doi: 10.1016/j.mex.2019.12.002
- George, S., Larsson, G., and Enfors, S. O. (1993). A scale-down two-compartment reactor with controlled substrate oscillations: metabolic response of *Saccharomyces cerevisiae*. *Bioprocess Eng.* 9, 249–257.
- George, S., Larsson, G., Olsson, K., and Enfors, S. O. (1998). Comparison of the Baker's yeast process performance in laboratory and production scale. *Bioprocess Eng.* 18, 135–142. doi: 10.1007/PL00008979
- Gimeno, C. J., Ljungdahl, P. O., Styles, C. A., and Fink, G. R. (1992). Unipolar cell divisions in the yeast *S. cerevisiae* lead to filamentous growth: regulation by starvation and RAS. *Cell* 68, 1077–1090. doi: 10.1016/0092-8674(92)90079-R
- Gresham, D., and Hong, J. (2015). The functional basis of adaptive evolution in chemostats. *FEMS Microbiol. Rev.* 39, 2–16. doi: 10.1111/1574-6976.12082
- Grünberger, A., Probst, C., Helfrich, S., Nanda, A., Stute, B., Wiechert, W., et al. (2015). Spatiotemporal microbial single-cell analysis using a high-throughput microfluidics cultivation platform. *Cytometry A* 87, 1101–1115. doi: 10.1002/cyto.a.22779
- Grünberger, A., van Ooyen, J., Paczia, N., Rohe, P., Schiendzielorz, G., Eggeling, L., et al. (2013). Beyond growth rate 0.6: *Corynebacterium glutamicum* cultivated in highly diluted environments. *Biotechnol. Bioeng.* 110, 220–228. doi: 10.1002/bit.24616
- Haidas, D., Napiorkowska, M., Schmitt, S., and Dittrich, P. S. (2020). Parallel sampling of nanoliter droplet arrays for noninvasive protein analysis in discrete yeast cultivations by MALDI-MS. *Anal. Chem.* 92, 3810–3818. doi: 10.1021/acs.analchem.9b05235

- Han, S., Delvigne, F., Brognaux, A., Charbon, G. E., and Sørensen, S. J. (2013). Design of growth-dependent biosensors based on destabilized GFP for the detection of physiological behavior of *Escherichia coli* in heterogeneous bioreactors. *Biotechnol. Progress* 29, 553–563. doi: 10.1002/btpr.1694
- Heins, A.-L., Johanson, T., Han, S., Lundin, L., Carlquist, M., Gernaey, K. V., et al. (2019). Quantitative flow cytometry to understand population heterogeneity in response to changes in substrate availability in *Escherichia coli* and *Saccharomyces cerevisiae* chemostats. *Front. Bioeng. Biotechnol.* 7:187. doi: 10.3389/fbioe.2019.00187
- Hewitt, C. J., Boon, L. A., McFarlane, C. M., and Nienow, A. W. (1998). The use of flow cytometry to study the impact of fluid mechanical stress on *Escherichia coli* W3110 during continuous cultivation in an agitated bioreactor. *Biotechnol. Bioeng.* 59, 612–620. doi: 10.1002/(SICI)1097-0290(19980905)59:5<612::AID-BIT12>3.0.CO;2-B
- Hewitt, C. J., Nebe-Von Caron, G., Axelsson, B., McFarlane, C. M., and Nienow, A. W. (2000). Studies related to the scale-up of high-cell-density *E. coli* fed-batch fermentations using multiparameter flow cytometry: effect of a changing microenvironment with respect to glucose and dissolved oxygen concentration. *Biotechnol. Bioeng.* 70, 381–390. doi: 10.1002/1097-0290(20001120)70:4<381::AID-BIT3>3.0.CO;2-0
- Hewitt, C. J., Nebe-von Caron, G., Nienow, A. W., and McFarlane, C. M. (1999). The use of multi-parameter flow cytometry to compare the physiological response of *Escherichia coli* W3110 to glucose limitation during batch, fed-batch and continuous culture cultivations. *J. Biotechnol.* 75, 251–264. doi: 10.1016/S0168-1656(99)00168-6
- Hewitt, C. J., Onyeaka, H., Lewis, G., Taylor, I. W., and Nienow, A. W. (2007). A comparison of high cell density fed-batch fermentations involving both induced and non-induced recombinant *Escherichia coli* under well-mixed small-scale and simulated poorly mixed large-scale conditions. *Biotechnol. Bioeng.* 96, 495–505. doi: 10.1002/bit.21127
- Ho, P., Westerwalbesloh, C., Kaganovitch, E., Grünberger, A., Neubauer, P., Kohlheyer, D., et al. (2019). Reproduction of large-scale bioreactor conditions on microfluidic chips. *Microorganisms* 7:105. doi: 10.3390/microorganisms7040105
- Hope, E. A., Amorosi, C. J., Miller, A. W., Dang, K., Heil, C. S., and Dunham, M. J. (2017). Experimental evolution reveals favored adaptive routes to cell aggregation in yeast. *Genetics* 206, 1153–1167. doi: 10.1534/genetics.116.198895
- Hosokawa, M., Nishikawa, Y., Kogawa, M., and Takeyama, H. (2017). Massively parallel whole genome amplification for single-cell sequencing using droplet microfluidics. *Sci. Rep.* 7:5199. doi: 10.1038/s41598-017-05436-4
- Ibanez, A. J., Fagerer, S. R., Schmidt, A. M., Urban, P. L., Jefimovs, K., Geiger, P., et al. (2013). Mass spectrometry-based metabolomics of single yeast cells. *Proc. Natl. Acad. Sci. U.S.A.* 110, 8790–8794. doi: 10.1073/pnas.1209302110
- Jackson, C. A., Castro, D. M., Saldi, G.-A., Bonneau, R., and Gresham, D. (2020). Gene regulatory network reconstruction using single-cell RNA sequencing of barcoded genotypes in diverse environments. *Elife* 9:e51254. doi: 10.7554/eLife.51254
- Jahn, M., Seifert, J., von Bergen, M., Schmid, A., Bühler, B., and Müller, S. (2013). Subpopulation-proteomics in prokaryotic populations. *Curr. Opin. Biotechnol.* 24, 79–87. doi: 10.1016/j.copbio.2012.10.017
- Jakiela, S., Kaminski, T. S., Cybulski, O., Weibel, D. B., and Garstecki, P. (2013). Bacterial growth and adaptation in microdroplet chemostats. *Angew. Chem. Int. Ed. Engl.* 52, 8908–8911. doi: 10.1002/anie.201301524
- Jansen, M. L. A., Daran-Lapujade, P., de Winde, J. H., Piper, M. D. W., and Pronk, J. T. (2004). Prolonged maltose-limited cultivation of *Saccharomyces cerevisiae* selects for cells with improved maltose affinity and hypersensitivity. *Appl. Environ. Microbiol.* 70, 1956–1963. doi: 10.1128/AEM.70.4.1956-1963.2004
- Jansen, M. L. A., Diderich, J. A., Mashego, M., Hassane, A., de Winde, J. H., Daran-Lapujade, P., et al. (2005). Prolonged selection in aerobic, glucose-limited chemostat cultures of *Saccharomyces cerevisiae* causes a partial loss of glycolytic capacity. *Microbiology (Reading, England)* 151(Pt 5), 1657–1669. doi: 10.1099/mic.0.27577-0
- Jariani, A., Vermeersch, L., Cerulus, B., Perez-Samper, G., Voordeckers, K., Van Brussel, T., et al. (2020). A new protocol for single-cell RNA-seq reveals stochastic gene expression during lag phase in budding yeast. *Elife* 9:e55320. doi: 10.7554/eLife.55320
- Jehmlich, N., Hübschmann, T., Gesell Salazar, M., Völker, U., Benndorf, D., Müller, S., et al. (2010). Advanced tool for characterization of microbial cultures by combining cytomics and proteomics. *Appl. Microbiol. Biotechnol.* 88, 575–584. doi: 10.1007/s00253-010-2753-6
- Joyce, A. R., and Palsson, B. Ø (2006). The model organism as a system: integrating “omics” data sets. *Nat. Rev. Mol. Cell Biol.* 7, 198–210. doi: 10.1038/nrm1857
- Kazemi Seresht, A., Cruz, A. L., de Hulster, E., Hebly, M., Palmqvist, E. A., van Gulik, W., et al. (2013). Long-term adaptation of *Saccharomyces cerevisiae* to the burden of recombinant insulin production. *Biotechnol. Bioeng.* 110, 2749–2763. doi: 10.1002/bit.24927
- Kopf, S. H., McGlynn, S. E., Green-Saxena, A., Guan, Y., Newman, D. K., and Orphan, V. J. (2015). Heavy water and 15 N labelling with NanoSIMS analysis reveals growth rate-dependent metabolic heterogeneity in chemostats. *Environ. Microbiol.* 17, 2542–2556. doi: 10.1111/1462-2920.12752
- Kortmann, H., Chasanis, P., Blank, L. M., Franke, J., Kenig, E. Y., and Schmid, A. (2009). The envirostat – a new bioreactor concept. *Lab Chip* 9, 576–585. doi: 10.1039/B809150A
- Krismer, J., Tamminen, M., Fontana, S., Zenobi, R., and Narwani, A. (2017). Single-cell mass spectrometry reveals the importance of genetic diversity and plasticity for phenotypic variation in nitrogen-limited *Chlamydomonas*. *ISME J.* 11, 988–998. doi: 10.1038/ismej.2016.167
- Kuchina, A., Brettner, L. M., Paleologu, L., Roco, C. M., Rosenberg, A. B., Carignano, A., et al. (2019). Microbial single-cell RNA sequencing by split-pool barcoding. *bioRxiv* Available online at: <https://doi.org/10.1101/869248> (accessed November 17, 2020).
- Kundu, K., Weber, N., Griebler, C., and Elsner, M. (2020). Phenotypic heterogeneity as key factor for growth and survival under oligotrophic conditions. *Environ. Microbiol.* 22, 3339–3356. doi: 10.1111/1462-2920.15106
- Kussell, E., and Leibler, S. (2005). Phenotypic diversity, population growth, and information in fluctuating environments. *Science (New York, N. Y.)* 309, 2075–2078. doi: 10.1126/science.1114383
- Kvitek, D. J., and Sherlock, G. (2013). Whole genome, whole population sequencing reveals that loss of signaling networks is the major adaptive strategy in a constant environment. *PLoS Genet.* 9:e1003972. doi: 10.1371/journal.pgen.1003972
- Lan, F., Demaree, B., Ahmed, N., and Abate, A. R. (2017). Single-cell genome sequencing at ultra-high-throughput with microfluidic droplet barcoding. *Nat. Biotechnol.* 35, 640–646. doi: 10.1038/nbt.3880
- Lara, A. R., Leal, L., Flores, N., Gosset, G., Bolivar, F., and Ramirez, O. T. (2006). Transcriptional and metabolic response of recombinant *Escherichia coli* to spatial dissolved oxygen tension gradients simulated in a scale-down system. *Biotechnol. Bioeng.* 93, 372–385. doi: 10.1002/bit.20704
- Larsson, G., and Enfors, S. O. (1988). Studies of insufficient mixing in bioreactors: effects of limiting oxygen concentrations and short term oxygen starvation on *Penicillium chrysogenum*. *Bioprocess Eng.* 3, 123–127. doi: 10.1007/BF00373475
- Li, W. V., and Li, J. J. (2018). An accurate and robust imputation method scImpute for single-cell RNA-seq data. *Nat. Commun.* 9:997. doi: 10.1038/s41467-018-03405-7
- Li, Y., Jiang, Y., Paxman, J., O’Laughlin, R., Klepin, S., Zhu, Y., et al. (2020). A programmable fate decision landscape underlies single-cell aging in yeast. *Science (New York, N. Y.)* 369, 325–329. doi: 10.1126/science.aax9552
- Li, Z., Wang, Z., Pan, J., Ma, X., Zhang, W., and Ouyang, Z. (2020). Single-cell mass spectrometry analysis of metabolites facilitated by cell electro-migration and electroporation. *Anal. Chem.* 92, 10138–10144. doi: 10.1021/acs.analchem.0c02147
- Lieder, S., Jahn, M., Seifert, J., von Bergen, M., Müller, S., and Takors, R. (2014). Subpopulation-proteomics reveal growth rate, but not cell cycling, as a major impact on protein composition in *Pseudomonas putida* KT2440. *AMB Express* 4:71. doi: 10.1186/s13568-014-0071-6
- Lin, H. Y., and Neubauer, P. (2000). Influence of controlled glucose oscillations on a fed-batch process of recombinant *Escherichia coli*. *J. Biotechnol.* 79, 27–37. doi: 10.1016/S0168-1656(00)00217-0
- Lindemann, D., Westerwalbesloh, C., Kohlheyer, D., Grünberger, A., and von Lieres, E. (2019). Microbial single-cell growth response at defined carbon limiting conditions. *RSC Adv.* 9, 14040–14050. doi: 10.1039/C9RA02454A

- Long, Z., Nugent, E., Javer, A., Cicuta, P., Sclavi, B., Cosentino Lagomarsino, M., et al. (2013). Microfluidic chemostat for measuring single cell dynamics in bacteria. *Lab Chip* 13, 947–954. doi: 10.1039/c2lc41196b
- Mashego, M. R., Jansen, M. L. A., Vinke, J. L., van Gulik, W. M., and Heijnen, J. J. (2005). Changes in the metabolome of *Saccharomyces cerevisiae* associated with evolution in aerobic glucose-limited chemostats. *FEMS Yeast Res.* 5, 419–430. doi: 10.1016/j.femsyr.2004.11.008
- Monod, J. (1950). Technique, theory and applications of continuous culture. *Ann. Inst. Pasteur* 79, 390–410.
- Monteiro, F., Hubmann, G., Norder, J., Hekelaar, J., Saldida, J., Litsios, A., et al. (2019). Measuring glycolytic flux in single yeast cells with an orthogonal synthetic biosensor. *bioRxiv* 15:e9071. doi: 10.1101/682302
- Nadal-Ribelles, M., Islam, S., Wei, W., Latorre, P., Nguyen, M., de Nadal, E., et al. (2019). Sensitive high-throughput single-cell RNA-seq reveals within-clonal transcript correlations in yeast populations. *Nature Microbiology* 4, 683–692. doi: 10.1038/s41564-018-0346-9
- Neubauer, P., Haggstrom, L., and Enfors, S. O. (1995). Influence of substrate oscillations on acetate formation and growth yield in *Escherichia coli* glucose limited fed-batch cultivations. *Biotechnol. Bioeng.* 47, 139–146. doi: 10.1002/bit.260470204
- Nikolic, N., Schreiber, F., Dal Co, A., Kiviet, D. J., Bergmiller, T., Littmann, S., et al. (2017). Cell-to-cell variation and specialization in sugar metabolism in clonal bacterial populations. *PLoS Genet.* 13:e1007122. doi: 10.1371/journal.pgen.1007122
- Novick, A., and Szilard, L. (1950). Description of the chemostat. *Science (New York, N. Y.)* 112, 715–716. doi: 10.1126/science.112.2920.715
- Oosterhuis, N. M., and Kossen, N. W. (1984). Dissolved oxygen concentration profiles in a production-scale bioreactor. *Biotechnol. Bioeng.* 26, 546–550. doi: 10.1002/bit.260260522
- Paulová, L., Hyka, P., Branská, B., Melzoch, K., and Kovar, K. (2012). Use of a mixture of glucose and methanol as substrates for the production of recombinant trypsinogen in continuous cultures with *Pichia pastoris* Mut+. *J. Biotechnol.* 157, 180–188. doi: 10.1016/j.jbiotec.2011.10.010
- Peebo, K., and Neubauer, P. (2018). Application of continuous culture methods to recombinant protein production in microorganisms. *Microorganisms* 6:56. doi: 10.3390/microorganisms6030056
- Peng, T., Zhu, Q., Yin, P., and Tan, K. (2019). SCRABBLE: single-cell RNA-seq imputation constrained by bulk RNA-seq data. *Genome Biol.* 20:88. doi: 10.1186/s13059-019-1681-8
- Rai, N., Huynh, L., Kim, M., and Tagkopoulos, I. (2019). Population collapse and adaptive rescue during long-term chemostat fermentation. *Biotechnol. Bioeng.* 116, 693–703. doi: 10.1002/bit.26898
- Rebner, C., Graf, A. B., Valli, M., Steiger, M. G., Gasser, B., Maurer, M., et al. (2014). In *Pichia pastoris*, growth rate regulates protein synthesis and secretion, mating and stress response. *Biotechnol. J.* 9, 511–525. doi: 10.1002/biot.201300334
- Reuven, P., and Eldar, A. (2011). Macromotives and microbehaviors: the social dimension of bacterial phenotypic variability. *Curr. Opin. Genet. Dev.* 21, 759–767. doi: 10.1016/j.gde.2011.09.011
- Robin, J., Lettier, G., McIntyre, M., Noorman, H., and Nielsen, J. (2003). Continuous cultivations of a *Penicillium Chrysogenum* strain expressing the expandase gene from *Streptomyces clavuligerus*: growth yields and morphological characterization. *Biotechnol. Bioeng.* 83, 361–368. doi: 10.1002/bit.10677
- Ryall, B., Eydallin, G., and Ferenci, T. (2012). Culture history and population heterogeneity as determinants of bacterial adaptation: the adaptomics of a single environmental transition. *Microbiol. Mol. Biol. Rev.* 76, 597–625. doi: 10.1128/MMBR.05028-11
- Saint, M., Bertaux, F., Tang, W., Sun, X.-M., Game, L., Köferle, A., et al. (2019). Single-cell imaging and RNA sequencing reveal patterns of gene expression heterogeneity during fission yeast growth and adaptation. *Nat. Microbiol.* 4, 480–491. doi: 10.1038/s41564-018-0330-4
- Sandoval-Basurto, E. A., Gosset, G., Bolivar, F., and Ramirez, O. T. (2005). Culture of *Escherichia coli* under dissolved oxygen gradients simulated in a two-compartment scale-down system: metabolic response and production of recombinant protein. *Biotechnol. Bioeng.* 89, 453–463. doi: 10.1002/bit.20383
- Sassi, H., Nguyen, T. M., Telek, S., Gosset, G., Grünberger, A., and Delvigne, F. (2019). Segregostat: a novel concept to control phenotypic diversification dynamics on the example of gram-negative bacteria. *Microb. Biotechnol.* 12, 1064–1075. doi: 10.1111/1751-7915.13442
- Schirmer, M., Wink, K., Ohla, S., Belder, D., Schmid, A., and Dusny, C. (2020). Conversion efficiencies of a few living microbial cells detected at a high throughput by droplet-based ESI-MS. *Anal. Chem.* 92, 10700–10708. doi: 10.1021/acs.analchem.0c01839
- Schmitz, J., Noll, T., and Grünberger, A. (2019). Heterogeneity studies of mammalian cells for bioproduction: from tools to application. *Trends Biotechnol.* 37, 645–660. doi: 10.1016/j.tibtech.2018.11.007
- Schreiber, F., Littmann, S., Lavik, G., Escrig, S., Meibom, A., Kuypers, M. M. M., et al. (2016). Phenotypic heterogeneity driven by nutrient limitation promotes growth in fluctuating environments. *Nat. Microbiol.* 1:16055. doi: 10.1038/nmicrobiol.2016.55
- Schweder, T., Krüger, E., Xu, B., Jürgen, B., Blomsten, G., Enfors, S. O., et al. (1999). Monitoring of genes that respond to process-related stress in large-scale bioprocesses. *Biotechnol. Bioeng.* 65, 151–159. doi: 10.1002/(SICI)1097-0290(19991020)65:2<151::AID-BIT4>3.0.CO;2-V
- Stubbington, M. J. T., Rozenblatt-Rosen, O., Regev, A., and Teichmann, S. A. (2017). Single-cell transcriptomics to explore the immune system in health and disease. *Science (New York, N. Y.)* 358, 58–63. doi: 10.1126/science.aan6828
- Thattai, M., and van Oudenaarden, A. (2004). Stochastic gene expression in fluctuating environments. *Genetics* 167, 523–530. doi: 10.1534/genetics.167.1.523
- Ullman, G., Wallden, M., Marklund, E. G., Mahmutovic, A., Razinkov, I., and Elf, J. (2013). High-throughput gene expression analysis at the level of single proteins using a microfluidic turbidostat and automated cell tracking. *Philos. Trans. R. Soc. Lond. B Biol. Sci.* 368:20120025. doi: 10.1098/rstb.2012.0025
- Vees, C. A., Veiter, L., Sax, F., Herwig, C., and Pflügl, S. (2020). A robust flow cytometry-based biomass monitoring tool enables rapid at-line characterization of *S. cerevisiae* physiology during continuous bioprocessing of spent sulfite liquor. *Anal. Bioanal. Chem.* 412, 2137–2149. doi: 10.1007/s00216-020-02423-z
- Walker, B. N., Antonakos, C., Retterer, S. T., and Vertes, A. (2013). Metabolic differences in microbial cell populations revealed by nanophotonic ionization. *Angew. Chem. Int. Ed. Engl.* 52, 3650–3653. doi: 10.1002/anie.201207348
- Wang, G., Wu, B., Zhao, J., Haringa, C., Xia, J., Chu, J., et al. (2018). Power input effects on degeneration in prolonged penicillin chemostat cultures: a systems analysis at flux, residual glucose, metabolite, and transcript levels. *Biotechnol. Bioeng.* 115, 114–125. doi: 10.1002/bit.26447
- Wang, P., Robert, L., Pelletier, J., Dang, W. L., Taddei, F., Wright, A., et al. (2010). Robust growth of *Escherichia coli*. *Curr. Biol.* 20, 1099–1103. doi: 10.1016/j.cub.2010.04.045
- Weibel, D. B., Diluzio, W. R., and Whitesides, G. M. (2007). Microfabrication meets microbiology. *Nat. Rev. Microbiol.* 5, 209–218. doi: 10.1038/nrmicro1616
- Wenger, J. W., Piotrowski, J., Nagarajan, S., Chiotti, K., Sherlock, G., and Rosenzweig, F. (2011). Hunger artists: yeast adapted to carbon limitation show trade-offs under carbon sufficiency. *PLoS Genet.* 7:e1002202. doi: 10.1371/journal.pgen.1002202
- Wick, L. M., Quadroni, M., and Egli, T. (2001). Short- and long-term changes in proteome composition and kinetic properties in a culture of *Escherichia coli* during transition from glucose-excess to glucose-limited growth conditions in continuous culture and vice versa. *Environ. Microbiol.* 3, 588–599. doi: 10.1046/j.1462-2920.2001.00231.x
- Wright, N. R., Rønne, N. P., and Thykaer, J. (2016). Scale-down of continuous protein producing *Saccharomyces cerevisiae* cultivations using a two-compartment system. *Biotechnol. Prog.* 32, 152–159. doi: 10.1002/btpr.2184
- Wright, N. R., Wulff, T., Palmqvist, E. A., Jørgensen, T. R., Workman, C. T., Sonnenschein, N., et al. (2020). Fluctuations in glucose availability prevent global proteome changes and physiological transition during prolonged chemostat cultivations of *Saccharomyces cerevisiae*. *Biotechnol. Bioeng.* 117, 2074–2088. doi: 10.1002/bit.27353
- Wu, L., Mashego, M., Proell, A., Vinke, J., Ras, C., Vandam, J., et al. (2006). In vivo kinetics of primary metabolism in *Saccharomyces cerevisiae* studied

- through prolonged chemostat cultivation. *Metab. Eng.* 8, 160–171. doi: 10.1016/j.ymben.2005.09.005
- Zhang, L., and Vertes, A. (2018). Single-cell mass spectrometry approaches to explore cellular heterogeneity. *Angew. Chem. Int. Ed. Engl.* 57, 4466–4477. doi: 10.1002/anie.201709719
- Zydney, A. L. (2016). Continuous downstream processing for high value biological products: a review. *Biotechnol. Bioeng.* 113, 465–475. doi: 10.1002/bit.25695

Conflict of Interest: NW and NR were employed by the company Novo Nordisk A/S.

The remaining author declares that the research was conducted in the absence of any commercial or financial relationships that could be construed as a potential conflict of interest.

Copyright © 2020 Wright, Rønne and Sonnenschein. This is an open-access article distributed under the terms of the Creative Commons Attribution License (CC BY). The use, distribution or reproduction in other forums is permitted, provided the original author(s) and the copyright owner(s) are credited and that the original publication in this journal is cited, in accordance with accepted academic practice. No use, distribution or reproduction is permitted which does not comply with these terms.



Selective Release of Recombinant Periplasmic Protein From *E. coli* Using Continuous Pulsed Electric Field Treatment

Felix Schottroff^{1,2†}, Jens Kastenhofer^{3†}, Oliver Spadiut³, Henry Jaeger¹ and David J. Wurm^{3*}

¹ Institute of Food Technology, University of Natural Resources and Life Sciences (BOKU), Vienna, Austria, ² BOKU Core Facility Food & Bio Processing, Vienna, Austria, ³ Research Division Biochemical Engineering, Integrated Bioprocess Development, Institute of Chemical, Environmental and Bioscience Engineering, TU Wien, Vienna, Austria

OPEN ACCESS

Edited by:

Peter Neubauer,
Technical University of Berlin,
Germany

Reviewed by:

Pau Loke Show,
University of Nottingham Malaysia
Campus, Malaysia
Stefan Junne,
Technical University of Berlin,
Germany
Ralf Takors,
University of Stuttgart, Germany

*Correspondence:

David J. Wurm
david.wurm@tuwien.ac.at

[†] These authors have contributed
equally to this work

Specialty section:

This article was submitted to
Bioprocess Engineering,
a section of the journal
Frontiers in Bioengineering and
Biotechnology

Received: 24 July 2020

Accepted: 29 December 2020

Published: 09 February 2021

Citation:

Schottroff F, Kastenhofer J,
Spadiut O, Jaeger H and Wurm DJ
(2021) Selective Release
of Recombinant Periplasmic Protein
From *E. coli* Using Continuous Pulsed
Electric Field Treatment.
Front. Bioeng. Biotechnol. 8:586833.
doi: 10.3389/fbioe.2020.586833

To date, high-pressure homogenization is the standard method for cell disintegration before the extraction of cytosolic and periplasmic protein from *E. coli*. Its main drawback, however, is low selectivity and a resulting high load of host cell impurities. Pulsed electric field (PEF) treatment may be used for selective permeabilization of the outer membrane. PEF is a process which is able to generate pores within cell membranes, the so-called electroporation. It can be readily applied to the culture broth in continuous mode, no additional chemicals are needed, heat generation is relatively low, and it is already implemented at industrial scale in the food sector. Yet, studies about PEF-assisted extraction of recombinant protein from bacteria are scarce. In the present study, continuous electroporation was employed to selectively extract recombinant Protein A from the periplasm of *E. coli*. For this purpose, a specifically designed flow-through PEF treatment chamber was deployed, operated at 1.5 kg/h, using rectangular pulses of 3 μ s at specific energy input levels between 10.3 and 241.9 kJ/kg. Energy input was controlled by variation of the electric field strength (28.4–44.8 kV/cm) and pulse repetition frequency (50–1,000 Hz). The effects of the process parameters on cell viability, product release, and host cell protein (HCP), DNA, as well as endotoxin (ET) loads were investigated. It was found that a maximum product release of 89% was achieved with increasing energy input levels. Cell death also gradually increased, with a maximum inactivation of -0.9 log at 241.9 kJ/kg. The conditions resulting in high release efficiencies while keeping impurities low were electric field strengths ≤ 30 kV/cm and frequencies ≥ 825 Hz. In comparison with high-pressure homogenization, PEF treatment resulted in 40% less HCP load, 96% less DNA load, and 43% less ET load. Therefore, PEF treatment can be an efficient alternative to the cell disintegration processes commonly used in downstream processing.

Keywords: continuous downstream processing, electroporation, host cell impurities, outer membrane, periplasmic protein, primary recovery, pulsed electric field, selective product release

Abbreviations: *E*, electric field strength (kV/cm); ET, endotoxins; *f*, pulse repetition frequency (Hz); HCP, host cell protein; HPH, high-pressure homogenization; IM, inner membrane; M, outer membrane; PEF, pulsed electric fields; SpA IgG, binding domain of *Staphylococcus aureus* Protein A; *W*_{spec}, specific energy input (kJ/kg).

INTRODUCTION

Periplasmic expression of recombinant proteins in *E. coli* has been investigated extensively in the past decades (Zhou et al., 2018; Sandomenico et al., 2020). The oxidative environment of the periplasm favors correct folding of proteins containing disulfide bridges and generally enhances solubility and stability of the product (Sandomenico et al., 2020). Translocation through the inner membrane is achieved by adding signal sequences initiating specific transport pathways to the product. Periplasmic expression has great potential for downstream processing because only the outer membrane (OM) has to be disrupted for extraction of the product and the periplasmic space contains less impurities, such as host cell protein (HCP) or DNA (Balasundaram et al., 2009a). However, selective disintegration of the OM is still hard to realize to date. Several approaches to make the OM “leaky” and selectively release the product from the periplasm have been reported in literature and are covered in extensive reviews (Balasundaram et al., 2009a; Kleiner-Grote et al., 2018). First, strains can be made leaky *in situ* on a genetic level for product release in the upstream process, for example, by knock-out of genes encoding structural cell envelope components and membrane proteins (Gao et al., 2018; Yang et al., 2018) or by inducible repression of cell proliferation (Kastenhofer et al., 2020). However, such strains may display reduced viability or require extensive optimization in the upstream process compared with industrial standard strains. Second, mechanical or non-mechanical methods can be applied to permeate the OM both in upstream (during cultivation) and in the downstream process (after harvest). Non-mechanical methods include (1) addition of chemicals like detergents, chaotropic agents, solvents, or acids (Wurm et al., 2017b; Schimek et al., 2020); (2) addition of lysozyme (Pierce et al., 1997); or (3) osmotic shock (Balasundaram et al., 2009a; Schimek et al., 2020). Although some of these methods show good selectivity, they are difficult to scale up due to the cost of chemicals or enzymes and the need to remove the additives in later downstream steps. Reported mechanical methods for periplasmic product release are ultrasonication or hydrodynamic cavitation (Balasundaram et al., 2009a; Eggenreich et al., 2017); however, their selectivity is still rather low and scale-up for sonication is hard to realize. Thus, high-pressure homogenization (HPH) remains the standard method for extraction of protein from *E. coli* cells (Eggenreich et al., 2020).

In this regard, pulsed electric field (PEF) may be a promising process to overcome some of the aforementioned limitations of protein recovery and purification. This treatment typically employs high voltage in the kilovolt range and associated electric field strengths of up to 40 kV/cm (Schottroff et al., 2017). Upon application of an external electric field, a transmembrane voltage is induced at the membrane of vegetative cells, which increases with increasing electric field strength. As a consequence, a shift of charges along the membrane takes place, accompanied by an accumulation of oppositely charged ions on both sides of the membrane. The occurring electro-compressive forces

are proportional to the magnitude of the applied electric field strength, ultimately leading to a dielectric breakdown of the membrane and associated pore formation, the so-called electroporation (Sale and Hamilton, 1967; Zimmermann et al., 1974; Coster and Zimmermann, 1975; Neumann et al., 1982). The cell-specific threshold value for the occurrence of electroporation is called the critical electric field strength E_{crit} (Grahls and Märkl, 1996). For *E. coli*, E_{crit} values around 10 kV/cm are reported (Schottroff et al., 2017). Depending on the treatment intensity, electroporation can be either reversible or irreversible, i.e., the cell may or may not be able to repair the occurring damage, which is accompanied by the maintenance of physiological functions, or loss of viability and eventual lysis.

The increase of cell membrane permeability due to electroporation is used by a variety of applications in food and biotechnology, as well as in medicine. Exemplarily, PEF treatment is currently used for gene transformation and transfection in genetic engineering (Kumar et al., 2019; Ozyigit, 2020), pretreatment of plant tissues for mass transfer enhancement (Fauster et al., 2018; Ostermeier et al., 2018), microbial inactivation (Schottroff et al., 2019; Timmermans et al., 2019), or electrochemotherapy (Campana et al., 2019; Geboers et al., 2020). PEF applications reach from laboratory scale to industrial scale, with throughput levels of several tons per hour (Siemer et al., 2018). An extensive overview of applications based on electroporation is given by Kotnik et al. (2015) and Siemer et al. (2018).

Electroporation may also be deployed as a method to selectively extract valuable compounds from microorganisms, including yeasts, microalgae, and bacteria, although it is not industrially implemented yet (Martínez et al., 2020). Studies conducted on the extraction of protein from *E. coli* are summarized in **Table 1**. Although these contributions indicated the potential of PEF for selective protein release, the applicability for downstream processing remains unproven. Most studies employed batch-wise PEF treatment, which, in contrast to continuous PEF treatment, does not allow high throughput for large-scale industrial application due to limitations in generator power. Moreover, detailed analysis of impurity release (HCP, DNA, and endotoxins) is missing. Lastly, release efficiencies were low or cells were resuspended in additional buffers with various additives, which would require additional steps during downstream processing.

For the first time, this work shows the applicability of PEF-assisted selective extraction of recombinant periplasmic protein from *E. coli* for continuous biomanufacturing. The aim of this study was to maximize product release and minimize release of HCP, DNA, and endotoxins (ETs). Consequently, a setup operated in continuous mode for treatment of the culture broth was employed and the effect of specific energy input (W_{spec}), pulse repetition frequency (f), and electric field strength (E) on cell viability, product release, and impurity load was evaluated. Finally, the parameter settings for the most efficient product release were determined and the results were compared with conventionally applied HPH. It was demonstrated that PEF

TABLE 1 | Comparison of studies on PEF assisted protein extraction from *E. coli*.

Modus operandi	PEF matrix	Field strength (kV/cm)	Pulse frequency (Hz)	Pulse duration (μ s)	Energy input (kJ/kg)	Target protein	Investigated process variables	Comments	References
Batch	Buffers containing NaCl, glycine, and PEG	7.5–10	50	≤ 1	100–280	Recombinant β -glucosidase ^a , α -amylase ^b , and cellobiohydrolase ^{a,b}	Protein release	Up to 89% release of α -amylase in combination with NaCl and PEG	Ohshima et al., 2000
Batch	dH ₂ O	5–20	1–1,000	100–1,000	5.5–533.8	Total protein ^{a,b}	Viability, protein release	~75% of total protein extracted	Haberl-Meglić et al., 2015; Haberl-Meglić et al., 2016
Continuous (0.08 L/h)	dH ₂ O, subsequent incubation in "post pulse buffers"	5.5–7.5	4	500–2,000	n.a.	Native PGK ^a and GAPDH ^a	Viability, protein release, HCP impurity (qualitative)	Up to ~90% release of native enzyme after incubation with specific buffers	Coustets et al., 2015
Continuous (0.6–1.98 L/h), recirculation to culture	Culture broth	12	2–3	n.a.	n.a.	Recombinant α -amylase ^b	Viability, protein release, HCP impurity (qualitative)	30% release of α -amylase using intermittent PEF treatment	Shiina et al., 2004, 2007
Continuous (1.5 L/h)	Culture broth	25.6–38.4	50–1,000	3	10.3–257.6	Recombinant Protein A ^b	Viability, protein release, HCP impurity (quantitative), DNA load, endotoxin load	Up to 89% release of recombinant periplasmic protein	This study

^aLocated in the cytoplasm.^bLocated in the periplasm.

treatment is a viable alternative to HPH for product recovery in continuous bioprocesses.

MATERIALS AND METHODS

Strain, Media, and Cultivation

Strain

In this study, an *E. coli* BL21(DE3) strain overexpressing the IgG binding domain of *Staphylococcus aureus* Protein A (SpA) was used. The SpA gene was inserted on a pET30a plasmid and contained the N-terminal signal sequence pelB for translocation to the periplasm.

Media

For preculture and bioreactor cultivation, minimal medium according to DeLisa et al. (1999) was used. The carbon source was glucose, with concentrations 8, 20, and 400 g/L for the preculture, batch, and feed media, respectively.

Preculture

Preculture medium (500 ml) was inoculated with 1 ml of a frozen cell stock in a baffled shake flask. The preculture was incubated overnight at 37°C and 200 rpm in a shaking incubator (Infors AG, Bottmingen, Switzerland).

Bioreactor Cultivation

The bioreactor cultivation was conducted in a Techfors-S reactor (Infors AG, Bottmingen, Switzerland) with a working volume of 10 L. The reactor was continuously aerated at 10 L/min and stirred at 900 rpm and dissolved oxygen (DO) was kept above 40% by adding pure oxygen if needed. pH was controlled at 7.0 by addition of 12.5% (v/v) $\text{NH}_4(\text{OH})$ and temperature was kept at 37°C unless stated otherwise.

Five hundred milliliters of the preculture was used to inoculate 4,500 ml of medium in the bioreactor. After the end of the batch phase that was detected by a spike in the DO signal, the feed was started and cells were grown to a cell dry weight (CDW) concentration of 35 g/L. Then, the temperature was lowered to 30°C and 0.5 mM isopropyl β -D-1-thiogalactopyranoside was added to induce heterologous gene expression. The feed rate was adjusted to an initial specific substrate uptake rate of 0.14 $\text{g}_{\text{glu}}/\text{g}_{\text{CDW}}/\text{h}$ and kept constant for 8 h. After an 8 h induction phase, the cultivation broth was harvested via a draining valve and immediately cooled on ice for further processing and to prevent changes in membrane composition by reducing metabolic activity (Inouye and Phadtare, 2004). It can be assumed that this chilling step did not result in membrane disintegration (Cao-Hoang et al., 2010). The CDW concentration at the time of harvest ($c_{X_{\text{harv}}}$) was gravimetrically determined to be 41.5 ± 0.16 g/L. The intracellular and extracellular SpA concentrations were 154 ± 10 $\text{mg}/\text{g}_{\text{CDW}}$ and 82 ± 1 $\text{mg}/\text{g}_{\text{CDW}}$, respectively, determined by HPLC (see Section “Analyses”).

PEF Treatment

Setup and Continuous Trials

After 1–2 h of cooling on ice ($\sim 2^\circ\text{C}$), the *E. coli* cultivation broth was continuously treated using PEFs. For this purpose, a semi-industrial-scale 6 kW generator (ScandiNova Systems AB, Uppsala, Sweden) was used, which is able to provide rectangular mono- or bipolar pulses, with a maximum magnitude of 25 kV, pulse widths of 0.5–5 μs , maximum current of 300 A, and a maximum pulse repetition frequency of 1 kHz. The use of pulses in the lower microsecond range enables the applicability of higher frequencies for a given level of energy input W_{spec} .

The generator was connected to a specifically designed self-built co-linear treatment chamber, comprising stainless steel electrodes and polyoxymethylene insulators (see Figure 1). A peristaltic pump (MBR PP 101; MBR Bio Reactor AG, Wetzikon, Switzerland) was used to provide the desired mass flow of 1.5 kg/h and was connected to the treatment chamber by silicone tubes ($d_i = 4$ mm; $d_o = 6$ mm). The implementation of the peristaltic pump in combination with sterilized tubes also allows for a sterile operation, if necessary.

For continuous trials, the system was started using saline solution with the same electrical conductivity as the bacterial suspension (10 mS/cm). Once a steady state was reached, the saline solution was replaced by the culture broth containing the *E. coli* cells. After 10 min, an appropriate amount of treated suspension was sampled and electrical parameters were changed. After 5 min, the next sample was taken. Samples were immediately cooled on ice for 1–2 h before further processing, which can be assumed not to have a disruptive effect on the cell membranes (Cao-Hoang et al., 2010). This was repeated until all parameter combinations were accomplished. Sampling times were based on previously determined residence time distribution profiles (data not shown) and an additional margin of safety. The residence time of volume elements within the treatment zone (inside the insulators) was 1.9 ms. Untreated negative control samples were passed through the equipment in a comparable manner, but without exposure to the electric field.

The process was designed in such a way that a specific average field strength E (kV/cm), the pulse frequency f (Hz) as well as a desired specific energy input level W_{spec} (kJ/kg_{broth}) were adjusted according to the experimental design (see section “Experimental Design”). To obtain E , the necessary voltage U (kV) to be adjusted at the generator was calculated according to Equation 1, taking into account a specific conversion factor C_{chamber} (1/cm). This conversion factor was determined based on a computational fluid dynamics simulation of the electric field distribution within the chamber (data not shown), as described elsewhere (Jaeger et al., 2009a). Briefly, ANSYS CFX 19.2 (ANSYS, Canonsburg, PA, United States) was used to solve a thermofluid dynamical model including equations for conservation of mass, momentum, energy, and electric charges. Boundary conditions were used as specified by Schottroff et al. (2020b), where further details considering the simulation and the underlying mathematical models can be found. For the

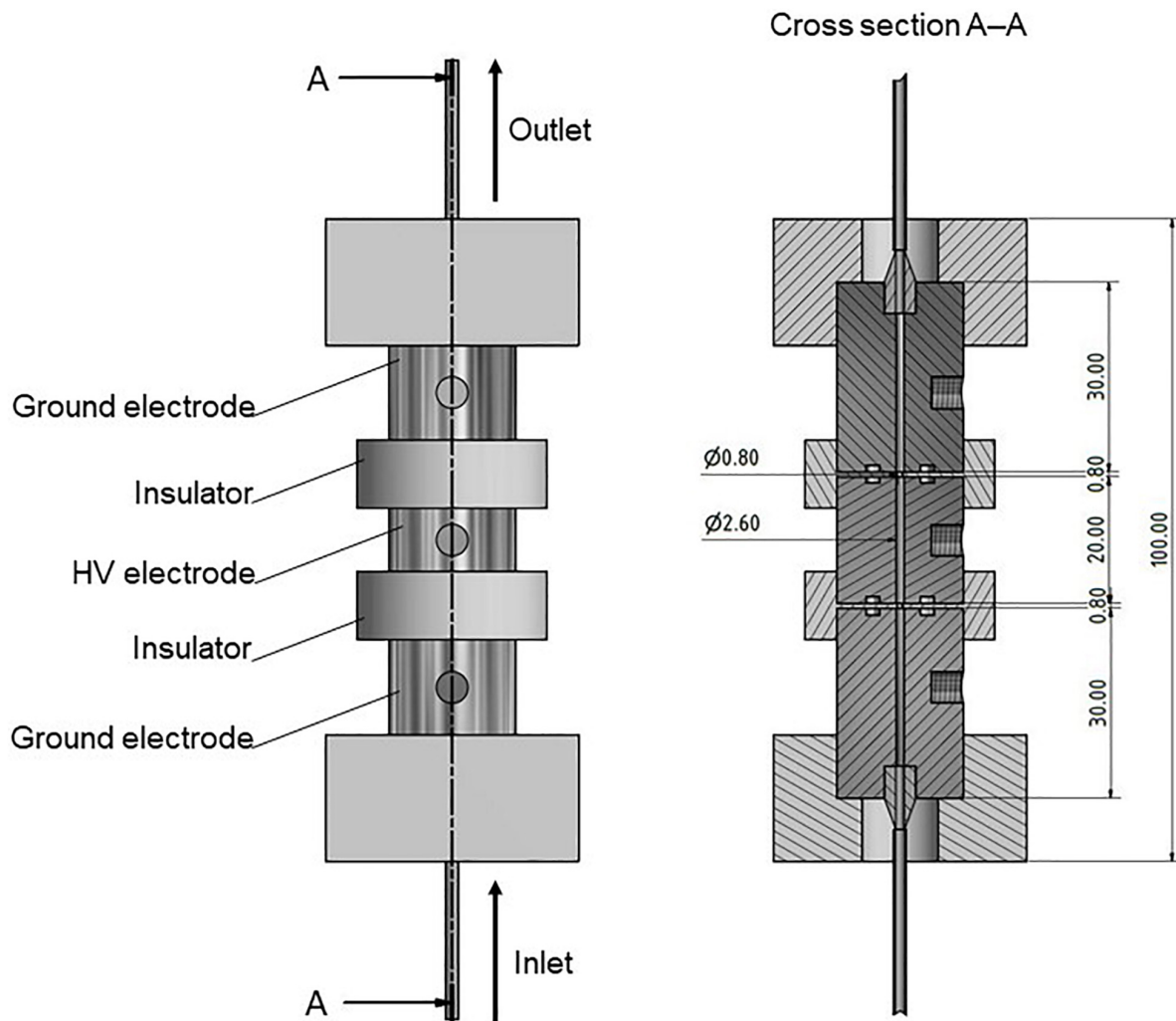


FIGURE 1 | Drawing (left) and cross-section (right) of the used co-linear PEF treatment chamber. The chamber was held together by threaded rods through the top and bottom plates (not shown). High voltage is abbreviated by HV. All dimensions are given in mm.

present geometry, a $C_{chamber}$ factor of 8.8/cm was determined. In comparison with the treatment chamber reported by Jaeger et al. (2009a), the chamber used in this study was down-scaled based on flow conditions by a factor of 5. The $C_{chamber}$ factor given by Jaeger et al. (2009a) was 1.6/cm, corresponding to a relation of the two different $C_{chamber}$ factors of 5.5-fold. Therefore, the obtained value is in accordance with the published literature.

$$E = C_{chamber} * U \quad (1)$$

W_{spec} (kJ/kg) is calculated according to Eq. 2, from the applied voltage U (kV) (which can be expressed as $E/C_{chamber}$ by rearranging Eq. 1), the current I (A), the pulse width τ (s), the pulse repetition frequency f (Hz), as well as the mass flow \dot{m} (kg/s). During each run, τ and \dot{m} were fixed, whereas I

was measured. Thus, the desired energy input was obtained by adjustment of U (respective E) and f .

$$W_{spec} = \frac{U * I * \tau * f}{\dot{m}} = \frac{E * I * \tau * f}{C_{chamber} * \dot{m}} = \Delta T * c_p \quad (2)$$

Temperature was measured directly before and after the treatment chamber, and the determined temperature increase ΔT (K) was correlated with the applied specific heat at constant pressure c_p [kJ/(kg K)] of the treated liquid (Eq. 2), to verify the validity of the applied processing conditions. For all reported trials, the initial sample temperature was set to 2°C, to reduce thermal load caused by the current flow during PEF treatment, especially for high-energy input levels. The resulting temperature increase levels are reported in **Supplementary Table 1**.

Experimental Design

Two factors were considered for the modulation of W_{spec} in the experimental design: E and f . As the real W_{spec} could only be

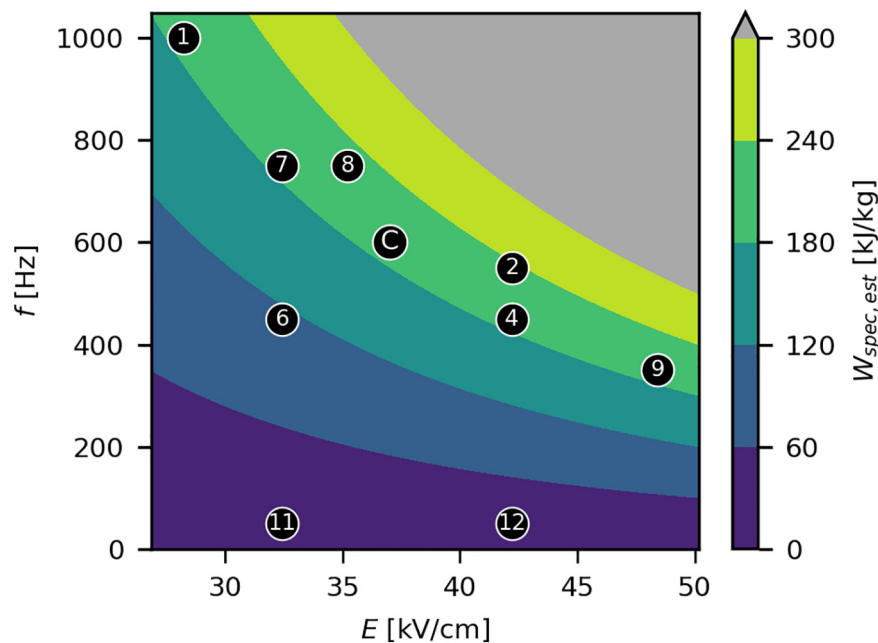


FIGURE 2 | Experimental design for the PEF treatments and $W_{spec,est}$ as a function of E and f . Black markers indicate the set points of E and f , with corresponding experiment numbers enclosed (**Supplementary Table 1**). The center point “C” was performed in triplicate. The gray area indicates technically infeasible parameter settings. $W_{spec,est}$ was estimated assuming a constant R of 390 Ω . The reported levels of W_{spec} for the experiments were based on measurements of all quantities (**Supplementary Table 1**) and differed therefore slightly, due to temperature related fluctuations in R .

calculated from measured values of I and thus was unknown before the trials, a constant resistance (R) of the load of 390 Ω was used (based on preliminary trials; **Supplementary Table 2**) to calculate the estimated specific energy input $W_{spec,est}$ during experimental design using Eq. 2 and Ohm’s law. The process conditions (E and f) were chosen in such a way to cover a wide range of realizable parameter combinations, also taking into account several parameter sets resulting in similar levels of W_{spec} (**Figure 2**). This allowed investigating the effect of W_{spec} and of the two factors E and f , independently of W_{spec} , on the process performance. A fixed τ of 3 μ s was chosen for all trials, based on a previous study (Schottroff et al., 2019), also given the narrow range of pulse widths provided by the generator. The mass flow \dot{m} was fixed at 1.5 kg/h to limit the degrees of freedom in the experimental design. Furthermore, the chosen \dot{m} lies within the typical range of laboratory-scale studies (**Table 1**) and was within the working range of the peristaltic pump used in this work. All factor combinations are listed in **Supplementary Table 1**. Due to temperature fluctuations, the real R (and thus I) during the experiments fluctuated between 350 and 474 Ω (**Supplementary Table 1**) and thus differed from the previously assumed R . The real values for W_{spec} , calculated from measured I , were used for data evaluation.

Analyses

PEF processed samples and the negative control were divided into 10 ml aliquots and centrifuged at 10,000 rcf for 10 min at 4°C. The biomass pellet and culture supernatant, hereafter referred to

as PEF extract, were frozen in liquid N_2 and stored at -20°C for later analysis. The reference method for product extraction was HPH (described later). For comparison with PEF treatment, the reference sample was the cell-debris-free homogenate of the culture broth from the negative control.

Viability

Subsequent to the treatments, PEF processed samples and the negative control were serially diluted in 1/4 strength Ringer’s solution (Merck KGaA, Darmstadt, Germany) and 50 μ l of the appropriate dilutions was drop plated onto tryptic soy agar (TSA; VWR International SPRL/BVBA, Leuven, Belgium) plates in duplicate and incubated at 37°C for 24 h. Colony-forming units (CFUs) were manually counted and the corresponding inactivation levels were calculated from the initial bacterial concentration, N_0 (CFU/ml), and the amount of viable cells after the treatment, N (CFU/ml), as $\log_{10}(N/N_0)$ (–). In the following paragraphs, \log_{10} will simply be referred to as log. For all trials, the initial counts were in the range of 4.7×10^{11} CFU/ml, and the detection limit was 8.15 log.

Product Quantification

For extraction of the product remaining inside the cells, the biomass pellets were resuspended in 30 ml TE buffer (100 mM TRIS, 10 mM EDTA, pH 7.4), with the exception of the reference sample, which was processed as the original cell suspension in the culture broth. The suspension was homogenized in a high-pressure homogenizer (Emulsiflex C-3; Avestin, Ottawa, Canada)

in three passages at 1,000 bar, which are optimal parameters for extraction of soluble product from *E. coli* according to Pekarsky et al. (2019). The homogenate was then centrifuged at 10,000 rcf (10 min, 4°C) to separate the cell debris from the soluble extract. SpA concentrations in the extracts from homogenization (intracellular, $c_{SpA,in}$) and from the PEF extract (extracellular, $c_{SpA,ex}$) were then quantified in triplicate via reversed phase HPLC (Thermo Fisher Scientific, Waltham, MA, United States) using a polyphenyl column (Waters, Milford, MA, United States). The mobile phase consisted of a gradient of water and acetonitrile, supplemented with 0.1% trifluoroacetic acid. The released SpA (%) was then calculated according to Eq. 3.

$$\text{Protein release} = \frac{c_{SpA,ex}}{c_{SpA,in} + c_{SpA,ex}} * 100 \quad (3)$$

Protein Impurity Release

The release of host cell proteins by electroporation was measured in triplicate by SDS-PAGE. PEF extracts and reference sample were diluted 10× and 3×, respectively, in dH₂O. Samples were further diluted in 2 × Laemmli buffer and incubated at 95°C for 10 min. Samples (10 μl) were then loaded onto precast SDS gels (4–15%, Mini-PROTEAN TGX; Bio-Rad, Hercules, CA), which were run at 180 V for 30 min. After staining with Coomassie Blue, the gels were imaged with a ChemiDoc system (Bio-Rad) and densitometric analysis was done with the GelAnalyzer software (version 19.1)¹. The impurity load in percent was consequently calculated according to Eq. 4 using the area from the integrated curves of the densitograms:

$$\text{Impurity load} = \frac{\text{area}_{\text{impurities}}}{\text{area}_{\text{impurities}} + \text{area}_{\text{SpA}}} * 100 \quad (4)$$

DNA Quantification

The PicoGreen assay kit (Thermo Fisher Scientific) was used for quantification of dsDNA in the PEF extracts, the negative control, and the homogenized reference sample. Triplicate measurements were done and SpA-specific DNA load (mg_{DNA}/g_{SpA}) was calculated according to Eq. 5:

$$\text{DNA load} = \frac{c_{DNA}}{c_{SpA}} \quad (5)$$

where c_{DNA} (mg/L) is the concentration of dsDNA and c_{SpA} (g/L) is the concentration of SpA in the extract.

Endotoxin Quantification

The ET levels in the PEF extracts, the negative control, and the homogenized reference sample were measured with the ENDOLISA Kit (bioMérieux SA, Marcy-l'Étoile, France) according to the manufacturer's instructions. Samples were diluted in ET free water by a factor 10⁶. The SpA-specific ET load (EU/g) was calculated with Eq. 6:

$$\text{ET load} = \frac{c_{ET}}{c_{SpA}} \quad (6)$$

where c_{ET} (EU/L) is the concentration of ETs and c_{SpA} (g/L) is the concentration of SpA in the extract.

Linear Regression

Multiple linear regression (MLR) was performed with the software MODDE 10 (Sartorius AG, Göttingen, Germany) to describe the investigated target variables [$\log(N/N_0)$, product release, HCP load, DNA load, ET load] as functions of E and f . The model coefficients were determined with a significance level of $\alpha = 0.05$ and corresponding values for “goodness of fit” R^2 and “goodness of prediction” Q^2 were calculated.

RESULTS AND DISCUSSION

This work aimed at the selective release of recombinant periplasmic protein from *E. coli* as a continuous product harvest step by PEF. A high extraction yield was targeted while keeping HCP, DNA, and ET loads to a minimum. For this purpose, the effect of electric field strength (E) and pulse repetition frequency (f), as well as the specific energy input (W_{spec}), on the mentioned target variables as well as on cell viability was evaluated.

Initial parameter studies were carried out using electroporation cuvettes, to determine a suitable range of process parameters (E and W_{spec}) for further investigation in a continuous process (data not shown). Likewise, it was investigated if the release efficiency of PEF treatment depended on biomass concentration (1–60 g_{CDW}/L), which was not the case (data not shown). Therefore, undiluted *E. coli* suspensions (41.5 g_{CDW}/L) from the bioreactor were used for PEF.

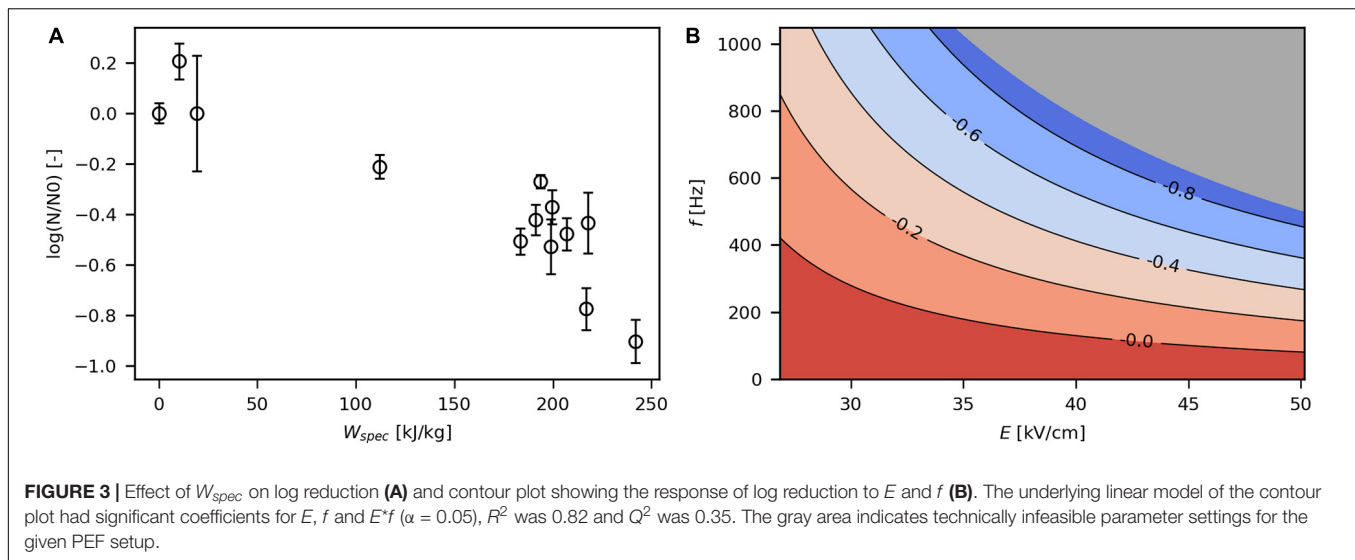
Influence of Process Parameters on Cell Viability

The impact of PEF treatment on viability was first assessed with respect to W_{spec} , as it cumulates all relevant process parameters of a PEF treatment (Eq. 2). Viability of bacteria decreased with increasing W_{spec} (Figure 3A), as expected (Haberl-Meglić et al., 2015; Schottroff et al., 2019). In general, for all reported trials, log-reduction covered a range of no effect on viability (below 20 kJ/kg) to -0.9 log at the highest investigated energy input (241.9 kJ/kg), corresponding to 13% viable cells. Moderate W_{spec} (112.1 kJ/kg) resulted in -0.2 log (63% viability). Thus, the majority of the parameter space employed in this study led to a certain extent of irreversible electroporation.

The obtained linear regression models were used to construct contour plots that allow evaluation of the effect of E and f on the target variables. Figure 3B shows the contour plot for log reduction of viable cells. As expected, high E and f resulted in increased loss of viability because both parameters contribute to W_{spec} . In fact, the influence of E and f on viability were interactive, so that the effect of one parameter on log reduction was enhanced with increasing levels of the other parameter and vice versa (see also Eq. 2).

Log reduction levels in the present study (down to -0.9 log) were low compared with usually targeted values for non-thermal inactivation of microorganisms by PEF (-5 to -7 log)

¹ www.gelanalyzer.com



(Food and Drug Administration, 2000). Comparably low overall inactivation levels might be due to the short electric field exposure times. Haberl-Meglić et al. (2015) employed similar W_{spec} and f as in the present study but applied pulse widths of 100–1,000 μ s (compared with 3 μ s in this study) and reported log-reductions of -1 to -3 log. Thus, the short pulse width applied in the present study might have prevented irreversible pore formation to an extent. Moreover, low inactivation may be explained by neutral pH during PEF treatment or high concentration of “solids,” which prevent inactivation of cells despite occurrence of electroporation (Jaeger et al., 2009b; Schottroff et al., 2020a).

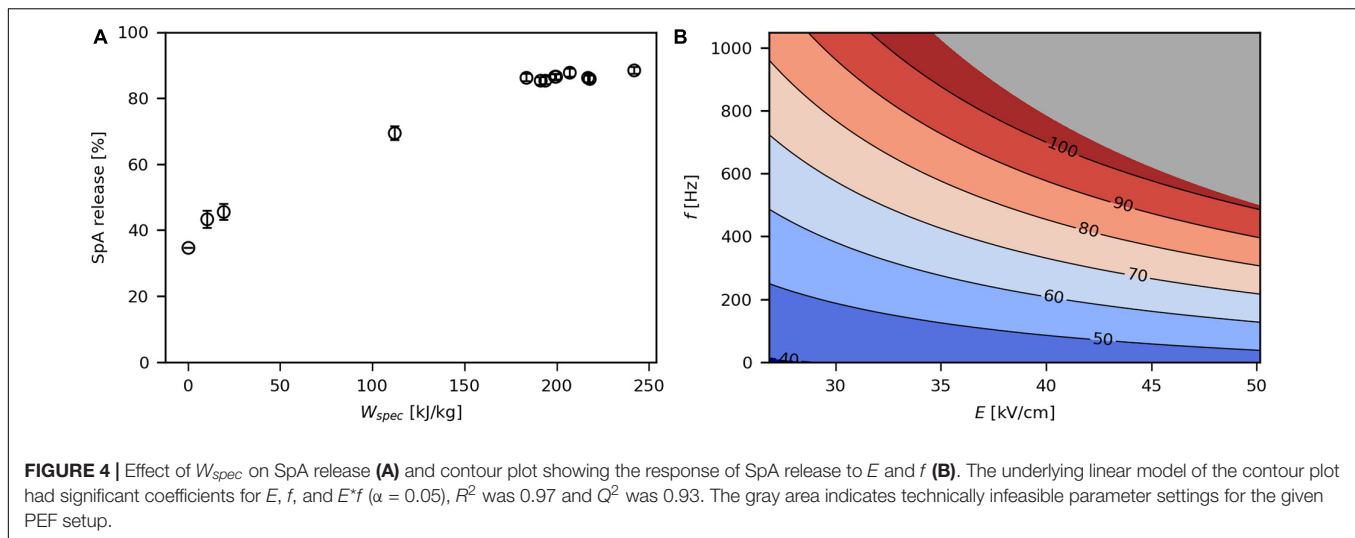
During the exposure of the bacterial suspension to the electric field, there was a noticeable temperature increase (see Eq. 2 and **Supplementary Table 1**). Outlet temperatures ranged between 17.7 and 55.3°C, but samples were cooled within 13.6 s after the temperature increase caused by PEF. Thermal effects might affect viability, especially at high energy inputs and consequent high temperatures of up to 55°C. However, temperatures were elevated only for short time periods in this study. Using kinetics from the inactivation of *E. coli* in culture media (Stringer et al., 2000), it was estimated that in the worst case (constant temperature of 55.3°C for 13.6 s), the generated heat resulted in a viability reduction of -0.05 log. Therefore, it can be assumed that there was only a minor effect of temperature on cell inactivation during PEF treatment.

While high viability is generally not a prerequisite in downstream processing, product harvest by reversible electroporation is potentially interesting for process intensification. Continuous product extraction with subsequent recultivation of cells during upstream processing might allow to use the “cell factory” more efficiently (Shiina et al., 2004, 2007). The setup and parameter settings in the present study did not result in useful viability levels for this purpose (mostly below 63%). Further research is necessary to explore the potential of reversible electroporation by PEF for continuous product extraction.

Influence of Process Parameters on Product Release

In the control sample without PEF treatment, 35% of SpA were released into the culture medium (**Figure 4A**). This is due to the common phenomenon that the OM of *E. coli* becomes permeable during recombinant protein production, leading to protein leakage into the extracellular space (Han et al., 2003; Wurm et al., 2017a; Kastenhofer and Spadiut, 2020). The release of periplasmic product increased with increasing W_{spec} until a plateau was reached at around 89% released SpA. Above a W_{spec} of 180 kJ/kg, the release efficiency did not increase any further. This may be due to cytosolic SpA that could not permeate through both membranes upon PEF treatment. In this range, viability does not correlate with SpA release (**Supplementary Figure 1**), thus any increase in power input merely inactivates cells without enhancing product extraction.

The impact of E and f on SpA release is depicted in **Figure 4B**. Similar to the log reduction, the effect of each parameter on product release increased at higher levels of the other parameter. Haberl-Meglić et al. (2015) also showed that total protein release from *E. coli* is affected by E . However, in contrast to their study, the obtained data suggest that f has a much stronger impact on SpA extraction than E over the investigated design space. Because the used levels for E (28.2–48.4 kV/cm) are far above the critical electric field strength E_{crit} (~ 10 kV/cm) for *E. coli* (Grahnl and Märkl, 1996), E was likely high enough in all tested parameter combinations to evoke pore formation in all cells. Therefore, an increase in E might not have drastically improved electroporation. On the other hand, increasing the total field exposure time via f may result in sufficiently long periods of “open pores” allowing high amounts of protein to pass through the OM (**Supplementary Figure 2**). High levels of f are particularly necessary, when higher volumetric throughputs are desired, as otherwise a sufficient number of pulses per volume element is not given. This might be the reason for the low release efficiency of 30% in the studies of Shiina et al.



(2004, 2007), who applied pulse repetition frequencies of 2–3 Hz (Table 1). Lastly, it could be shown that microsecond pulses can be efficiently used for the extraction of protein from *E. coli*. This is in contrast to the studies of Coustets et al. (2015) and Haberl-Meglić et al. (2015), who reported improved release efficiency at long pulse widths in the millisecond range, possibly due to lower values for E or f employed in their studies (Table 1).

Influence of Process Parameters on Host Cell Impurities

At low W_{spec} (below 20 kJ/kg), between 66 and 71% of extracellular proteins were HCPs, while higher W_{spec} (above 100 kJ/kg) resulted in a reduction of HCP load to levels between 32 and 47% (Figure 5A). Thus, high levels of W_{spec} led to a higher selectivity. This may be due to high intracellular product concentration (154 mg/g_{CDW}) or small size (34 kDa) of the recombinant SpA compared with the HCP (Schimek et al., 2020). Both E and f had a significant effect on HCP load, which is due to their contribution to W_{spec} (Figure 5B). The origin of the HCP was not identified in the present study, although it may be assumed that periplasmic HCP was more prone to be released during PEF treatment than cytoplasmic protein (Ohshima et al., 2000). Yet it is likely that in the present study small amounts of cytoplasmic HCP were released as well, because DNA was also detected in the culture medium.

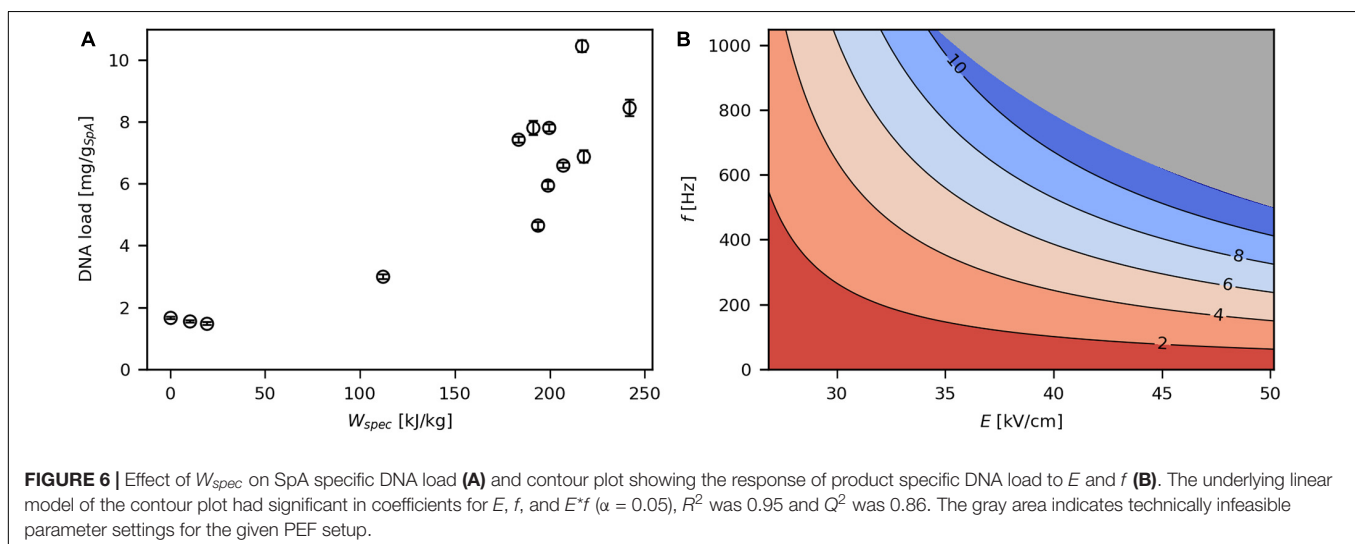
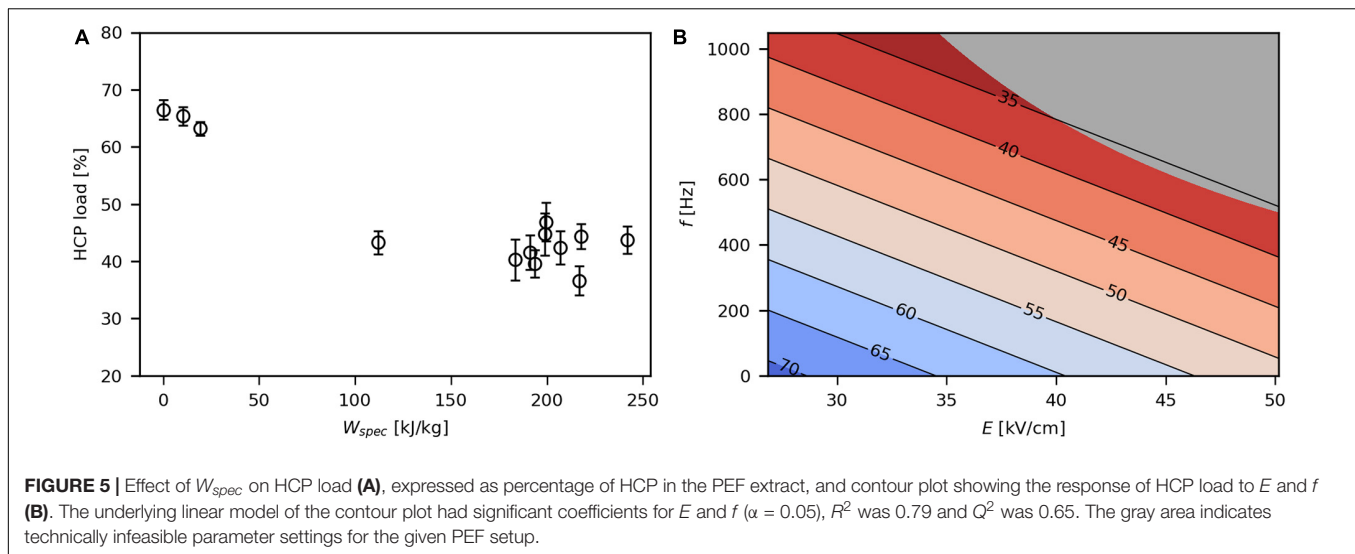
SpA-specific DNA load increased with rising levels of W_{spec} (Figure 6A) to a maximum of 10.5 mg/g_{SpA}, which corresponds to 2.1 mg/g_{CDW} or 6.9% of the total DNA content of the *E. coli* cells (Neidhardt and Umberger, 1996). The effects of E and f on DNA release (Figure 6B) were similar compared with viability and SpA release, such that the effect of one parameter on DNA leakage increased at higher levels of the other parameter and vice versa. As mentioned earlier, the release of DNA to the culture supernatant indicates pronounced pore formation in the IM. Interestingly, although cells seemed to be largely intact even at a high W_{spec} of 216.7 kJ/kg (6.9% of DNA released),

only 17% of cells remained viable at that point. Thus, PEF treatment seems to be detrimental to physiological functions by disrupting membrane potential, pump activity as well as metabolic activity (Schottroff et al., 2017), while cells do not completely lyse.

ETs, mainly composed of lipopolysaccharides, are present in the outer leaflet of the OM and are continuously excreted by *E. coli* during cultivation. They elicit severe immune responses in humans, which is why they need to be almost completely removed from biopharmaceutical compounds (Carta and Jungbauer, 2010). Therefore, the present work aimed at minimal ET release during PEF processing. Product-specific ET load decreased with increasing levels of W_{spec} (Figure 7A), which is due to higher amounts of SpA released at high energy inputs. Correspondingly, ET impurity was significantly affected by f (Figure 7B) because this parameter has a strong impact on product release as well. Still, ET load was in the same order of magnitude (10^9 EU/g_{SpA}) at all investigated parameter settings and even in the untreated sample. Thus, in contrast to the proposal of Haberl-Meglić et al. (2015) that ET release during electroporation may be a problem linked to OM degradation upon cell death, obtained data show that ETs are present before PEF treatment, and various processing conditions have no significant impact on release of ETs, regardless of their effect on viability.

Applicability of PEF for Continuous Downstream Processing

Within the selected design space, the best settings of E and f were determined, resulting in maximal product release efficiency and minimal HCP, DNA, and ET loads, respectively (the so-called sweet spot). For this, the accepted ranges for the individual target variables were defined. They were chosen as an arbitrary range close to the theoretical maximum for product release and the theoretical minimum for HCP, DNA, and ET loads. The final ranges were 80–100% SpA release, 0–45% HCP load, 0–5 mg/g_{SpA} DNA load, and $0\text{--}4.5 \times 10^9$ EU/g_{SpA} ET load. The



obtained criteria were then imposed on the solutions of the model equations to retrieve the sweet spot plot (Figure 8). It was deduced that the sweet spot is achieved with E below 30 kV/cm and f above 825 Hz for the studied conditions (treated suspension with 10 mS/cm electrical conductivity, 3 μ s pulse width, 1.5 kg/h mass flow). This can be explained by the fact that the used magnitudes of E were already sufficient for electroporation to occur; therefore, higher values of E likely did not increase the amount of electroporated cells, however may contribute to the formation of irreversible pores associated with cell death and lysis. On the other hand, as a flow-through process was used, higher levels of f allow the application of an increased number of pulses per volume element, thus increasing the electric field exposure time, resulting in high levels of protein release.

To show the benefit of PEF for periplasmic protein release, the results from an experimental point within the determined sweet spot ($E = 28.2$ kV/cm; $f = 1,000$ Hz) were compared with HPH (Table 2). Although HPH is an unselective method for

the disintegration and subsequent extraction of proteins from cells, it is still commonly applied for the release of product from both cytoplasm and periplasm due to its high efficiency and scalability. While the release efficiency of PEF was 15% lower compared with HPH, there was a clear improvement in HCP and DNA loads. ET load was in the same order of magnitude for both processes (10^9 EU/g). Considering the accepted ET levels in biopharmaceutical products of 10^1 – 10^3 EU/g (McCullough, 2011), similar steps would be required for ET reduction for samples treated with PEF or HPH. However, the DNA load was drastically reduced in the PEF process (by 96% relative to HPH) and would therefore mitigate the burden on the final product. In addition, the load of DNA, which has a strong negative charge, on the frequently used anion-exchange chromatography columns would be greatly reduced. Furthermore, low amounts of DNA also reduce viscosity-related issues in downstream processing (Balasundaram et al., 2009b; Carta and Jungbauer, 2010). Finally, the lower HCP impurity load after PEF-assisted product

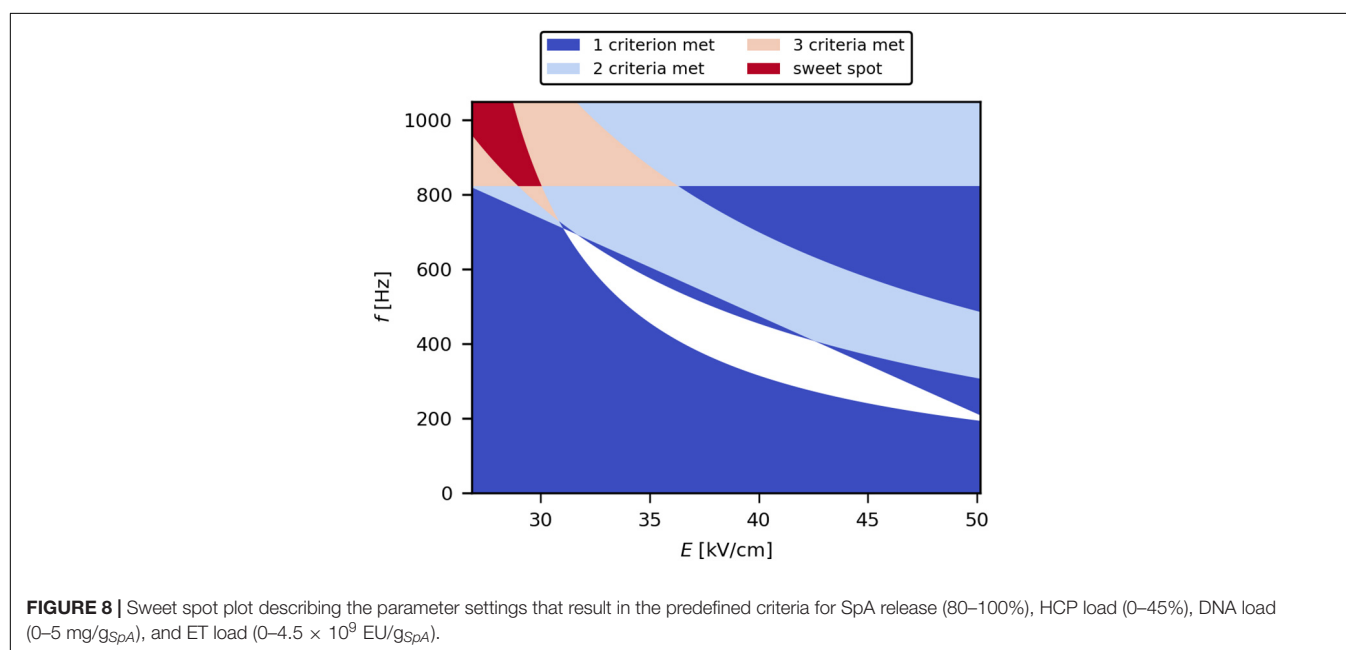
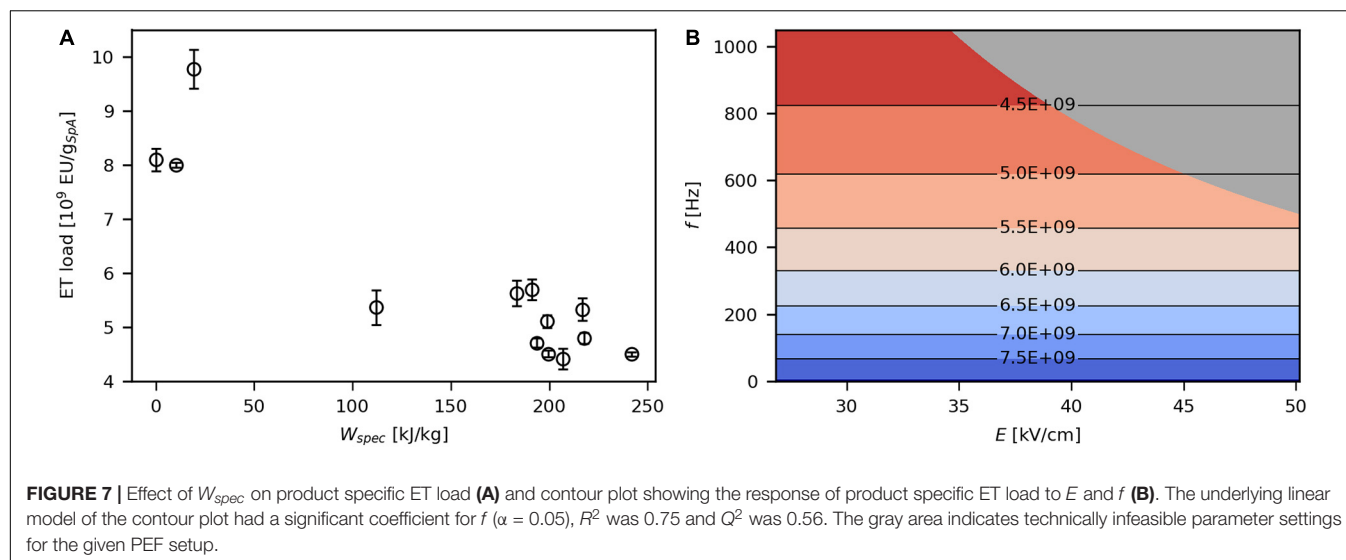


TABLE 2 | Comparison between HPH and PEF treatment for release of SpA.

	Log reduction	Product release	Impurity load		DNA load		ET load	
	(logN/N0)	(%)	(%)	Reduction (%)	(mg/g SpA)	Reduction (%)	(EU/g SpA)	Reduction (%)
HPH	−3 ^a	100	69 ± 2	–	112.2 ± 8.7	–	8.2 ± 0.2 × 10 ⁹	–
PEF	−0.27	85 ± 1	41 ± 3	40 ± 4	4.7 ± 0.1	96 ± 0	4.7 ± 0.08 × 10 ⁹	43 ± 2

^aAssuming −1 log per passage at 1,000 bar (Wuytack et al., 2002).

extraction (reduced by 40% relative to HPH) may reduce the number of purification steps needed.

Regarding product stability and activity, both HPH and PEF may have detrimental effects on product quality to varying degrees. While HPH is characterized by cavitation and high shear forces, which may influence the protein structure (Vertessy et al.,

2014; Han et al., 2020), the occurring temperature increase during the process may also be detrimental to the protein quality. The electric field present during PEF treatment, on the other hand, is reported to have limited effects on some proteins, especially enzymes with a metal ion in the prosthetic group (Castro et al., 2006). However, the accompanying temperature increase during

the treatment seems to exert distinctly more pronounced effects (Jaeger et al., 2010). Therefore, outlet temperature should be carefully monitored and controlled during PEF treatment.

The continuous mode of operation of PEF further exemplifies the potential of its implementation in downstream processing, especially because such systems are scalable and already developed for other applications. The corresponding generator technology for large-scale production already exists, e.g., for food pasteurization with up to 5,000 L/h and a maximum power of 100 kW (Siemer et al., 2018). In comparison, HPH equipment with a similar throughput at 1,000 bar operates at twice the maximum power (200 kW) of a PEF generator (GEA, 2016). In terms of downstream applications related to PEF, a variety of future research needs may be addressed in further studies. This includes upscaling trials with higher throughput levels, considering transferability of results, and treatment homogeneity of larger systems. Moreover, only standard treatment chamber configurations were reported for PEF-assisted product recovery from microorganisms so far, although design and optimization of equipment may contribute to revealing the full potential of the technology for this application. Furthermore, other bacterial host organisms than *E. coli* as well as yeast cells, microalgae, and animal cell culture should be investigated to further evaluate the potential of continuous PEF treatment for product release.

CONCLUDING REMARKS

In conclusion, it was shown that PEF is a useful process for the selective recovery of periplasmic proteins from *E. coli*. It was found that the investigated target variables (viability, product release, HCP, DNA, and ET loads) were mostly dependent on W_{spec} , and the effects of the individual parameters E and f on these variables were similar to their contributions to W_{spec} . Moreover, low electric field strengths ($E < 30$ kV/cm) and high pulse repetition frequencies ($f > 825$ Hz) were determined as the optimal parameter settings within the investigated design space, allowing efficient product release, while keeping the impurities to a minimum. With parameter settings within the sweet spot, a release efficiency of 85% and a significant reduction of HCP (40%), DNA (96%), and ET loads (43%) compared with HPH was achieved. Thus, PEF constitutes an interesting alternative

for downstream applications in bioprocesses, as it can be readily applied to the culture broth in continuous mode.

DATA AVAILABILITY STATEMENT

The original contributions presented in the study are included in the article/**Supplementary Material**, further inquiries can be directed to the corresponding author/s.

AUTHOR CONTRIBUTIONS

FS and DW developed the idea for the study. FS, JK, and DW designed and performed the experiments and carried out analyses. FS and JK wrote the article. HJ and OS gave input toward the study. HJ, OS, and DW proofread the article. All authors contributed to the article and approved the submitted version.

FUNDING

The authors gratefully acknowledge the Austrian Research Promotion Agency (FFG) (grant number 872643) for funding of this research. The authors thank the TU Wien Bibliothek for financial support through its Open Access Funding Program.

ACKNOWLEDGMENTS

The study was supported by the BOKU Core Facility Food & Bio Processing. Part of the equipment used in this study was financed by EQ BOKU VIBT GmbH and belongs to the Center for Preservation and Aseptic Processing. We thank Justus Knappert (TU Berlin) for the determination of the treatment chamber conversion factor ($C_{chamber}$).

SUPPLEMENTARY MATERIAL

The Supplementary Material for this article can be found online at: <https://www.frontiersin.org/articles/10.3389/fbioe.2020.586833/full#supplementary-material>

REFERENCES

- Balasundaram, B., Harrison, S., and Bracewell, D. G. (2009a). Advances in product release strategies and impact on bioprocess design. *Trends Biotechnol.* 27, 477–485. doi: 10.1016/j.tibtech.2009.04.004
- Balasundaram, B., Nesbeth, D., Ward, J. M., Keshavarz-Moore, E., and Bracewell, D. G. (2009b). Step change in the efficiency of centrifugation through cell engineering: co-expression of staphylococcal nuclease to reduce the viscosity of the bioprocess feedstock. *Biotechnol. Bioeng.* 104, 134–142. doi: 10.1002/bit.22369
- Campana, L. G., Edhemovic, I., Soden, D., Perrone, A. M., Scarpa, M., Campanacci, L., et al. (2019). Electrochemotherapy – emerging applications technical advances, new indications, combined approaches, and multi-institutional collaboration. *Eur. J. Surg. Oncol.* 45, 92–102. doi: 10.1016/j.ejso.2018.11.023
- Cao-Hoang, L., Dumont, F., Marechal, P. A., and Gervais, P. (2010). Inactivation of *Escherichia coli* and *Lactobacillus plantarum* in relation to membrane permeabilization due to rapid chilling followed by cold storage. *Arch. Microbiol.* 192, 299–305. doi: 10.1007/s00203-010-0555-y
- Carta, G., and Jungbauer, A. (2010). *Protein Chromatography*. Weinheim: WILEY-VCH Verlag.
- Castro, I., Macedo, B., Teixeira, J. A., and Vicente, A. A. (2006). The effect of electric field on important food-processing enzymes: comparison of inactivation kinetics under conventional and ohmic heating. *J. Food Sci.* 69, C696–C701. doi: 10.1111/j.1365-2621.2004.tb09918.x
- Coster, H. G. L., and Zimmermann, U. (1975). The mechanism of electrical breakdown in the membranes of *Valonia utricularis*. *J. Membr. Biol.* 22, 73–90. doi: 10.1007/bf01868164

- Coustets, M., Ganeva, V., Galutzov, B., and Teissie, J. (2015). Millisecond duration pulses for flow-through electro-induced protein extraction from *E. coli* and associated eradication. *Bioelectrochemistry* 103, 82–91. doi: 10.1016/j.bioelechem.2014.08.008
- DeLisa, M. P., Li, J., Rao, G., Weigand, W. A., and Bentley, W. E. (1999). Monitoring GFP-operon fusion protein expression during high cell density cultivation of *Escherichia coli* using an on-line optical sensor. *Biotechnol. Bioeng.* 65, 54–64.
- Engenreich, B., Rajamanickam, V., Wurm, D. J., Fricke, J., Herwig, C., and Spadiut, O. (2017). A combination of HPLC and automated data analysis for monitoring the efficiency of high-pressure homogenization. *Microb. Cell Fact.* 16:134. doi: 10.1186/s12934-017-0749-y
- Engenreich, B., Wurm, D. J., Rajamanickam, V., Klausser, R., Slouka, C., and Spadiut, O. (2020). High pressure homogenization is a key unit operation in inclusion body processing. *J. Biotechnol. X* 7:100022. doi: 10.1016/j.btecx.2020.100022
- Fauster, T., Schlossnikl, D., Rath, F., Ostermeier, R., Teufel, F., Toepfl, S., et al. (2018). Impact of pulsed electric field (PEF) pretreatment on process performance of industrial French fries production. *J. Food Eng.* 235, 16–22. doi: 10.1016/j.jfoodeng.2018.04.023
- Food and Drug Administration (2000). Overarching principles: kinetics and pathogens of concern for all technologies. *J. Food Sci.* 65, 16–31. doi: 10.1111/j.1750-3841.2000.tb00615.x
- Gao, W., Yin, J., Bao, L., Wang, Q., Hou, S., Yue, Y., et al. (2018). Engineering extracellular expression systems in *Escherichia coli* based on transcriptome analysis and cell growth state. *ACS Synth. Biol.* 7, 1291–1302. doi: 10.1021/acssynbio.7b00400
- GEA (2016). *GEA Ariete Homogenizer 5200*. Available online at: https://www.gea.com/en/binaries/DataSheet-GEA-Ariete-homogenizer-5200-LR_tcm11-41698.PDF (accessed December 5, 2020)
- Geboers, B., Scheffer, H. J., Graybill, P. M., Ruars, A. H., Nieuwenhuizen, S., Puijk, R. S., et al. (2020). High-voltage electrical pulses in oncology: irreversible electroporation, electrochemotherapy, gene electrotransfer, electrofusion, and electroimmunotherapy. *Radiology* 295, 254–272. doi: 10.1148/radiol.2020192190
- Grahl, T., and Märkl, H. (1996). Killing of microorganisms by pulsed electric fields. *Appl. Microbiol. Biotechnol.* 45, 148–157. doi: 10.1007/s002530050663
- Haberl-Meglić, S., Levičnik, E., Luengo, E., Raso, J., and Miklavčič, D. (2016). The effect of temperature and bacterial growth phase on protein extraction by means of electroporation. *Bioelectrochemistry* 112, 77–82. doi: 10.1016/j.bioelechem.2016.08.002
- Haberl-Meglić, S., Marolt, T., and Miklavčič, D. (2015). Protein extraction by means of electroporation from *E. coli* with preserved viability. *J. Membr. Biol.* 248, 893–901. doi: 10.1007/s00232-015-9824-7
- Han, L., Enfors, S. O., and Häggström, L. (2003). *Escherichia coli* high-cell-density culture: carbon mass balances and release of outer membrane components. *Bioprocess Biosyst. Eng.* 25, 205–212. doi: 10.1007/s00449-002-0300-2
- Han, T., Wang, M., Wang, Y., and Tang, L. (2020). Effects of high-pressure homogenization and ultrasonic treatment on the structure and characteristics of casein. *LWT* 130:109560. doi: 10.1016/j.lwt.2020.109560
- Inouye, M., and Phadtare, S. (2004). Cold shock response and adaptation at near-freezing temperature in microorganisms. *Sci. Signal.* 2004:e26. doi: 10.1126/stke.2372004pe26
- Jaeger, H., Meneses, N., and Knorr, D. (2009a). Impact of PEF treatment inhomogeneity such as electric field distribution, flow characteristics and temperature effects on the inactivation of *E. coli* and milk alkaline phosphatase. *Innov. Food Sci. Emerg. Technol.* 10, 470–480. doi: 10.1016/j.ifset.2009.03.001
- Jaeger, H., Schulz, A., Karapetkov, N., and Knorr, D. (2009b). Protective effect of milk constituents and sublethal injuries limiting process effectiveness during PEF inactivation of *Lb. rhamnosus*. *Int. J. Food. Microbiol.* 134, 154–161. doi: 10.1016/j.ijfoodmicro.2009.06.007
- Jaeger, H., Meneses, N., Moritz, J., and Knorr, D. (2010). Model for the differentiation of temperature and electric field effects during thermal assisted PEF processing. *J. Food Eng.* 100, 109–118. doi: 10.1016/j.jfoodeng.2010.03.034
- Kastenhofer, J., Rettenbacher, L., Feuchtenhofer, L., Mairhofer, J., and Spadiut, O. (2020). Inhibition of *E. coli* host RNA polymerase allows efficient extracellular recombinant protein production by enhancing outer membrane leakiness. *Biotechnol. J.* 11:e2000274. doi: 10.1002/biot.202000274
- Kastenhofer, J., and Spadiut, O. (2020). Culture medium density as a simple monitoring tool for cell integrity of *Escherichia coli*. *J. Biotechnol. X* 6:100017. doi: 10.1016/j.btecx.2020.100017
- Kleiner-Grote, G. R. M., Risse, J. M., and Friehs, K. (2018). Secretion of recombinant proteins from *E. coli*. *Eng. Life Sci.* 18, 532–550. doi: 10.1002/elsc.201700200
- Kotnik, T., Frey, W., Sack, M., Haberl Meglič, S., Peterka, M., and Miklavčič, D. (2015). Electroporation-based applications in biotechnology. *Trends Biotechnol.* 33, 480–488. doi: 10.1016/j.tibtech.2015.06.002
- Kumar, P., Nagarajan, A., and Uchil, P. D. (2019). DNA transfection by electroporation. *Cold Spring. Harb. Protoc.* 2019:db.rot095471. doi: 10.1101/pdb.prot095471
- Martínez, J. M., Delso, C., Álvarez, I., and Raso, J. (2020). Pulsed electric field-assisted extraction of valuable compounds from microorganisms. *Compr. Rev. Food Sci. Food Saf.* 19, 530–552. doi: 10.1111/1541-4337.12512
- McCullough, K. Z. (2011). *The Bacterial Endotoxins Test: A Practical Approach*. Bethesda, MD: DHI Publishing.
- Neidhardt, F. C., and Umbarger, H. E. (1996). “Chemical composition of *Escherichia coli*,” in *Escherichia coli and Salmonella: Cellular and Molecular Biology*, ed. F. C. Neidhardt (Washington, DC: ASM Press).
- Neumann, E., Schaeferriidder, M., Wang, Y., and Hofschneider, P. H. (1982). Gene-transfer into mouse lyoma cells by electroporation in high electric-fields. *EMBO J.* 1, 841–845. doi: 10.1002/j.1460-2075.1982.tb01257.x
- Ohshima, T., Hama, Y., and Sato, M. (2000). Releasing profiles of gene products from recombinant *Escherichia coli* in a high-voltage pulsed electric field. *Biochem. Eng. J.* 5, 149–155. doi: 10.1016/s1369-703x(00)00055-3
- Ostermeier, R., Giersemehl, P., Siemer, C., Töpfl, S., and Jäger, H. (2018). Influence of pulsed electric field (PEF) pre-treatment on the convective drying kinetics of onions. *J. Food Eng.* 237, 110–117. doi: 10.1016/j.jfoodeng.2018.05.010
- Ozyigit, I. I. (2020). Gene transfer to plants by electroporation: methods and applications. *Mol. Biol. Rep.* 47, 3195–3210. doi: 10.1007/s11033-020-05343-4
- Pekarsky, A., Spadiut, O., Rajamanickam, V., and Wurm, D. J. (2019). A fast and simple approach to optimize the unit operation high pressure homogenization - a case study for a soluble therapeutic protein in *E. coli*. *Prep. Biochem. Biotechnol.* 49, 74–81. doi: 10.1080/10826068.2018.1536988
- Pierce, J. J., Turner, C., Keshavarz-Moore, E., and Dunnill, P. (1997). Factors determining more efficient large-scale release of a periplasmic enzyme from *E. coli* using lysozyme. *J. Biotechnol.* 58, 1–11. doi: 10.1016/s0168-1656(97)00116-8
- Sale, A. J. H., and Hamilton, W. A. (1967). Effects of high electric fields on microorganisms: I. Killing of bacteria and yeasts. *Biochim. Biophys. Acta Gen. Subj.* 148, 781–788. doi: 10.1016/0304-4165(67)90052-9
- Sandomenico, A., Sivaccumar, J. P., and Ruvo, M. (2020). Evolution of *Escherichia coli* expression system in producing antibody recombinant fragments. *Int. J. Mol. Sci.* 21:6324. doi: 10.3390/ijms21176324
- Schimek, C., Egger, E., Tauer, C., Striedner, G., Brocard, C., Cserjan-Puschmann, M., et al. (2020). Extraction of recombinant periplasmic proteins under industrially relevant process conditions: Selectivity and yield strongly depend on protein titer and methodology. *Biotechnol. Prog.* 36:e2999. doi: 10.1002/btpr.2999
- Schottroff, F., Gratz, M., Krottenthaler, A., Johnson, N. B., Bédard, M. F., and Jaeger, H. (2019). Pulsed electric field preservation of liquid whey protein formulations – influence of process parameters, pH, and protein content on the inactivation of *Listeria innocua* and the retention of bioactive ingredients. *J. Food Eng.* 243, 142–152. doi: 10.1016/j.jfoodeng.2018.09.003
- Schottroff, F., Johnson, K., Johnson, N. B., Bédard, M. F., and Jaeger, H. (2020a). Challenges and limitations for the decontamination of high solids protein solutions at neutral pH using pulsed electric fields. *J. Food Eng.* 268:109737. doi: 10.1016/j.jfoodeng.2019.109737
- Schottroff, F., Knappert, J., Eppmann, P., Krottenthaler, A., Horneber, T., McHardy, C., et al. (2020b). Development of a continuous pulsed electric field (PEF) vortex-flow chamber for improved treatment homogeneity based on hydrodynamic optimization. *Front. Bioeng. Biotechnol.* 8:340. doi: 10.3389/fbioe.2020.00340
- Schottroff, F., Krottenthaler, A., and Jaeger, H. (2017). “Stress induction and response, inactivation, and recovery of vegetative microorganisms by pulsed electric fields,” in *Handbook of Electroporation*, ed. D. Miklavcic (Cham: Springer Nature), 1–19.

- Shiina, S., Ohshima, T., and Sato, M. (2004). Extracellular release of recombinant α -amylase from *Escherichia coli* using pulsed electric field. *Biotechnol. Prog.* 20, 1528–1533. doi: 10.1021/bp049760u
- Shiina, S., Ohshima, T., and Sato, M. (2007). Extracellular production of α -amylase during fed-batch cultivation of recombinant *Escherichia coli* using pulsed electric field. *J. Electrostat.* 65, 30–36. doi: 10.1016/j.elstat.2005.03.093
- Siemer, C., Toepfl, S., Witt, J., and Ostermeier, R. (2018). *Use of Pulsed Electric Fields (PEF) in the Food Industry*. Available online at: https://www.dlg.org/fileadmin/downloads/lebensmittel/themen/publikationen/expertenwissen/lebensmitteltechnologie/e_2018_5_Expertenwissen_PEF.pdf (accessed July 7, 2020)
- Stringer, S. C., George, S. M., and Peck, M. W. (2000). Thermal inactivation of *Escherichia coli* O157:H7. *Symp. Ser. Soc. Appl. Microbiol.* 29, 79S–89S. doi: 10.1111/j.1365-2672.2000.tb05335.x
- Timmermans, R. A. H., Mastwijk, H. C., Berendsen, L. B. J. M., Nederhoff, A. L., Matser, A. M., Van Boekel, M. A. J. S., et al. (2019). Moderate intensity pulsed electric fields (PEF) as alternative mild preservation technology for fruit juice. *Int. J. Food. Microbiol.* 298, 63–73. doi: 10.1016/j.ijfoodmicro.2019.02.015
- Vertessy, B. G., Tribst, A. A. L., Cota, J., Murakami, M. T., and Cristianini, M. (2014). Effects of high pressure homogenization on the activity, stability, kinetics and three-dimensional conformation of a glucose oxidase produced by *Aspergillus niger*. *PLoS One* 9:e103410. doi: 10.1371/journal.pone.0103410
- Wurm, D. J., Marschall, L., Sagmeister, P., Herwig, C., and Spadiut, O. (2017a). Simple monitoring of cell leakiness and viability in *Escherichia coli* bioprocesses—a case study. *Eng. Life Sci.* 17, 598–604. doi: 10.1002/elsc.201600204
- Wurm, D. J., Slouka, C., Bosilj, T., Herwig, C., and Spadiut, O. (2017b). How to trigger periplasmic release in recombinant *Escherichia coli*: a comparative analysis. *Eng. Life Sci.* 17, 215–222. doi: 10.1002/elsc.201600168
- Wuytack, E. Y., Diels, A. M. J., and Michiels, C. W., (2002). Bacterial inactivation by high-pressure homogenisation and high hydrostatic pressure. *Int. J. Food Microbiol.* 77, 205–212. doi: 10.1016/s0168-1605(02)00054-5
- Yang, H., Lu, X., Hu, J., Chen, Y., Shen, W., and Liu, L. (2018). Boosting secretion of extracellular protein by *Escherichia coli* via cell wall perturbation. *Appl. Environ. Microbiol.* 84:e1382-18. doi: 10.1128/AEM.01382-18
- Zhou, Y., Lu, Z., Wang, X., Selvaraj, J. N., and Zhang, G. (2018). Genetic engineering modification and fermentation optimization for extracellular production of recombinant proteins using *Escherichia coli*. *Appl. Microbiol. Biotechnol.* 102, 1545–1556. doi: 10.1007/s00253-017-8700-z
- Zimmermann, U., Pilwat, G., and Riemann, F. (1974). Dielectric breakdown of cell membranes. *Biophys. J.* 14, 881–899. doi: 10.1016/S0006-3495(74)85956-4

Conflict of Interest: The authors declare that the research was conducted in the absence of any commercial or financial relationships that could be construed as a potential conflict of interest.

Copyright © 2021 Schottroff, Kastenhofer, Spadiut, Jaeger and Wurm. This is an open-access article distributed under the terms of the Creative Commons Attribution License (CC BY). The use, distribution or reproduction in other forums is permitted, provided the original author(s) and the copyright owner(s) are credited and that the original publication in this journal is cited, in accordance with accepted academic practice. No use, distribution or reproduction is permitted which does not comply with these terms.

Advantages of publishing in Frontiers



OPEN ACCESS

Articles are free to read
for greatest visibility
and readership



FAST PUBLICATION

Around 90 days
from submission
to decision



HIGH QUALITY PEER-REVIEW

Rigorous, collaborative,
and constructive
peer-review



TRANSPARENT PEER-REVIEW

Editors and reviewers
acknowledged by name
on published articles

Frontiers

Avenue du Tribunal-Fédéral 34
1005 Lausanne | Switzerland

Visit us: www.frontiersin.org

Contact us: frontiersin.org/about/contact



REPRODUCIBILITY OF RESEARCH

Support open data
and methods to enhance
research reproducibility



DIGITAL PUBLISHING

Articles designed
for optimal readership
across devices



FOLLOW US

@frontiersin



IMPACT METRICS

Advanced article metrics
track visibility across
digital media



EXTENSIVE PROMOTION

Marketing
and promotion
of impactful research



LOOP RESEARCH NETWORK

Our network
increases your
article's readership